UNIVERSITY OF BELGRADE

FACULTY OF PHYSICS

Miljan Dašić

MODELING THE BEHAVIOUR OF CONFINED DIPOLAR AND IONIC SYSTEMS

Doctoral dissertation

Belgrade, 2019

УНИВЕРЗИТЕТ У БЕОГРАДУ

ФИЗИЧКИ ФАКУЛТЕТ

Миљан Дашић

МОДЕЛОВАЊЕ ПОНАШАЊА ПРОСТОРНО ОГРАНИЧЕНИХ ДИПОЛНИХ И ЈОНСКИХ СИСТЕМА

Докторска дисертација

Београд, 2019

Thesis advisor, Committee member:

Dr. Igor Stanković

Associate Research Professor

Institute of Physics Belgrade

University of Belgrade

Committee member:

Prof. Dr. Đorđe Spasojević

Professor

Faculty of Physics

University of Belgrade

Committee member:

Prof. Dr. Milan Knežević

Professor

Faculty of Physics

University of Belgrade

Date of the defense: 23.9.2019.

Посвећујем ову докторску тезу својој породици,
оцу Драгану, мајци Смиљи и брату Стефану,
са искреном и јаком жељом да кући Дашића вазда буде на понос.

Acknowledgments

I thank Dr. Aleksandar Bogojević, the director of IPB, for giving me the opportunity to work at IPB.

During my doctoral studies, I was taking active participation in the Petnica Science Center (PSC) seminars of physics for several years, as a lecturer and as a mentor on yearly projects. It was my sincere pleasure to be a mentor of talented high school students on their research projects in physics and to guide them in their first steps into science. I enjoyed seeing the joy for research of those high school students, who reminded me of myself in their age, since I used to be a participant of the same seminar back in the days when I was a high school student. It is an interesting fact worth of mentioning, that my mentor on two of my PSC projects was Dr. Aleksandar Bogojević and that I had a great opportunity to come in contact with SCL back in those days. That first sparkle of interest in numerical simulations in physics which was lighted up then still glows and it attracted me to SCL for my master and doctoral studies, after completing undergraduate studies of physical electronics at the Faculty of Electrical Engineering, University of Belgrade. The results of my mentorship on PSC physics seminars are three completed yearly projects, presented at the annual conferences called "A step into science", which were held in Petnica (municipality of Valjevo, Serbia). The reports of those projects in a form of scientific paper have been published in "Petničke sveske". Happiness of my PSC students coming from the successful completion of their projects made me happy as well and inspired my own research efforts.

I am also thankful to all my friends and relatives whose support and love mean a lot to me. Especially, I would like to mention my friends, members of the Society of Gusle Players "Serdar Janko Vukotić" from Belgrade, with whom I share interest for epic poetry and singing to the accompaniment of the gusle (a single-stringed traditional musical instrument). Sincerely thanks for all the memorable hours that we have spent listening to the sounds of our favourite musical instrument.

Finally, I am infinitely thankful to my family, father Dragan, mother Smilja and brother Stefan, for their unconditional love, understanding and support.

Modeling the behaviour of confined dipolar and ionic systems

Abstract

In this doctoral thesis confined dipolar and ionic systems have been modelled and investigated, namely dipolar tubes and helices composed of dipolar hard spheres and ionic liquids. Mutual for those systems is the fact that their structure and behaviour are dominated by long-range interactions, i.e., dipole-dipole interaction in case of dipolar systems and Coulombic interaction in case of ionic systems. The feature of pronounced ordering of formed configurations and possibility of manipulating them via externally applied fields (magnetic/electric field in case of magnetic/electric dipoles and electric field in case of ions) attract attention of condensed matter physics.

The first part of this doctoral thesis, which is dedicated to dipolar systems, is dealing with the investigation of the structure and cohesive energy in tubes and helices composed of dipolar hard spheres. A complex dependence of cohesive energy on surface packing fraction and dipole moment orientation has been observed. In case that single-thread helices are considered, the lowest cohesive energy is achieved at the highest surface packing fraction. Besides that, an interesting non-monotonic behaviour of the cohesive energy as a function of the surface packing fraction has been obtained. In case of multi-thread helices, a new phase, showing remarkably lower cohesive energy, has been determined. This phase is referred to as ZZ tube and it consists of threads following the confining cylinder's axis, labeled as the z axis, in terms of both spatial and dipole moment orientation. Actually, in case of ZZ tubes dipolar hard spheres are arranged into a local triangular lattice, with densely packed threads following the z axis.

In the scope of this doctoral thesis dipolar configurations under the condition of cylindrical confinement are considered, meaning that dipolar spheres are placed on a confining cylinder. First question which arises is what are the possible configurations, since there is an interplay between the two components, i.e., positioning

and dipole moment orientation of the particles. For a fixed geometry, only certain dipole moment orientations lead to stable configurations. The above mentioned two components can be treated as independent variables, while dependent variable is the cohesive energy emerging from the dipole-dipole interactions. Accordingly, geometry is kept fixed, while dipole moment orientation is varied and the dependence of cohesive energy on dipole moment orientation is determined. In an analogous way, dipole moment orientation is kept fixed, while geometry is varied, i.e., the radius of confining cylinder, leading to the dependence of cohesive energy on geometry. Besides the cohesive energy, some other dependent variables are considered, like the total polarization of a dipolar configuration. Except from the theoretical relevance, dipolar tubes and helices represent *model systems* which might be useful for other scientific areas. Modeling of dipolar tubes and helices might provide better understanding of certain biological structures (for example, microtubules) or macromolecules (protein folding is dominated by electric dipole-dipole interactions). Due to the mechanical flexibility of dipolar structures and possibilities of manipulating them by external electric or magnetic fields, they might be useful in the synthesis of electronic devices.

In the second part of this doctoral thesis, which is dedicated to ionic systems, a molecular dynamics (MD) based modeling approach for simulating mesoscopic phenomena related to lubrication with ionic liquid (IL) lubricants has been developed. In that approach, geometry of the system allows a variable confinement gap between solid plates and consequently a varying amount of lubricant in the gap. A coarse grain MD description of: (i) IL lubricant, which can expand into lateral reservoirs, and (ii) FCC (111) structured solid plates has been employed. Namely, two models of IL: (a) the salt-like model (SM) and (b) the tailed model (TM) have been implemented. In case of (a) SM model, IL consists of spherical cations and anions, while in case of (b) TM model, a neutral spherical tail is attached to the cation via an elastic spring. Three relevant TM models have been examined by varying the size of neutral tail. The effects of confinement on flow and lubrication properties of SM and TM ionic liquids, that were subjected to dynamic regimes of cyclic loading and shearing, have been investigated. The impact of confinement on ionic arrangement

and mechanical response of SM and TM ionic liquids has been studied in detail and compared to bulk properties. In case of TM models the influence of the molecular geometry of the cation on the response of IL to confinement and imposed mechanical deformations (normal load, cyclic loading and shearing) has been investigated. Although it is simple, TM model recovers a wide range of structures seen in bulk ILs: simple cubic lattice for small tails, liquid-like state for symmetric cation-tail dimers, and layering for large tails. The dependence of normal force on interplate gap can be related to ionic layering inside the gap. In investigated TM models of IL, specific friction is low and friction force decreases with neutral tail size. As a concluding remark, it has been found that the size of neutral tail from cation-tail dimer has a huge impact on structure and tribological behaviour of confined ionic liquids.

Ionic liquids are composed of large asymmetric and irregularly shaped organic cations and anions. Irregularity effectively prevents low-temperature ordering and crystallization of ILs, hence they are usually in the melted or glassy state. Physical properties of ILs: negligible vapour pressure, high-temperature stability, high ionic conductivity, chemical stability and possibility of external control, make them relevant to various applications. Modeling of ionic liquids is an interesting problem from the theoretical point of view due to their ordering and possibility of manipulating them via external electric fields. On the other side, ionic liquids are high quality lubricants used for friction reduction and wear prevention and modeling of ILs gives an insight about their industrial applications.

Keywords: dipolar hard spheres, tubes, helices, Lekner summation, ionic liquids, tribological behaviour, molecular dynamics

Scientific field: Physics

Research area: Condensed matter physics

UDC number: 538.9

Моделовање понашања просторно ограничених диполних и јонских система

Сажетак

У овој докторској тези моделовани су и испитани просторно ограничени диполни и јонски системи, тачније диполне тубе и хеликси састављени од дипол-них чврстих сфера и јонске течности. Заједничко за ове системе је чињеница да су им структура и понашање претежно одређени дугодометним интеракци-јама, дипол-диполном интеракцијом у случају диполних система, односно Ку-лоновом интеракцијом у случају јонских система. Одлика наглашеног струк-турног уређивања формираних конфигурација и могућност манипулације њима преко екстерно примењених поља (магнетно/електрично поље у случају магнет-них/електричних дипола, односно електрично поље у случају јона) привлаче пажњу са аспекта физике кондензоване материје.

Први део ове докторске тезе, који је посвећен диполним системима, бави се истраживањем структуре и кохезионе енергије у тубама и хеликсима који су састављени од диполних чврстих сфера. Добијена је комплексна зависност кохезионе енергије од површинске густине паковања и оријентације диполних момената. У случају једноструко намотаних хеликса, најнижа кохезиона ен-ергија постигнута је при највишој површинској густини паковања. Поред тога, добијена је занимљива немонотона зависност кохезионе енергије од површинске густине паковања. У случају вишеструко намотаних хеликса откривена је нова фаза, која показује приметно нижу кохезиону енергију. Ова фаза названа је ZZ туба, а састоји се од нити које прате осу конфинирајућег цилиндра, означену као z оса, у смислу просторне и оријентације диполних момената. Заправо, у случају ZZ туба диполне чврсте сфере су уређене у локално троугаону решетку, са густо пакованим нитима које су паралелне са z осом.

У оквиру ове докторске тезе разматране су диполне конфигурације при услову цилиндричног просторног конфинирања, што значи да су диполне сфере постављене на конфинирајући цилиндар. Прво питање које се поставља јесте

које су могуће конфигурације, са обзиром да постоји преплитање две компоненте, просторног позиционирања и оријентације диполних момената честица. За фиксирану геометрију, само одређене оријентације диполних момената доводе до стабилних конфигурација. Поменуте две компоненте могу се третирати као независне променљиве, а зависна променљива је кохезиона енергија услед дипол-диполних интеракција. Према томе, геометрија је фиксирана, а диполна оријентација се варира и одређује се зависност кохезионе енергије од оријентације диполних момената. На аналоган начин, диполна оријентација је фиксирана, а геометрија се варира, рецимо радијус конфинирајућег цилиндра, што доводи до зависности кохезионе енергије од геометрије. Осим кохезионе енергије, разматране су и друге зависне променљиве, као што је укупна поларизација диполне конфигурације. Поред теоријског значаја, диполне тубе и хеликси представљају *моделне системе* који могу бити корисни у другим научним областима. Моделовање диполних туба и хеликса може пружити боље разумевање одређених биолошких структура (на пример, микротубула) или макромолекула (савијање протеина доминантно је одређено електричним дипол-диполним интеракцијама). Услед механичке флексибилности диполних структура и могућности за манипулацију њима преко екстерних магнетних или електричних поља, дате структуре могу бити корисне у синтези електронских уређаја.

У другом делу ове докторске тезе, који је посвећен јонским системима, развијен је приступ у моделовању на бази молекуларне динамике (MD) за симулирање мезоскопских феномена повезаних са подмазивањем јонским течностима. У том приступу, геометрија система омогућава променљиви конфинирајући процеп између чврстих плоча и последично променљиву количину подмазивача у процепу. Примењен је опис на бази MD укрупњавања скала: (i) јонске течности као подмазивача који се може проширити у латералне резевоаре и (ii) FCC (111) структурираних чврстих плоча. Наиме, имплементирана су два модела јонске течности: (a) модел на бази соли (SM) и (b) модел са репом (TM). У случају (a) SM модела јонска течност се састоји од сферичних катиона и аниона, док је у случају (b) TM модела неутрални сферични

реп везан за катион еластичном опругом. Испитана су три релевантна TM модела варирањем величине неутралног репа. Истражени су ефекти конфинирања на протицање и подмазивачке особине SM и TM јонских течности које су изложене динамичким режимима цикличног пуњења и смицања. Утицај конфинирања на уређивање јона и на механички одзив SM и TM јонских течности детаљно је проучен и упоређен са особинама датих јонских течности у балку. У случају TM модела испитан је утицај молекуларне геометрије катиона на одзив јонске течности при конфинирању и при задатим механичким деформацијама (нормална сила, циклично пуњење и смицање). Иако једноставан, TM модел реконструише широки опсег структура виђених код балк јонских течности: једноставна кубична решетка за мале репове, течно стање за симетричне катион-реп димере и уређивање у слојеве за велике репове. Зависност нормалне силе од величине процепа између чврстих плоча може се повезати са уређивањем јона у слојеве унутар процепа. У испитаним TM моделима јонске течности, специфично трење је мало, а сила трења опада са порастом величине неутралног репа. Као закључна напомена може се навести да је установљено да величина неутралног репа из катион-реп димера има велики утицај на структуру и триболошко понашање конфинираних јонских течности.

Јонске течности су састављене од великих асиметричних органских катиона и аниона неправилног облика. Неправилност облика спречава уређивање на ниским температурама и кристализацију јонских течности, тако да су јонске течности углавном у топљеном или стакластом стању. Физичке особине јонских течности: занемарљив притисак паре, високотемпературна стабилност, висока јонска проводљивост, хемијска стабилност и могућност екстерне контроле чине их релевантним за различите примене. Моделовање јонских течности је интересантан проблем са теоријског становишта услед структурног уређивања и могућности за манипулацију јонским течностима преко екстерних електричних поља. Са друге стране, јонске течности су високо квалитетни подмазивачи који се користе за смањење трења и спречавање хабања, а моделовање јонских течности даје увид о њиховим индустријским применама.

Contents

Chapter 1 Introduction

1.1 General overview

In this doctoral thesis there are two research topics involving systems with long-range interactions, namely structures composed of dipolar hard spheres and ionic liquids. Investigation of dipolar hard spheres is directed towards exploring the cohesive energy-packing relations, while investigation of ionic liquids is dedicated to determining the structure, flow properties and tribological behaviour of confined ionic liquids. In a higher instance the topics share two important aspects which unify them: long-range interactions and accentuated self-assembly behaviour. Both dipole-dipole interaction in dipolar systems and Coulombic interaction in ionic systems are long-ranged. An interaction $V(r)$ depending on the distance between the interacting particles r as $V(r) \propto r^{-p}$ is considered to be *long-range interaction* if it meets the condition: $p \leq n_{\mathrm{d}}$, where n_{d} is the dimensionality of the system. In case of the dipole-dipole interaction, which has the same functional form (up to a constant) for magnetic and electric dipoles, it stands $V_{\mathrm{dd}} \propto r^{-3}$, while in case of Coulombic interaction $V_{\mathrm{Clb}} \propto r^{-1}$. In case of a $3D$ system, i.e., $n_{\mathrm{d}} = 3$, both of the mentioned interactions meet the criterion of being long-range interactions. Another mutual feature of both of those systems is accentuated self-assembly under the conditions of spatial confinement. Dipolar hard spheres self-assemble into tubes and helices on a confining cylinder. It is possible to obtain ordering of ionic liquid into regular cationic-anionic layers, starting from a random arrangement of ions, in case that ionic liquid is placed into a gap between two solid surfaces. A common consequence of long-range interactions is ordering of the particles on length scales which are much longer than the size of the particles itself. One might expect that the na-

ture of long-range interactions combined with the conditions of spatial confinement should lead to the emerging of ordered and stable structures. The systems that have been investigated in this thesis are $3D$ and they are also infinite: (i) tubular and helical dipolar structures are $1D$ infinite and periodic, (ii) ionic liquid is $2D$ infinite. Besides the self-assembly under conditions of spatial confinement, mutual for both systems is rich behaviour in terms of state and phase transitions.

1.2   Confined dipolar systems

Particles with permanent dipole moment are known for outstanding self-assembly properties [1–3]. Self-assembly of hard dipolar spheres is an active research topic dedicated to the investigation of the mechanisms by which ordered dipolar structures form. To be more precise, we are focused on the self-assembly of spatially confined dipolar systems. Spatial confinement imposes formation of specific structures, e.g., cylindrical confinement imposes self-assembly of particles into tubular and helical structures. Interaction of each pair of dipolar particles is the dipole-dipole interaction, which is described by the same term (up to a constant) in case of both magnetic and electric dipoles. Therefore, we consider structures composed of dipolar hard spheres in a general case. Depending on given examples in nature or technology, we compare considered structures with building elements composed of particles with permanent magnetic or electric dipole moment. Self-assembly of dipolar particles and a large number of different ways for their application have always been attracting interest due to a spontaneous transition from disordered into ordered state. This topic is attractive because it is relevant from theoretical point of view since dipole-dipole interaction is a long-range and anisotropic interaction which leads to the complexity of structures formed via dipole-dipole interaction. Besides that, examples of dipolar structures in nature and technology are numerous, especially in biology and some areas of nanotechnology.

Generally speaking from the aspects of geometry and without the need for the presence of dipole-dipole interaction in given examples, tubular and helical structures are basic structural elements in many biological systems. Those structures are

important building blocks of cells. Illustrative examples include bacterial flagella [4] and microtubules [5, 6]. Additional examples of tubular and helical structures can be found in various materials with specific building blocks, which can be: coiled carbon nanotubes [7], DNA molecule [8], nanoparticles [9], amphiphilic molecules [10–12]. In biology there is an example of magnetotactic bacteria whose dynamics is especially sensitive under external magnetic field, so that microstructures formed by those bacteria can be manipulated via application of external magnetic field [13].

Another example of the importance of dipole-dipole interaction in biology is the formation of proteins. All processes in protein formation, i.e., folding of individual aminoacids into a secondary structure and later-on formation of tertiary and quaternary structures, depend on electric dipole-dipole interactions [14, 15]. Formation of erythrocytes, which have a vital importance for human health, is realized through several steps. Each of those steps includes electric dipole-dipole interactions. Any kind of mutation which harms the dipole-dipole interaction suppresses proper formation of erythrocytes, which as a response disables their capability of transporting oxygen in the blood system.

In nanotechnology self-assembly of binary mixtures of magnetic nanoparticles can lead to the synthesis of very strong magnets [16]. Interaction between magnetic planar layers can enable formation of $3D$ structures with a great potential of applications in microfabrication of electronic devices [17]. Ground states of microstructures in ferofluid monolayers, in which the interaction between magnetic particles is the dipole-dipole interaction, have been studied in detail [18].

In the following text an overview of the accomplishments in experimental and numerical studies of helical structures' formation is given. Self-assembly of cubic magnetic nanoparticles [19] and colloidal magnetic clusters [20] into helical structures has been accomplished experimentally, without the need for the pre-existing templates. Another result following this research line tells that hard spherical particles confined inside narrow cylinders spontaneously group themselves into helical structures. This has been achieved both via numerical simulations [21, 22] and experimentally [23]. Hard spheres with a permanent dipole moment can be utilized as a model for describing more complex helical molecular structures [24] and

microtubules [25, 26].

The overview of the topic related to the self-assembly of dipolar particles should mention the pioneering theoretical work of Jacobs and Beans [27] followed by the work of De Gennes and Pincus [28]. Those works have provided the insight into the microstructure of self-assembled spatially free spherical dipoles. More recently, ground states of self-assembled magnetic structures have been thoroughly investigated via numerical simulations [29]. The results of that paper have shown that for the number of particles $N \geq 14$ ground state is obtained via ring stacking into tubes. In the experimental work [30] mechanical properties of the chains, rings and tubes composed of ferromagnetic hard spheres of macroscopic dimensions (e.g., diameter of particles is 6 mm) have been investigated. Besides that, the authors of that work have provided an illustrative example which shows a spontaneous wrapping of a straight chain into a tube. A general scientific problem of understanding the mechanisms via which the building blocks, i.e. dipolar hard spheres, self-assemble into structures and gain functionality is demanding and has a wide scientific importance [31–34].

In this thesis one of the two directions of research is dedicated to the modeling of confined dipolar systems. By confinement we assume cylindrical confinement, i.e., dipolar hard spheres are constrained to compose a configuration on top of an imagined cylinder, at a cylinder's prescribed radius. Following this problem definition, we systematically investigate long tubes and helices. The tubes are formed via ring stacking, i.e., by periodical repeating of an unit cell containing a ring along an axis. The helices are formed by rolling of one or multiple threads on a cylindrical confinement surface. In terms of geometry, rolling is very much like $1D$ crystal formation, which is conducted by replicating a patch of dipolar spheres on a cylindrical confinement surface along the helix backbone. There is an endless number of different helical configurations, but we point out that the densely packed structures exist at well-defined points in parameter space.

In Reference [35], very much in analogy to carbon nanotubes ($CNTs$), it was shown that densely packed helices are defined by two numbers: lattice patch dimensions n_1, n_2. The lattice patch dimension n_1 is an integer which counts the number

of spheres in one full turn around the confining cylinder and it is directly related to the radius of a helix. An increase of n_1 corresponds to the increase of the radius of a helix. On the other side, the lattice patch dimension n_2 is an integer which counts the number of threads building up the helix and equivalently it counts the number of spheres along the confining cylinder's surface between two consecutive helix turns. Realizing the fact that helix formation is dictated by those two preferential directions, i.e., turns around the cylinder's surface (related to n_1) and threads along the cylinder's surface (related to n_2), we have decided to assign to the particles dipole moments following those two preferential directions. We have defined $\vec{a}_1$ and $\vec{a}_2$ dipole moment orientations. In both of them the dipole moment of a certain sphere points to its consecutive sphere, where in the first case consecutive spheres compose turns around the confining cylinder, while in the second case they follow the threads along the cylinder's surface. Besides those two dipole moment orientations assigned according to the geometrical features of helices, we have performed energy minimization in order to obtain dipole moment orientation which corresponds to the ground state and that type of dipole moment orientation is called *ground state dipole moment orientation*. We show that pairs (n_1, n_2) represent the two numbers of threads which can generate geometrically the same densely packed helices, however those helices are energetically completely different depending on the type of their dipole moment orientation. We should mention that densely packed tubes are basically sub-classes of helices (similar to armchair and zig-zag $CNTs$) for special cases of the values of lattice patch dimensions n_1, n_2.

1.2.1 Outline of the research on cylindrically confined dipolar systems

The goal of the study of confined dipolar systems, i.e., dipolar tubes and helices, is to address the intimate link between the microstructure and cohesive energy. In order to do so, it was necessary to precisely define the geometry, establish dipole moment orientations and appropriately calculate cohesive energy. The research dealing with confined dipolar systems (except for the parts related to introduction and

conclusions) is placed in the chapter *Confined dipolar systems*, which consists of five sections. In the section *Geometry of helices and tubes composed of hard spheres* the geometry is explained in details. Next, the dipolar interaction model is introduced and a link between the dipole distribution and the microstructure is established in the section *Dipole moments*. Speaking in terms of cohesive energy, since the dipolar hard spheres interact via two interaction potentials: potential of hard spheres and dipole-dipole interaction potential, an appropriate method for summing the dipole-dipole interactions should be implemented. Once that task is realized, an efficient energy minimization method for determining the ground state of dipolar structures should be introduced. In the section *Methods* the Lekner-type method for summing the dipole-dipole interactions which we have implemented for calculating the cohesive energy of considered dipolar structures is presented. Besides that, the method for obtaining the ground state dipole moment orientation of a given dipolar structure is presented as well. At that point, after the geometry, dipole moments and method for treating long-range dipole-dipole interactions are established, it is possible to switch the focus to configuration-cohesive energy relations. Namely, in the section *Degeneracy in 2D triangular and square lattice and properties of tubes* it is shown that triangular and square lattices of dipolar hard spheres posses degeneracy in terms of cohesive energy, which breaks-up with curvature in case of *AA* and *AB* tubes. In the following section *Cohesive energy-packing relations in dipolar helices* starting from the simplest case corresponding to a single-thread helix, the relationship between the surface packing and the resulting macroscopic properties, such as cohesive energy or overall polarization, is discussed. Then, the more complex situation of multi-thread helices with densely packed constitutive particles is addressed. There, the degree of alignment (especially in the ground state) between dipole moment orientation and helix axis is analyzed. In the section *Confined dipolar systems* of the chapter *Conclusions*, the conclusions and possible connections of the investigated model system with some real systems, namely with biological microtubules, are given.

1.3   Motivation for the research of ionic liquids

Tribology is the name of a multidisciplinary scientific area which is related to the phenomena of friction, lubrication and wear. In tribology, the knowledge and competences of physics, chemistry and high performance computing are overlapped and combined [36]. Term nanotribology is related to the specific branch of tribology which studies the phenomena of friction, lubrication and wear at the nanoscale. Scientific discipline of computational nanotribology has been well-established in the last couple of decades [36, 37]. Powerful computational resources enable application of the methods of computational nanotribology in the cases of increasing complexity.

There are numerous systems which are of interest in the field of computational nanotribology, however we have focused on ionic liquids. They are a promising candidate for the applications as a high quality lubricant, especially in automotive industry. Bearing that in mind, our investigation in the framework of this topic is directed towards the understanding of physical properties of ionic liquids related to the friction, lubrication and wear phenomena. After gaining a relevant expertise, we might realize the potential of using ionic liquids as a lubricant in automotive industry. Let us start the considerations with this, in a certain way surprising fact, that approximately one-third of the fuel energy in a passenger car is consumed by friction [38]. Therefore, understanding of the lubrication mechanisms in an automotive vehicle's engine is highly important. Numerical simulations at the molecular scale can provide insights which are necessary for understanding the mechanisms governing the system's behaviour, such as structural changes in the lubricant layers during shearing and normal load application, as well as the interaction between the lubricant and solid surfaces. In recent studies of the nanoscopic friction phenomenon, based on the Molecular Dynamics (MD) method, ionic liquids are considered as a lubricant [39]. The width of lubricating films of just a few molecular layers is relevant for suppressing wear and achieving low friction [40–43]. In 2001, for the first time it was published that ionic liquids have a great potential as lubricants. Since then, they attract attention in the field of tribology due to their remarkable characteristics relevant for lubrication and wear prevention, when compared to conventional

lubricating oils which are generally used. The number of publications dealing with ionic liquids is constantly increasing, in both forms of journal articles and industrial patents. Therefore, there is a wide interest for this topic from both fundamental and industrial aspects [44].

In industrial applications, there are considerations of using ionic liquids as a neat lubricant and as an additive [45–47]. Significant improvements in friction and wear reduction have been achieved experimentally [46]. Namely, in Reference [46] the authors have achieved coefficient of friction reduction for 60% and wear reduction for three orders of magnitude. They have added and mixed certain ionic liquids with synthetic lubricating oils.

Understanding and description of nanoscopic friction in ionic liquids, as well as their structure under imposed conditions, represents a challenging scientific problem and so far there have been just a couple of studies in this direction, e.g., References [48, 49]. Detailed studies of ILs at the nanoscale using the methods of computational physics provide a wider perspective as compared to experimental studies where the investigation is restricted to certain ILs which posses certain values of relevant physical parameters. On the other side, in simulations ILs are considered in a generic way and it is possible to explore a wide range of parameter values. Practically, it means that simulations enable the design of favourable characteristics of ILs, and later–on it is possible to experimentally synthesize certain ILs, based on the simulated ones.

In this thesis one of the two directions of research is dedicated to the modeling of confined ionic systems, namely ionic liquids (ILs). In order to better understand the structure and behaviour of confined ionic liquids, we investigate the same ionic liquids in the bulk state, as well. We have started from the basis, by implementing and studying the simplest IL model which includes a positively charged spherical cation and a negatively charged spherical anion, i.e., SM (salt-like model). This was followed by the implementation and investigation of a more realistic IL model which includes a positively charged spherical head connected by an elastic spring with a neutral spherical tail and a negatively charged spherical anion, i.e., TM (tailed model). Our interest in modeling ionic liquids comes from its scientific im-

portance. However, we bear in mind potential applications of ILs as high quality lubricants, hence we guide our research towards exploring IL lubricating properties. Simulation setup with two solid plates between which IL is confined, is designed with the aspirations of probing IL lubricating abilities. To enclose this exposé, in this section we provide general introduction into ionic liquids, which is followed by the introduction into SM and TM model based studies, respectively.

Ionic liquids are two-component systems composed of large asymmetric and irregularly shaped organic cations and anions. The feature of irregularity is important as it is effectively preventing low-temperature ordering and crystallization. Therefore, ILs are usually in the melted or glassy state. Physical properties of ILs like negligible vapour pressure, high-temperature stability, high ionic conductivity and also a great variety of ILs and their mixtures highlight them as potentially relevant to lubrication [44, 50]. In addition, their properties can be modified by an applied voltage using confining charged surfaces in order to build–up an electric field across the nanoscale film. The applied potential can affect the structure of IL layers and lead to externally controllable lubricating properties [49, 51, 52].

A large number of variations in IL composition is possible, estimated at the order of magnitude of 10^{18} different ILs [53]. From their variety stems the possibility of tuning their physicochemical properties which can affect lubrication such as viscosity, polarity, surface reactivity by varying their atomic composition, as well as the cation-anion combination. Hence, it would be advantageous if we could deduce the general relations between the molecular structure and the anti-wear and lubrication properties of ILs.

Previous work employing Lennard-Jones fluids has provided insights into the complete dynamic diagram of confined liquids, including wall slip, shear banding and solid friction. In terms of fluid complexity these studies have mainly employed mono-molecular systems, and only a few authors have considered mixtures of molecules [54, 55]. In addition to inherently being a mixture of cation and anion molecules, ILs involve long-range Coulombic interactions inducing long-range order on far greater scales than the IL itself [39, 43, 56]. Detailed investigation of ILs as lubricants at the nanoscale is therefore essential for exploring the potentials of implementing

them in lubrication systems.

Our specific goal, related to industrial applications of IL lubricants, is to achieve a representation of the tribological system which is relevant to automotive power-train applications. As approximately 45% of the engine friction losses occur in the piston assembly [38], our initial target is to mimic the conditions observed in the piston ring–cylinder liner contact, in terms of pressure, temperature and shear rates. In addition, in order to be able to achieve length– and time– scales that can be of relevance to the real–life systems, it is necessary to apply appropriate simulation methodologies, such as the use of coarse grain molecular dynamics [57–60].

1.3.1 Salt model of ionic liquid

The focus of our study employing the SM ionic liquid, which contains salt–like spherical cations and anions, is on investigating lubricating ability and flow proper-ties of ILs. Regarding the ability of ionic liquids to dynamically penetrate between surfaces, i.e. wetting, sometimes it is considered that a low contact angle of the lubricant indicates the affinity between the liquid and the surface, since the liquid is more likely to stay in the area in which it was initially placed. It is also expected that a lubricant is going to penetrate into small–gap components. However, the effect of wettability of the ionic liquids is not understood well. The wetting of plate surfaces such as mica is known to be partial by at least some ILs [61, 62]. Lubrication necessarily involves intimate molecular features of the liquid–solid plate interface, related with those mechanisms determining the ionic liquid's wetting of the plate. When ILs are used as lubricants and, as such, confined between solid plates, their ions are ordered into layers and adsorbed onto surfaces [63]. These adsorption layers can reduce friction and wear, particularly in the case of boundary lubrication [63].

Recent studies of IL lubricants [49, 51, 52, 64] have shown that if the molecules interact via non–bonded potentials (Lennard–Jones and Coulombic potential), this can capture all main physical attributes of the IL–lubricated nanotribological sys-tem. Therefore, molecular–scale simulations can provide important insights which are necessary for understanding the differences in flow behaviour between bulk and confined liquid lubricants and the mechanisms behind, such as boundary layers for-

mation in case of shearing and/or applied normal load.

We utilize our coarse grain MD simulation setup consisting of two solid plates and an ionic liquid lubricant placed between them [64]. The motivation for the chosen values of relevant model parameters (i.e. velocities, pressures, temperatures, time duration of simulations) comes from potential applications of ILs as lubricants in automotive industry. Under typical operation of internal combustion engines, the conditions inside the combustion chamber vary significantly. Temperature can range from 300 K to the values higher than 2000 K, while pressure ranges from atmospheric to the values higher than 10 MPa [38]. The piston reciprocates with a sinusoidal velocity variation with speeds varying from zero to over 20 m/s, with a typical velocity being around 1 m/s. The time required for one revolution of the engine is of the order of 10^{-2} s, while the total distance travelled by the piston over this period is of the order of 0.2 m. Such scales are typically modeled using continuum mechanics simulations. However, such simulations cannot provide the physical insight which is necessary for understanding the molecule–dependent processes that affect the tribological phenomena. Therefore, we have implemented a coarse grain MD simulation setup which can, inter alia, provide useful insights into lubrication mechanisms of piston ring–cylinder liner contact in automotive engines. Our simulation setup consists of two solid plates and an IL placed between them. It also includes lateral reservoirs into which the IL can dynamically expand.

The determination and design of new applicable lubricants require understanding of both general and specific behaviour of liquids when exposed to nanoscale confinement, shearing and normal load. In accordance with those facts, our focus is on determining general features of ILs as nanoscale lubricants. Hence, we have chosen the model of a generic IL which is simple in order to provide a wide perspective of relevant mechanisms governing the IL lubrication principles.

1.3.2 Tailed model of ionic liquid

Since 2001., when ionic liquids were first considered for lubrication applications [65], there has been a large number of experimental studies in that direction. It has been observed that the alkyl chain length of the cations affects the IL viscosity [44],

melting point [44] and pressure-viscosity coefficients [66]. Related specifically to lubrication, References [53, 67] explored the impact of cationic alkyl chain's length on the tribological properties of ILs. ILs considered in those references have the same cations but different anions: symmetric hexafluorophosphate $[PF_6]^-$ and asymmetric bis(trifluoromethylsulfonyl) imide $[Tf_2N]^-$, respectively. Still, while the authors of Reference [67] observed that the coefficient of friction (COF) decreases from 0.25 to 0.15 with the increase of alkyl chain length $n_C = 2$ to 12 (n_C is the number of carbon atoms), the authors of Reference [53] observed that the COF increases from 0.025 to 0.1. The $IL's$ wetting properties are also sensitive to its molecular geometry. ILs change wetting behaviour depending on the anion size [61, 62, 68]: from the absence of wetting to partial or complete wetting. A well–studied IL $[BMIM]^+ [PF_6]^-$ exhibits full wetting at the interface with mica substrates [62, 68]. On contrary, $[BMIM]^+ [TFSI]^-$ shows partial wetting on mica [61, 62]. In these examples, ILs have the same cation and different anions.

An important observation about the structure of confined ILs is their arrangement into positively and negatively charged ionic layers and adsorption onto solid surfaces [63, 69]. These ionic adsorption layers should reduce friction and prevent wear, especially in the case of boundary lubrication [63]. The wear is reduced primarily in two ways: via high load-carrying capability and self-healing of adsorbed IL layers. Still, these two processes seem conflicting with each other since high load-carrying capability requires strong adsorption of the lubricant to the surface while self-healing requires high mobility [36]. Understanding the driving forces between them requires relating the molecular structure and flow properties of confined IL. In Reference [70] the authors have evaluated tribological properties of different ionic liquids by pendulum and ball on disk tribo testers. They have considered ILs consisting of imidazolium cations with different alkyl chain length and $[Tf_2N]^-$ anion as lubricants. Their main observation is that the increment of alkyl chain length can reduce friction and wear of sliding pairs in the elastohydrodynamic lubrication regime (EHL) as a consequence of increased viscosity. Generally, the conclusion is that longer alkyl chains lead to better tribological performance. Related to the impact of alkyl chain length on the structure of ILs, in Reference [71] the authors have experi-

mentally obtained the formation of tail–to–tail bilayers of cations if their alkyl chain length is large, in case of confinement between solid surfaces. Their observations are in accordance with other experimental investigations of IL lubricants [72–74]. It is worth of mentioning that we have obtained similar configurations via numerical simulations of ILs confined between two solid plates, where tail–to–tail formation in the middle of the interplate gap is visible.

The focus of our TM model based study is on the systematic investigation of the flow properties and lubrication mechanisms of ionic liquids modeled with a generic coarse grain model which considers a variable shape of the cation. We investigate the impact of cationic tail size on the structural and tribological properties of ILs via MD simulations. Such an idea is meaningful since previous theoretical studies have pointed out that confinement modifies the behaviour of ILs and despite the good wetting nature, the slip is present at the plates [43]. Coulombic interactions in ILs induce long-range ordering [39, 43, 56], which in turn can influence their lubrication response. Previously, coarse grain MD simulations [40–42, 57–60] were used to study thin lubricant films subjected to the shearing between solid plates.

1.3.3   Outline of the research on model ionic liquids

The research dealing with ionic systems (except for the parts related to introduction and conclusions) is presented in chapter *Ionic liquids*, which consists of four sections. Let us present them briefly in the following text. A method of choice for studying the structure and lubrication characteristics of ionic liquids at the nanoscale, in the framework of this doctoral thesis, is Molecular Dynamics (MD) method. Accordingly, in section *Methods MD* method and $LAMMPS$ code for molecular dynamics are introduced. This is followed by section *Simulation setup and models of ionic liquid* which describes the SM and TM models of ionic liquid in detail, as well as the implemented MD simulation setup. The focus of *Bulk ionic liquid* section is first on obtaining the relaxed structure and then on calculating the viscosity coefficient of bulk SM and TM ionic liquids. In the following *Confined ionic liquid* section, static and dynamic behaviour of confined SM and TM ionic liquids are presented and discussed. This section also presents the results of confined $IL's$ tribological

behaviour. In chapter *Conclusions*, section *Ionic liquids*, conclusions and prospects of future directions in the investigation of ILs from both, theoretical and industrial aspects, are given.

Chapter 2   Confined dipolar systems

2.1   Geometry of helices and tubes composed of hard spheres

2.1.1   Geometry of helices

2.1.1.1   Geometry of single-thread helices

In the framework of this study, helices are composed of hard spherical particles and they are confined to a cylinder's surface, i.e., the helices are formed by rolling threads of hard spherical particles on the cylindrical surface of radius R_{cyl} [75]. Geometrical parameters that define a single helix are: the azimuthal angular shift Γ between the centers of two successive particles and the radius of the helix $R = R_{cyl} + d/2$, where d stands for the hard sphere diameter, see Figure 2.1. The radius R physically represents the distance of the closest approach between cylinder axis and center of the spherical particle. The Cartesian coordinates of particle i in a single helix are calculated as:

$$
\begin{aligned}
x_i &= R \cos{(i\Gamma)}, \\
y_i &= R \sin{(i\Gamma)}, \\
z_i &= i\Delta z,
\end{aligned}
\tag{2.1}
$$

where $i \in Z$ and assuming that one particle is at $(x, y, z) = (R, 0, 0)$. The distance between the centers of each two successive particles along the helix axis is labelled as Δz, see Figure 2.1. When constructing a helix, its radius R and azimuthal angular distance Γ have to be chosen in a way which ensures non-overlapping of hard spheres. The non-overlapping constraint is expressed for any two particles i, j
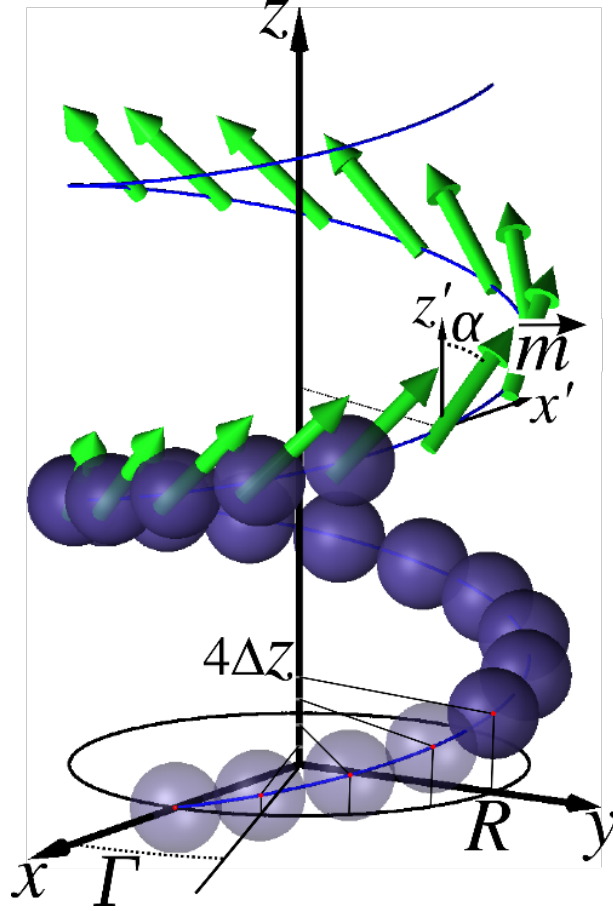
Figure 2.1: Illustration of a single thread helix with relevant geometrical parameters $(R, \Gamma, \Delta z)$ labelled. The black bold line connecting spherical particle centers represents backbone of the helix. In upper part of the figure, the azimuthal dipole moment orientation α is defined in a local coordinate system with its origin corresponding to the particle center. The z' axis is parallel to the cylinder axis.

as $|\vec{r_{ij}}| \geq d$. Since the helix thread is connected everywhere, any two successive particles are touching. Starting from Equation 2.1 we can obtain Δz as a function of other two variables, i.e., as a function of R and Γ. Let us write down Equation 2.1 taking the values of the index $i = 1, 2$: $x_1 = R \cos \Gamma, y_1 = R \sin \Gamma, z_1 = \Delta z; x_2 = R \cos (2\Gamma), y_2 = R \sin (2\Gamma), z_2 = 2\Delta z$. Distance between the centers of those two successive spheres is equal to the sphere diameter d, hence it stands:

$$d = \sqrt{(x_2 - x_1)^2 + (y_2 - y_1)^2 + (z_2 - z_1)^2}. \tag{2.2}$$

16

Taking the relations: $x_2 - x_1 = R(\cos 2\Gamma - \cos \Gamma)$, $y_2 - y_1 = R(\sin 2\Gamma - \sin \Gamma)$, $z_2 - z_1 = \Delta z$, and replacing them into Equation 2.2 we obtain:

$$d^2 = R^2 (\cos 2\Gamma - \cos \Gamma)^2 + R^2 (\sin 2\Gamma - \sin \Gamma)^2 + \Delta z^2. \tag{2.3}$$

From Equation 2.3 we obtain:

$$
\begin{aligned}
d^2 &= R^2 \left(\cos^2 2\Gamma - 2\cos 2\Gamma \cos \Gamma + \cos^2 \Gamma + \sin^2 2\Gamma \right. \\
&\left. -2\sin 2\Gamma \sin \Gamma + \sin^2 \Gamma \right) + \Delta z^2.
\end{aligned}
\tag{2.4}
$$

Bearing in mind the relations of trigonometry: $\sin^2 x + \cos^2 x = 1$, $\sin 2x = 2\sin x \cos x$, $\cos 2x = \cos^2 x - \sin^2 x$, we obtain:

$$d^2 = 2R^2 (1 - \cos \Gamma) + \Delta z^2. \tag{2.5}$$

Rearrangement of the previous equation leads to the relation expressing Δz as a function of R and Γ:

$$\Delta z = \sqrt{d^2 + 2(\cos \Gamma - 1)R^2}. \tag{2.6}$$

Thereby, variables Δz, R and Γ are not independent. Clearly, with decreasing Δz (i.e., increasing Γ) helices become more compact. Because of the connectivity, every particle in a helix has at least two neighbors, i.e., the coordination number, n_c, is always greater or equal than two ($n_c \geq 2$). We define *coordination number of a helix* as the number of neighbors each particle has, with the exception in case of particles at helix ends, since they have less neighbors. The highest packing density of the particles for prescribed helix radius R will be achieved when successive helix turns touch. In this situation of touching turns, the coordination number n_c can be either four or six. Therefore, in general, $n_c \in \{2, 4, 6\}$, where the case $n_c = 2$ corresponds to non-touching turns. Based on the coordination number n_c, we can classify helices as follows (see Figure 2.2(a)-(c)). Examples of helices with two neighbors $n_c = 2$ and four neighbors $n_c = 4$ at a prescribed cylindrical confinement, e.g., $R/d = 1.78$, are sketched in Figure 2.2(a) and (b), respectively. For a number of well-defined

(a) $n_c = 2$ (b) $n_c = 4$ (c) $n_c = 6$ (d) AA tube (e) AB tube (f) Z tube
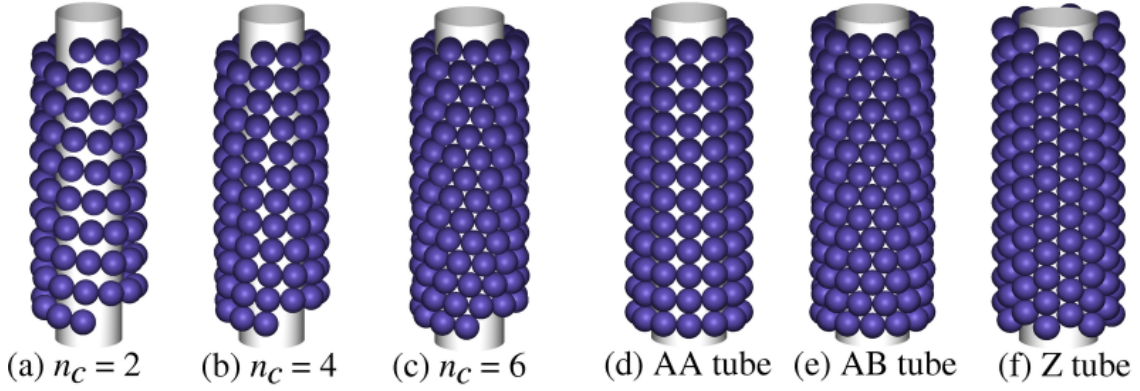
Figure 2.2: Illustration of different classes of helices, based on coordination number $n_c = \{2, 4, 6\}$. (a) Helix with non-touching turns ($n_c = 2$). (b) Helix with touching turns ($n_c = 4$). (c) Densely packed helix ($n_c = 6$). The other panels illustrate, the so called, (d) AA, (e) AB, and (f) Z tubes. The tubes can be created by strict axial stacking of unit rings. For AA and AB tubes unit rings are flat, whereas, for Z tubes the unit ring has a 'zig-zag' shape. The radii of AA and AB tubes are the same $R/d = 1.93$.

radii, as discussed in details in the coming sections, densely packed helices with six neighbors ($n_c = 6$) can be formed, see Figure 2.2(c). In the following sections of this chapter, we will also investigate stacked rings forming the so-called tubes, also depicted in Figure 2.2(d)-(f).

2.1.1.2 Order parameters for single-thread helices

The surface packing fraction is defined as the ratio of the area $S = \pi d^2/4$ covered by one particle and the area available for one particle S_{avail}, in an unrolled configuration:

$$\eta = S/S_{\mathrm{avail}}. \tag{2.7}$$

Since the distance along the z axis between successive particles is Δz, by parameterization of the helix backbone we obtain for arc length covered by one particle $L_1 = [(\Gamma R)^2 + (\Delta z)^2]^{1/2}$. The available area per particle is $S_{\mathrm{avail}} = (2\pi/\Gamma)\Delta z L_1$.

Following the definition of the surface packing density we obtain:

$$\eta = \frac{d^2}{8\Delta z R}. \tag{2.8}$$

For comparison we are going also to derive packing fraction for the tubes:

- The surface packing fraction of AA tubes is given by:

$$\eta_{\mathrm{AA}} = N_{\mathrm{ring}}d/8R_{\mathrm{AA}}, \tag{2.9}$$

  for an AA tube with N_{ring} particles per ring and the confinement radius $R_{\mathrm{AA}}/d = 1/\left[2\sin\left(\pi/N_{\mathrm{ring}}\right)\right]$, see Figure 2.2(d) for a microstructure with $R_{\mathrm{AA}}/d = 1.93$.

- Similarly, for AB tubes, the packing fraction is:

$$\eta_{\mathrm{AB}} = N_{\mathrm{ring}}d^2/8R_{\mathrm{AB}}\Delta z_{\mathrm{AB}}, \tag{2.10}$$

  with $R_{\mathrm{AB}} = R_{\mathrm{AA}}$. Here, the elevation Δz_{AB} between two consecutive rings is:

$$\Delta z_{\mathrm{AB}} = (d/2)\sqrt{2 + 2\cos\left(\pi/N\right) - \cos^2\left(\pi/N\right)}. \tag{2.11}$$

- For Z tubes, the packing fraction is:

$$\eta_{\mathrm{Z}} = N_{\mathrm{ring}}d/8R_{\mathrm{Z}}, \tag{2.12}$$

  with confinement radius $R_{\mathrm{Z}}/d = \sqrt{3}/\left[4\sin\left(\pi/N_{\mathrm{ring}}\right)\right]$.

To further characterize the helical microstructures, we introduce an additional geometrical order parameter ξ which is valid for $n_{\mathrm{c}} = 4$ and 6. This order parameter connects an individual reference particle 0 located at $\vec{r}_0$ in the helix with its two neighbors: its immediate successive particle 1 in the turn ($(\vec{r}_{01} = \vec{r}_1 - \vec{r}_0)$ and a neighboring particle 2 from the next turn ($\vec{r}_{02} = \vec{r}_2 - \vec{r}_0$), see Figure 2.3(a). The
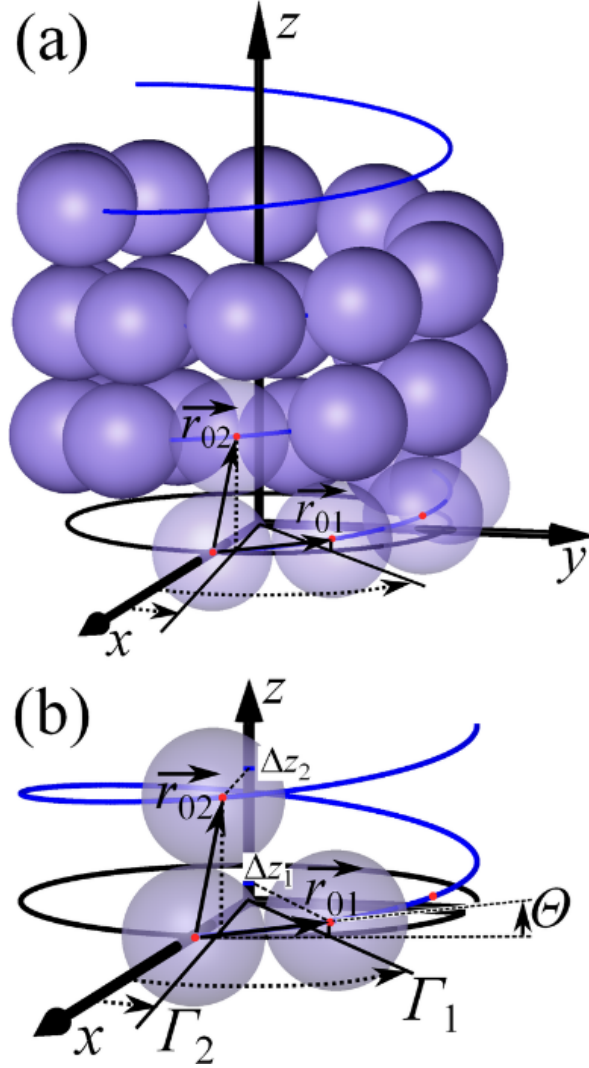
Figure 2.3: (a) Illustration of a helix made of hard spheres, helix backbone (solid line), and the vectors connecting a reference particle 0 located at $(x, y, z) = (R, 0, 0)$ with its neighbours: an immediate successive particle 1 in the turn located at $(\vec{r}_{01})$ and a neighbouring particle 2 from the next thread turn at $(\vec{r}_{02})$. (b) Overview of the principal geometrical parameters of $n_c = 4, 6$ helices: elevation angle Θ and azimuthal angular shifts Γ_1 and Γ_2 (see Equation 2.17). The corresponding elevation distances of successive particles along helix axes $\Delta z_{1,2}$ (see Equation 2.20) are also given for two possible rolling of the same helix configuration.

angular coordination order parameter is conveniently defined as:

$$\xi = 2 \frac{|\vec{r_{01}} \cdot \vec{r_{02}}|}{d^2}. \tag{2.13}$$

In the two limiting cases, the angular coordination order parameter has values:

$\xi_{\min} = 0$, for a locally square lattices on a cylinder (e.g., AA tubes, check Figure 2.2(d)) and $\xi_{\max} = 1$, for a locally triangular lattice (e.g. AB tubes, check Figure 2.2(e)). In all other cases, the value of the angular coordination order parameter ξ is between those two extreme values, i.e., $0 \leq \xi \leq 1$.

2.1.1.3   Geometry of multi-thread helices

The densely packed helices ($n_{\rm c} = 6$) can be created, in analogy with carbon nanotubes, by rolling a ribbon of a triangular lattice on a cylinder surface [35]. We deal with cylindrical geometry, infinite in one direction. We can generate these helical structures by periodical reproduction of a curved patch (unit cell) along the helical line with spanning vectors $(\vec{a}_1, \vec{a}_2)$. This curved unit cell has n_1 particles along the $\vec{a}_1$ direction and n_2 particles in the $\vec{a}_2$ direction. The values n_1 and n_2 can be seen as the two possible widths of the ribbon generating the same helical structure.

Since we deal with hard spheres and we aim to build very dense structures, the parameter space $(R, \Delta z, n_1, n_2)$ is significantly restricted. We are going to find out that only two of these parameters are independent. There exists a relationship linking the elevation angle $\Theta = \arcsin(\Delta z/d)$ and the confinement radius R, see Reference [35]. Bearing in mind that for any pair (n_1, n_2) or equivalently (n_2, n_1), we have a unique corresponding structure with $n_{\rm c} = 6$, one arrives at the following two independent equations:

$$\Theta(n_1, n_2) = \arctan\left(\frac{\sqrt{3}n_2}{2n_1 + n_2}\right) \tag{2.14}$$

and

$$
\begin{aligned}
\pi = {} & n_1 \arcsin\left[\left(\frac{d}{4R}\right)\frac{2n_1 + n_2}{\sqrt{n_1^2 + n_2^2 + n_1 n_2}}\right] \\
& + n_2 \arcsin\left[\left(\frac{d}{4R}\right)\frac{2n_2 + n_1}{\sqrt{n_1^2 + n_2^2 + n_1 n_2}}\right].
\end{aligned} \tag{2.15}
$$

We have solved those two equations in Mathematica software package [76] and obtained the sets $(\Theta, R/d)$ shown in Figure 2.4. For each value of R there are two

different values of Θ, symmetric around $\Theta = 30°$, which correspond to lattice constant pairs (n_1, n_2) and (n_2, n_1), respectively. The (n_1, n_2) pairs are actually identical structures with opposite chirality [77]. The six-fold rotational symmetry of the lattice restricts $\Theta \in [0°, 60°]$.

We now look into properties of (n_1, n_2) pairs in order to characterize the multi-thread structure of six neighbor helices $(n_c = 6)$. First, we identify the link between $n_c = 6$-tubes and the (n_1, n_2) pair values. The pairs $(0, n_2)$ and $(n_1, 0)$ leading to $\Theta = 60°$ and $0°$, respectively, represent AB tubes, check Figure 2.4. The pairs with $n_1 = n_2$ corresponding to $\Theta = 30°$ lead to Z tubes that are characterized by constitutive straight filaments parallel to the Z tube axis, see Figure 2.2(f). The curve with $n_1 = 1$ (with $n_2 \geq 3$) corresponds to a single helix, $n_1 = 2$ (with $n_2 \geq 3$) corresponds to a double helix, $n_1 = 3$ (for any $n_2 \geq 4$) corresponds to a triple helix, and more generally an n_1-helical structure is obtained when $n_2 \geq n_1 + 1$. We employ Cartesian coordinates to express positions of particles in an $n-$helix similarly to the single helix case, using two indices, $i \in Z$ and $j = \{1, n\}$:

$$
\begin{aligned}
x_{i+jn} &= R \sin\left(i\Gamma_1 + j\Gamma_2\right), \\
y_{i+jn} &= R \cos\left(i\Gamma_1 + j\Gamma_2\right), \\
z_{i+jn} &= i\Delta z_1 + j\Delta z_2.
\end{aligned}
\tag{2.16}
$$

In Equation 2.16, Γ_1 represents the azimuthal angular shift between each two consecutive particles along a given thread and Γ_2 is the angular shift between threads, i.e., densely packed directions in a superstructure, see Figure 2.3(b). The azimuthal angle Γ_1 is merely provided by :

$$
\Gamma_1 = \arccos\left[1 - \left(\frac{d}{\sqrt{2}R}\cos\Theta\right)^2\right].
\tag{2.17}
$$

The angular shift Γ_2 between threads is more delicate to derive. Knowing that starting from the reference particle it is possible to reach the same particle position following two paths along threads (in $\vec{a}_1$- or $\vec{a}_2$-direction), one can arrive at a relation
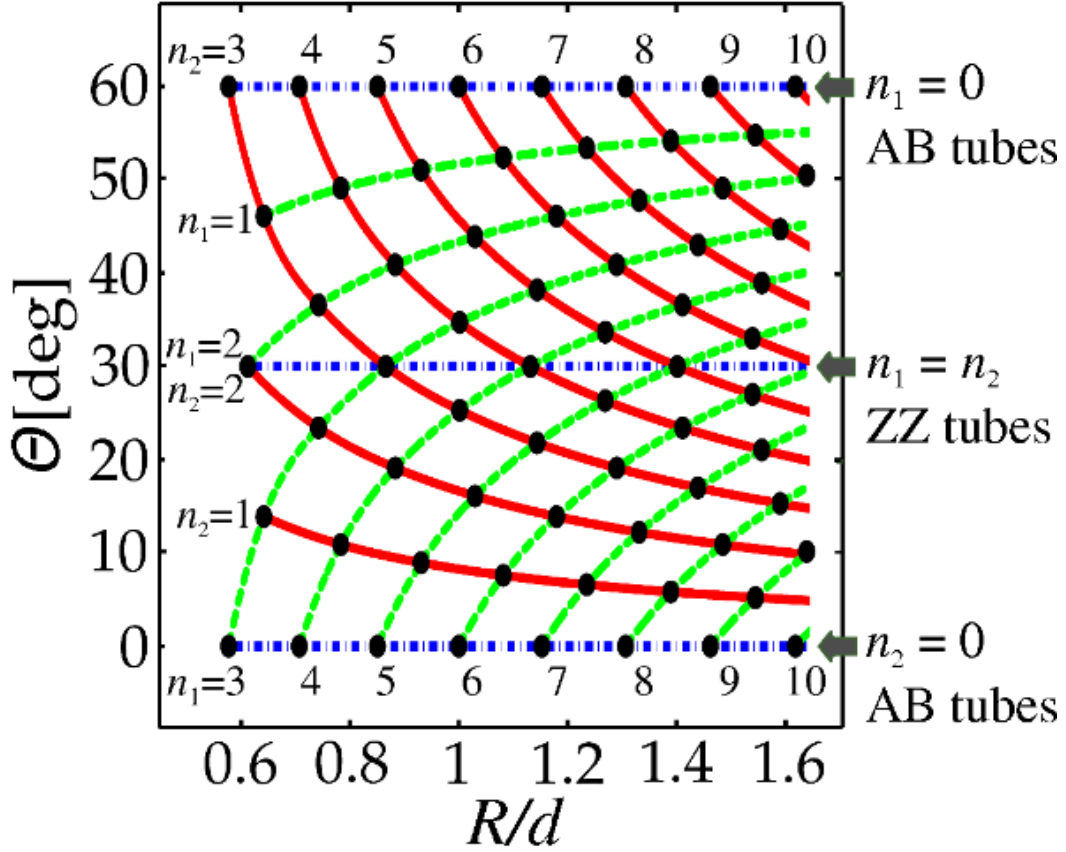
Figure 2.4: State diagram in the $(\Theta, R/d)$-plane showing possible unit cells characterized by (n_1, n_2) pairs. Solid lines represent unit cells with n_2 fixed, and the dashed ones represent unit cells with n_1 fixed. The three horizontal lines (dot-dashed) correspond to tubes.

linking Γ_1 and Γ_2:

$$2\pi = (n_1 + n_2)\Gamma_1 - n_2\Gamma_2. \tag{2.18}$$

The dependence of angle parameters Γ_1 and Γ_2 on the reduced helix radius R/d is displayed in Figure 2.5, for $\Theta < 30°$ in the single helix $(n_2 = 1, n_1 \geq 4)$, the double helix $(n_2 = 2, n_1 \geq n_2)$ and the quadruple helix $(n_2 = 4, n_1 \geq n_2)$. In our notation, multi-thread helices are named after the smallest unit patch particle dimension, i.e., the smallest number of generating threads. As the helix radius R/d increases, the value of Γ_1 monotonically decreases, since additional particles are added to a turn. The angular parameter Γ_2 monotonically decreases only for $n_2 = 1$. The scenario becomes qualitatively different at $n_2 \geq 2$ where non-monotonic behavior is found, see Figure 2.5. This feature can be rationalized as follows. The smallest compatible
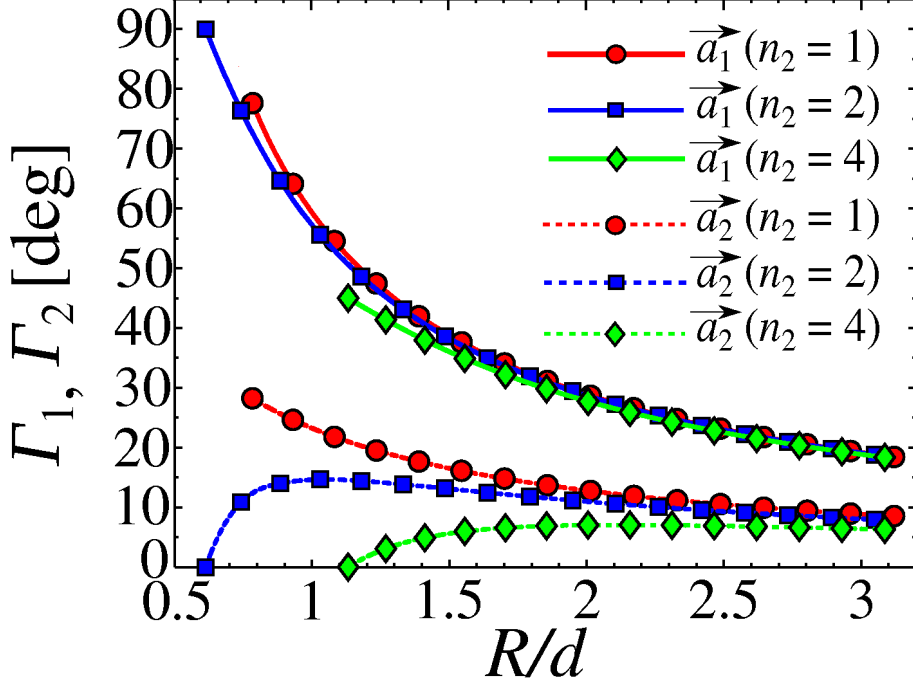
Figure 2.5: Dependence of azimuthal angular shift parameters Γ_1, Γ_2 coming from corresponding spanning vectors $\vec{a}_1, \vec{a}_2$, respectively, on reduced helix radius R/d, for single thread ($n_2 = 1$), double thread ($n_2 = 2$), and four-thread ($n_2 = 4$) helices.

radii R with $n_2 \geq 2$ and $\Theta < 30°$, are obtained when $n_1 = n_2$ (check Figure 2.4) corresponding to Z tubes where $\Gamma_2 = 0$. Besides that, Γ_2 tends to zero for vanishing cylinder curvature ($R/d \to \infty$). These are the reasons why the profile of $\Gamma_2(R/d)$ is non-monotonic when $n_2 \geq 2$. The surface packing fraction of densely packed multiple helices is simply obtained by multiplying the surface packing fraction of a single helix with the number of threads n_2 ($\eta_{multi} = n_2 \eta$, see Equation 2.8):

$$\eta_{multi} = n_2 \frac{d^2}{8 \Delta z_1 R}, \tag{2.19}$$

where the elevation distance Δz_1 (shown in Figure 2.3(b)) is given by:

$$\Delta z_1 = \sqrt{d^2 - 4R^2 \sin^2\left(\frac{\Gamma_1}{2}\right)}. \tag{2.20}$$

The calculated surface packing fraction of single ($n_2 = 1$), double ($n_2 = 2$), and quadruple ($n_2 = 4$) helices is shown in Figure 2.6. At a given confinement curvature (fixed R/d), adding threads results in higher surface packing fraction, see Figure 2.6.
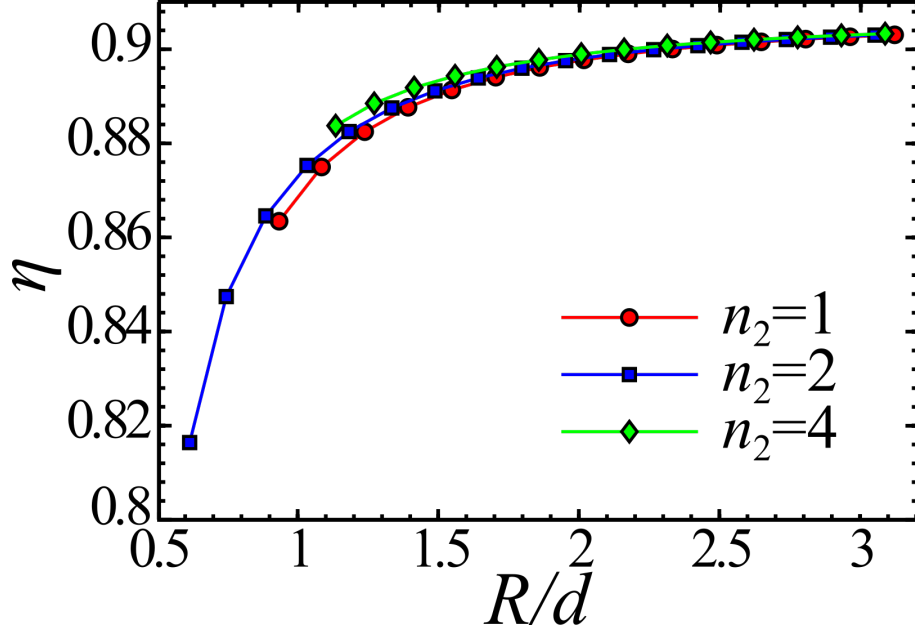
Figure 2.6: Surface fraction η, see Equation 2.19 as a function of reduced helix radius R/d for single thread ($n_2 = 1$), double thread ($n_2 = 2$), and four-thread ($n_2 = 4$) helices.

2.1.2 Tubes as sub-sets of helices

We refer to tubes made by stacking of rings. In AA tubes all constitutive rings are exactly aligned, see Figure 2.2(d), and in AB tubes every ring is shifted for half of the particle's diameter, in respect to its preceding ring, see Figure 2.2(e). Alternatively, AA or AB tubes could be generated by rolling of square or triangular lattices on cylindrical confinement, respectively.

Particle i−positions in AA tubes are calculated as:

$$
\begin{aligned}
x_i &= R cos(2\pi i/N), \\
y_i &= R sin(2\pi i/N), \\
z_i &= \lfloor i/N \rfloor d,
\end{aligned}
\tag{2.21}
$$

where $\lfloor x \rfloor$ is the greatest integer function and gives the largest integer less than or equal to x, while N is the number of particles in a constitutive ring. To simplify discussion, we refer to N also as *curvature* since there is a correspondence with the tube's geometrical curvature $R/d = 1/2 \sin(\pi/N)$, e.g., we obtain $R/d = \sqrt{2}/(\sqrt{3} -$

1) ≈ 1.3 for $N = 8$ ring.

One of the ways to obtain AB tubes is stacking of a pair of two successive rings. Total number of particles in the tube N_{tube} is a multiple of the number of particles in the ring N and the number of rings N_{rings}, i.e., $N_{\text{tube}} = N_{\text{rings}} \cdot N$.

In both rings particle positions are calculated based on their index $i = 1, N_{\text{tube}}$:

$$
\begin{aligned}
x_i &= R\cos\left(2\pi i/N + \theta_i\right), \\
y_i &= R\sin\left(2\pi i/N + \theta_i\right), \\
z_i &= \lfloor i/N \rfloor \Delta z,
\end{aligned}
\tag{2.22}
$$

where θ_i is angular displacement of rings:

$$
\theta_i = \pi \quad \text{mod}\left(\lfloor i/N \rfloor, 2\right)/N
\tag{2.23}
$$

and the displacement between successive rings along AB tube's axis is:

$$
\Delta z = \sqrt{d^2 - 2R^2[1 - \cos\left(\pi/N\right)]}.
\tag{2.24}
$$

We have already explained when discussing the Figure 2.4 that densely packed tubes, i.e. AB and Z tubes, can be seen as sub-classes of helices. Bearing this in mind, in addition to stacking of the rings, we point out that the tubes can be created by rolling a ribbon with square or triangular lattice on a cylindrical surface. In fact, every ordered tubular structure can be generated by reproduction of a curved unit cell along helical lines defined through curved spanning vectors in analogy to crystals in two dimensions. This curved unit cell has n_1 and n_2 particles along two spanning directions $\vec{a_1}$ and $\vec{a_2}$, respectively.

2.2 Dipole moments

2.2.1 Dipolar interaction model

We have explained the geometry of helices and tubes composed of hard spheres in section 2.1 of this chapter. In this section we want to address the situation where the

constitutive particles are dipolar. Each particle carries an identical dipole moment in magnitude, $m = |\vec{m}_i|$, where $\vec{m}_i = (m_i^x, m_i^y, m_i^z)$ defines the dipole moment of a particle i, see also Figure 2.1 in section 2.1. The potential energy of interaction $U(\vec{r}_{ij})$ between two point-like dipoles whose centers are located at $\vec{r}_i$ and $\vec{r}_j$ can be written as:

$$U(\vec{r}_{ij}) = C\frac{1}{r_{ij}^3}\left[\vec{m}_i \cdot \vec{m}_j - 3\frac{(\vec{m}_i \cdot \vec{r}_{ij})(\vec{m}_j \cdot \vec{r}_{ij})}{r_{ij}^2}\right], \qquad (2.25)$$

for $r_{ij} \geq d$ or ∞ otherwise, where C represents a constant that depends on the intervening medium, and $r_{ij} = |\vec{r}_{ij}| = |\vec{r}_j - \vec{r}_i|$. It is convenient to introduce the energy scale defined by $U_{\uparrow\uparrow} \equiv Cm^2/d^3$ that physically represents the repulsive potential value for two parallel dipoles at contact standing side by side, as clearly suggested by the notation. Therefore, the total potential energy of interaction in a given structure U_{tot} is given by:

$$U_{tot} = \sum_{\substack{i,j \\ i>j}} U(\vec{r}_{ij}). \qquad (2.26)$$

One can then define the reduced potential energy of interaction u (per particle) of N magnetic spheres. It reads $u = U_{\text{tot}}/(U_{\uparrow\uparrow}N)$, which will be referred to as the cohesive energy. Since we are dealing with infinitely long structures (in one direction), we shall consider only periodic structures in that direction, so this imposed condition greatly facilitates the calculation of the cohesive energy. Our method of choice is the Lekner-type summation method for systems with periodicity in one direction which we have presented in section 2.3. The central feature in Lekner-type methods is the choice of the periodic cell. For structures with coordination number $n_c = 2, 4$ we can always find helical parameters with a finite number of particles in the unit cell. The periodicity is achieved by imposing a condition on the angular shift parameter Γ that a helix has to make an integer number of turns within the unit cell.

2.2.2   Relevant dipole moment orientations

Taking into account the symmetry of helices it is intuitive to assume dipole moments following helix threads. In order to have dipole moments tangential to the helical
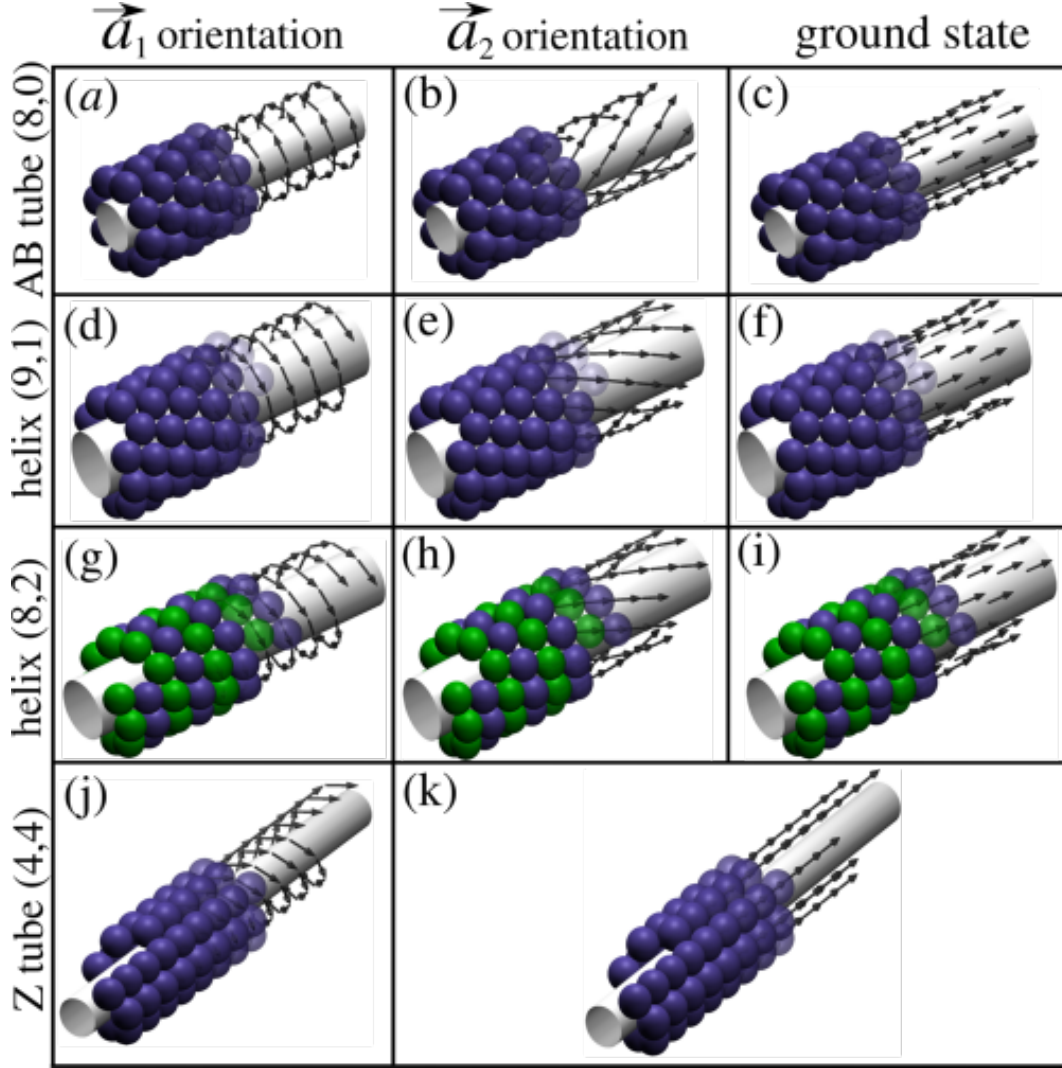
Figure 2.7: The representative structures including dipole moment distributions are displayed. For AB tube with patch parameters $(n_1, n_2) = (8, 0)$ dipole distributions which correspond to spanning unit cell vectors (a) $\vec{a}_1$ (oblique to cylinder's axis), (b) $\vec{a}_2$ (closer to cylinder's axes), as well as, (c) ground state dipole distribution. For single thread helix $(n_1, n_2) = (9, 1)$ dipole distributions which correspond to (d) $\vec{a}_1$ and (e) $\vec{a}_2$ (closer to helix axes) spanning vectors, as well as, (f) ground state dipole distribution. For double thread helix $(n_1, n_2) = (8, 2)$ dipole distributions which correspond to (g) $\vec{a}_1$, (h) $\vec{a}_2$ (closer to helix axes) spanning vectors, and (i) ground state dipole distribution. In case of Z tube (j) $\vec{a}_1$ and (k) $\vec{a}_2$ dipole distributions are shown. Ground state of Z tube follows $\vec{a}_2$ dipole distribution (parallel to cylinder's axis).

backbone, we introduce two components of dipole moments. The parallel component with respect to the helix axis (we have chosen to orient a helix along the z direction)

is given by:

$$m^z = m\Delta z/d, \tag{2.27}$$

and the orthogonal one is given by:

$$|\vec{m}^{xy}| = m\sqrt{1 - (\Delta z/d)^2}. \tag{2.28}$$

Hence, the dipole moment of a particle i in the single thread helix reads:

$$
\begin{aligned}
m_i^x &= -m^{xy}\sin(i\Gamma), \\
m_i^y &= m^{xy}\cos(i\Gamma), \\
m_i^z &= m_z.
\end{aligned}
\tag{2.29}
$$

In the multi-thread case, the Cartesian dipole moment components are given by:

$$
\begin{aligned}
m_{ij}^x &= -m^{xy}\sin(i\Gamma_1 + j\Gamma_2), \\
m_{ij}^y &= m^{xy}\cos(i\Gamma_1 + j\Gamma_2), \\
m_{ij}^z &= m\Delta z/d,
\end{aligned}
\tag{2.30}
$$

where $i \in Z$ is the internal particle label within a thread and $j = \{1, n_2\}$ stands for the thread's label. In dense helices ($n_c = 4, 6$) dipole moments can follow two directions $\vec{a}_1$ and $\vec{a}_2$.

In general, the dipole moments do not have to follow helix threads. In order to find the dipole moment orientation that ensures minimal cohesive energy, we perform minimization of the cohesive energy using a constrained minimization algorithm which we have presented in section 2.3.

We have considered three relevant dipole moment orientations: $\vec{a}_1$ and $\vec{a}_2$ orientations which are defined by the helix threads and the ground state dipole moment orientation, which is determined via cohesive energy minimization procedure. In Figure 2.7, representative dipole moment distributions are shown.

2.3 Methods

In this chapter we present the methods applied in the study of confined dipolar systems. We have carefully and in details derived the Lekner-type summation method for summing the dipole–dipole interactions in $1D$ periodic dipolar systems, check appendix A. In subsection 2.3.1 we present the overview of available methods for summing the dipole-dipole interactions of infinite periodic structures, followed by our selection of the proper method and the final expressions of the Lekner-type method that we have implemented. Next, we describe the energy minimization method which we have used for determining the ground state dipole orientation of our dipolar structures.

2.3.1 Methods for summing the dipole-dipole interactions of infinite periodic structures

2.3.1.1 Overview of available methods

Energy of a dipolar structure with finite number of particles can be calculated via direct summation of potential energies of the dipole-dipole interaction (DDI) of every pair of particles. On the other hand, we might be interested in calculating the energy of infinite periodic dipolar structures. As DDI is a long-range interaction, a proper approach is needed. We present a brief overview of available numerical techniques for summing the long-range interactions of spatially periodic structures.

In case of $3D$ periodic structures a standard method of choice for summing the long-range interactions is the Ewald method [78]. Besides the periodicity in all three spatial dimensions, there are three-dimensional systems having the periodicity in one or two dimensions, let us note them as $1D$ and $2D$ periodic systems. Hence, those are $3D$ systems possessing the periodicity along one- or two- dimensions. Ewald type methods for these kinds of periodic systems have been established [79–84]. For example, a $2D$ Ewald method for the electrostatic [79–81] and dipole-dipole interactions [79, 80] has been developed. Such a method computes properly the long range DDI, however its disadvantage is the bad scaling of computational time

with the number of dipoles N (i.e., it scales $\propto N^2$). A computationally more efficient method for summing DDI in a $2D$ periodic system has been presented in [82]. It represents a modification of the previously mentioned computationally inefficient $2D$ Ewald method since its computational time scales $\propto N$. A mutual feature of Ewald type methods [79–81] is the need for an arbitrary convergence parameter necessary for the control of the accuracy of summations. Convergence parameter is a numerical factor related to computation and without physical interpretations. The modified $2D$ Ewald method [82, 83] requires one additional parameter, while the modified $1D$ Ewald method requires even two additional parameters [84].

Summation techniques which avoid the usage of convergence parameters are advantageous, leading to both the reduction of complexity and computational time. For example, such a method for summing long-range Coulombic interactions in periodic systems has been originally introduced by Lekner [85]. Since it opened a new direction in the field of long-range interaction summations, this type of approach has been known under the term *Lekner summation.* Modifications and improvements based on Lekner's work [85] led to the development of *Lekner–type* methods [86–88]. In Lekner–type methods [85–88] the forces are calculated first and the interaction energy is obtained by integrating the force expressions. On the other side, an approach has been introduced in which the expression for the interaction energy is directly derived [89, 90]. In the next two References [89, 90] Coulombic interaction is considered, while in Reference [91] the approach is applied to the DDI.

To conclude our overview, there are several Ewald type [78–84] and Lekner–type [85–88] methods for summing both Coulombic and dipole-dipole interactions in all possible cases of periodicity of the system (i.e., $1D$, $2D$ or $3D$ periodic systems).

2.3.1.2   Selection of the proper method

We are interested in calculating the energy of infinite $1D$ periodic dipolar tubes and helices. We have arbitrary chosen to orient them along the z axis, so they are periodic along this direction. According to that we have chosen the Lekner–type method for summing the DDI of $1D$ periodic systems, presented in [91].

Let us explain the key features of this method. An infinite dipolar structure is

represented by its elementary cell which is periodically replicated along the z axis. Interaction energy of a structure (i.e., structure's cohesive energy) is determined as a sum of *self energy* E_{self} and *cross energy* E_{cross}, which are calculated based on the elementary cell of that structure. Elementary cell is infinitely replicated along the z axis in both directions, hence we might speak about the particles in the cell and about their images in the replicas of the cell. Knowing this, we define the self energy as a sum of the interactions of a given particle from the elementary cell with all its images. On the other side, the cross energy includes interactions of a given particle with all other particles belonging to the elementary cell and with all their images.

In Reference [91] the authors consider the DDI which decays with the distance between the dipoles $\propto r^{-3}$, hence the expressions for the self and cross energy are derived for this type of long-range interaction. Our opinion was that it might be useful to round-up the derivation and come up with the expressions for the self and cross energy in function of parameter s which is defined by setting that the DDI decays with the distance $\propto r^{-2s}$. Once we accomplish this and derive closed-form expressions in function of s, we can simply set $s = 3/2$ and obtain the final expressions for the self and cross energy in case of DDI.

2.3.1.3 Application of the derived Lekner-type method in case of infinite $1D$ periodic dipolar structures

We have derived the expressions which define the self energy E_{self} and cross energy E_{cross} in a Lekner type method for summing the DDI in case of $1D$ periodic structures. Since our investigation considers $1D$ periodic infinite dipolar helices, this method is appropriate for calculating their cohesive energy. We can state that the cohesive energy of a dipolar structure corresponds to the potential energy of DDI between the hard dipolar spheres which the structure is composed of. In every structure we should determine its periodic cell and within this cell we should calculate the self and cross energy. Expression for the self energy A.10 is the same in case of any periodic cell. On the other hand, we should carefully choose the expression for the cross energy depending whether the condition $\overrightarrow{\rho_{ij}} \neq 0$ does or does not apply, the indices i and j can take any value from the range $\overline{1,N}$, where N is the total

number of particles in the periodic cell. As in case of infinite dipolar tubes and helices the elementary cell of every structure fulfills the condition $\overrightarrow{\rho_{ij}} \neq 0$, we take the expression A.120 for the cross energy. Hence, the total energy of an infinite dipolar tube or helix, where N is the total number of particles in its periodic cell, is computed using the next expression:

$$
\begin{aligned}
E_{\text{tot}} = E_{\text{cross}} + E_{\text{self}} \quad = \quad & \frac{1}{2} \sum_{i=1}^{N} \sum_{j=1, j \neq i}^{N} \left\{ -\frac{8\pi}{L_z^2} \left[\frac{2 \left(\overrightarrow{\mu_i}^\rho \cdot \overrightarrow{\rho_{ij}} \right) \left(\overrightarrow{\mu_j}^\rho \cdot \overrightarrow{\rho_{ij}} \right)}{\rho_{ij}^3} - \frac{\left(\overrightarrow{\mu_i}^\rho \cdot \overrightarrow{\mu_j}^\rho \right)}{\rho_{ij}} \right] \right. \\
& \times \sum_{k=1}^{+\infty} k \cos \left(k \eta_{ij}^z \right) K_1 \left(k \eta_{ij}^\rho \right) \\
& -\frac{16\pi^2}{L_z^3} \left[\frac{\left(\overrightarrow{\mu_i}^\rho \cdot \overrightarrow{\rho_{ij}} \right) \mu_j^z + \left(\overrightarrow{\mu_j}^\rho \cdot \overrightarrow{\rho_{ij}} \right) \mu_i^z}{\rho_{ij}} \right] \\
& \times \sum_{k=1}^{+\infty} k^2 \sin \left(k \eta_{ij}^z \right) K_1 \left(k \eta_{ij}^\rho \right) \\
& -\frac{16\pi^2}{L_z^3} \left[\frac{\left(\overrightarrow{\mu_i}^\rho \cdot \overrightarrow{\rho_{ij}} \right) \left(\overrightarrow{\mu_j}^\rho \cdot \overrightarrow{\rho_{ij}} \right)}{\rho_{ij}^2} - \mu_i^z \mu_j^z \right] \\
& \times \sum_{k=1}^{+\infty} k^2 \cos \left(k \eta_{ij}^z \right) K_0 \left(k \eta_{ij}^\rho \right) \\
& \left. -\frac{2}{L_z} \left[\frac{2 \left(\overrightarrow{\mu_i}^\rho \cdot \overrightarrow{\rho_{ij}} \right) \left(\overrightarrow{\mu_j}^\rho \cdot \overrightarrow{\rho_{ij}} \right)}{\rho_{ij}^4} - \frac{\left(\overrightarrow{\mu_i}^\rho \cdot \overrightarrow{\mu_j}^\rho \right)}{\rho_{ij}^2} \right] \right\} \\
& +\frac{1}{L_z^3} \sum_{i=1}^{N} \left[|\overrightarrow{\mu_i}^\rho|^2 - 2 (\mu_i^z)^2 \right] \zeta(3).
\end{aligned} \tag{2.31}
$$

Cohesive energy of a dipolar structure is defined per particle, hence we just have to divide E_{tot} by the number of particles in the periodic cell:

$$
E_{\text{cohesive}} = E_{\text{tot}}/N. \tag{2.32}
$$

2.3.2 Energy minimization method for obtaining ground state dipole orientation of dipolar structures

In dipolar structures' analysis an obvious question which arises is related to the determination of the dipole moment orientation of a structure. By this term *dipole moment orientation* we consider a logical and meaningful rule of orienting the dipole

moment of each particle. We have deduced that dipole orientations which follow the thread structure (i.e., $\vec{a}_1$ and $\vec{a}_2$ dipole orientation) are relevant, since there is a tight relation between the geometry of a dipolar structure and a favourable dipole orientation. Dipolar structures which we consider are spatially $3D$ structures, however with a $1D$ periodicity along the z direction. Hence, there are two threads a structure is made of: a circular thread (leading to $\vec{a}_1$ dipole orientation) and a slanted thread (leading to $\vec{a}_2$ dipole orientation). We have asked ourselves how would an optimal dipole orientation look like, i.e., a dipole orientation which minimizes the cohesive energy of a structure. Besides that, we should in general determine dipole orientations which allow a negative cohesive energy: $E_{\text{cohesive}} < 0$, i.e., realistically possible configuration of dipolar spheres. To do so, we perform minimization of cohesive energy using a constrained minimization algorithm [29, 92], namely the *fmincon* minimization procedure from *Matlab* software package [93]. The name of the *fmincon* procedure has been constructed according to its purpose which is *function minimization under constraints*. Minimization procedure *fmincon* [93] finds a minimum of a constrained nonlinear multivariable function. Its mathematical definition is given as:

$$\min f(x) \text{ over } x \text{ under the constraints:}$$

$$c(x) \leq 0, c_{\text{eq}}(x) = 0, A \cdot x \leq b, A_{\text{eq}} \cdot x = b_{\text{eq}}, lb \leq x \leq ub,$$

where b and b_{eq} are vectors, A and A_{eq} are matrices, $c(x)$ and $c_{\text{eq}}(x)$ are functions which return vectors, $f(x)$ is a function being minimized which returns a scalar value. The argument x over which minimization is performed can be a vector or a matrix, lb and ub are the lower and upper boundaries for the argument x, respectively, hence they are the same data type as x, i.e., a vector or a matrix. A dipolar structure has a given fixed geometry which is not subjected to minimization, hence the particles stay in place during the minimization. Their dipole moments $\vec{\mu_i}$ are subjected to minimization. A randomly oriented dipole moment is assigned to every particle of a dipolar structure, defined in the spherical coordinate system using two angles: θ and φ. Those angles are standard coordinates of a spherical coordinate

system. Each particle i is assigned with a randomly oriented dipole moment, where $\theta_i \in [0, \pi]$ and $\varphi_i \in [0, 2\pi]$. Mathematically speaking, we can write down the previous considerations (bearing in mind that $\mathrm{rand}\,(1)$ returns a random real number in the range $[0, 1]$) as:

$$
\begin{aligned}
\theta_i &= \pi \cdot \mathrm{rand}\,(1), \\
\varphi_i &= 2\pi \cdot \mathrm{rand}\,(1).
\end{aligned}
\tag{2.33}
$$

The dipole moment of i-th particle, i.e., $\overrightarrow{\mu_i} = (\mu_i^x, \mu_i^y, \mu_i^z)$ in spherical coordinate system is:

$$
\begin{aligned}
\mu_i^x &= \sin\,(\theta_i)\cos\,(\varphi_i), \\
\mu_i^y &= \sin\,(\theta_i)\sin\,(\varphi_i), \\
\mu_i^z &= \cos\,(\theta_i),
\end{aligned}
\tag{2.34}
$$

where $i = \overline{1, N}$, with N being the total number of particles in a dipolar structure.

The function which we minimize is the cohesive energy of a given dipolar structure, i.e., $f = E_{\mathrm{cohesive}}$ and the argument $x = \theta_1, \theta_2, ..., \theta_N; \varphi_1, \varphi_2, ..., \varphi_N$. The lower and upper boundaries are: $lb = 0, 0, ..., 0; 0, 0, ..., 0$ and $ub = \pi, \pi, ..., \pi; 2\pi, 2\pi, ..., 2\pi$, respectively. We have determined two important features emerging from energy minimization computations employing the *fmincon* procedure [93]:

(i) dipole moments are tangential to the confining cylinder's surface, and

(ii) component of a dipole moment in the z-axis direction m_z of a given dipolar structure is identical for all particles.

We have found that under some circumstances the dipole moment orientations alternate, i.e., we have obtained the antiferromagnetic-like coupling between the neighbouring threads. This actually occurs with any AA tube. Similar behaviour is reported for some moderately dense $n_c = 4$-helical structures. Therefore, we need just one angular parameter to characterize the dipole moment orientation. We choose the dipole moment angular parameter, $\alpha \in [-\pi, \pi]$, relative to the z axis, see

Figure 2.1. Doing so we arrive at:

$$
\begin{aligned}
m_{ij}^x &= -m \sin(\alpha) \sin(i\Gamma_1 + j\Gamma_2), \\
m_{ij}^y &= m \sin(\alpha) \cos(i\Gamma_1 + j\Gamma_2), \\
m_{ij}^z &= m \cos(\alpha),
\end{aligned}
\tag{2.35}
$$

where the indices i and j have the same meaning as in Equation 2.30. Consequently, the angular parameter α is most of the time a unique variable, at prescribed helical structures, entering into the energy minimization procedure. Obtaining an optimal dipole orientation which leads to the minimal cohesive energy of a certain dipolar structure, in other words obtaining *ground state dipole orientation*, comes down to determining the right value of the angular parameter α. In general, except for some cases where we have obtained the antiferromagnetic-like dipole orientation, dipole moments of all particles are parallel, building the same angle α with the z axis direction.

To sum up, we have started with the most general case of each particle having an independent and randomly oriented dipole moment. Application of the *fmincon* minimization procedure [93] significantly narrowed down the diversity of possible dipole orientations, leading to just one scalar parameter α determining the ground state dipole orientation. This is a significant finding, meaning that for obtaining the ground state dipole orientation of a dipolar structure we do not need computationally demanding *fmincon* procedure [93] anymore. Just a simple direct search over the range of α, using a reasonable precision (i.e., $\alpha \in [-\pi, \pi]$ with a step of 10^{-3}), solves our optimization problem.

2.4 Degeneracy in $2D$ triangular and square lattice and properties of tubes

2.4.1 Ground state of $2D$ triangular and square lattice

First, we investigate the dependence of ground state energy on dipole moment orientation. All dipoles in triangular lattice are parallel and allowed to rotate only

around a fixed axis orthogonal to the plane, see Figure 2.8(a). There is a continuous ground state for any in-plane angle θ with cohesive energy value $u_{\mathrm{AB}} \simeq -2.7586$, which is the cohesive energy of an infinite triangular two dimensional lattice. This value is defined as [94, 95]:

$$u_{\mathrm{AB}} = -2\zeta(3) + 16\pi^2 \sum_{k=1}^{+\infty} \sum_{l=1}^{+\infty} \cos\left(kl\pi\right) K_0\left(kl\sqrt{3}\pi\right). \tag{2.36}$$

For an infinite square two dimensional lattice, similarly, there is a continuous degeneracy of its ground state, described in Figure 2.8(b)-(c). A continuous state, in this case, involves a unit cell of four particles. The moments in a unit cell are synchronously coupled and in our notation take directions θ, $\pi - \theta$, $\pi + \theta$, and $-\theta$, in anti-clockwise direction in Figure 2.8(b). The ground states found are obviously antiferromagnetic, with the total dipole moment within the cell conserved and equal to zero. The most striking is the so-called *vortex state* for $\theta = \pi/4$ with a fully enclosed circulation of the magnetic dipole moment within the unit cell. The ground state cohesive energy value is $u_{\mathrm{AA}} \simeq -2.5494$, which is the cohesive energy of an infinite square two dimensional lattice. This value is defined as [94, 95]:

$$u_{\mathrm{AA}} = -2\zeta(3) + 16\pi^2 \sum_{k=1}^{+\infty} \sum_{l=0}^{+\infty} k^2 \left\{ K_0\left[4k(l+1)\pi\right] - K_0\left[2k(2l+1)\pi\right] \right\}. \tag{2.37}$$

We will use the calculated ground state energy value as an absolute point for comparison of energies of different states in tubes with square or triangular lattice structure.
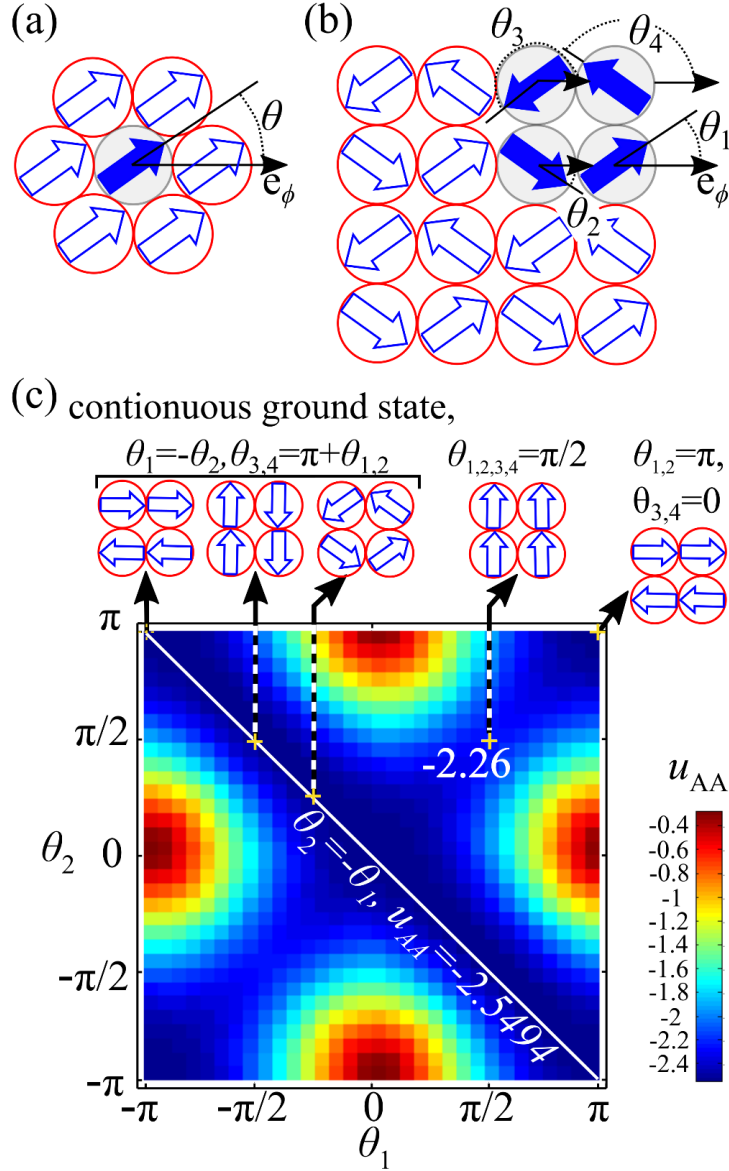
Figure 2.8: Visualization of degenerate states in infinite (a) triangular and (b) square lattice, i.e., AB and AA packings, respectively. The dipoles are depicted as arrows located in the center of the spheres. In case of triangular lattice the unit cell consists of a single particle (as noted in panel (a) of this figure) and in case of square lattice it consists of four particles (as noted in panel (b) of this figure). (c) Energy landscape for square lattice is shown with respect to two θ_1 and θ_2 out of four magnetic moments in the unit cell. Other two moments were oriented so the energy of the system is minimal. One can observe a flat valley of degenerate ground state, $\theta_2 = -\theta_1$, with energy $u_{AA} \simeq -2.5494$. The saddle point which represents square plane with uniform dipole moment orientation with energy $u_{AA}^{sdd} = -2.26$ is also marked. The curves are drawn through the discrete points and they are smooth. The results are in principle scale independent.

2.4.2 Degeneracy break-up with curvature in case of AA and AB tubes

Wrapping of the plane around the confinement cylinder will make the system quasi one-dimensional and break the degeneracy [96]. We will discuss repercussions of the degeneracy breakup on cohesive energy for different dipole moment orientations. We analyze the degeneracy breakup in infinite tubes: according to tube's cylindrical geometry, we represent the dipole moment of the $i-$th particle in cylindrical coordinates like:

$$\vec{m}_i = m_{i\phi}\vec{e_\phi} + m_{iz}\vec{e_z}, \tag{2.38}$$

with constraints $m^2 = m_{i\phi}^2 + m_{iz}^2$ $(i = 1, \ldots, N)$. The parallel component with respect to tube's axis is given by m_z and the orthogonal component is m_ϕ (i.e., m_ϕ is tangential to cylinder's circumstance). In Figure 2.9, we follow the dependence of energy on angular parameter θ, $m_{iz} = m\sin(\theta)$. We find that axial dipole moment orientation (i.e., $\theta = \pi/2$) represents the ground state for both AA and AB tubes while circular orientation (i.e., $\theta = 0$) is the most unfavorable, as seen in Figure 2.9.

Between circular and axial dipole moment orientation (i.e., for the range $0 < \theta < \pi/2$), we observe a continuous decrease of cohesive energy with increasing axial alignment of dipole moment orientation. These transition states we call *vortex* in case of square AA tubes and *helical* in case of triangular AB tubes, e.g., $\theta = \pi/4$ in Figures 2.9(a) and (b), respectively. The cohesive energy of different configurations in Figure 2.9 converges to a continuously degenerate state with increasing curvature N following the next power law (see inset in Figure 2.9):

$$u^N - u^\infty \sim N^{-2}. \tag{2.39}$$
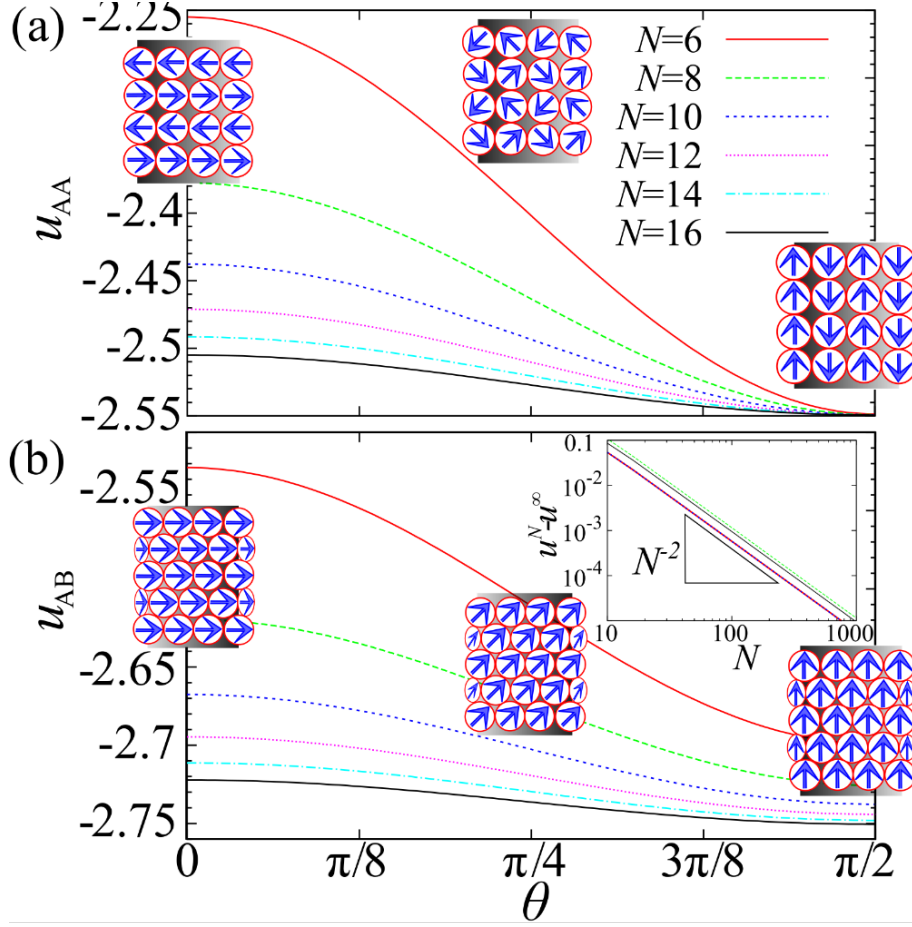
Figure 2.9: Cohesive energy spectrum of configurations for dipole orientations in Figure 2.8 on a curved surface of the infinitely long tube for (a) square AA and (b) triangular AB tubes. Breaking of degeneracy with respect to angle θ due to the curvature, i.e., proportional to the number of particles in the constitutive ring N, is shown. The axial dipole moment orientation corresponds to $\theta = \pi/2$. The inset shows convergence of cohesive energies for $\theta = 0$ and $\theta = \pi/4$ to the infinite two dimensional planar value u (for square lattice $u_{AA} = -2.5494$ and for triangular lattice $u_{AB} = -2.7586$).

2.5 Cohesive energy-packing relations in dipolar helices

We have described geometry of helices and tubes composed of hard spheres in section 2.1. In the following section 2.5 we have introduced dipolar interaction model and three relevant dipole moment orientations. Setting up the geometry and dipole moments represents a preparation for the key considerations which are dedicated to the investigation of cohesive energy-configuration relations of dipolar helices (and

dipolar tubes, as their sub-classes). A dipolar configuration is determined by the next two components: (i) structure by means of geometry (how are the hard spheres positioned spatially) and (ii) dipole moment orientation (how are the dipole moments of those hard spheres oriented). Two dipolar configurations can be identical in structure, but can have different dipole moment orientation, and vice versa they can have a different structure and the same dipole moment orientation. In this chapter we present our findings about the relations of both configurational components with cohesive energy in case of dipolar configurations under investigation.

2.5.1   Compression of a single-thread helix

A simple way to deform a helix is to compress (or extend) it along its axis, i.e., the z-direction, while ensuring the dipole moments follow the thread. Compression of a helix results in a continuous increase of its surface packing fraction η. Figure 2.10 shows the dependence of cohesive energy u_R on the surface packing fraction η for a single helix with reduced radius ($R/d \simeq 1.7$, chosen in the vicinity of $n_c = 6$ point). Recalling geometrical considerations in section 2.1 the increase of the azimuthal angular shift Γ at prescribed curvature results in a continuous decrease of Δz and in a compression of a helix. The compression process begins with a fully extended helix (i.e., $\eta \to d/8R \approx 0.073$) where the chain stands up with $\Delta z/d = 1$, and the cohesive energy of an infinite chain is $u \simeq -2.404$ [29]. The compression ends when two successive turns of the helix touch, i.e., the coordination number of particles in the helix changes from $n_c = 2$ to $n_c = 4$. We also address the minimal energy of the helix with respect to the dipole moment orientation (i.e., not necessarily prescribed by tangentially following the helix). From Figure 2.10, we observe that $u_R = u_R(\eta)$ is non-monotonic. We can identify two regimes: (i) At small packing fraction up to $\eta \leq 0.4$ (with no touching turns), the compression of the helix requires energy input and therefore cohesive energy increases. The reason for this is that two distant consecutive turns of the helix experience weaker attraction upon increasing η. (ii) In the regime of high $\eta \geq 0.4$ where successive turns are allowed to be close or even touching, the cohesive energy starts to decrease as η increases, i.e., the helix would compress on its own without the input of energy. This is a consequence of
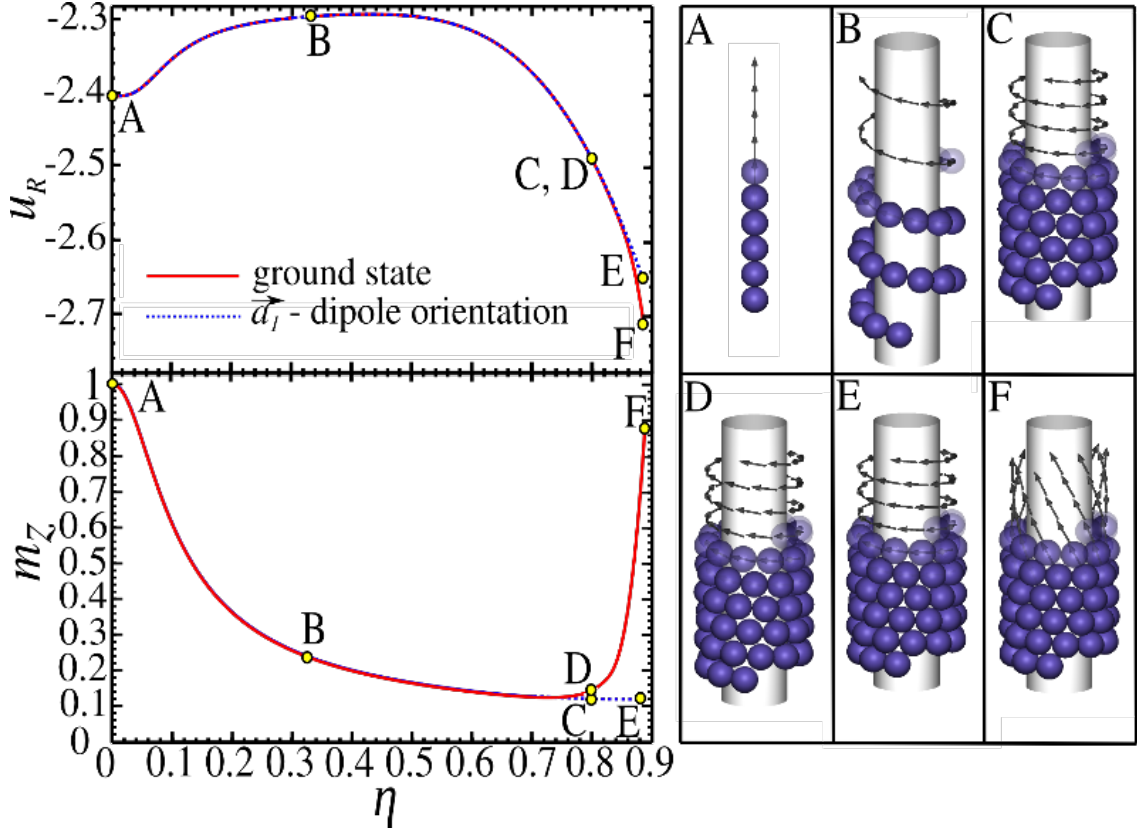
Figure 2.10: Compression of single thread helix on a cylindrical confinement with fixed radius ($R/d \simeq 1.7$). Dependence of cohesion energy (upper left panel) and axial component of the dipole moment (lower left panel) on packing fraction is shown for two characteristic dipole moment orientations: one that follows the thread structure, i.e., spanning vector $\vec{a}_1$, and ground state dipole moment orientation obtained by full energy minimization (check subsection 2.3.2 of section 2.3) . The illustrations of characteristic structures and corresponding dipole moment orientations are provided as well, in the panels on the right side.

enhanced attraction caused by the discreteness of the constitutive dipolar spheres, see Reference [97]. The overall polarization order parameter $\langle m_z \rangle$ is also analyzed in Figure 2.10. During most of the course of the helix compression, see Figure 2.10, a dipole moment orientation following the helix corresponds to the ground state structure up to $\eta \approx 0.8$, check points C and D in Figure 2.10 (the details of ground state calculations are presented in section 2.3). Only for very high packing fractions, i.e., $\eta > 0.8$, the helix direction is accompanied by a significant reduction in cohesive energy (see points E and F in Figure 2.10). The highest difference in $\langle m_z \rangle$

occurs for $\eta \approx 0.887$, where $n_c = 4$ helix with touching turns is formed, and the energy difference is $u_R^E - u_R^F \simeq 0.06$. Corresponding values of axial dipole moment component m_z for points E and F are $m_z^{\mathrm{E}} \simeq 0.12$, $m_z^{\mathrm{F}} \simeq 0.88$, respectively.

2.5.2 From square to triangular arrangement of a single-thread helix

The crucial question which we ask about dipolar helices and tubes is: how does their cohesive energy depend on structural changes and especially on curvature (quantified by the helix radius R). With increasing curvature the structure changes from the triangular to square arrangement and vice versa through a continuous series of rhombic configurations. We study first in detail systems with dipole moments following the spanning vector that are most oblique to helix axes, see Figure 2.7(d). For the sake of comparison with tubes (AA/AB tubes), we also chose dipole moments that are building vortices along the rings, check Fig 2.7(a). Motivation for that choice stems from a previous study [29], where it has been shown that finite AB tubular systems are energetically favorable, see Figure 2.7(a) (dipole moment orientation is perpendicular to the tube's axis).

The surface packing fraction η (Equation 2.8), the angular coordination order parameter ξ (Equation 2.13), and the cohesive energy per particle u_R (Equation 2.26), are plotted versus the reduced helix radius R/d in Figure 2.11. Actually, the energy and structural properties change in an oscillatory quasi-periodic manner and they are enveloped from both sides with the properties of AA and AB tubes, see Figure 2.11. In Figure 2.12 behavior of these observables is depicted within one period ($R/d \in [2.09, 2.26]$, which has been chosen arbitrary). In one period, the number of particles (n) in a constitutive ring of (AA/AB) tubes is increased for one, i.e., from n-ring to $n+1$-ring. Within this period, the order parameter changes from $\xi = 0$, i.e., square arrangement, to $\xi = 1$, i.e., triangular arrangement, via a continuous rhombic transformation, see Figure 2.12(a). The radii of densely packed helices are roughly in the middle between two corresponding (AB/AA) tube radii, see Figure 2.12(a). This is a result of the radial constraint and excluded volume.
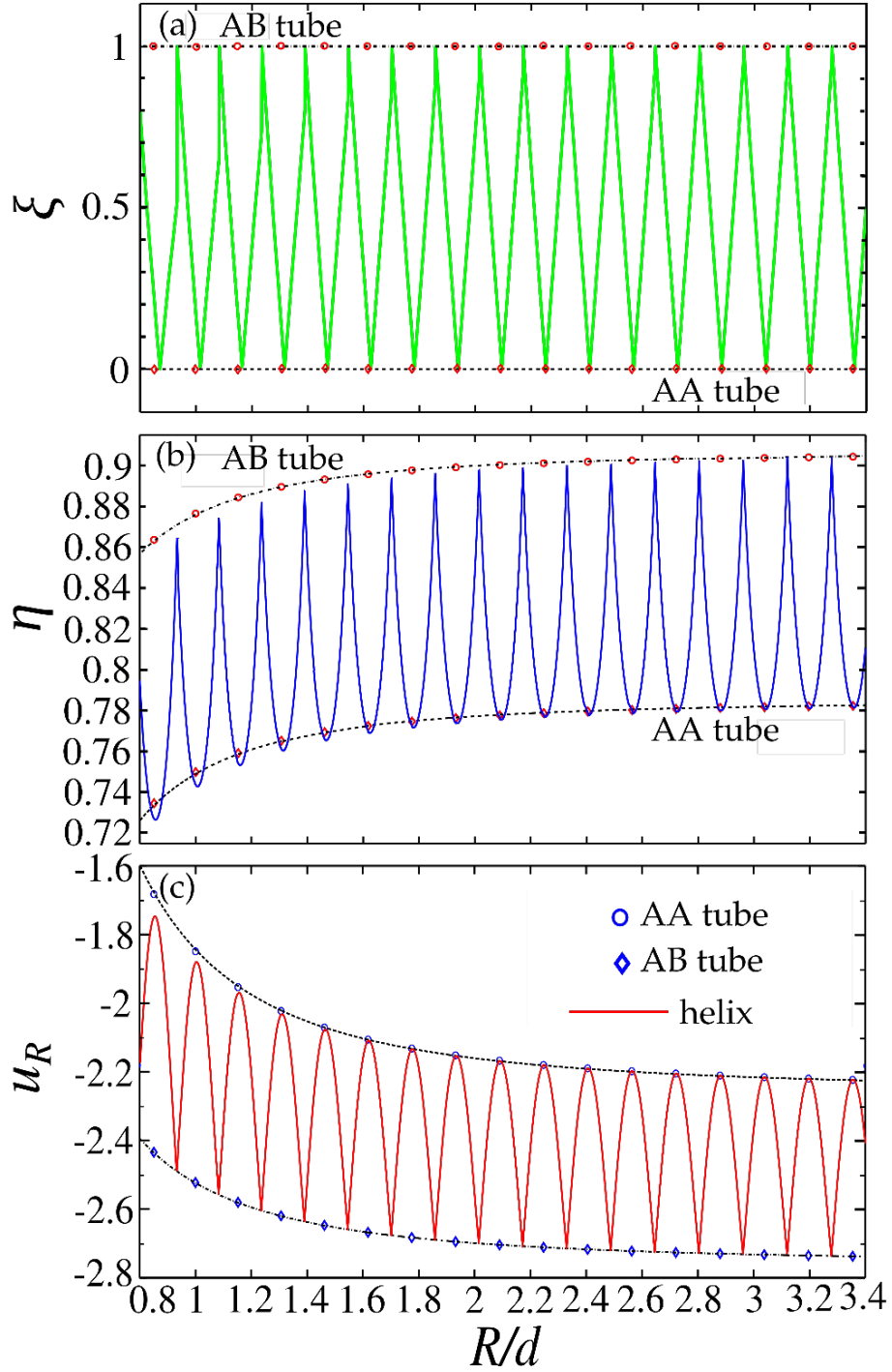
Figure 2.11: Dependence of (a) angular coordination order parameter ξ, (b) packing density η and (c) cohesive energy u_R on helix radius R/d, for $\vec{a}_1$ dipole orientation. AA and AB tube points are clearly indicated, they bracket the parameter values of helices, like a kind of envelopes (solid and dashed lines connecting the tube points are power law fits).
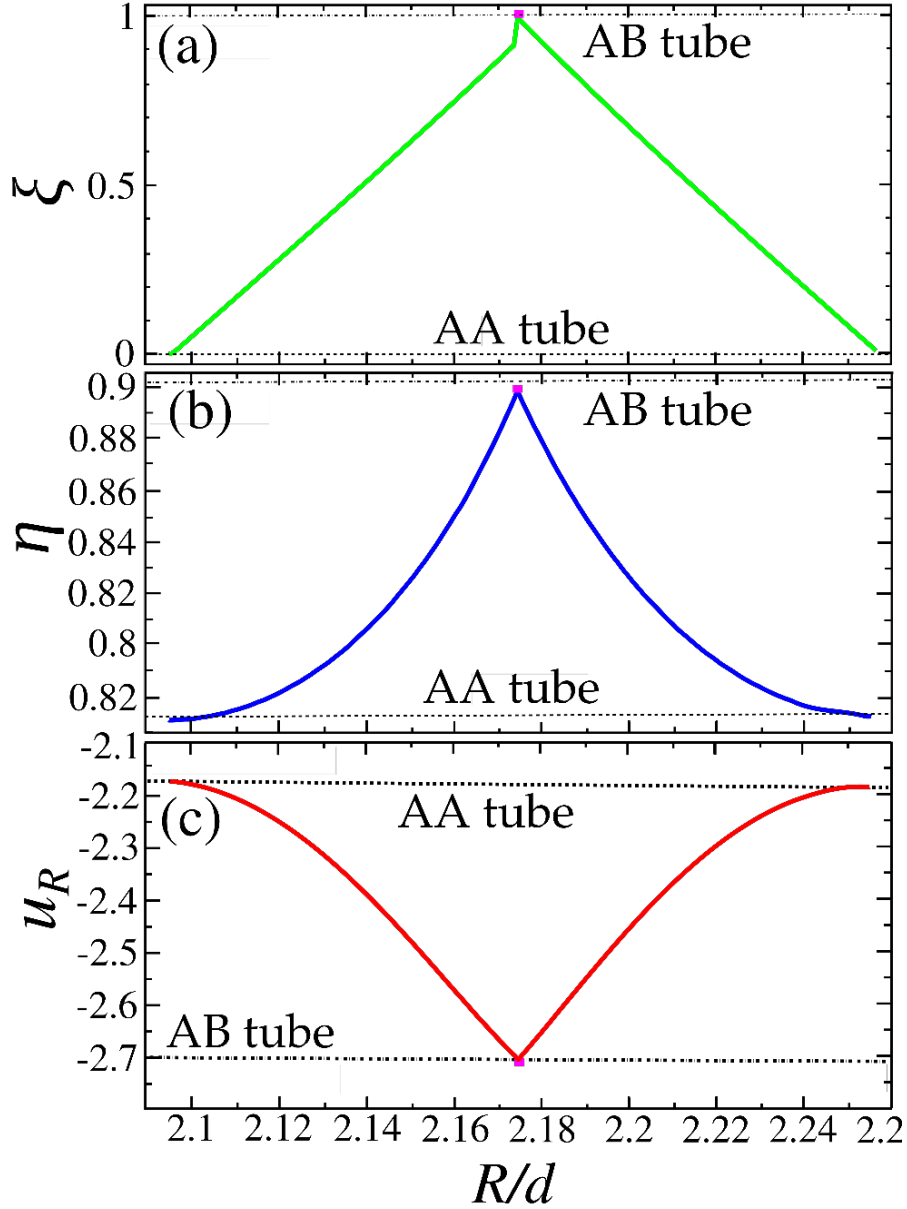
Figure 2.12: Dependence of (a) angular coordination order parameter ξ, (b) packing density η and (c) cohesive energy u_R on helix radius R/d, for a segment in vicinity of $R_{(13,1)}/d = 2.17$ of Figure 2.11. AA and AB tubes are represented with discrete points since they can be formed only with a fixed number of particles in a ring, the fitted (power law) curves serve only as a guide to the eye.

Though in a single thread helical structure we cannot close rings in the plane perpendicular to the cylinder axis, one can nevertheless realize a full $360°$ helix turn with roughly $n + 1/2$ particles. We observe discontinuity and strong asymmetry of

the angular coordination order parameter ξ at the mid-period ($R_{(13,1)}/d \approx 2.17$), see Figure 2.12(a). This is due to a change of the number of lateral threads n_2, see Figure 2.7(e), at the mid period going from $n_2 = 9$ to $n_2 = 10$, see Figure 2.12(a). With decreasing curvature, the surface packing fraction increases globally, see Figure 2.11(b). We observe oscillatory behavior as the system continuously evolves from the square to triangular arrangement and vice versa. The AA and AB tubes still roughly bound the values taken by the surface packing fraction. At the helix radius $R/d > 3.4$, see Figure 2.11(b), we are already within 3% of the asymptotic expected values in the planar case. In contrast to the angular coordination parameter ξ, the surface packing fraction η is continuous everywhere, compare Figures 2.12(a) and (b). Moreover, at the mid-period the η value is slightly (and systematically, see Figure 2.11(b)) above the interpolated value stemming from AB tubes (see Figure 2.12(b)). In Figure 2.11(b) and (c), it can be clearly seen that the profiles of energy oscillations u_R and the surface packing fraction η are anti-correlated. The mid-period values u_R coincide with interpolated values stemming from AB tube radii (confirmed by Figures 2.11(c) and 2.12(c)).

2.5.2.1 Looking for the ground state

At this point, we would like to discuss mechanisms which govern the minimal energy dipole moment orientation near the mid-period transition point (more details about implementation are provided in section 2.3). There are three privileged directions in a helix: two which follow helix spanning vectors (determined by $\vec{a}_1, \vec{a}_2$) and the third one which is the direction of the helix axis. These privileged directions come into play in two competing mechanisms: (i) The first mechanism is typically dictated by first neighbor interactions which favor dipole moments following the thread directions. (ii) The distant-neighbor interactions favor the distribution of dipole moments parallel to the helix axis. We can justify these two mechanisms as follows. It is well known for a small finite system that rings are formed with dipole moments building vortices, see Reference [29]. When a helix turn is projected along the z-axis, the resulting figure is highly reminiscent of the vortex discussed above. The head to tail configuration is favored at long distances, explaining the second advocated

mechanism. The abrupt change in dipole orientation in the direction of the axis $\langle m_z \rangle$, seen in Fig 2.13(b), is correlated with the discontinuous change in the angular coordination order parameter ξ in the vicinity of transition, see Figure 2.12(a). At the mid-period point $R_{(13,1)}/d = 2.17$ dipole orientation in the direction of the axis $\langle m_z \rangle$ is close to one, but not exactly one, see Figure 2.13. For the sake of comparison with tubes (AA/AB tubes), we choose dipole moments that are parallel with the helix axis, see Figure 2.7(c). The fact that the system is able to relax its dipole moment orientation to the ground state results in more dependence of energy on confinement curvature around the mid-point. The degree of asymmetry of u_R is stronger around the transition point, see Figure 2.13(b), than in the excited state in Figure 2.12(c). The ground state calculations confirm the high stability of AB tubes (see Figure 2.12(c)).

2.5.3 Cohesive energy of multi-thread helices at high surface packing fraction

In this part, we consider the high surface packing fraction regime with $n_c = 6$. Some representative structures including dipole moment streamlines are displayed in Figure 2.7. The streamlines following spanning unit cell vectors $\vec{a}_1$ (oblique to the helix axis) and $\vec{a}_2$ (more aligned to the helix axis) are also shown. It is possible to polarize the helix by a homogeneous external field parallel to its axis. For symmetry reasons, a reversal of the external field should result in the reversal of the dipole orientation. In the case of magnetic dipoles, it should also be possible to polarize the system to follow $\vec{a}_1$ and $\vec{a}_2$ spanning vectors by combination of a curling magnetic field of electric current flowing through the confining cylinder and the homogeneous external magnetic field parallel to its axis. Dipole moment distributions in the ground states are also indicated for comparison in Figure 2.7. In analogy with the study of a single helix case, we start analysis with a dipole moment distribution prescribed by tangentiality with thread backbone. In Figure 2.14, cohesive energy for the $\vec{a}_1$-generated dipole moment distribution is shown for different helical structures. The cohesive energy in a planar triangular lattice, $u_\infty \simeq -2.759$, represents the energy

value which will be reached asymptotically ($R/d \rightarrow +\infty$) for all considered structures. As already found for AB tubes in Reference [29], cohesive energy exhibits the scaling law of the form $u_R - u_\infty \sim R^{-2}$, see Figure 2.14. The cohesive energies of all three helices and AB tubes are weakly dependent on the number of threads for $\vec{a}_1$-generated dipole moment distribution. This is in accordance with surface packing fraction behavior reported in Figure 2.6. A comparison with the azimuthal angular shift parameter Γ_1, see Figure 2.5, and the corresponding cohesive energy (for $\vec{a}_1$-generated dipole moment distribution) clearly reveals a correlation between there two quantities. In Figure 2.15, cohesive energy for $\vec{a}_2$-generated dipole moment distribution is compared with ground state energy for different number of threads. There exists an analogous correlation (as discussed for $\vec{a}_2$-dipole distribution) between the azimuthal shift Γ_2 and the resulting cohesive energy, compare Figures 2.5 and 2.15. The smallest compatible radius R for multi thread helices ($n_2 = 2, 4$) is obtained for ZZ tubes ($n_1 = n_2$). In Figure 2.15, the corresponding radii read $R_{(2,2)}/d = 0.61$ and $R_{(4,4)}/d = 1.13$. In this case the $\vec{a}_2$ and ground state dipole moment orientations are the same, see Figure 2.7(k). Strikingly, ZZ tube ground states converge very fast to the expected planar value u_∞ at the smallest accessible radii, i.e., the largest curvature, within less than 1% of the planar case, see Figure 2.15 for $R_{(2,2)}/d = 0.61$. A structural similarity of ZZ tubes, with typical experimental images of microtubules is striking, see Figure 2.7(k). ZZ tubes can be created by closing the rectangular strip on a cylinder. We should notice the structural characteristic of ZZ tubes' decomposition into chains which are analogous to filaments in microtubules.
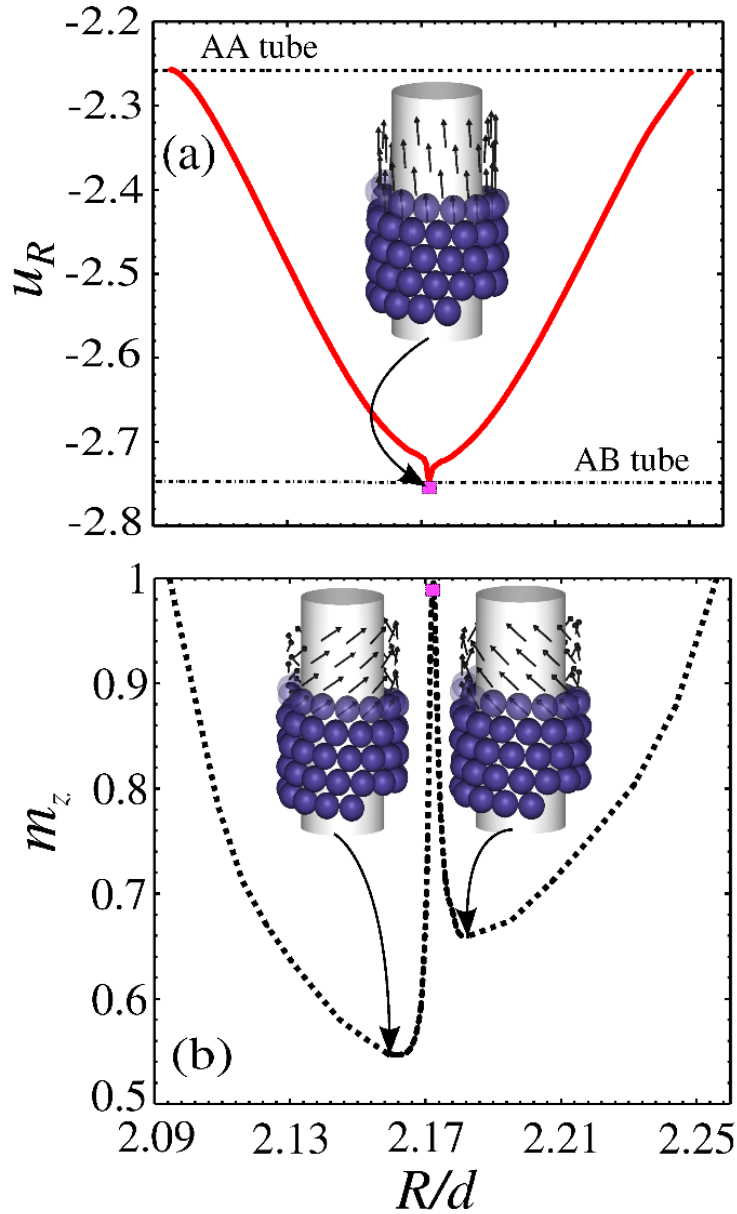
Figure 2.13: Dependence of (a) cohesive energy, and (b) polarization in the direction of z axis m_z on helix radius R/d (in the ground state), for a chosen segment of Figure 2.11. AA and AB tubes are represented with discrete points since they can be formed only with a fixed number of particles in a ring, the fitted (power law) curves serve only as a guide to the eye. The point which represents the dense helix with $(n_1, n_2) = (13, 1)$ and $R_{(13,1)}/d = 2.17$, is marked with a rectangle.
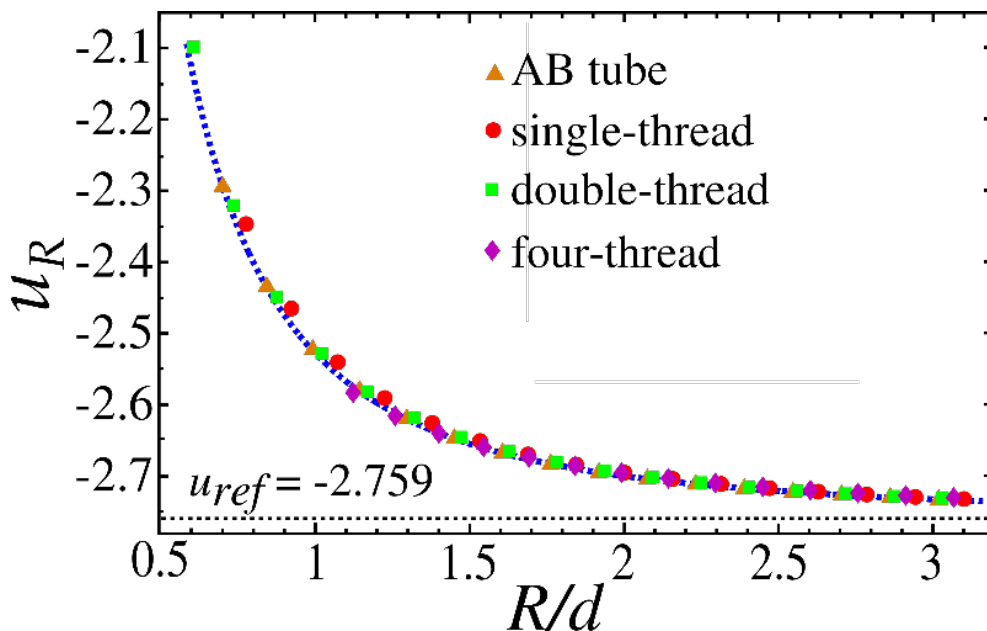
Figure 2.14: Dependence of cohesive energy u_R on helix radius R/d, for different families of helices having $\{1, 2, 4\}$ threads, and AB tubes, with $\vec{a}_1$ dipole orientation.
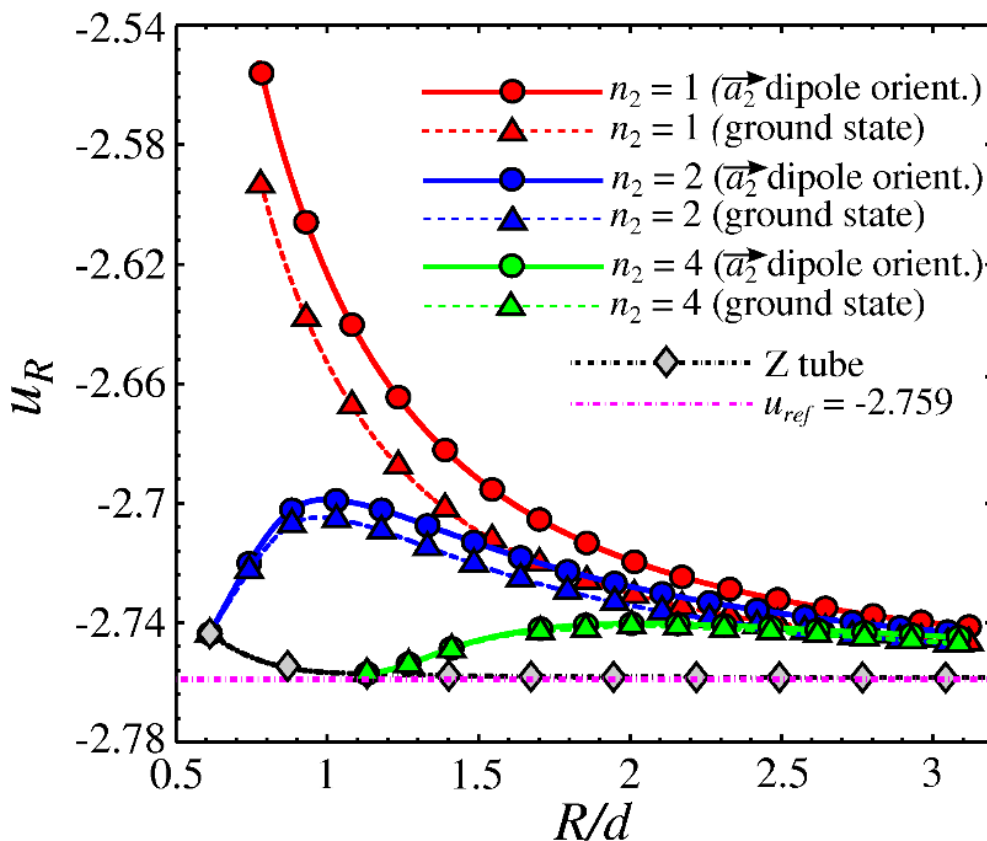
Figure 2.15: Dependence of cohesive energy u_R on helix radius R/d, for different families of helices having $\{1, 2, 4\}$ threads, and AB tubes, with $\vec{a}_2$ and optimized dipole moment orientation.

Chapter 3   Ionic liquids

3.1   Methods

In this section we present the methods applied in the study of ionic systems. First we explain the basics of the molecular dynamics (MD) method. Next, we give a short overview of the $LAMMPS$ code for MD simulations, since all MD simulations presented in this thesis were performed using the $LAMMPS$ software package [98].

3.1.1   Molecular Dynamics method

Molecular dynamics (MD) represents a simulation technique which generates trajectories of a system of N particles by numerical time integration of Newton's classical mechanics equations of motion [99]. An MD simulation is defined by: the interaction potential by which the particles interact, initial conditions (IC) and boundary conditions (BC). Let us consider a system of N particles (check Figure 3.1) in a volume V. The Newton's equations of motion for the system of N particles are:

$$m\frac{d^2\vec{r}_{\mathrm{i}}}{dt^2} = \vec{F}_{\mathrm{i}}\left(\vec{r}_1, \vec{r}_2, ..., \vec{r}_{\mathrm{N}}\right), i = 1, ..., N, \tag{3.1}$$

where $\vec{r}_{\mathrm{i}}$ are the position vectors and $\vec{F}_{\mathrm{i}}$ are the forces acting on the particles of a system. It is often case in MD simulations that the forces can be derived from interaction potential functions $U\left(\vec{r}_1, \vec{r}_2, ..., \vec{r}_{\mathrm{N}}\right)$, representing the potential energy of the system:

$$\vec{F}_i\left(\vec{r}_1, \vec{r}_2, ..., \vec{r}_{\mathrm{N}}\right) = -\nabla_{\vec{r}_{\mathrm{i}}} U\left(\vec{r}_1, \vec{r}_2, ..., \vec{r}_{\mathrm{N}}\right). \tag{3.2}$$

Equation 3.2 is consistent with the conservation of the total energy. We might define mechanical energy of the system as: $E = K + U$, where kinetic energy is defined as:

$$K = \sum_{i=1}^{N} \frac{1}{2} m_i \left(\frac{d\vec{r}_{\mathrm{i}}}{dt} \right)^2, \tag{3.3}$$

and potential energy is defined as:

$$U = U \left(\vec{r}^N (t) \right), \tag{3.4}$$

where $\vec{r}^N (t)$ denotes position vectors of all N particles in the system. We emphasize that E should be a conserved quantity, if the system is isolated. The potential of an isolated system (no external forces present) can be written in the simplest case as a sum of pairwise interactions:

$$U = \sum_{i=1}^{N} \sum_{j>i}^{N} u \left(r_{\mathrm{ij}} \right), \tag{3.5}$$

where $\vec{r}_{\mathrm{ij}} = \vec{r}_{\mathrm{i}} - \vec{r}_{\mathrm{j}}, r_{\mathrm{ij}} = |\vec{r}_{\mathrm{ij}}|$ and $i > j$ eliminates the double counting of the particle pairs. Practically it means that the forces acting on the particles are resultants of the forces coming from the individual interactions with the rest of the particles:

$$\vec{F}_{\mathrm{i}} = \sum_{j \neq i}^{N} \vec{f}_{\mathrm{ij}}, \vec{f}_{\mathrm{ij}} = -\frac{du \left(r_{\mathrm{ij}} \right)}{dr_{\mathrm{ij}}} \cdot \frac{\vec{r}_{\mathrm{ij}}}{r_{\mathrm{ij}}}. \tag{3.6}$$

According to the Newton's third law it stands: $\vec{f}_{\mathrm{ji}} = -\vec{f}_{\mathrm{ij}}$. Computational effort of solving the equations of motion 3.1 is proportional to N^2 and is mostly related to the force computations. Accordingly, to speed-up the computations it is desirable to express the forces analytically. In order to further more reduce the computational effort, it is a standard practice in MD simulations to cut off the potential at some limiting distance, i.e., we neglect the potential if the distance between two interacting atoms is $r_{\mathrm{ij}} > r_{cut}$, where r_{cut} is reasonably chosen. For example, in case of the Lennard-Jones potential (standard potential in MD simulations) usually it is set that $r_{cut} = 2.5 \cdot \sigma$, where σ determines the length scale.

In principle, we might treat an MD simulation as a numerical experiment [100], hence the methodology is practically the same like in a real experiment, as we can see in the schematic of a typical MD simulation in Figure 3.2.
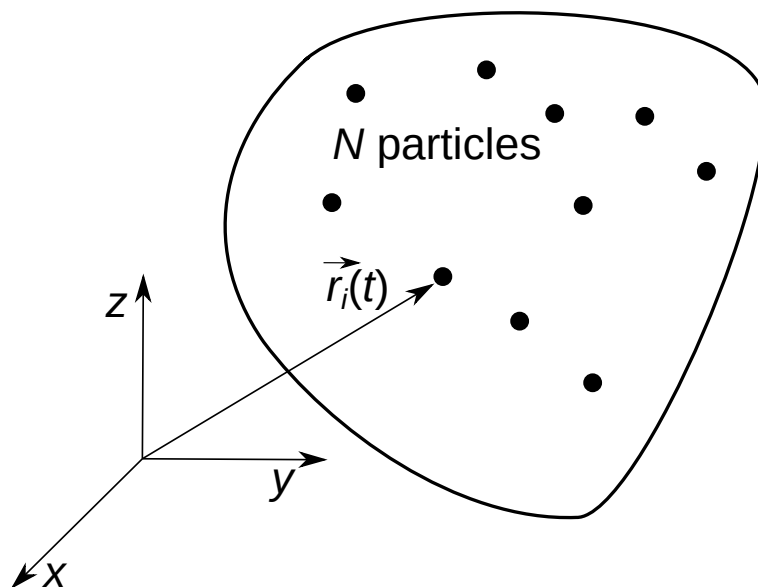
Figure 3.1: Illustration of an MD system with N particles.
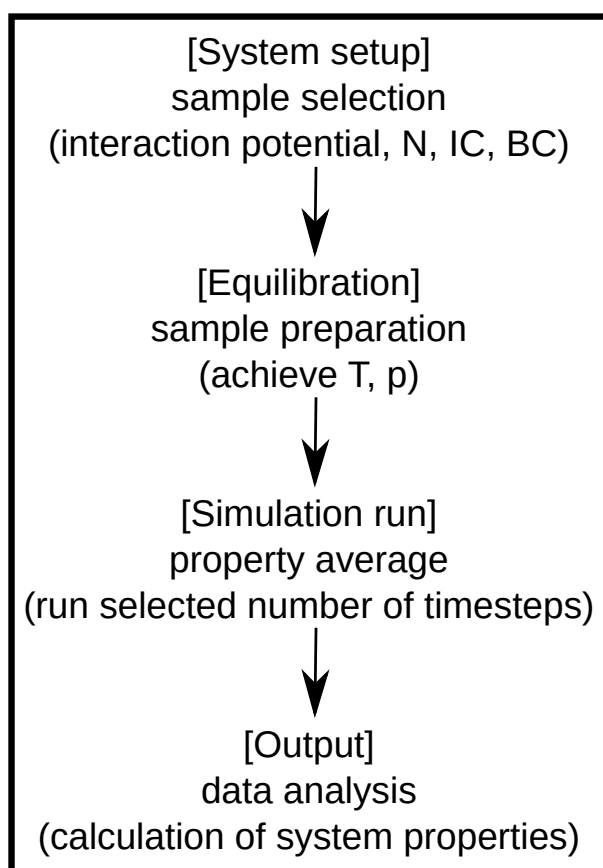
Figure 3.2: Basic schematic of an MD simulation.

In the first step we should setup the system, which means: selecting a proper interaction potential, choosing the number of particles in the system and setting up

their properties (shape, mass, charge), defining initial and boundary conditions. The subsequent step, after the system setup has been done, is the system equilibration which means achievement of desired temperature and pressure (macroscopic properties which depend on the microstate of the system). After the system setup and equilibration are done, simulation is run a given number of simulation steps and averaged characteristics are calculated (for example, radial distribution function $g(r)$). In the end, output data is analyzed and based on that, the desired quantities are computed. Besides equilibrium MD simulations, there are non–equilibrium molecular dynamics ($NEMD$) simulations. For example, a system is exposed to perturbation or high external forces and its response is analyzed, like in simulations of mechanical deformations. We have used $NEMD$ simulations in the way that shearing of the simulation box (mechanical deformation) was imposed, and by analyzing bulk $IL's$ response to the imposed shearing, we have determined $IL's$ viscosity coefficient. There are five key components of MD simulations and those are: (i) initial conditions (IC), (ii) boundary conditions (BC), (iii) force computation, (iv) integrator and (v) computation of system's characteristics.

3.1.1.1 The Lennard-Jones potential

The most common pair potential for describing the interaction of van der Waals systems is the Lennard-Jones potential (LJ potential), given by the formula:

$$U^{LJ}(r_{ij}) = 4\epsilon\left[\left(\frac{\sigma}{r_{ij}}\right)^{12} - \left(\frac{\sigma}{r_{ij}}\right)^{6}\right], \tag{3.7}$$

where r_{ij} is the distance between the atoms i and j. The ϵ parameter defines the strength of the LJ interaction and the σ parameter defines the length scale. LJ potential is strongly repulsive at short distances, it crosses zero at $r_{ij} = \sigma$, i.e., $U^{LJ}(r_{ij} = \sigma) = 0$. LJ potential reaches its minimum $U^{LJ}(r_m) = -\epsilon$ at $r_m = 2^{1/6}\sigma \approx 1.1225\sigma$ and it has an attractive tail at long distances. Values of the parameters $\{\epsilon, \sigma\}$ are chosen to model physical properties of a real system. For example, LJ potential was initially proposed to model liquid argon. Let us now analyze the two terms from the square brackets of Equation 3.7. The term

$\propto r_{ij}^{-12}$ dominates at short distances and it models the repulsion due to the non-bonded overlap of electronic orbitals. It might have an arbitrary form meaning that other exponents or even other functional forms are possible. However, we should think about minimizing the computational effort, hence in most cases this form with $\left(\frac{\sigma}{r_{ij}}\right)^{12}$ is fine. The term $\propto r_{ij}^{-6}$ dominates at long distances and models the van der Waals forces caused by the dipole-dipole interactions due to the fluctuation of dipoles. These weak forces are responsible for the bonding character of systems like rare gases, such as argon or krypton. The interaction force due to the interaction via LJ potential, see Equation 3.7 is:

$$\vec{f}_{ij} = \frac{48\epsilon}{r_{ij}^2} \left[\left(\frac{\sigma}{r_{ij}}\right)^{12} - \frac{1}{2} \left(\frac{\sigma}{r_{ij}}\right)^6 \right] \vec{r}_{ij}. \tag{3.8}$$

As the force is expressed analytically, this is advantageous in terms of the reduction of computational effort.

3.1.1.2 Thermodynamic properties

Key thermodynamic properties of an MD system are the temperature and pressure. Temperature of the system might be introduced via mean kinetic energy of the system:

$$\frac{1}{2N} \sum_{i=1}^{N} m_i \left(\frac{d\vec{r}_i}{dt}\right)^2 = \frac{3}{2} k_B T \Rightarrow T = \frac{1}{3Nk_B} \sum_{i=1}^{N} m_i \left(\frac{d\vec{r}_i}{dt}\right)^2. \tag{3.9}$$

By expressing the temperature T in function of the kinetic energy K we obtain the next relation:

$$T = \frac{2K}{3Nk_B}. \tag{3.10}$$

In case that we consider the temperature T and the density ρ as independent variables, we might express the energy of the system E and the pressure p. These quantities link the microscopic and macroscopic level and can be easily measured in an MD simulation. We should mention that in an MD simulation usually the energy is conserved, while the temperature fluctuates, hence the average temperature

$\langle T \rangle$ should be used instead of T. Pressure is defined by the formula:

$$pV = Nk_BT + \frac{1}{3}\langle \sum_{i=1}^{N} \vec{r}_i \cdot \vec{F}_i \rangle. \tag{3.11}$$

In case of a pair potential this formula is:

$$pV = Nk_BT + \frac{1}{3}\langle \sum_{i<j}^{N} \vec{r}_{ij} \cdot \vec{f}_{ij} \rangle. \tag{3.12}$$

Bearing in mind the relation 3.10 between the temperature T and the kinetic energy K, we express the pressure p as:

$$p = \frac{\rho}{3N}\langle 2K + \sum_{i<j}^{N} \vec{r}_{ij} \cdot \vec{f}_{ij} \rangle. \tag{3.13}$$

Contrary to the total energy $E_{\text{tot}} = K + U$ which should be conserved during a simulation, the temperature and the pressure fluctuate and should be averaged over a chosen number of timesteps.

3.1.1.3 Analysis of the key components of a typical molecular dynamics simulation

In the following text we briefly analyze the key components of a typical MD simulation, which include: (i) initial conditions (IC), (ii) boundary conditions (BC), (iii) force computation, (iv) integrator and ensemble and (v) computation of system's characteristics [99].

(i) **Initial conditions (IC)**

As Newton's equations of motion are ordinary differential equations of the second order, initial conditions are defined as:

$$\vec{r}^N(t=0) = \vec{r}^{N(0)}; \frac{d\vec{r}^N}{dt}(t=0) = \frac{d\vec{r}^{N(0)}}{dt}. \tag{3.14}$$

Generating of IC is simple for ordered systems like crystals, but in case of amorphous solids or for polymer chains it should be treated carefully. Setting the IC is important
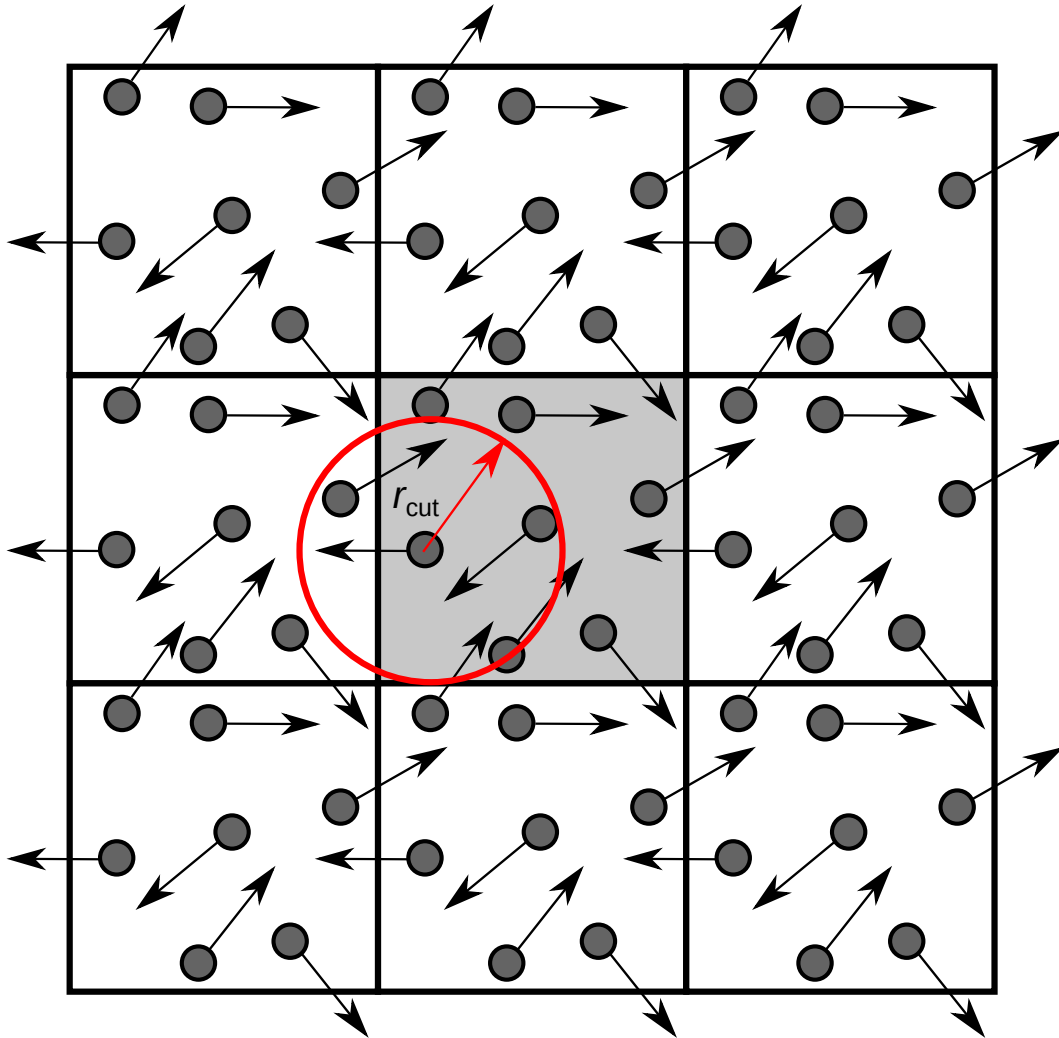
Figure 3.3: Illustration of periodic boundary conditions (PBC). Trajectories of only the atoms in the central cell, also known as supercell (square filled with gray) are explicitly followed. The supercell is infinitely replicated in a given $2D$ or $3D$ space. In this figure we show an example of a $2D$ system with periodic boundaries in both directions in a plane. An atom (let us label it as referent atom) from the supercell interacts with other atoms from the supercell, as well as with the atoms from neighbouring copies of the supercell, under the condition that their distance from the referent atom is within the cutoff radius. Interaction is neglected in case the distance is larger than the cutoff radius.

because often it causes errors. For example, if the particles are positioned too close at the beginning of a simulation, the forces between them get too high.

Related to assignment of initial velocities, it should be taken into account that each independent degree of freedom should carry kinetic energy of $k_B T/2$. Such

a condition can be met by taking initial velocities from the Maxwell-Boltzmann distribution.

(*ii*) **Boundary conditions (BC)**

The behaviour of finite systems is quite different from the behaviour of infinite systems. The number of particles for simulating bulk properties of macroscopic systems has an important role, unless we simulate clusters of atoms in which case the number of constituents is well-defined. No matter how large the simulated system is, the number of particles N is negligible as compared to the number of particles contained in a macroscopic system (at the order of $10^21 \text{to} 10^23$). In case of macroscopic systems just a small fraction of the particles are located close to the boundaries (walls of the container in which the system is placed). In case of a typical liquid with the order of magnitude of $N = 10^21$ particles, the number of particles in the vicinity of the walls is at the order of $N^{2/3} = 10^14$, which means that 1 out of 10^7 is a surface particle. Therefore, in systems like liquids the fraction of particles in the vicinity of the walls is negligible. In modern MD simulations the typical number of particles which can be handled is at the order of 10^6 particles. In such a system, the fraction of the surface particles is more significant and the behaviour of the system is very impacted by the surface effects. An efficient solution for solving the finite-size problem and for minimizing the surface effects is the application of periodic boundary conditions. When periodic boundary conditions are applied the particles are enclosed in the simulation box, which is replicated to infinity by translation in all three directions $\{x, y, z\}$ completely filling the space. When a particle enters or leaves the simulation box, an image particle leaves or enters the simulation box, hence the number of particles is kept constant. Accordingly, the surface effects are suppressed. Summing up the previous discussion, we note that there are two types of boundary conditions: isolated (IBC) and periodic (PBC) boundary conditions (for the illustration of PBC check Figure 3.3). IBC are suitable for the analysis of clusters and molecules, while PBC are suitable for the analysis of bulk materials. There are mixed boundary conditions as well, where the system is periodic along one or two dimensions, but not in all three dimensions. In case of PBC a system of particles is surrounded by vacuum, those particles interact between each other and

do not interact with anything outside the system, except in case that some external force is introduced.

(*iii*) **Force computation**

Equation of motion for the i-th particle can be written as [99]:

$$m_i \frac{d^2 \vec{r}_i}{dt^2} = -\sum_{j \neq i} \frac{\partial U\left(r_i - r_j\right)}{\partial \left(r_i - r_j\right)}, i = 1, ..., N. \qquad (3.15)$$

Computation of the right-hand side of the above equation is the key step which consumes the most computational time in MD simulations, so the efficiency of that computation is of crucial importance. For long-range Coulombic interaction there are special algorithms which break it into two terms: one term represents short-range interaction and the other term represents smooth interaction, like a field. Both of those terms can be computed efficiently in different ways. When PBC are applied, movement of particles within the basic cell is monitored and the basic cell is surrounded by its periodic copies. A consequence of the application of PBC is that each particle i in the simulation box interacts not only with the other particles in the box, but with their images also. This means that the number of interacting pairs is very large. However, this obstacle us usually overcome by setting a cutoff distance, since the interaction of two particles separated by a distance larger than the chosen r_{cut} is neglected. There is the term *minimum image criterion* which claims that among all images of a particle we should consider only the closest ones and neglect the others.

(*iv*) **Integrator and ensemble**

Newton's equations of motion represent a set of ordinary differential equations of the second order, which can be very nonlinear. Transforming them into ordinary differential equations of the first order in $6N$-dimensional space $\left\{\vec{r}^N, \vec{v}^N\right\}$, general numeric algorithms for solving ordinary differential equations can be applied, such as Runge-Kutta method. However, general numeric algorithms are rarely applied in MD simulations, because the existence of Hamiltonian enables more accurate integration algorithms, such as predictor-corrector integrator. There are three main ensembles: micro-canonical, canonical and grand-canonical ensemble. They are dis-

tinguished based on the distribution of initial conditions. When the system is defined by a certain ensemble, it should strictly follow equations of motion, with conserved mechanical energy. Ensemble and integrator are often grouped since there is a class of methods which generate desired ensemble under time integration. In a micro-canonical (NVE) ensemble, system is isolated from the changes in the number of particles (N), volume (V) and energy (E). It corresponds to an adiabatic process in which there is no heat exchange. Micro-canonical MD trajectory can be seen as exchange of potential and kinetic energy, under the condition that the total energy is conserved. In a canonical (NVT) ensemble, the number of particles (N), volume (V) and temperature (T) are conserved. Canonical ensemble is often called constant temperature molecular dynamics ($CTMD$). In NVT ensemble the energy of endothermic and exothermic processes is exchanged with a thermostat. There is a large number of thermostat algorithms which add or remove energy keeping temperature constant. It is not easy to obtain canonical distribution of spatial arrangement and velocities using thermostat algorithms. A wide and relevant topic is which thermostat should be chosen and how its parameters should be set, how does that depend on the system size, how to choose the timestep and integrator. Grand-canonical ensemble represents possible states of a system of particles which is kept in thermodynamic equilibrium (thermal and chemical) with a reservoir. System is considered to be open, in a sense that it can exchange the energy and particles with a reservoir and accordingly, possible states of a system differ in terms of total energy and total number of particles. Volume is the same in all possible states of a system. Thermodynamic variables of a grand-canonical system are chemical potential and temperature. It is called (μVT ensemble, since each of those three quantities is an ensemble constant. There are two main classes of MD integrators: (i) low-order integrators like leapfrog, Verlet, velocity Verlet which is characterized by easy implementation and stability, and (ii) predictor-corrector integrators which are characterized by high accuracy for large timesteps.

- Examples of integrators

We present common integrators in MD simulations, namely: (i) The Leapfrog algorithm, (ii) The Verlet algorithm and (iii) The Velocity Verlet algorithm. In

all three examples the integration of Newton's equations of motion is done with a small timestep δt. In the following text index i is used for an i-th particle where $i = 1, ..., N$, where N is the total number of particles in the system. Its position, velocity and acceleration are labeled as $\vec{r}_i, \vec{V}_i = \frac{d\vec{r}_i}{dt}, \vec{a}_i = \frac{d^2\vec{r}_i}{dt^2}$, respectively.

(i) **The Leapfrog algorithm**

In the Leapfrog algorithm the velocities are first computed at the time moment $t + \frac{\delta t}{2}$ and these are used to compute the positions $\vec{r}_i$, at the time moment $t + \delta t$:

$$\vec{r}_i\left(t + \delta t\right) = \vec{r}_i\left(t\right) + \vec{V}_i\left(t + \frac{\delta t}{2}\right)\delta t. \tag{3.16}$$

In this way, the velocities leap over the positions, then the positions leap over the velocities:

$$\vec{V}_i\left(t + \frac{\delta t}{2}\right) = \vec{V}_i\left(t - \frac{\delta t}{2}\right) + \vec{a}_i\left(t\right)\delta t. \tag{3.17}$$

The advantage of this algorithm is that the velocities are explicitly calculated. However, the disadvantage is that the velocities are not calculated at the same time moment as the positions. The velocities at the time moment t can be computed as:

$$\vec{V}_i\left(t\right) = \frac{1}{2}\left[\vec{V}_i\left(t - \frac{\delta t}{2}\right) + \vec{V}_i\left(t + \frac{\delta t}{2}\right)\right]. \tag{3.18}$$

(ii) **The Verlet algorithm**

New positions and velocities of particles are computed after every timestep. Position of a particle i in time moment $t + \delta t$ can be computed via Taylor expansion over degrees of timestep δt:

$$\vec{r}_i\left(t + \delta t\right) = \vec{r}_i\left(t\right) + \delta t\frac{d\vec{r}_i}{dt}\left(t\right) + \frac{1}{2}\delta t^2\frac{d^2\vec{r}_i}{dt^2}\left(t\right) + \frac{1}{6}\delta t^3\frac{d^3\vec{r}_i}{dt^3}\left(t\right) + ... \tag{3.19}$$

In a similar way, position of particle i in previous timestep can be written as:

$$\vec{r}_i\left(t - \delta t\right) = \vec{r}_i\left(t\right) - \delta t\frac{d\vec{r}_i}{dt}\left(t\right) + \frac{1}{2}\delta t^2\frac{d^2\vec{r}_i}{dt^2}\left(t\right) - \frac{1}{6}\delta t^3\frac{d^3\vec{r}_i}{dt^3}\left(t\right) + ... \tag{3.20}$$

Summing of previous two equations leads to the expression which determines posi-

tion of particle i in time moment $t + \delta t$

$$\vec{r}_i(t + \delta t) = 2\vec{r}_i(t) - \vec{r}_i(t - \delta t) + \delta t^2 \frac{d^2 \vec{r}_i}{dt^2}(t) + O\left(\delta t^4\right). \qquad (3.21)$$

This integrator is called Verlet algorithm, as we can see from Equation 3.21 it uses positions and accelerations at time moment t and positions at time moment $t - \delta t$ to compute new positions at time $t + \Delta t$. The Verlet algorithm does not use explicit velocities. There are two main advantages of the Verlet algorithm: (i) its straightforwardness, and (ii) reasonable storage requirements. The disadvantage is the algorithm's moderate precision. Acceleration of particle i is determined from Newton's equation of motion:

$$\frac{d^2 \vec{r}_i}{dt^2} = -\frac{1}{m_i} \sum_{j \neq i} \frac{\partial U(r_i - r_j)}{\partial(r_i - r_j)}. \qquad (3.22)$$

Position of a particle is computed with precision of δt^4 as it is noted with $O\left(\delta t^4\right)$. Velocity of particle i in time moment t can be determined from its positions in time moments $t + \delta t$ and $t - \delta t$ with precision of $O\left(\delta t^3\right)$, by subtracting the equation for $\vec{r}_i(t - \delta t)$ from the equation for $\vec{r}_i(t + \delta t)$:

$$\frac{d\vec{r}_i}{dt} = \frac{\vec{r}_i(t + \delta t) - \vec{r}_i(t - \delta t)}{2\delta t} + O\left(\delta t^3\right). \qquad (3.23)$$

Positions and velocities of all particles in a system are computed in each step of MD simulation, producing complete time evolution of the system. In order for this time evolution to be of high accuracy, integration timestep δt should be much shorter than the shortest characteristic time of the system. Simple Verlet integrator is used for systems with constant number of particles, constant volume and constant total energy, which is micro-canonical (NVE) ensemble.

(iii) **The Velocity Verlet algorithm**

In the Velocity Verlet algorithm, positions, velocities and accelerations at time moment t are used for computing position at time moment $t + \delta t$:

$$\vec{r}_i(t + \delta t) = \vec{r}_i(t) + \vec{V}_i(t)\delta t + \frac{1}{2}\vec{a}_i(t)\delta t^2. \qquad (3.24)$$

For computing velocity at time moment $t + \delta t$, velocity at time moment t and acceleration at time moments t and $t + \delta t$ are used:

$$\vec{V}_i(t + \delta t) = \vec{V}_i(t) + \frac{1}{2}[\vec{a}_i(t) + \vec{a}_i(t + \delta t)]\delta t. \tag{3.25}$$

(v) **Computation of system's characteristics**

A big advantage of MD simulations is their applicability at the level of classical atoms. All characteristics which are well defined in classical and statistical mechanics can be computed. The two main problems to be taken into account when performing MD simulations, are accuracy and efficiency. System's characteristics can be roughly divided into four categories:

(1) Structural characteristics, for example radial distribution function

(2) State equation, for example phase diagrams, static response like coefficient of thermal expansion

(3) Transport characteristics, for example viscosity, thermal conductivity, diffusivity

(4) Non-equilibrium response - for example plastic deformation

Physical quantity $\langle A \rangle$ is determined as mean value of its values $A(t)$ in time moments t during a long time interval (large number n of MD steps) after initial relaxation during long enough time (with relaxation time t_0) [99]:

$$\langle A \rangle = \frac{1}{n}\sum_{j=1}^{n} A(t_0 + j\delta t). \tag{3.26}$$

If simulation is long enough so that the system can achieve equilibrium state (if simulation is much longer than all relaxation times), this time averaging of quantity $\langle A \rangle$ is equivalent to the ensemble averaging.

3.1.2 $LAMMPS$ code for molecular dynamics

An usual algorithm for developing MD simulations can be roughly divided into next subsequent steps:

(i) geometric formation of the simulation setup

(ii) definition of the atom types and their attributes (e.g., shape, mass, charge)

(iii) definition of the interactions between all atom types

(iv) implementation of the model and MD simulation of a certain physical phenomenon, (e.g., in our case we simulate effects related to nanoscopic tribological behaviour of ionic liquids)

(v) storage of the relevant data and its analysis with the goal of obtaining results $LAMMPS$ (Large-scale Atomic/Molecular Massively Parallel Simulator) is a well-known and widely used MD code [98]. Development of MD simulations in $LAMMPS$ code can be roughly divided into three subsequent phases:

(a) pre-processing, which includes points (i), (ii), (iii) from the above list

(b) processing, actually this is MD simulation which corresponds to the point (iv) from the above list and

(c) post-processing, which corresponds to the point (v) from the above list

Processing is done via development of $LAMMPS$ scripts, while for pre- and post-processing we write codes in C programming language. MD simulations are computationally highly demanding since we work with systems that contain tens of thousands of atoms. The key advantage of $LAMMPS$ is parallelization, which means that $LAMMPS$ codes can be run on a supercomputer. We write Linux bash scripts for submitting simulations to the supercomputer, as well as for the efficient manipulation with the output files. For visualization we use VMD (Visual Molecular Dynamics) software package [101].

3.1.2.1 Multi-level summation method for summing long-range Coulombic interactions

Long-range Coulombic interactions are treated in LAMMPS with methods that work in the inverse k-space [102–104]. In our LAMMPS simulations we apply the Multi-level summation (MSM) method which maps the charge of atoms onto a 3D mesh and uses hierarchy of several levels of coarse-graining of the mesh on which it directly computes Coulombic interaction. Competitive methods to MSM method for summing Coulombic interactions are Ewald and Particle Particle Particle Mesh ($PPPM$) methods, but they can be applied in case of a 3D simulation just if periodic boundary conditions are present along all three directions. On the other

side, MSM method can be applied in case of a 3D simulation without restrictions related to periodic boundary conditions, i.e., it can be applied for non-periodic as well as for mixed periodic and non-periodic boundary conditions. When we work with bulk ILs, our system is periodic in all three directions. On the other side, in case of confined ILs, our system is periodic along the x and y directions and it is fixed along the z direction. Actually, we might state that our system with confined IL includes mixed periodic (along two directions) and non-periodic (along one direction) boundary conditions, hence MSM method is adequate for treating long-range Coulombic interactions in our simulations.

3.2 Simulation setup and models of ionic liquid

3.2.1 Simulation setup

We have developed our simulation setup bearing in mind lubrication role of IL, hence it consists of two solid plates and IL which is confined between them and also present in the lateral reservoirs. Schematic of simulation setup together with configuration snapshots in three cross-sections, i.e., xz, yz, xy cross-sections which are exported from the VMD (Visual Molecular Dynamics program [101]) is shown in Figure 3.4 in case of SM model and in Figure 3.5 in case of TM model (e.g., diameter of neutral tail is arbitrary chosen to be the same as the diameter of cationic head). Schematic in simulation setup figures (i.e., Figures 3.4 and 3.5) indicates the number of particles used and the imposed normal load F_z and lateral velocity V_x. In VMD configuration snapshots dimensions of the system along the three axes, i.e., x, y, z, are noted. The simulation setup was loosely inspired by previously published research by others [39, 49, 51, 52]. By implementing such a geometry we have attempted to achieve:

(i) a realistic particle squeeze–out behaviour with the formation of two lateral lubricant regions (in a similar manner to the simulations of Capozza et al. [52]) and

(ii) a system that allows the lubricant to be externally pressurized.

For the description of the solid surfaces we have combined rigid layers of particles moving as a single entity on which the external force or motion is imposed, denoted
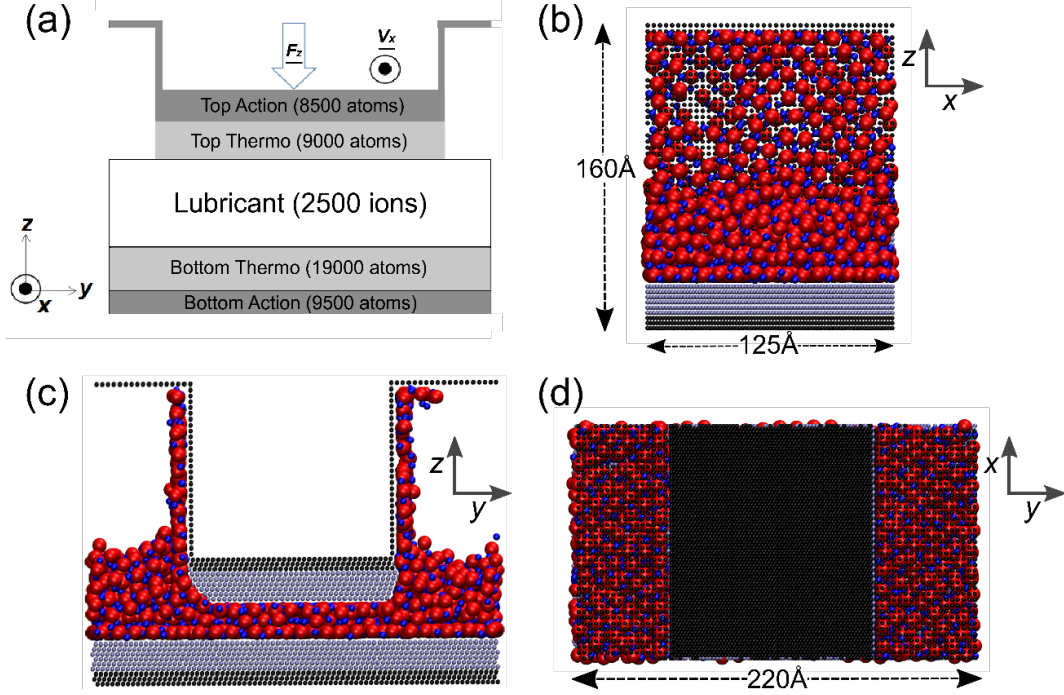
Figure 3.4: (a) Schematic of the simulation setup shown as yz cross-section. There are two solid plates at the top and bottom of the system, consisting of two regions: at the outermost ones the particles are moving as a single entity (Top/Bottom Action) and at the innermost ones the particles are at a controlled temperature (Top/Bottom Thermo). The thermalized layers are in direct contact with the lubricant while the action layers are used to impose external velocity and/or force to the solid plates. (b)-(d) Side views of the typical simulation configuration and key dimensions of the geometry. (b) Side (xz) view with respect to the shear direction. (c) Front (yz) view in the direction of the Top plate motion. (d) Top (xy) view of the system. The solid plates are made up of FCC (111) atomic layers. The ionic liquid is composed of an equal number of cations (blue spheres) and anions (red spheres).

by "Top Action" and "Bottom Action" in Figures 3.4 and 3.5 (a), with thermalized layers (denoted by "Top Thermo" and "Bottom Thermo") in which particles vibrate thermally at $T = 330$ K.

The Nose-Hoover NVT thermostat is used to control the temperature. As in previous MD simulations [43, 49, 51, 52, 56], under similar operating conditions, the details of the adopted dissipation scheme are not expected to change the essence of the system response on mechanical deformation. The relaxation time of the Nose-Hoover NVT thermostat for the lubricant and the solids is 200 fs (check Reference [43]). The plates were treated as rigid bodies, with the lower one being fixed
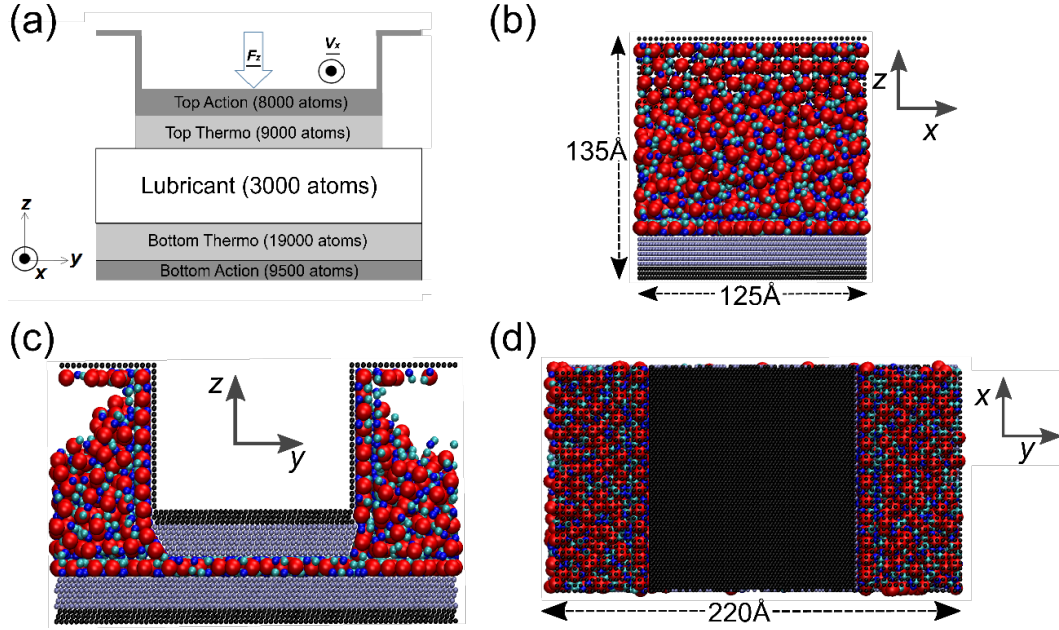
Figure 3.5: Schematic of the simulation setup shown as yz cross-section. Dimensions of the system along the y and z axes, together with the directions of the imposed normal load F_z and lateral velocity V_x are noted. The total system length in the x direction is 125 Å. There are two solid plates at the top and bottom of the system. Ionic liquid is composed of an equal number of cation–tail pairs and anions (cations: blue spheres; tails: cyan spheres; anions: red spheres). (a) Schematic of the simulation setup presented as yz cross-section, showing the number of atoms in each region. (b) Side (xz) view of the system showing the dimensions along the x and z direction. (c) Side (yz) view of the system. (d) Top (xy) view of the system showing the dimension along the y direction.

and the upper one subjected to a force oriented along the z direction, i.e., normal load F_z , as shown in Figures 3.4 and 3.5 (a) and driven along the x direction at a constant velocity V_x. The solid plates were made up of densely packed atomic layers at a FCC (111) lattice arrangement. Periodic boundary conditions were applied in the x and y directions. The Bottom plate can therefore be considered to be infinite, while the Top plate is surrounded by vacuum pockets on its sides, the so called lateral reservoirs, in which the lubricant can freely expand. The lateral reservoirs were implemented as a mechanistic way for allowing the lubricant to be dynamically squeezed in or out as an external load or velocity is applied, or due to local fluctuations during the simulation progression. At the same time, the lubricant remains an infinite continuous body in the x and y directions, similar to the conditions

observed in a real tribological system from a mesoscopic point of view. This is especially important if the system experiences partial or complete crystallization under compression, check Figure 3.29 in section 3.4. While the total number of considered lubricant molecules is constant, the finite upper plate width and the resulting free space enable the particles to be squeezed-out into the lateral reservoirs. The number of lubricant molecules effectively confined inside the gap can therefore dynamically change depending on the loading conditions. This is important for exploring the possible states of a mechanical system of particles that is being maintained in thermodynamic equilibrium (thermal and chemical) with a lubricant reservoir (i.e., void spaces in tribological system). The nanotribological system is open in the sense that it can exchange energy and particles, realizing an effectively grand-canonical situation, check Figures 3.4 and 3.5 (c) and Reference [105].

3.2.2 Models of ionic liquid

In this subsection we present implementation details about the modeled solid plates and IL lubricants in case of SM and TM models of ionic liquid, respectively.

3.2.2.1 Salt model of ionic liquid

The model used in this work is a coarse–grained model of IL which has already been exploited in previous studies [49, 51, 52, 64] and it is known as SM model (salt–like model). It is a charged Lennard–Jones system consisting of cations and anions. There are two types of interatomic interactions in our system and both of them are non–bonded: Lennard–Jones (LJ) potential and Coulombic electrostatic potential. In the current work we are comparing bulk and confined IL properties. Therefore, there are three different atom types taken into consideration: (i) cations, (ii) anions and (iii) solid plate atoms. The solid plates consist of nine densely packed layers in a FCC (111) lattice arrangement. Between all types of atoms we apply full LJ 12-6 potential, with the addition of Coulombic electrostatic potential for the interactions between ions. In our system the cations and the anions are charged particles, while the solid plate atoms are electroneutral. Accordingly, we have implemented a LJ

12-6 potential combined with Coulombic electrostatic potential:

$$V_{\alpha\beta}\left(r_{ij}\right) = 4\epsilon_{\alpha\beta}\left[\left(\frac{\sigma_{\alpha\beta}}{r_{ij}}\right)^{12} - \left(\frac{\sigma_{\alpha\beta}}{r_{ij}}\right)^{6}\right] + \frac{1}{4\pi\epsilon_0\epsilon_r}\frac{q_iq_j}{r_{ij}}, \qquad (3.27)$$

where $i,j = 1,\ldots,N$ are particle indices, and N is the total number of particles. Parameters $\{\epsilon_{\alpha\beta}, \sigma_{\alpha\beta}\}$ define the LJ potential between different types of particles: $\alpha, \beta \in \{A, C, P\}$ which refer to anions, cations and solid plate atoms, respectively. The diameter of cations and anions is set to $\sigma_{CC} = 5$ Å and $\sigma_{AA} = 10$ Å, respectively. The mass of cations and anions is $m_C = 130$ g/mol and $m_A = 290$ g/mol, respectively. The asymmetry of ion sizes is typical in many experimentally explored systems and the parameters have already been explored in literature, check Reference [52, 64]. The atoms of the solid plates have a diameter of $\sigma_{PP} = 3$ Å. The mass of the solid plate atoms is $m_P = 65$ g/mol. The LJ potential has a short–range impact, since it vanishes rapidly as the distance increases $\propto r^{-6}$, while the Coulombic potential has a long–range impact, $\propto 1/r$. To handle long–range interactions, we have used a multi–level summation method (MSM) [104], since it scales well with the number of ions and allows the use of mixed periodic (in x and y directions) and non-periodic (in z direction) boundary conditions, which are present in our simulation setup with confined IL. On the other hand, in our simulation setup with bulk IL, periodic boundary conditions are applied in all three directions ($\{x, y, z\}$). Ions are modeled as coarse grain particles, the charge of which is set equal to elementary: $q_C = +e$ and $q_A = -e$, i.e., $e = 1.6 \cdot 10^{-19}$ C. The dielectric constant is set to $\epsilon_r = 2$ to account for the dielectric screening, as in Refs. [51, 52, 64].

In engineering applications, the lubricant molecules typically interact with metal surfaces. Computationally efficient many–body potentials such as embedded atom method (EAM) potential [106, 107] can be applied for the description of such solids. Such schemes have been employed extensively for modeling a wide range of systems including metals [107] and metal-metal oxide interfaces [108]. In addition, in order to account for the induced charges on the metallic conductor surface by the ions, the Drude-rod model developed by Iori and Corni [109] which consists of the addition of an embedded dipole into each metal atom, thus rendering it polarizable, has been

applied in previous studies [39]. In this study, modeling the elasticity of metallic plates plays a secondary role (central role belongs to IL lubricant). Therefore, we have selected a simplified model in which plate atoms interact strongly with each other if they belong to the same plate, i.e., $\epsilon_{PP} = 120$ kCal/mol, as opposed, to a very weak interaction between the different plates $\epsilon_{top/bottom} = 0.03$ kCal/mol. The parameter ϵ_{PP} is so strong in order to ensure that the initial configuration of the solid bodies will basically remain unchanged (apart from high frequency oscillations). Furthermore, even though typical engineering systems are often metallic, our initial coarse grained MD studies of liquid behaviour according to the applied conditions justified the implementation of a simpler solid system which does not feature substrate polarization, check Reference [64]. Finally, it is possible that the actual surfaces might feature carbon coatings or depositions, in which case the surface polarization can be of secondary importance. In the Table 3.1 we present the values of $\{\epsilon_{\alpha\beta}, \sigma_{\alpha\beta}\}$ parameters used in our model. Cross-interaction parameters are calculated by Lorentz-Berthold mixing rules: $\epsilon_{\alpha\beta} = \sqrt{\epsilon_\alpha \cdot \epsilon_\beta}$ and $\sigma_{\alpha\beta} = (\sigma_\alpha + \sigma_\beta)/2$. The starting configuration for our MD simulations was obtained via a relaxation process. In order to obtain a stable and reproducible initial configuration, the relaxation was performed through a step-wise increase of absolute ion charge at steps of $\Delta|q_i| = e/10$, $i = \{A, C\}$. Each time the charge of the ions was increased, a minimization of the system's energy through conjugated gradient method was performed. In this way, the system characteristics were gradually converted from pure LJ to a Coulomb interaction dominated system through a series of stable configurations. As we are aiming at understanding the lubricant behaviour at mesoscopic conditions observed in a ring–liner system, we have attempted to include in our MD model the potential IL pressurization that can occur due to the liquid flow resistance, as well as the variable pressure arising from the reacting gas in the combustion chamber. Inserting gas molecules directly in the simulation for this purpose would require a reduction of the time step due to higher thermal velocities of the gas. In turn, the computational cost would increase significantly making simulations impossible to run in realistic computational time. Therefore, in order to understand the effect of external pressure on the IL behaviour, we have applied a repulsive force between

Table 3.1: List of LJ parameters of SM model of ionic liquid.

pair $\alpha\beta$	$\epsilon_{\alpha\beta}$ [kCal/mol]	$\sigma_{\alpha\beta}$ [Å]
CC	0.03	5
AA	0.03	10
CA	0.03	7.5
PC	0.3	4
PA	0.3	6.5
PP	120	3

the topmost rigid solid layer and the IL particles in the form of a truncated and shifted LJ potential. Two cases with cut-off distances at 15 Å and 4 Å above the outermost Top plate layer were studied so that the IL inside the confinement gap would remain outside the influence zone of this mechanistic force. By appropriate selection of the LJ parameters for this potential, the resulting external pressures applied on the unconfined surface of the IL were 120 kPa and 250 kPa, respectively.

3.2.2.2 Tailed model of ionic liquid

In this study, we have applied a generic coarse grained IL model, introduced in Reference [52]. In this model, the anion is represented as a negatively charged large–sized spherical particle, while the cation is a dimer consisting of a positively charged small–sized spherical particle (i.e. cationic head), and a neutral spherical particle (tail) attached to the corresponding cationic head via an elastic spring, see Figure 3.6 and Reference [110]. Since the cationic tail is the principal feature of the model used in this paper, we will refer to it as tail model (TM). The asymmetry of the cation leads to amorphous (glassy) states for realistic values of interaction parameters (e.g., for hydrocarbons), in contrast to the simplest coarse–grained model of IL known as SM model (salt–like model), where both cations and anions are spherical. The SM model has already been exploited in previous studies [49, 52, 64, 111]. Despite an obvious advantage of simplicity, in order to avoid crystallization, the SM model relies on a very weak non-bonded Lennard-Jones interaction which makes any comparison with real IL only qualitative.
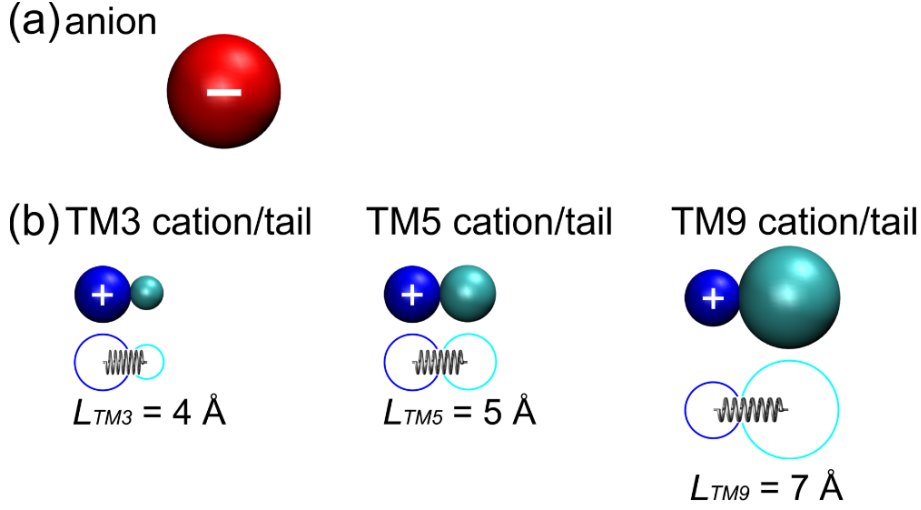
Figure 3.6: Schematic representation of (a) anion and (b) cation molecules in TM model. The anion is represented by a spherical particle with a diameter $\sigma_{\mathrm{AA}} = 10$ Å. The cation molecule consists of a charged head with a diameter $\sigma_{\mathrm{CC}} = 5$ Åand a neutral tail. In order to be more concise, we refer just to cationic head as the cation. The cation and its tail are connected by a spring with length $L = (\sigma_{\mathrm{C}} + \sigma_{\mathrm{T}})/2$. The size of the tail has been varied and (a) $TM3$, (b) $TM5$ and (c) $TM9$ ionic liquids have a tail diameter of 3, 5 and 9 Å, respectively. The molecular asymmetry is a feature of real ionic liquids and chosen parameters resemble $[BMIM]^{+}[PF_6]^{-}$ IL properties, check References [49, 51].

In addition, the SM model cannot account for molecular asymmetry featured in real ILs. Nevertheless, the SM model has been proven to be quite useful for the development of the simulation methodology, as it reduces computational complexity and enables faster equilibration (e.g., for obtaining static force-distance characteristics as in Reference [64]). More complex extensions of TM coarse grain models can involve several tails of different size, like in Reference [49]. For simplicity reasons, we restrain our considerations in this study to a single neutral tail of a variable size. Although a whole cationic dimer is an entity which actually represents a cation, in order to be more concise we refer just to cationic head as the cation. One might raise a question what are the reasons for the attaching of a neutral tail to a cation? First of all, real ILs usually include cations that consist of the cationic head (positively charged) and alkyl chain (neutral part of cation). Alkyl chains can have different lengths (different number of C atoms). Furthermore, the tail enhances the general

tendency of ILs to form a glass rather than a crystal at low temperatures [52]. As the previous studies have shown, the shape of IL molecules may affect their layering structure [49]. According to that, the central question which we address in this study is how does the tail size affect the structure, static and dynamic behaviour, as well as, lubrication properties of a generic IL represented via tailed–model.

- Interaction model

In the current work we are dealing with both bulk and confined ILs. Hence, in case of simulation setup with confined ILs, there are two solid plates consisting of solid plate atoms. To sum up, in total there are four different atom types taken into consideration:

(i) cations, (ii) tails, (iii) anions and (iv) solid plate atoms.

In cation–tail dimers an elastic spring connects cations and tails enabling the tail's freedom of moving independently from its cation, since their connection is not rigid. Interatomic interactions taken into consideration in our molecular dynamics simulations are:

(i) non–bonded interactions (Lennard–Jones (LJ) and Coulombic electrostatic potential) and

(ii) bonded interaction (elastic spring potential in cation–tail pairs). The next equation defines the interaction potential:

$$V_{\alpha\beta}\left(r_{ij}\right) = 4\epsilon_{\alpha\beta}\left[\left(\frac{\sigma_{\alpha\beta}}{r_{ij}}\right)^{12} - \left(\frac{\sigma_{\alpha\beta}}{r_{ij}}\right)^{6}\right] + \frac{1}{4\pi\epsilon_0\epsilon_r}\frac{q_i q_j}{r_{ij}}, \qquad (3.28)$$

where $i, j = 1, \ldots, N$ are particle indices, and N is the total number of particles. Particles which comply to the interaction potential written in the above equation, i.e., Equation 3.28, can be of different types: $\alpha, \beta \in \{A, C, P\}$ which refer to anions, cations and solid plate atoms, respectively. On the other hand, interaction of tails with all other atom types, including tails themselves, is implemented using a purely repulsive potential, namely a shifted and cut LJ 12-6 potential. It means that full LJ 12-6 potential is shifted up for the value of potential well depth (ϵ) and cut at the distance corresponding to the potential well minimum ($r_{\text{cut}} = 2^{1/6}\sigma$). The next

equation defines the above mentioned interaction potential:

$$V_{\alpha\beta}\left(r_{ij}\right) = \epsilon_{\alpha\beta} + 4\epsilon_{\alpha\beta}\left[\left(\frac{\sigma_{\alpha\beta}}{r_{ij}}\right)^{12} - \left(\frac{\sigma_{\alpha\beta}}{r_{ij}}\right)^{6}\right], r_{ij} \leq 2^{1/6}\sigma_{\alpha\beta} \qquad (3.29)$$

and $V_{\alpha\beta}\left(r_{ij}\right) = 0, r_{ij} > 2^{1/6}\sigma_{\alpha\beta}$, where in Equation 3.29 at least one of indices $\alpha, \beta = T$ which refers to tails. The ionic liquid is electroneutral, i.e., the number of cations and anions is the same. The total number of ionic liquid molecules (cation–tail dimers and anions) is $N_{\mathrm{IL}} = 3000$. Therefore, the total number of ions is $N_C = N_A = 1000$ and the number of tails is $N_T = N_C = 1000$.

   - Model Parameters

In this study we have fixed the diameter of the cationic heads and anions to $\sigma_{\mathrm{CC}} = 5$ Å and $\sigma_{\mathrm{AA}} = 10$ Å, respectively. Such choice respects the asymmetry that exists in ILs and it is consistent with other models, as well as, for example $[BMIM]^+[PF_6]^-$ ionic liquid, check Reference [49, 51, 52, 64]. The solid plate atoms have a diameter of $\sigma_{\mathrm{PP}} = 3$ Å. We have taken into consideration three different TM models of IL depending on the tail size which is defined as Lennard–Jones σ_{TT} parameter: small–tail cationic dimer (i.e., $TM3$ model with $\sigma_{\mathrm{TT}} = 3$ Å), symmetric cationic dimer (i.e., $TM5$ model with $\sigma_{\mathrm{TT}} = \sigma_{\mathrm{CC}} = 5$ Å) and large–tail cationic dimer (i.e., $TM9$ model with $\sigma_{\mathrm{TT}} = 9$ Å). The values of the tail size are chosen to take into account their relation to the size of the cationic head which is $\sigma_{\mathrm{CC}} = 5$ Å, hence our choice can be described as: tail size less–, equal to– and greater than– the size of cation.

   Drawing a comparison with the experiment in Refs. [53, 67], the TM IL mimics a folded alkyl chain and the radius of the sphere is related to the gyration radius of the chains. Depending on the length of the alkyl chain, the sphere has a smaller or lager radius. Thus, the size of a sphere which represents a neutral tail in TM ILs does not compare directly with the alkyl chain length. However, we can make a qualitative analogy. While the representation of the alkyl chain as a neutral LJ sphere does not include all the microscopic level features, we will show that the three selected radii, i.e., $\sigma_{\mathrm{TT}} = \{3, 5, 9\}$ Å, result in clear differences of the bulk properties of ILs and their lubrication response. Each cation–tail pair is connected via identical elastic spring defined by the next two parameters: elastic constant

Table 3.2: List of LJ parameters of TM models of ionic liquid; the tail size is denoted by σ_{TT} since it is variable.

pair $\alpha\beta$	$\epsilon_{\alpha\beta}^{\mathrm{LJ}}$ [kCal/mol]	$\sigma_{\alpha\beta}$ [Å]
CC	1.1	5
AA	1.1	10
TT	1.1	σ_{TT}
CA	1.1	7.5
CT	1.1	$(5 + \sigma_{\mathrm{TT}})/2$
AT	1.1	$(10 + \sigma_{\mathrm{TT}})/2$
PC	5.3	4
PA	5.3	6.5
PT	5.3	$(3 + \sigma_{\mathrm{TT}})/2$
PP	120	3

$K = 80$ kcal/molÅ^2 and equilibrium length of the spring $l_0 = (\sigma_{\mathrm{CC}} + \sigma_{\mathrm{TT}})/2$. The strength of the LJ interactions between different charged parts of ions ($i, j = \{A, C\}$) is $\epsilon_{\mathrm{ij}} = 1.1$ kcal/mol. The LJ parameters are chosen to compare well with one of the most widely studied ionic liquids $[BMIM]^+[PF_6]^-$, check Reference [49, 51]. The charge of ions is set to elementary: $q_C = +e$ and $q_A = -e$, where $e = 1.6 \cdot 10^{-19}$ C. The strength of the ion-substrate interaction was tuned to ensure complete wetting, $\epsilon_{\alpha\mathrm{P}} = 5.3$ kcal/mol, $\alpha \in \{A, C, T\}$. Only when the strength of ion-substrate LJ interaction $\epsilon_{\alpha\mathrm{P}}$ equals the strength of inter-ionic LJ interaction $\epsilon_{\alpha\beta}$, partial wetting is observed, i.e., $\epsilon_{\alpha\mathrm{P}} = 1.1$ kcal/mol, where $\alpha, \beta \in \{A, C, T\}$ (more details about the wetting behaviour of TM ionic liquids are provided in section 3.3 in the subsubsection 3.3.2.3). In the table 3.2 we present the values of $\{\epsilon_{\alpha\beta}, \sigma_{\alpha\beta}\}$ parameters used in our models. Cross-interaction parameters are calculated by Lorentz-Berthold mixing rules: $\epsilon_{\alpha\beta} = \sqrt{\epsilon_\alpha \cdot \epsilon_\beta}$ and $\sigma_{\alpha\beta} = (\sigma_\alpha + \sigma_\beta)/2$.

3.3   Bulk ionic liquid

The main focus of our research is oriented towards revealing the properties and behaviour of confined IL, since IL accomplishes its lubricating role when confined

between solid surfaces. The length scale of confinement we are interested in is expressed in nanometers, hence the nanoscale confinement affects the structure and behaviour of IL. In order to better understand the effects of nanoconfinement on IL, we should first understand the IL itself, which means that we should first characterize bulk IL. For this purpose we have relaxed bulk IL and determined its viscosity characteristics, as well as its wetting behaviour. This section is dedicated to our study of bulk IL in case of SM model (subsection 3.3.1) and in case of three representative TM models (subsection 3.3.2).

3.3.1 Bulk salt model of ionic liquid

3.3.1.1 Solidification and melting of bulk salt model of ionic liquid

In order to confirm that the SM modeled IL used in our MD simulations remains in a liquid state for the conditions of interest, its liquid–solid and solid–liquid phase transitions have been studied. The bulk ionic liquid was implemented by randomly placing a chosen number of ions ($N_C = N_A = 1000$) into a $3D$ simulation box that is periodic in all three directions, with pressure kept constant at 100 kPa. Phase transitions were then achieved via the application of linear ramping to the temperature, in a similar approach to the calculations performed in Reference [52]. Starting from an initial temperature $T_1 = 330$ K where the IL is in a liquid state, the temperature was decreased linearly down to $T_2 = 180$ K. The absolute rate of temperature change was: $|dT|/dt = 1.67\ K\ ns^{-1}$. A liquid–solid phase transition was observed during the IL cooling.

After reaching $T_2 = 180$ K, the temperature was increased back to the initial value of $T_1 = 330$ K. A solid–liquid phase transition was observed during this heating process. In Figure 3.7 the IL internal energy change ΔE_{int} and temperature T are shown as functions of time t. The temperature profile follows the applied conditions and its superimposition to internal energy change allows the observation of the dynamic behaviour of the liquid. By plotting the averaged internal energy change of the IL against its temperature in Figure 3.8, the hysteresis behaviour in the solidification–melting cycle is clearly observed, while the phase transition locations
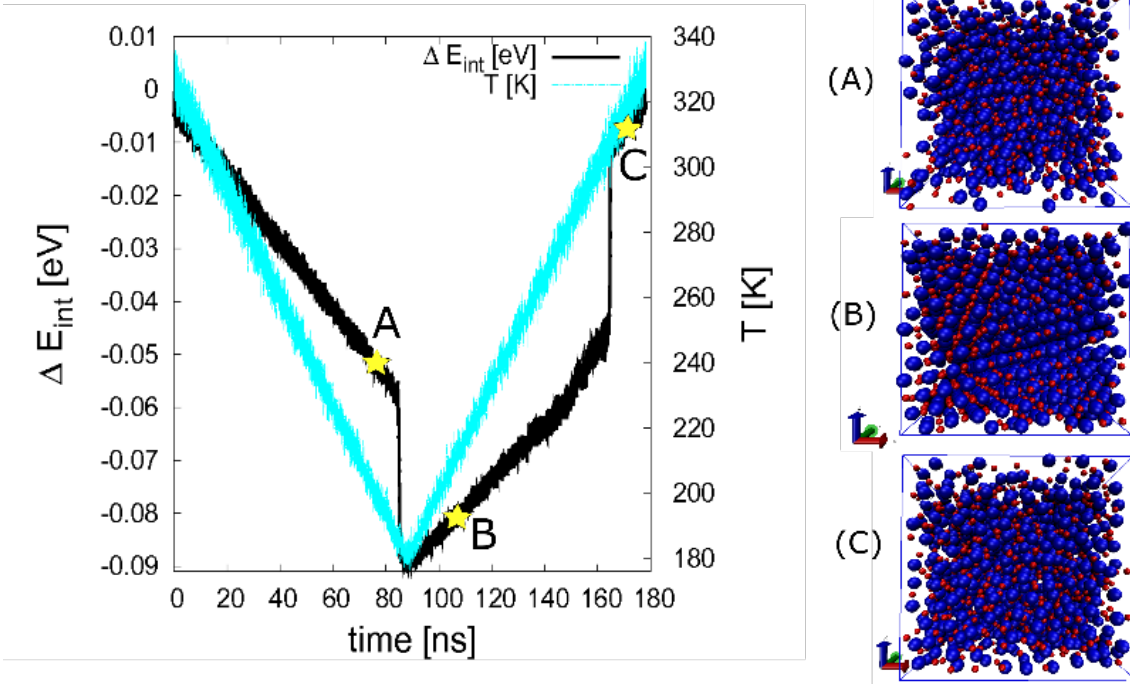
Figure 3.7: (Left panel): Bulk internal energy change and temperature of the ionic liquid as a function of simulation time. (Right panel) Snapshots of ion arrangement at liquid (A), (C) and solid (B) state.

can be clearly defined. It can be seen that during the cooling process, the internal energy of IL linearly decreases until the temperature reaches $T_{\mathrm{ls}} = 190$ K, at which point a sharp drop is observed. This indicates a first order thermal phase transition (liquid–solid). During the heating process, a similar sharp jump of energy is observed at $T_{\mathrm{sl}} = 305$ K which corresponds to an opposite phase transition (solid–liquid). The obtained results are in a good agreement with Reference [52] and confirm that the IL behaves as a liquid for temperatures higher than 310 K, under atmospheric pressure conditions. In the rest of our calculations a temperature value of $T = 330$ K was applied, in order to allow a liquid state that is combined with local solidification under elevated contact pressure conditions.

3.3.1.2 Relaxation simulations

We have revealed the solidification and melting phase transitions of bulk SM ionic liquid, under the condition of atmospheric pressure. The subsequent step was to
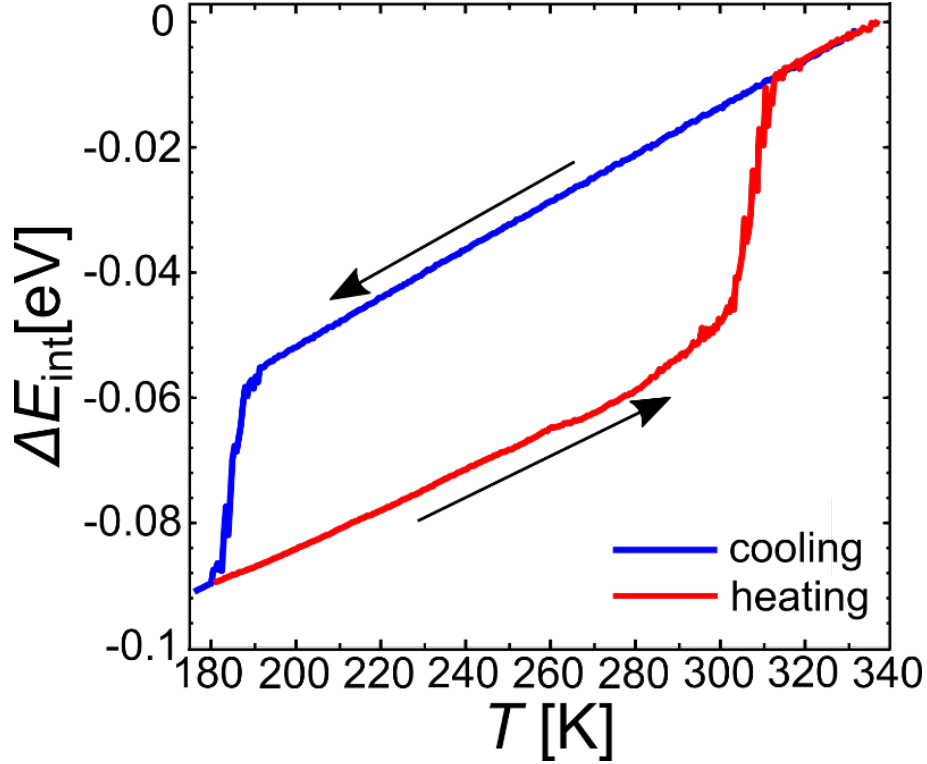
Figure 3.8: Bulk internal energy change of the ionic liquid as a function of temperature. The internal energy was calculated by averaging on segments of $\Delta T = 0.5K$.

make the bulk IL comparable with its confined counterpart and to do so we had to determine simulation box volume which enables the pressure experienced by the confined IL. More specifically, for the present system of bulk SM ionic liquid confined between the solid plates (c.f. Figure 3.4), the pressure was $p \approx 1$ MPa. The Nose–Hoover NVT thermostat was used to control the temperature and was set to $T = 330$ K. The system was relaxed for $t_{\text{tot}} = 3 \cdot 10^7$ fs until the internal energy had converged and the pressure had approached the desired value. The simulation timestep was $dt = 0.5$ fs. We have obtained pressure stabilization at $\langle p \rangle = 1.1$ MPa with a side length of the cubic simulation box at $L = 99$ Å. The energy relaxed to a value of $\langle E_{\text{int}} \rangle = 0.7597$ kCal/mol. The molar and mass density of the bulk IL was $\rho_n = 3400$ mol/m^3 and $\rho_m = 719$ kg/m^3 respectively.

3.3.1.3 Viscosity characteristics

We have calculated the viscosity in two ways: using the Green–Kubo relation since the viscosity of a system can be represented as an integral of the auto-correlation
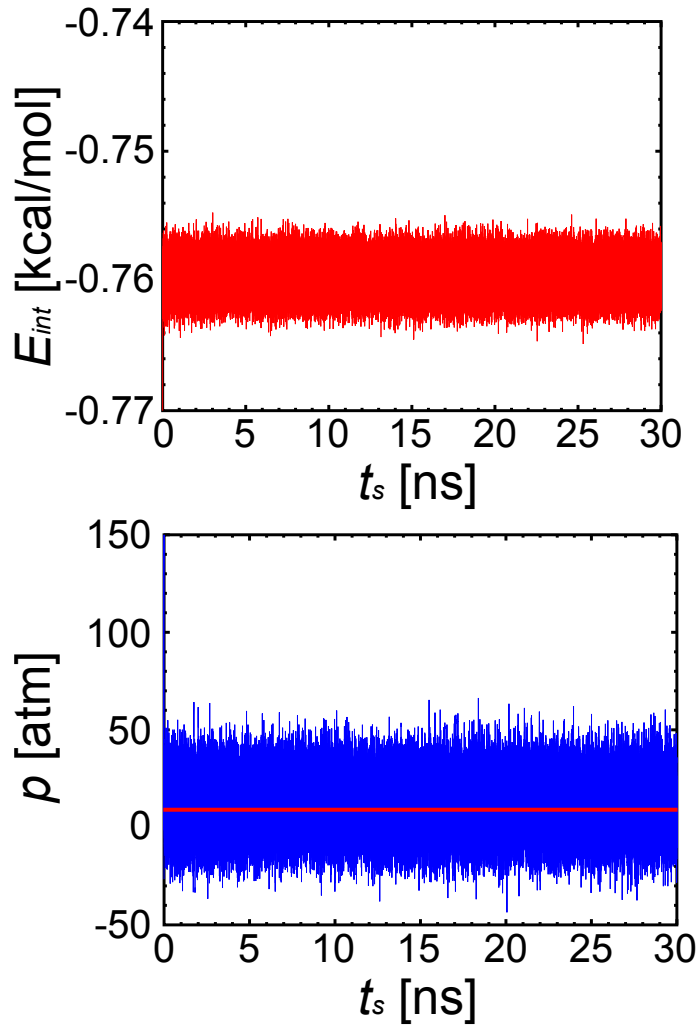
Figure 3.9: Dependences of internal energy E_{int} and pressure p on simulation time t_s in case of bulk SM ionic liquid. Solid line in $p\,(t_s)$ plot denotes the value of target pressure $p = 1$ MPa ($p \approx 10$ atm).

function [112], and using non–equilibrium molecular dynamics simulations with different shear strains.

In the non–equilibrium shearing simulations, the bulk IL is placed into a triclinic (non–orthogonal) simulation box with periodic boundary conditions applied in all three directions. Due to the deformation of the simulation box, every point in the box has an additional velocity component (a so called *streaming velocity*). In order to prevent the streaming velocity from affecting the thermal kinetic energy, we use the so-called $SLLOD$ thermostat [113, 114]. The $SLLOD$ thermostat accounts for the streaming velocity which depends on an atom's position within the simulation box
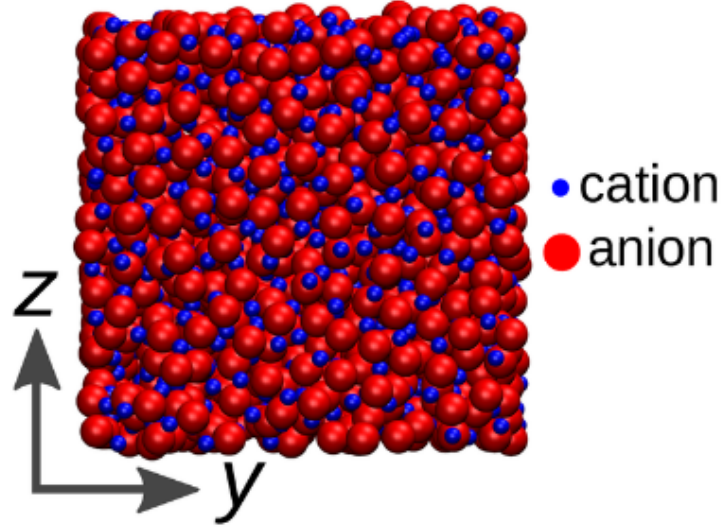
Figure 3.10: Configuration snapshot (yz cross–section) of a bulk IL at the end of relaxation simulation. Cations are represented as smaller blue spheres and anions as larger red spheres.

and it needs to be accounted for controlling the temperature. Controlled shearing of the simulation box results in a stress acting on IL, which is quantified via the stress tensor. The relation between the stress tensor components τ_{ij} and the shear rate $\dot{\gamma}_{ij}$ of corresponding shear strain ϵ_{ij}, with coefficient of viscosity η_{ij} as a proportionality constant is:

$$\tau_{ij} = \eta_{ij} \cdot \dot{\gamma}_{ij}, \tag{3.30}$$

where $ij = \{xy, xz, yz\}$. We have applied three independent shear strains ($\epsilon_{xy}, \epsilon_{xz}, \epsilon_{yz}$). For each of them we have calculated its corresponding stress tensor component ($\tau_{xy}, \tau_{xz}, \tau_{yz}$). All shear strains were the same, i.e., $\epsilon_{xy} = \epsilon_{xz} = \epsilon_{yz} = \epsilon = 1$ leading to the shear rate of:

$$\dot{\gamma} = \epsilon \cdot \frac{1}{t_{\text{tot}}} = \frac{1}{t_{\text{tot}}}, \tag{3.31}$$

where t_{tot} is the total simulation time of the shearing simulations. We have performed simulations at four orders of magnitude of the total simulation time: $t_{\text{tot}} = \{0.1, 1, 10, 100\}$ ns, and thus at four orders of magnitude of the corresponding shear rate. In this way we wanted to check the quality of our relaxation procedure and if there are shear rate dependence changes in the system. We have iterated the shearing simulations (at a shearing velocity of 1 m/s) using the output of the previous
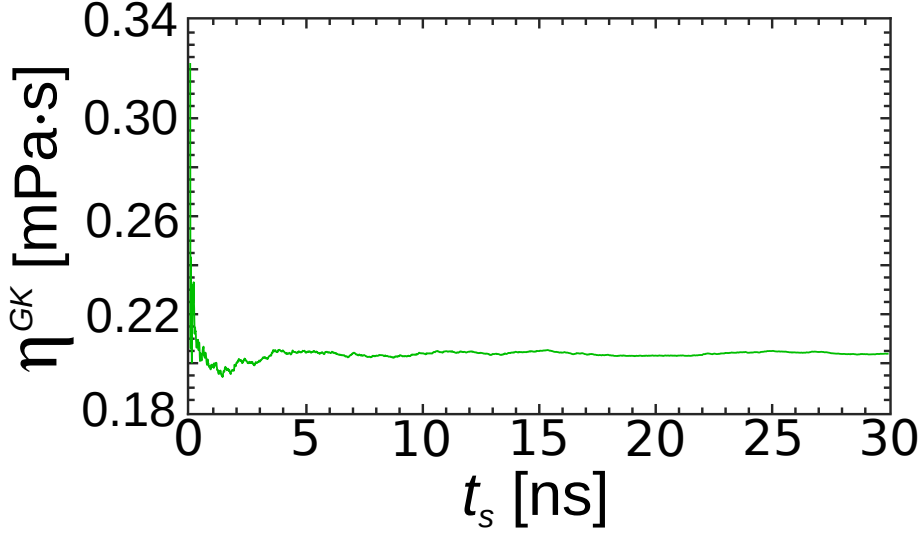
Figure 3.11: Dependence of Green–Kubo (GK) viscosity coefficient η^{GK} on simulation time t_s in case of bulk SM ionic liquid. The time needed to obtain the viscosity coefficient is around $t_{\text{rel}} = 5$ ns.

run as the input of the next run, obtaining higher strains (up to a strain of 5). We did not observe a strain dependence in the response of the system, meaning that the result is unaffected if the strain is further increased.

In Figure 3.11, we show the time relaxation of the Green–Kubo viscosity coefficient, which stabilizes around $\eta^{\text{GK}} = 0.2039$ mPa $\cdot$ s. The configuration snapshot of the bulk IL at the end of the simulation (check Figure 3.10) shows that the ions remain randomly positioned, like they were at the start of simulation, which indicates the liquid state of the bulk ionic liquid. The simulations for all three shear strains give similar values of stress components, and resulting values are shown in Figure 3.12. The points $\{\dot{\gamma}, \tau\}$ were obtained via shearing simulations and the solid line was obtained according to $\tau = \eta^{\text{GK}} \cdot \dot{\gamma}$, where η^{GK} was obtained via Green–Kubo relation. Hence, we conclude that the results of shearing simulations are in agreement with the results of relaxation simulation and therefore there are no changes in the bulk system which are shear rate dependent.

3.3.1.4 Wetting properties

Besides the necessary relaxation of bulk IL and determination of its viscosity characteristics, the liquid–solid interface should be well–known so that we can understand
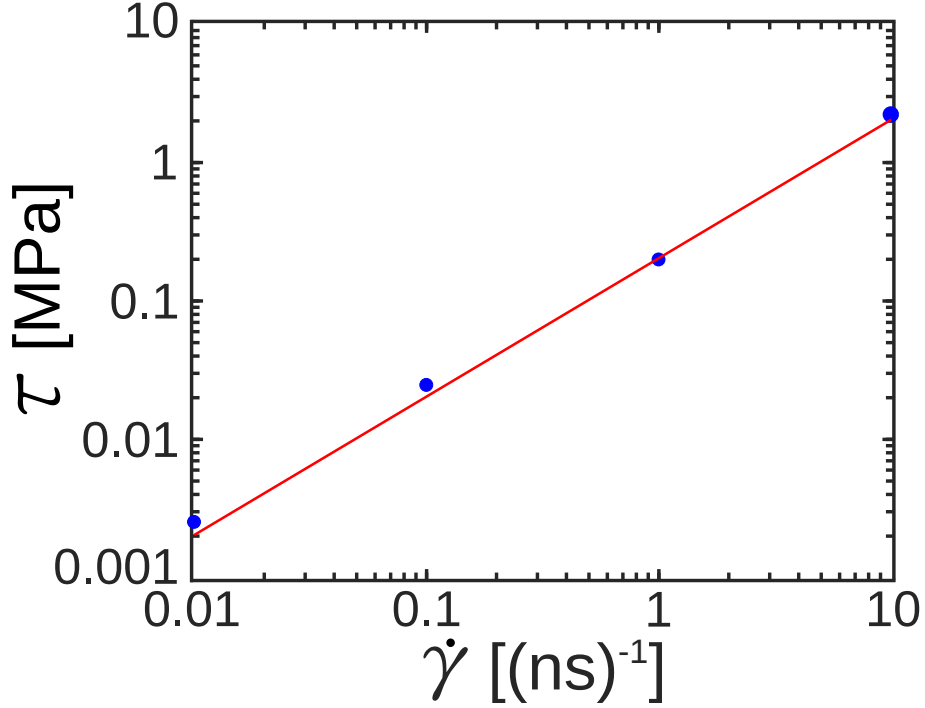
Figure 3.12: Average stress tensor component τ in function of the shear rate $\dot{\gamma}$ of a bulk SM ionic liquid. We have conducted shearing simulations on four orders of magnitude of the shear rate $\dot{\gamma}$, therefore with three orders of magnitude span, which is followed by three orders of magnitude span of τ. Points are obtained via shearing simulations and solid line is obtained according to: $\tau = \eta^{\mathrm{GK}} \cdot \dot{\gamma}$, where η^{GK} is obtained via Green–Kubo relation.

the behaviour of liquids confined between solid plates. Accordingly, it is important to investigate the wetting properties of modeled ILs. For this purpose we examine the wetting properties of SM ionic liquid by placing an IL droplet consisting of $N_{\mathrm{IL}} = 2000$ ions, i.e., $N_C = N_A = 1000$, above a neutral solid plate (where the term above means a higher z coordinate) which consists of one atomic layer in a FCC (111) lattice.

Wetting properties simulation consist of two parts: (1) movement of the solid plate at a constant velocity of $V_z = 1$ m/s towards the IL droplet, which promotes the contact of IL droplet with the plate. Due to the LJ interaction between the ions and solid plate atoms, the IL droplet starts covering the plate. The ending configuration of this part (1) simulation is used as the starting configuration of the part (2) simulation in which the solid plate rests and a long simulation time of $t_s = 5$ ns is given to the ionic liquid, so that it can spread over the plate. In the end
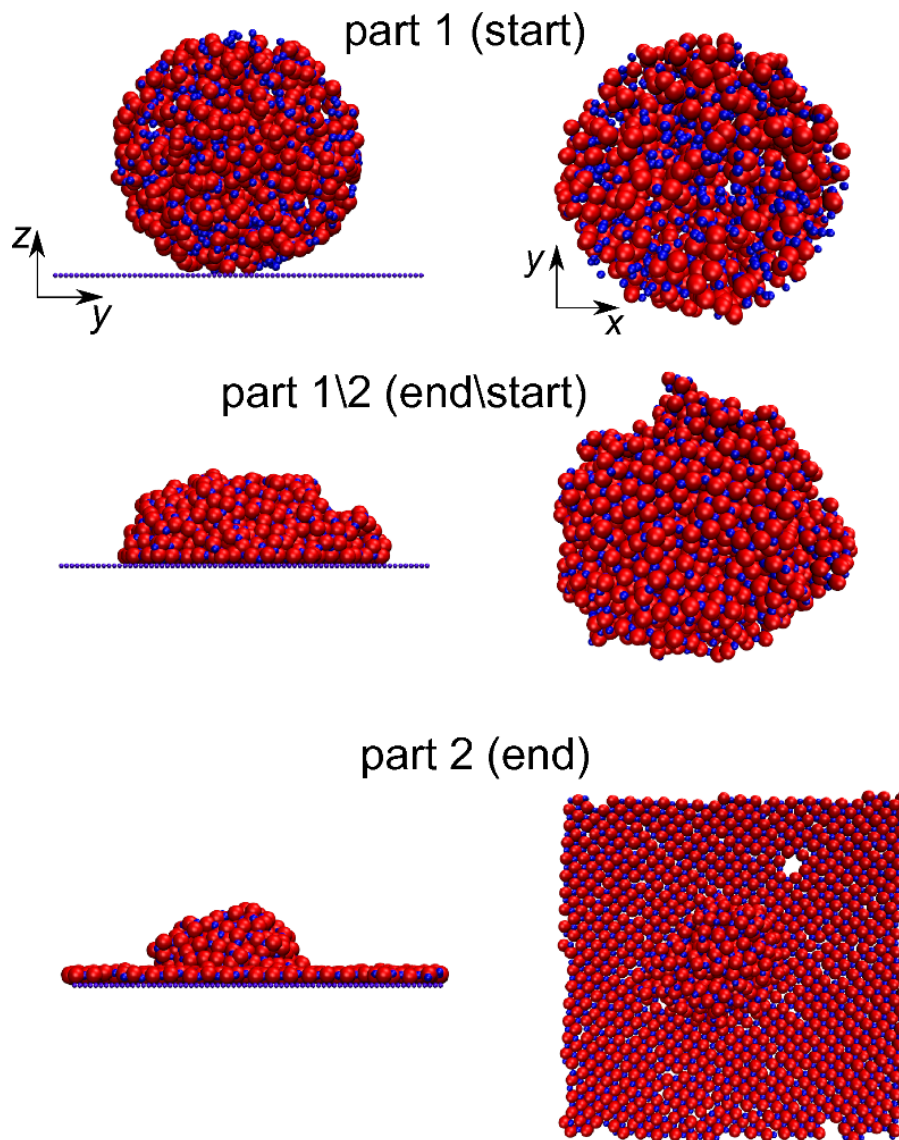
Figure 3.13: Results of wetting properties simulation in case of SM ionic liquid. Left panels show yz cross–section, while right panels show xy cross–section of the system consisting of an SM ionic liquid droplet and a solid plate.

of the part (2) simulation, the ionic liquid is placed on the solid plate in the way that it forms a cationic-anionic layer over the whole plate, with an amorphous droplet in the center of the plate. We might conclude that, for the value of the strength of ions-plate LJ interaction, i.e., $\epsilon_{\mathrm{IP}} = 0.3$ kCal/mol, SM ionic liquid completely wets the given solid plate (LJ interaction parameters $\{\sigma_{\alpha\beta}, \epsilon_{\alpha\beta}\}$ are taken from Table 3.1 in subsubsection 3.2.2.1 of section 3.2). In Figure 3.13 we show the results of wetting properties simulation in three vertical panels: the top one shows the yz (in the left-

hand side of the panel) and xy (in the right-hand side of the panel) configuration of the system at the start of part (1) simulation. The middle panel shows the same two configurations of the system at the end of part (1) simulation, which is taken as the start of part (2) simulation. The bottom panel shows the same two configurations of the system at the end of part (2) simulation.

3.3.2 Bulk tailed models of ionic liquid

3.3.2.1 Relaxation simulations

In an analogous way like in the case of bulk SM ionic liquid, check subsubsection 3.3.1.2, we have performed relaxation simulations in case of three representative TM ionic liquids. An initial configuration for a bulk TM ionic liquid was obtained by a random placement of ions ($N_C = N_T = N_A = 1000$) into the simulation box (cube) with periodic boundary conditions in all three directions. We have chosen the simulation box volume which ensures, after the relaxation of the IL structure, the pressure comparable to the one experienced by confined IL. In case of the present system the pressure was $p \approx 10$ MPa, which corresponds to the normal force of 10^3 pN acting on a surface of 10^4 Å^2 (see Figures 3.5 and 3.35). We provide implementation details related to the relaxation simulations: a Nose–Hoover NVT thermostat at $T = 330$ K is used to control the temperature; the system is relaxed for $t_{\text{tot}} = 3 \times 10^7$ fs until internal energy converges and pressure approaches the desired value of $p \approx 100$ atm; simulation timestep is $dt = 0.5$ fs.

Table 3.3: Overview of the results of relaxation simulations: σ_{TT} is the tail size, L is the side length of cubic simulation box, t_{rel} is the estimated relaxation time, $\langle p \rangle$ and $\langle E_{\text{int}} \rangle$ are the mean values of pressure and internal energy respectively, averaged over the time span $t_{\text{rel}} \leq t \leq t_{\text{tot}}$, where t_{tot} is the total simulation time.

σ_{TT} [Å]	L [Å]	t_{rel} [ns]	t_{tot} [ns]	$\langle p \rangle$ [atm]	$\langle E_{\text{int}} \rangle$ [kCal/mol]
3	104.5	11	30	95.31	−0.62
5	110	0	19	103.81	−0.57
9	129	20	30	118.21	−0.54
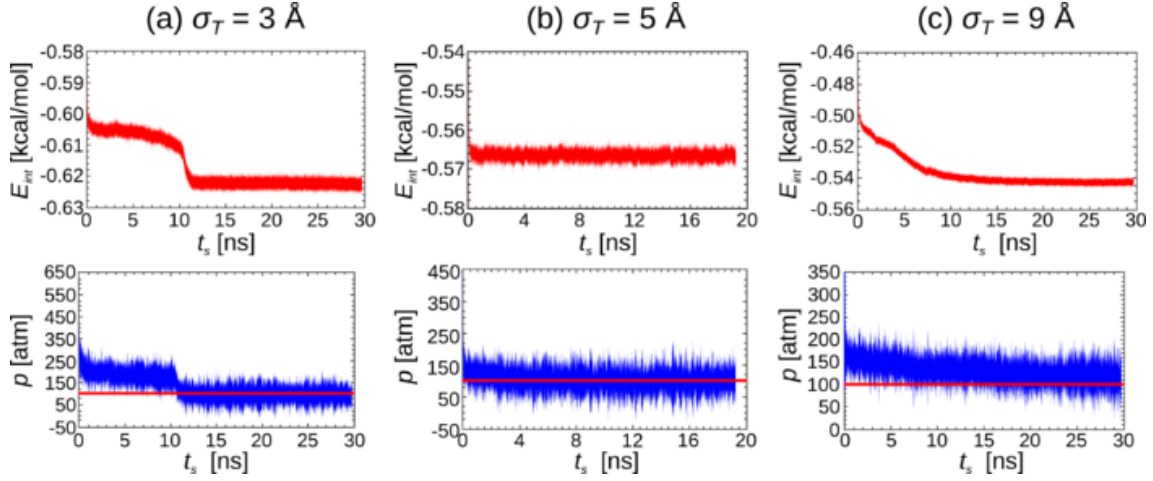
Figure 3.14: Dependences of internal energy E_{int} and pressure p on simulation time t_s in case of bulk (a) $TM3$, (b) $TM5$ and (c) $TM9$ ionic liquid. Solid lines in $p(t_s)$ plots denote the value of target pressure $p = 10$ MPa ($p \approx 100$ atm) in all cases.

In Table 3.3 we are showing the overview of the relevant parameters of relaxation simulations, for $TM3$, $TM5$ and $TM9$ bulk IL. In Figure 3.14 we are showing the dependences of bulk $IL's$ internal energy E_{int} and pressure p on simulation time t_s for bulk (a) $TM3$, (b) $TM5$ and (c) $TM9$ ionic liquid. Figure 3.15 presents the xy cross–section snapshots of bulk IL configurations at the end of relaxation simulations for (a) $TM3$, (b) $TM5$ and (c) $TM9$ model. Those results have clearly revealed a strong dependence of $IL's$ structure on the tail size. We have obtained three completely different outcomes of relaxation simulations in terms of internal energy and structure (check Figure 3.14), depending on the tail size.

- Tail significantly smaller than cation (TM3 model)

We can notice three different segments (check Figure 3.14(a)) in the dependences of internal energy and pressure on simulation time. First, there is a smooth decrease of both parameters over the time interval of $t \leq 10$ ns. The first segment is followed by a sudden drop of E_{int} and p in the time interval $10 \leq t_s \leq 11$ ns. For $t_s \geq 11$ ns both system parameters remain stable in terms of their average values. Therefore, we might estimate the relaxation time as $t_{\text{rel}} \approx 11$ ns. Actually, the values of E_{int} and p are oscillating around their averages (a common result in MD simulations) which remain fixed in the time span $t_{\text{rel}} \leq t_s \leq t_{\text{tot}}$. Since the temperature is thermostated

at $T = 330$ K we might not speak about a phase transition, but those sharp drops of internal energy and pressure are a demonstration of a state transition. Structural changes consistently follow the changes in system parameters, hence there is a clear transition from initially randomly positioned atoms into an ordered structure. We might conclude that a small tail does not affect the cationic–anionic ordering into a cubic lattice, which arises due to Coulombic interaction. We should emphasize that the obtained cubic lattice is not an ordinary simple cubic lattice, but it is tilted. Ionic layers are oriented in the way that they follow the face diagonal of the cube. A conclusion is that $TM3$ bulk IL does not stay in initially assigned liquid state during the relaxation process, but it leaves the relaxation process as an ordered structure (check Figure 3.15(a)).

- Tail of the same size like cation (i.e. symmetric cationic dimer, TM5 model)

Both system parameters E_{int} and p remain stable (check Figure 3.14(b)) and with practically the same average values throughout the whole simulation, indicating that a state transition does not happen. The structure of bulk IL remains the same during the simulation, which is consistent with the behaviour of those parameters. We can claim that relaxation of bulk $TM5$ ionic liquid gives a liquid state as the outcome (check Figure 3.15(b)).

- Tail significantly larger than cation (TM9 model)

There is a continuous and smooth decrease of both E_{int} and p over a long time span $t_s \leq 20$ ns (check Figure 3.14(c)). Later during the relaxation simulation those parameters remain stable, hence we estimate the relaxation time in this case as $t_{\mathrm{rel}} \approx 20$ ns. It is almost two times longer than the relaxation time of $TM3$ model. Structural changes are consistent with system parameters' changes, hence we notice a clear state transition from initially randomly positioned atoms into an ordered structure (check Figure 3.15(c)). We can state that a large tail enables cationic-anionic ordering, which arises due to Coulombic interaction. All layers are oriented along the face diagonal of the cube and they are composed of alternating ionic and tail layers, namely ionic layers consisting of two cationic–anionic sublayers separated by tail layers consisting of two tail sublayers. Tail sublayers are organized

(a) TM3 (σ_T = 3 Å)   (b) TM5 (σ_T = 5 Å)   (c) TM9 (σ_T = 9 Å)

- TM3 tail (σ_T = 3 Å)
- TM5 tail (σ_T = 5 Å)
- cation (σ_C = 5 Å)
- TM9 tail (σ_T = 9 Å)
- anion (σ_A = 10 Å)
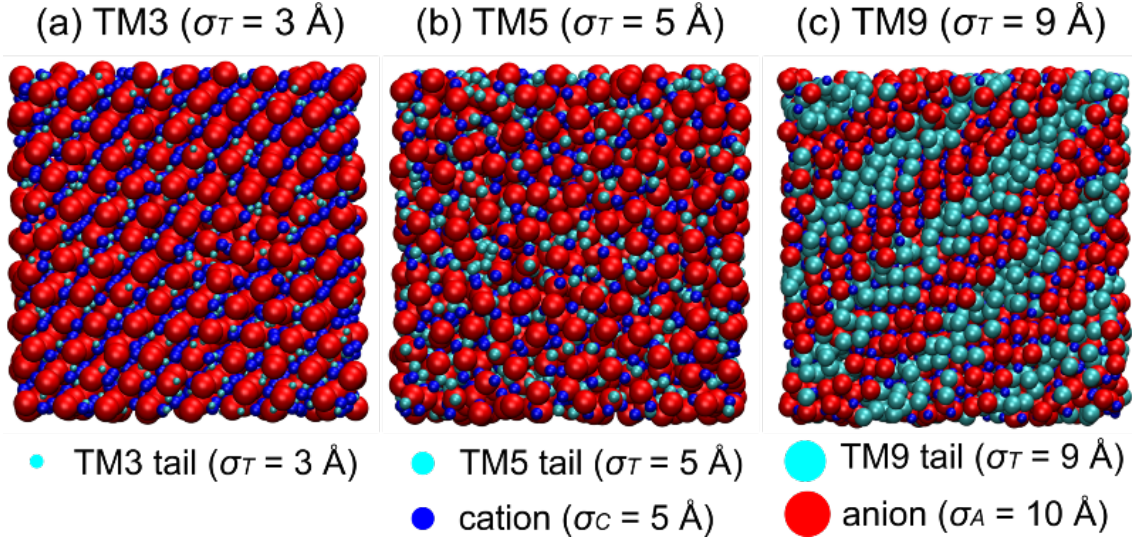
Figure 3.15: Configuration snapshots of bulk (a) $TM3$, (b) $TM5$ and (c) $TM9$ ionic liquid (i.e., with tail of diameter 3, 5 and 9 Å, respectively). We may notice that each configuration snapshot represents a different state, i.e. $TM3$ bulk IL crystallizes into a tilted simple cubic crystal structure, oriented along the face diagonal; $TM5$ bulk IL is in liquid state; $TM9$ bulk IL crystallizes into crystal planes with alternating ionic–tail layers, oriented along the face diagonal as well.

in the way that the tails of cationic sublayers in successive ionic layers belong to the tail layer which separates those successive ionic layers. Simply said, the structure looks like this: ionic layer (consisting of two cationic–anionic sublayers) - tail layer (consisting of two tail sublayers) - ionic layer - tail layer and so on.

These observations are in agreement with Reference [115] in which the authors discuss the relationship between the length of alkyl chain and the structure of bulk IL. When the cationic alkyl chain is short Coulombic forces are dominant, enabling ordering. We observe this kind of result with $TM3$ model. Alkyl chain must be long enough in order to suppress Coulombic interaction, e.g. number of C atoms $n_C \approx 12$, which corresponds to $(n_C - 1) \cdot 1.53$ Å $= 16.83$ Å of tail length, taking into account that a C-C bond has a length of 1.53 Å. Suppressed Coulombic interaction suppresses lattice arrangement, as we obtain with $TM5$ model. However, alkyl chain should not be too long since cohesive interactions increase with the length of non-polar groups. This leads to a reappearance of structural ordering, like in the case of $TM9$ model.
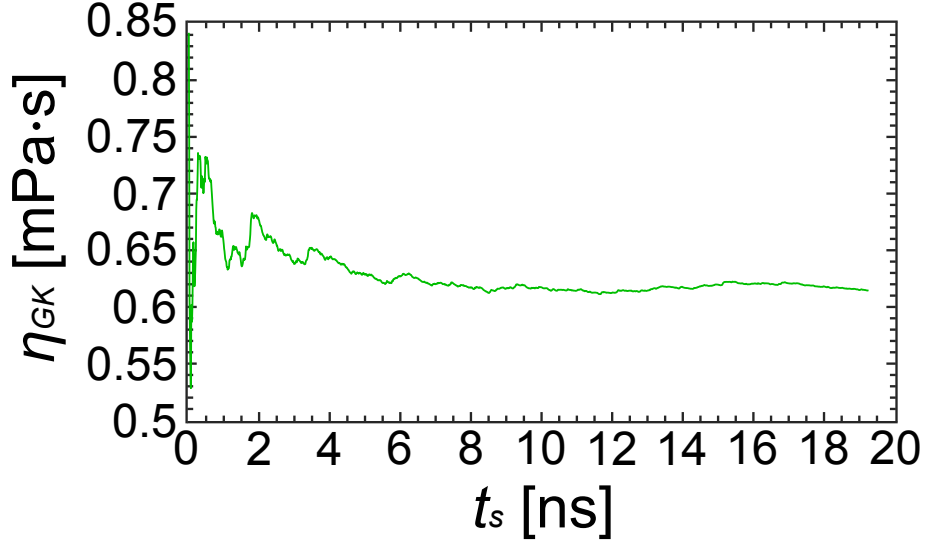
Figure 3.16: Dependence of Green–Kubo (GK) viscosity coefficient η^{GK} on simulation time t_s in case of bulk $TM5$ ionic liquid. The time needed to obtain the viscosity coefficient is around $t_{\text{rel}} = 10$ ns.

3.3.2.2 Viscosity characteristics

In an analogous way like in the case of bulk SM ionic liquid, we have calculated the viscosity coefficient of bulk TM ionic liquids using non–equilibrium molecular dynamics ($NEMD$) simulations with different shear strains, taking configurations obtained by relaxation. For each value of the shear rate $\dot{\gamma}$ in the range $0.01 - 10$ ns^{-1}, we calculate the average stress tensor component: $\tau = \left(\tau_{xy} + \tau_{xz} + \tau_{yz}\right)/3$. The average stress tensor component τ and shear rate $\dot{\gamma}$ are connected by the relation:

$$\tau = \eta \cdot \dot{\gamma}^{\alpha}, \tag{3.32}$$

where η is a generalized viscosity coefficient and α is an exponent. Besides the $NEMD$ method of simulation box shearing, we have also calculated the viscosity coefficient using Green-Kubo (GK) relation. In Figure 3.16, we show the time relaxation of the GK viscosity coefficient of bulk $TM5$ ionic liquid, which stabilizes around $\eta^{\text{GK}} = 0.62$ mPa·s. In Figure 3.17 we present the dependence of the average stress tensor component τ on the shear rate $\dot{\gamma}$ for $TM3$, $TM5$ and $TM9$ bulk IL.

We notice that the average tensor component stays within the same order of magnitude in $TM3$ and $TM9$ cases, although the shear rate changes four orders
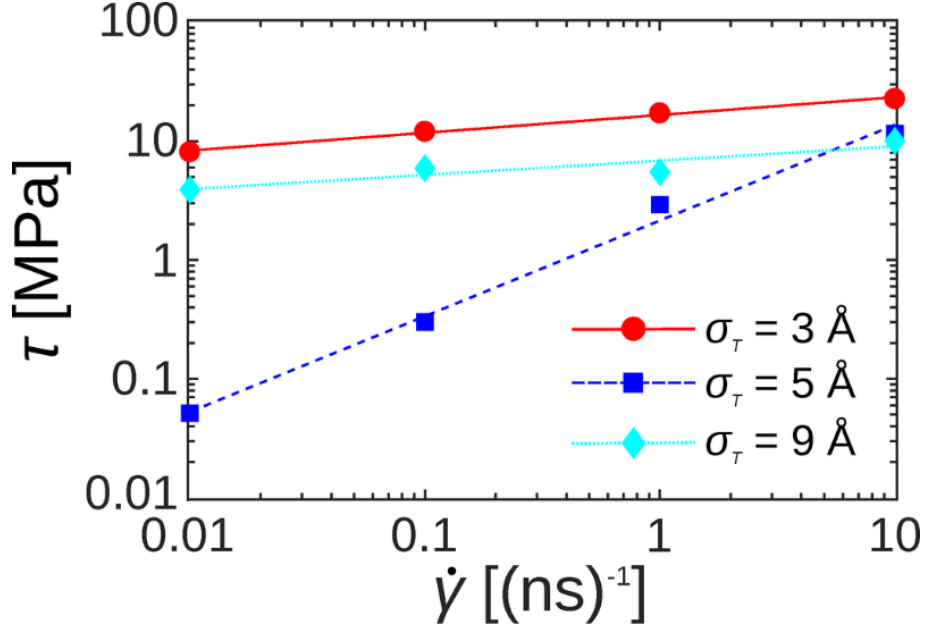
Figure 3.17: Average stress tensor component τ in function of shearing rate $\dot{\gamma}$ of $TM3$, $TM5$ and $TM9$ bulk IL. We have conducted shearing simulations with four orders of magnitude of the shearing rate ($\dot{\gamma} = 0.01 - 10$ ns^{-1}). The lines are obtained by fitting the points with Equation 3.32.

of magnitude. Contrary to that, in case of $TM5$ model there is a two orders of magnitude change of the average stress tensor component. We have obtained ordered bulk IL in case of $TM3$ and $TM9$ model, hence their values of α are low, i.e. $\alpha_{\text{TM3}} = 0.15 \pm 0.02, \alpha_{\text{TM9}} = 0.12 \pm 0.04$. We have obtained rather high values of their GK viscosity coefficients, i.e. $\eta_{\text{TM3}}^{\text{GK}} = 4.72$ mPa $\cdot$ s, $\eta_{\text{TM9}}^{\text{GK}} = 1.67$ mPa $\cdot$ s, which makes sense due to their ordered structure. In case of $TM5$ model we have obtained $\alpha_{\text{TM5}} = 0.8 \pm 0.1$, which is fair enough close to the viscous fluid, i.e., $\alpha = 1$. This is in accordance with the liquid-like state of $TM5$ model, as obtained in relaxation simulations, check Figure 3.15(b). Viscosity coefficients determined via shearing simulations and via GK method in case of $TM5$ model are different, however they are of the same order of magnitude: $\eta_{\text{TM5}} = 0.1435$ mPa $\cdot$ s, $\eta_{\text{TM5}}^{\text{GK}} = 0.6144$ mPa $\cdot$ s.

3.3.2.3 Wetting properties

Analogously to the case of SM ionic liquid, we have determined the wetting properties of TM ionic liquids. The relaxed bulk IL obtained via relaxation simulations

represents the input of wetting simulations, i.e. a liquid droplet (with a cubic shape initially) is placed on a neutral solid plate which consists of one atomic layer in a FCC (111) lattice. The LJ interaction parameters take the values $\epsilon_{\text{II}} = 1.1$ kCal/mol and $\epsilon_{\text{IP}} = 5.3$ kCal/mol in all cases (i.e. for $TM3$, $TM5^1$ and $TM9$ model) except in case of $TM5^2$ model where they are equal (i.e. $\epsilon_{\text{II}} = \epsilon_{\text{IP}} = 1.1$ kCal/mol), where $\epsilon_{\text{II}}, \epsilon_{\text{IP}}$ correspond to ion–ion and ion–plate LJ interaction, respectively. The results of wetting simulations are presented in Figure 3.18. We have obtained partial wetting (to lower or higher extent) in all cases except in case of $TM5^2$ model in which practically there is no wetting. We notice that with the increase of the tail size σ_{TT} the wetting angle increases, i.e. partial wetting becomes weaker. The wetting process occurs in the way that a mixed cationic–anionic layer forms right next to the surface (a monolayer coating), and the rest of ions get "spilled" over this first layer. The tail size affects the quality of wetting. Neutral tails are responsible for the weakening of Coulombic interaction between the cations and anions. The formation of a monolayer coating is a mutual mechanism of wetting for every tail size, but the spilling of ions over that first layer becomes lower with the increase of the tail size. Comparison of $TM5^1$ and $TM5^2$ cases indicates that the strength of ϵ_{IP} parameter affects the wetting properties strongly. We have obtained a transition from partial to non– wetting behaviour when changing the value of ϵ_{IP} from 5.3 to 1.1 kCal/mol. This result is in agreement with Reference [49] where they conclude that the increase of LJ interaction between IL and substrate increases the quality of wetting.

3.4 Confined ionic liquid

We have learned about the characteristics of bulk IL and consequently prepared for exploring the confined IL, which is the main focus of our modeling of ionic liquids. This section is dedicated to the study of confined IL in case of SM model (subsection 3.4.1) and in case of three representative TM models (subsection 3.4.2). Each of those subsections includes three subsubsections, which are dealing with the static and dynamic force-distance characteristics of given ILs, as well as with their
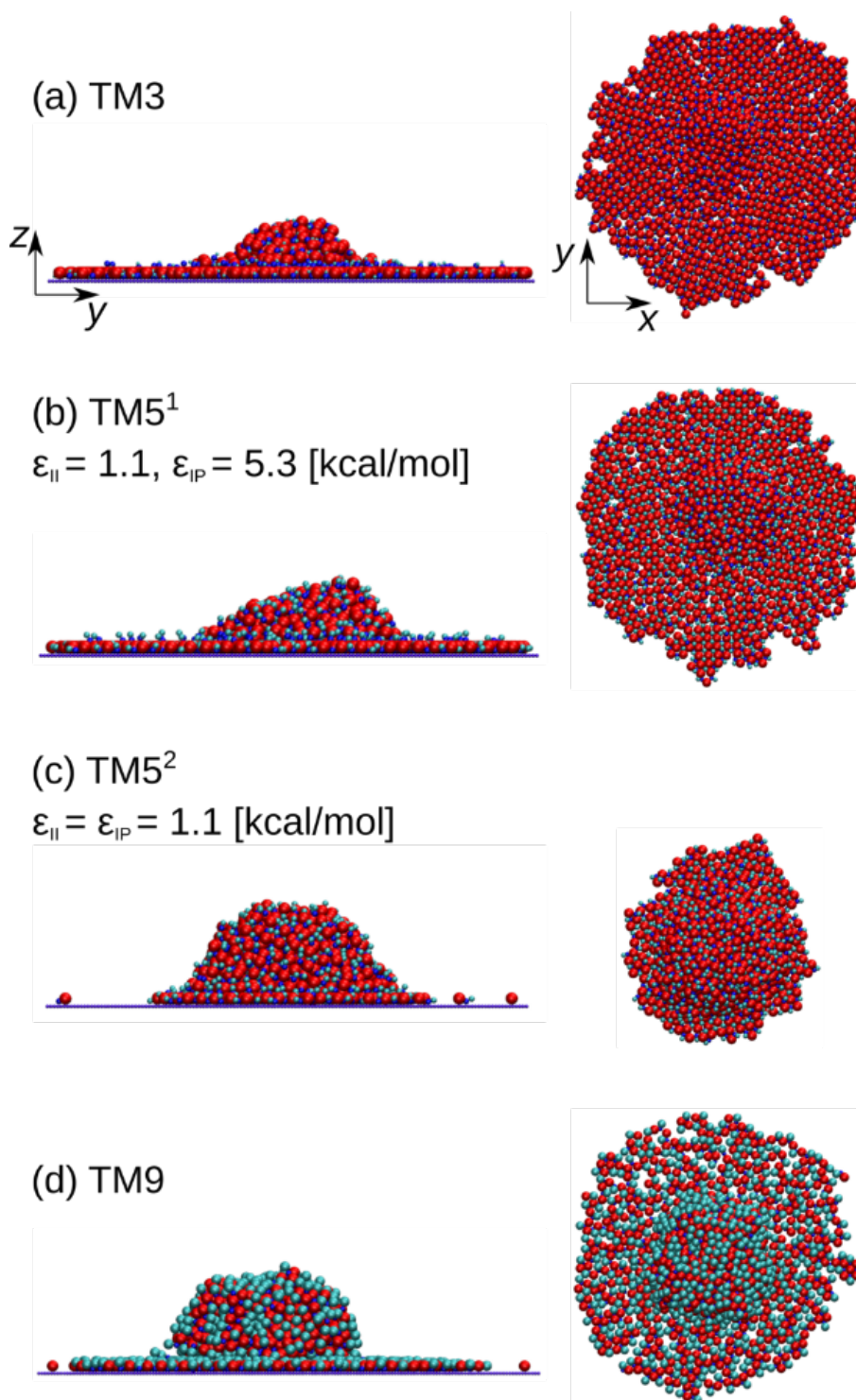
Figure 3.18: Wetting properties results in case of: (a) $TM3$, (b) $TM5^1$, (c) $TM5^2$ and (d) $TM9$ model of IL. Left panels show yz cross–section of the system, while right panels show xy cross–section of the system.

tribological behaviour.

3.4.1 Confined salt model of ionic liquid

We have shown that our bulk IL is a Newtonian fluid: the validity of $\tau = \eta^{\text{GK}} \cdot \dot{\gamma}$ relation over the whole range of shearing rate $\dot{\gamma}$ supports that fact. Our model does not assume the nature of viscous response of IL. Only based on simulation results we conclude that bulk salt model (SM) IL behaves as a Newtonian fluid. For a different choice of parameters one could obtain power law or solid like behaviour. On the other hand, confinement strongly impacts the structure of ILs in thin films [64, 69, 105, 116], therefore when the same IL is confined it does not behave as a Newtonian fluid, as we will show in the rest of this section.

3.4.1.1 Static force-distance characteristic

The confinement has a profound influence on the structure of ILs in thin films [69, 105, 116]. The confining surfaces can induce ordering of the particles in their vicinity. The resulting structure and forces are a result of the interplay between the limited volume and the particles which fill the space.

We have used MD simulations to obtain the static force–distance characteristic. In order to determine a reliable static force–distance characteristic, at each calculation point we have to ensure that the system is in equilibrium. Concerning the realization of those simulations the interplate gap is modified in the following manner: the gap is increased or decreased (i.e., the Top–Bottom plate distance is changed) with a constant velocity $V_z = 5$ m/s for a *move* period of time $t_{move} = 20$ ps; thereafter, we apply conjugated gradient minimization on the ions in order to minimize their internal energy and relax them after the *move* period. As the energy minimization is performed, the ions take positions which ensure their minimal internal energy and the Top plate stays fixed for a *stay* period of time $t_{stay} = 50$ ps, during which period the average value of the normal force is calculated; that value is presented as a simulation point in $F_z(d_z)$ static characteristic, check Figures 3.19 and 3.21. The process was repeated until a distance $d_{z,min} = 11$ Å was reached. In order to avoid systematic errors due to the initial position or direction, the plate movement

is performed in different directions and from different initial configurations, hence Figures 3.19 and 3.21 show the averaged values of several realizations.

- Detailed analysis of the static force-distance characteristic

In Figure 3.19, the static force-distance characteristic of our system is presented. The red horizontal line denotes the zero normal force level (i.e., $F_z = 0$). A non–monotonous behaviour of the normal force F_z acting on the Top plate can be observed as the plate-to-plate distance is changing. This distance corresponds to the gap between the plates where the IL is under confinement. The points (d_z, F_z) have been obtained through our simulations, while the dashed line serves as a visual guide. It can be seen that the normal force strongly depends on the interplate distance. The presence of negative values of normal force F_z can be understood as the IL trying to reduce the plate-to-plate distance due to adhesion phenomena. These changes of the normal force are correlated with the extraction and inclusion of IL layers into the gap, as already observed experimentally, check Reference [69]. During the performed stationary state simulations, the cationic–anionic layers were squeezed out in pairs, in order to keep the system locally neutral, as observed in experimental studies [63, 69, 105, 116, 117]. In order to understand the structural evolution of our system, snapshots of the system from the MD simulations corresponding to several characteristic points in the $F_z(d_z)$ curve from Figure 3.19 were selected and studied in more detail. Figure 3.20 shows the configuration and ionic density distribution along the z–direction for eight characteristic points $\{A, B, C, D, E, F, G, H\}$, corresponding to plate-to-plate distances $d_z = \{11, 14, 17, 20, 22, 24, 27, 32\}$ Å respectively. The ions are deliberately depicted smaller than their LJ radii in order to allow a direct observation of the layering. The position of the atomic centers of the innermost atomic layers of the Top and Bottom plate are indicated in Figure 3.20 as z_T and z_B respectively. As the Bottom plate was fixed, z_B remains constant while z_T changes with the Top plate displacement.

A general feature observed under all conditions was the formation of cationic layer close to the plates. The reason for this is the smaller size of the cations ($\sigma_{CC} = 5$Å) compared to the anions ($\sigma_{AA} = 10$Å). Following this, the second layer gets induced by the first one (due to Coulombic interaction) and it is populated by
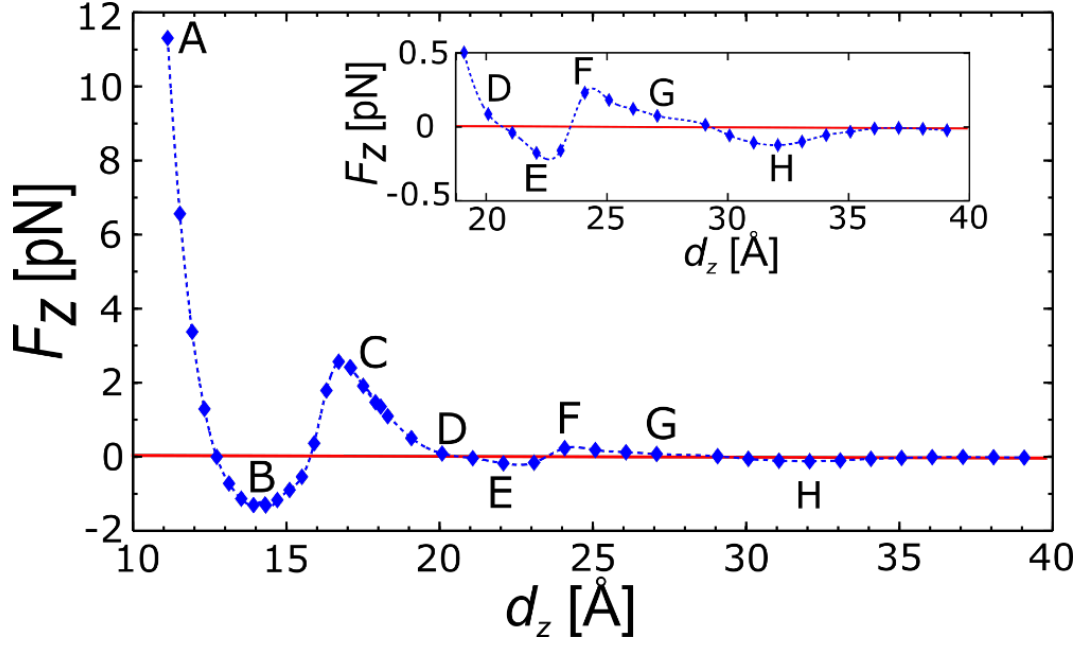
Figure 3.19: Dependence of normal force F_z on plate-to-plate distance d_z. Eight characteristic points $\{A, B, C, D, E, F, G, H\}$ with corresponding interplate distances $d_z = \{11, 14, 17, 20, 22, 24, 27, 32\}$ Å are marked on the $F_z(d_z)$ curve. The horizontal solid line denotes $F_z = 0$ pN. The dashed line connects the points obtained from the simulation and serves as a visual guide.

anions. The distance between the first and the second layer from the bottom is in the range of $1 - 2.5$ Å, meaning that while the centers of mass of the particles are in different layers, the layers themselves overlap as their distance is smaller than the particle diameters. From Figure 3.20 we observe that the anionic monolayer thickness is roughly 7Å and corresponds to $10/\sqrt{2}$Å, i.e., the anions are placed in the centers of the squares formed by the cations of the neighboring layers (the diameter of an anion is 10Å). We will present the changes in the number of layers as the interplate gap is reduced and correlate them with the changes in the normal force F_z which is acting on the Top plate.

For the minimum simulated plate-to-plate distance $d_z = 11$ Å, shown in Figure 3.20(A) we can observe a pronounced peak in the anion density distribution close to the Bottom plate which is aligned with a well-defined anionic layer inside the gap. The anion peak is marked with the $1CU$ indication. In the case of cations, there are two peaks attached below and above the anionic peak. This situation
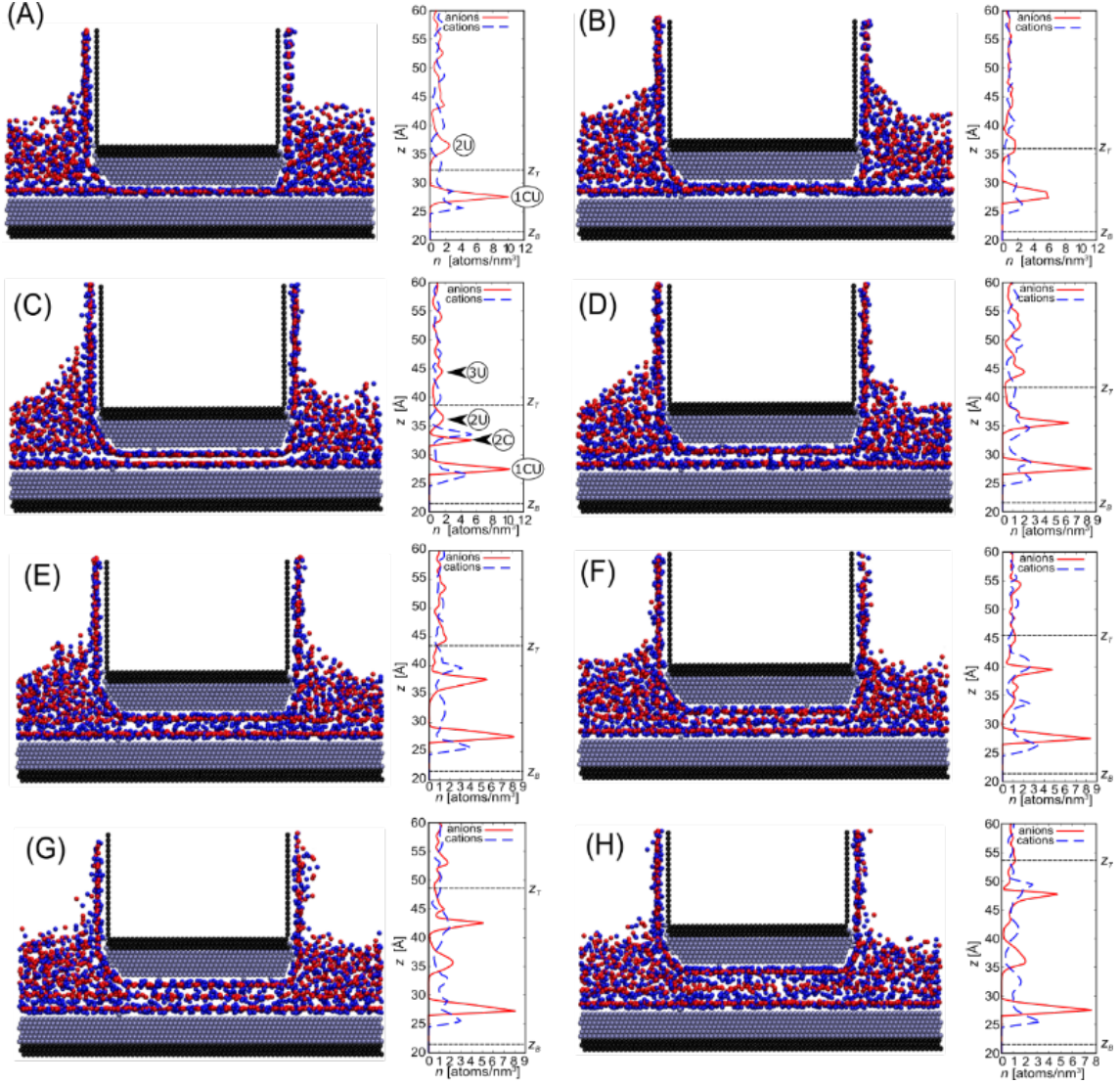
Figure 3.20: Snapshots of system configurations at points $\{A, B, C, D, E, F, G, H\}$ from Figure 3.19 and corresponding density distribution of cations/anions along the z axis. The position of the atomic centers of the innermost layer of the Top and Bottom plate is denoted by z_T and z_B, respectively. The Bottom plate is fixed and $z_B = 21$ Å. The ions are deliberately depicted smaller than their LJ radii in order to allow a direct observation of the layering. In Figures (A) and (C) the annotations indicate the anion layer vertical order from the bottom (1, 2, 3) and the lateral placement: (C)onfined and (U)nconfined.

corresponds to the formation of two incomplete cationic layers inside the gap. With increasing plate-to-plate distance d_z the normal force F_z is decreasing, with a sign change of F_z at $d_z = 12.7$ Å. In the range 12.7 Å$< d_z <$ 15.7 Å the normal force

remains negative. This means that the IL is pulling the plates together, since the ions strive to reduce their interlayer distance, as well as the distance between themselves and the plate atoms. Such behaviour is typically observed in systems exhibiting layering transition, already seen in systems of both neutral molecules [36] and ILs [69]. With further increase of d_z the force becomes positive again, and reaches a local maximum at the point (C) in Figure 3.19. At this point we observe a change in the number of anion layers confined in the gap from one to two, as shown in Figure 3.20(C). In Figure 3.20(C), the plate-to-plate distance is $d_z = 17$ Å and the two bottom peaks of the anion/cation density distribution, denoted by $1CU$ and $2C$, are inside the gap. A third smaller anion/cation density peak, denoted by $2U$ in Figure 3.20(C), is the result of the ordering initiated at the Bottom plate's surface and is actually outside the confinement gap. The vertical distance between the peaks $2C$ and $2U$ is approximately 3.5 Å and corresponds to the effect of the compression of the IL from the Top plate. Further increase of the plate-to-plate distance results in a continuous decrease of the normal force without a sign change as the positions of peaks $2C$ and $2U$ become aligned, check Figure 3.20(D) for a distance $d_z = 20$ Å. Further increase of the interplate distance results once more in a reversal of the sign of the normal force (i.e., $F_z < 0$ for 21 Å $< d_z <$ 23.5 Å). At the midpoint between the plates a broad maximum of cation density distribution can then be observed, see Figure 3.20(E). The cations, as smaller particles, have a tendency to fill the space between the more stable anionic layers. When the anions also start to form a third layer at the midpoint between the two plates the corresponding cationic peak of density becomes sharper and the normal force becomes positive again, see Figure 3.20(F). In this case the cations can form a layer more easily while the anions remain scattered. This is the opposite behaviour to the one typically observed, where the larger anions tend to order more strongly due to the excluded volume effect [118]. From Figure 3.20(F) to Figure 3.20(G) an interesting transition can be observed, during which the single well resolved cation peak disappears and a less pronounced cation–anion pair peak takes its place. Finally in Figure 3.20(H) at $d_z = 32$ Å, we observe the clear formation of three anion and four cation peaks. Considering engineering applications, the steep rise of the normal

force at small plate-to-plate distances, i.e., $d_z < 14$ Å can be beneficial for protecting against solid-solid contact and consequent wear.

- Analysis of the static force-distance characteristic over intervals

There is a strongly decreasing trend of the maximal normal force which can be sustained by the system as the number of ionic layers confined between the plates increases, i.e., for the two ionic layers the maximal force $F_{z,max}^I = 3$ pN, while for the three ionic layers it is $F_{z,max}^{II} = 0.25$ pN. In our model, the Lennard-Jones interaction between the plates and the ions is ten times stronger than between the ions themselves. The ionic layers closest to the plates are therefore more stable than the layers in the midpoint of the gap (interval II). As a result, the three-layer system becomes less dense and can build up a lower normal force compared to the two-layer system.

We have selected two intervals of interest for the interplate distance which capture the presence of local maxima and subsequent minima of the normal force F_z accompanied with the compression of IL. This corresponds to the expulsion of a cation–anion layer pair from the gap. The intervals are: $d_z^I = [14.2, 20]$ Å, $d_z^{II} = [22, 27]$ Å, and they are labeled as I and II respectively. In order to understand the changes of the system configurations and to correlate them with the changes of the interplate distance, snapshots of the system from the MD simulations corresponding to several characteristic points of the intervals I and II have been selected and studied in more detail: $I_{1,2}$, $II_{1,2}$ which correspond to the limits of the intervals, and the local maximum of the interval I, labeled as I_3.

The left vertical panel of Figure 3.22 shows the system configuration in the yz cross-section and the ionic density distribution along the z–direction obtained in the equilibrium force–distance simulations for the three characteristic points of the interval I: $\{I_1, I_2, I_3\}$, corresponding to the interplate distances $d_z = \{14.2, 20, 17.2\}$Å, respectively. In Figure 3.23 the left vertical panels show analogous results for the two characteristic points of the interval II: $\{II_1, II_2\}$, corresponding to the interplate distances $d_z = \{22, 27\}$Å, respectively. In addition to the yz cross–section configuration snapshots together with the ionic density distribution along the z axis, shown in the left panels of Figures 3.22 and 3.23 for the cases of intervals I and II, respec-

tively, we have prepared the xy cross–section configuration snapshots, shown in the left panels of Figures 3.24 and 3.25.
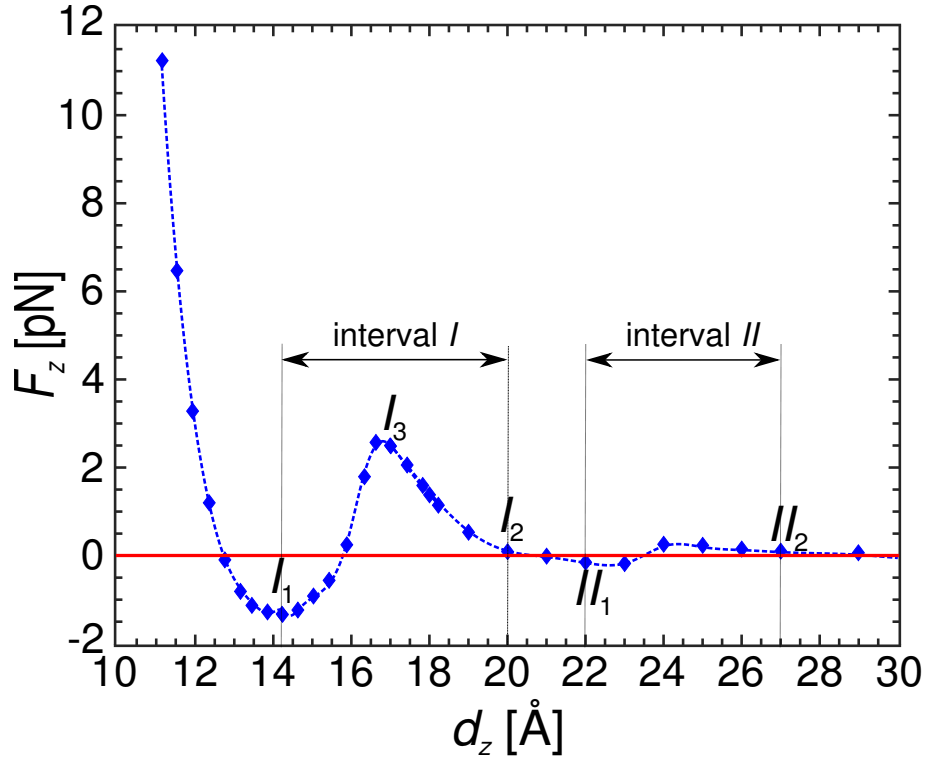
Figure 3.21: Dependence of normal force F_z acting on the Top plate on interplate distance d_z. Five characteristic points $\{I_1, I_2, I_3, II_1, II_2\}$ with corresponding interplate distances $d_z \approx \{14, 20, 17, 22, 27\}$ Å are marked on the $F_z(d_z)$ curve. Also, the two characteristic intervals of d_z are labeled, where the interval I is bounded by the points I_1 and I_2, while the interval II is bounded by the points II_1 and II_2. The horizontal solid line denotes $F_z = 0$ pN. The dashed line connects the points obtained from the simulation and serves as a visual guide.
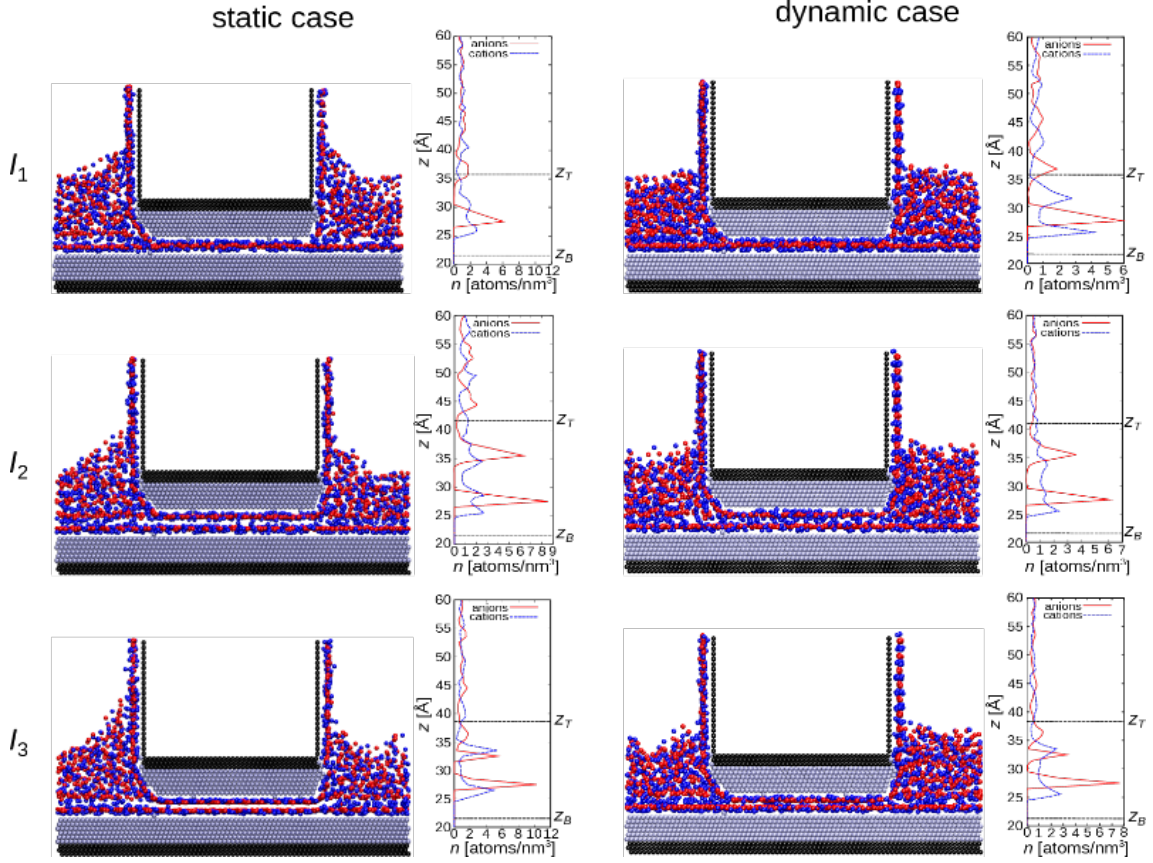
Figure 3.22: Configuration snapshots (yz cross–section) accompanied with ionic density distribution along the z direction in three representative points of the interval I: $\{I_1, I_2, I_3\}$. Left panels correspond to the static case of Top plate's movement, while right panels correspond to the dynamic case of Top plate's movement.

3.4.1.2 Dynamic force-distance characteristic

We have investigated the dynamic behaviour of the IL during a periodic linear movement of the Top plate along the z axis, between the two limiting points of the intervals I and II. The space between the solid plates was in this way periodically expanded and compressed. Periodic movements of the Top plate were performed at three constant velocities $V_z = \{0.1, 1, 10\}$ m/s but no velocity dependent differences in the system behaviour were observed. We have performed ten cycles in order to determine how much do the cycles differ and to determine a statistically reliable average cycle. The confined ionic liquid lubricant responds to the cyclic movement with a hysteresis in the normal force $F_z(d_z)$ as shown in Figure 3.26. We present
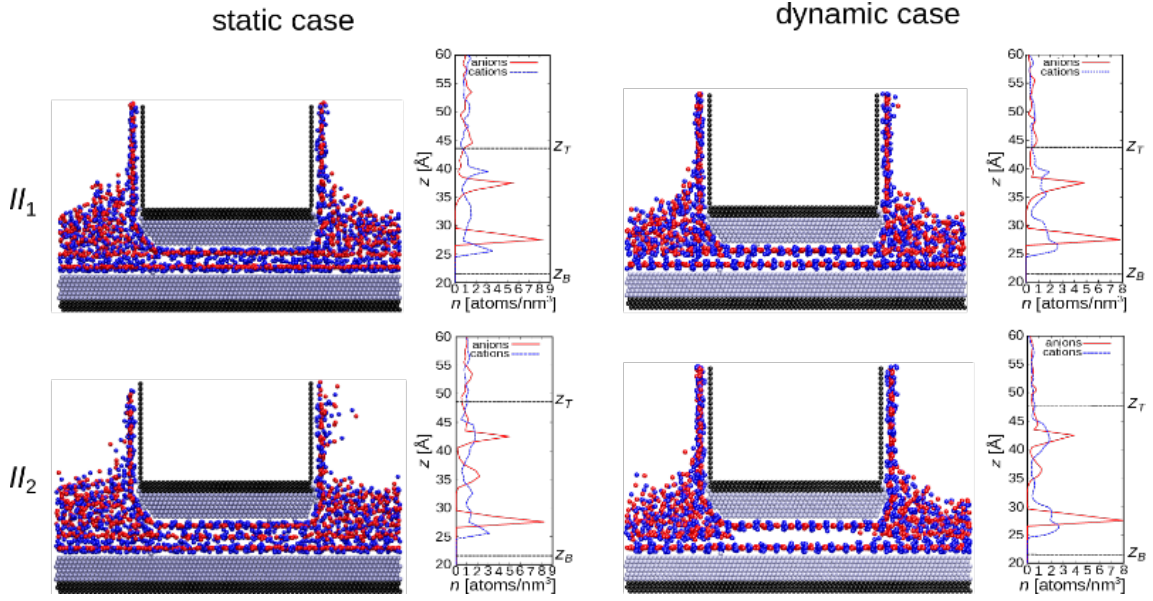
Figure 3.23: Configuration snapshots (yz cross–section) accompanied with ionic density distribution along the z direction in two representative points of the interval II: $\{II_1, II_2\}$. Left panels correspond to the static case of Top plate's movement, while right panels correspond to the dynamic case of Top plate's movement.
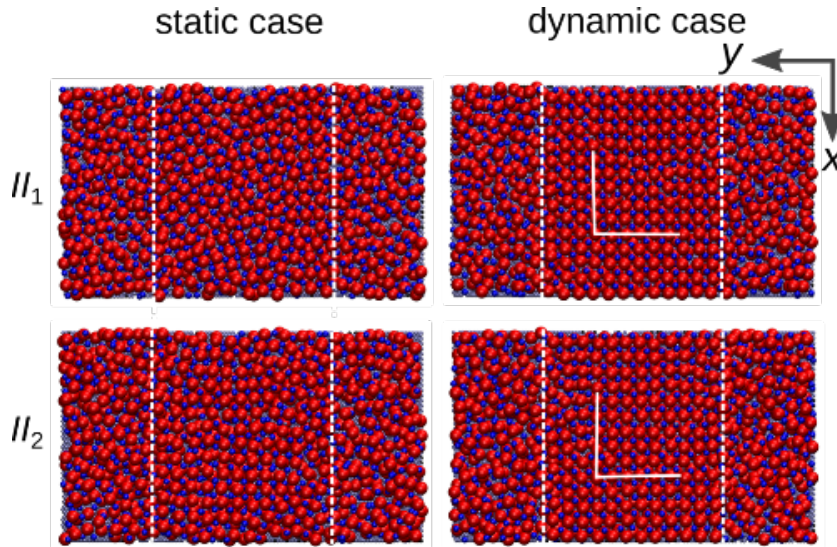
Figure 3.24: Configuration snapshots (xy cross–section) in two representative points of the interval II: $\{ II_1, II_2\}$. Left panels correspond to the static case of Top plate's movement, while right panels correspond to the dynamic case of Top plate's movement. We have highlighted the confined region with dashed lines (Top plate's width along the y axis is a half of the total system's width) and also we have sketched crystallization patterns with solid lines.
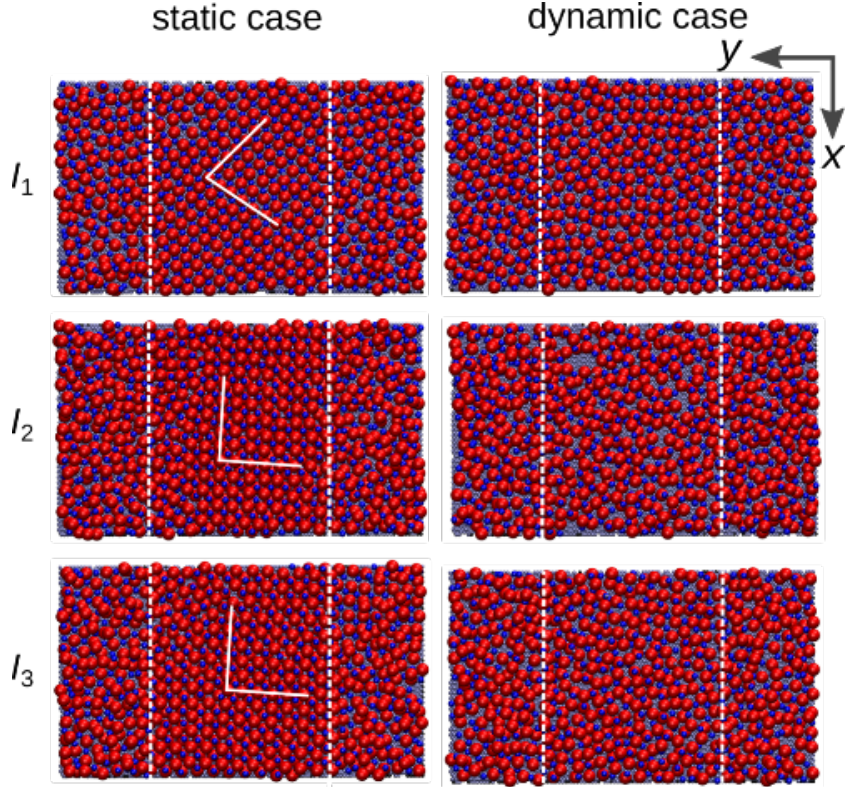
Figure 3.25: Configuration snapshots (xy cross–section) in three representative points of the interval I: $\{I_1, I_2, I_3\}$. Left panels correspond to the static case of Top plate's movement, while right panels correspond to the dynamic case of Top plate's movement. We have highlighted the confined region with dashed lines (Top plate's width along the y axis is a half of the total system's width) and also we have sketched crystallization patterns with solid lines. Periodic boundary conditions are applied in the x and y directions, while simulation box, which is cubic, is kept fixed in the z direction.

both the raw data of all cycles (thin solid lines) and a smooth average cycle (thick solid line). In the case of interval I there are three points of interest $\{I_1, I_2, I_3\}$, corresponding to the points noted in Figure 3.21. Points I_1 and I_2 are the starting and ending point respectively and the point I_3 corresponds to the maximum of the normal force F_z in the smooth average cycle. We observe that between each two of those points there are clear tendencies in the average cycle of the normal force as a function of the interplate distance $F_z(d_z)$. First, in the segment $I_1 \rightarrow I_2$, i.e., in the extension half of the cycle, there is a continuous increase of the normal force F_z from negative values up to the value around zero in point I_2. In point I_1 there is one anionic layer confined in the gap and normal force F_z has a negative value. With the

dynamic increase of the gap ions are pulled–in from lateral reservoirs into the gap. In point I_2 an additional cationic–anionic layer pair is fully formed in the gap, hence increasing the number of confined anionic layers to two. Next, there is the segment $I_2 \rightarrow I_3$ where the ions are compressed within the gap, which is consistent with the continuous increase of the normal force F_z. In this segment, the normal force F_z takes positive values meaning that the ionic liquid shows resistance to the compression but does not flow out. After that, in segment $I_3 \rightarrow I_1$ there is a sharp decrease of the normal force F_z which is correlated with the squeezing–out of the additional cationic-anionic layer taken in from the lateral reservoirs during the extension half–cycle. During the compression half–cycle there is a return to the initial state I_1, where the interplate gap contains one compact anionic layer. We should note that the distributions of cations and anions in the dynamic case for interval I bear close resemblance. Let us now discuss the changes in the number of confined ionic layers as a function of the interplate distance and correlate them with the changes in the normal force F_z acting on the Top plate: in the range $d_z = [11, 14.2]$ Å the normal force F_z acting on the Top plate has a steep decrease, reaching the minimum at point I_1. For the point I_1 at $d_z = 14.2$ Å, check Figure 3.22, we can observe a pronounced peak in the anion density distribution which is aligned with a well–defined anionic layer inside the gap. In the case of cations, there are two peaks attached below and above the anionic peak. This situation corresponds to the formation of two incomplete cationic layers inside the gap. The value of normal force F_z is negative and in point I_1 it has the deepest minimum when considering the whole $F_z(d_z)$ characteristic. With increasing plate-to-plate distance d_z the normal force F_z is increasing, with a sign change of normal force F_z around $d_z = 15.7$ Å in the equilibrium case and $d_z = 17.8$ Å in the dynamic case, check Figures 3.21 and 3.26(a), respectively. This means that before this point the IL is pulling the plates together, since the ions strive to reduce their interlayer distance. After this point, for $F_z > 0$, enough ions are pulled inside the gap and the IL now pushes the plates apart. Such behaviour is typically observed in systems exhibiting layering transition, already seen in systems of both neutral molecules [36] and ILs [69]. With reversing into compression in Figure 3.26(a), the normal force F_z reaches a local maximum
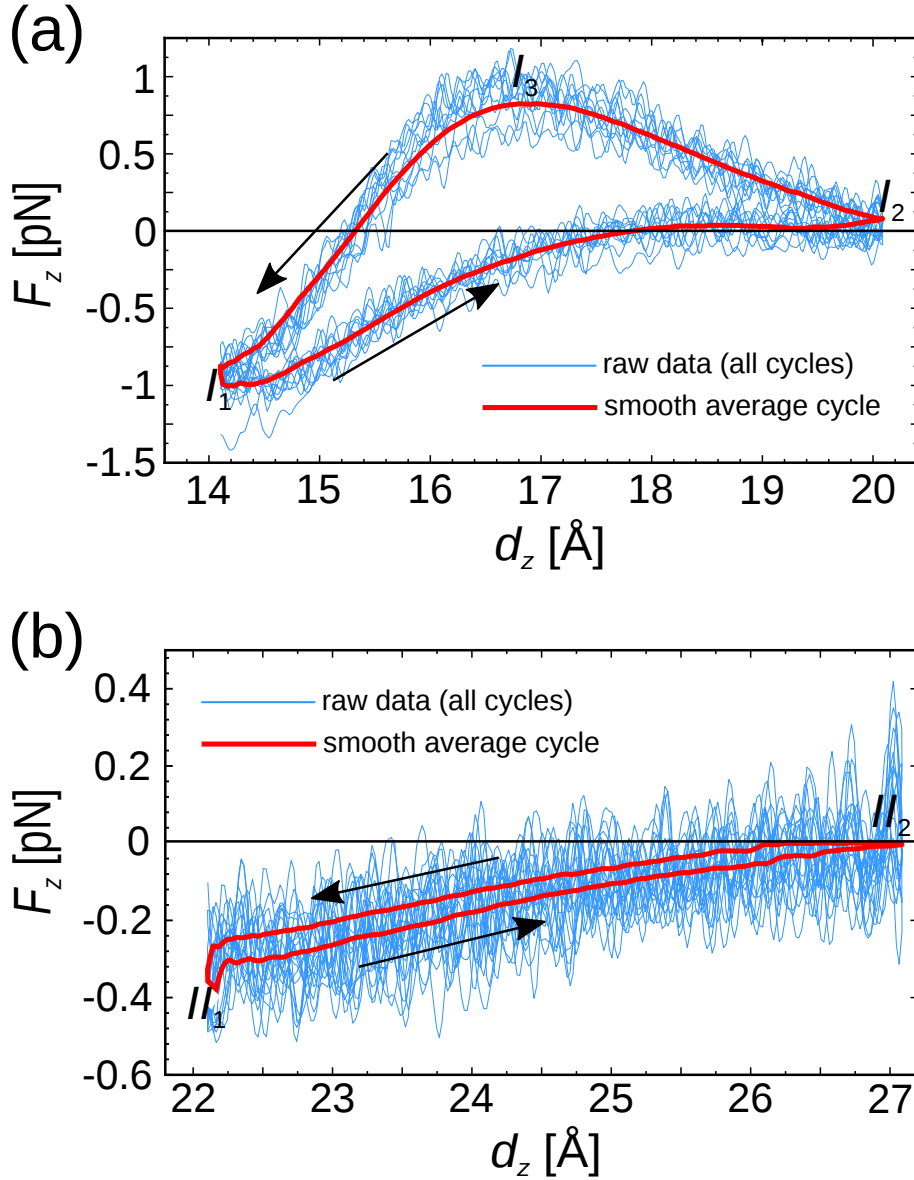
Figure 3.26: This figure presents the results of dynamic extension–compression cycles in the intervals I and II. In panel (a) we present dynamic $F_z\left(d_z\right)$ characteristic in the interval I: thin lines represent the hystereses of ten dynamic cycles, solid line on top of them is the smooth average hysteresis. There is also a solid horizontal line which corresponds to $F_z = 0$. Panel (b) is analogous to the panel (a), just it presents the results in the interval II.

in the point I_3 at $d_z = 17.2$ Å. This is actually the location of the maximum in the equilibrium case as well, check Figure 3.21. With the further decrease of d_z beyond the point I_3 there is a continuous decrease of the normal force up to the distance $d_z = 14.2$ Å as IL starts flowing out of the gap. Still, one should note that there

are two differences between the two systems:

(i) the sign of the normal force in point I_2 and

(ii) the magnitude of the normal force at local maximum I_3.

In the case of cyclic (dynamic) movement of the plates, the normal force is positive $F_z > 0$, i.e. the IL keeps pulling apart the plates at point I_2 and the maximum of the normal force in the point I_3 ($F_z^{dyn} = 1$ pN) is lower than in the static case ($F_z^{stat} = 3$ pN). Both observations indicate that the plate's motion is preventing the ionic liquid to fully fill the void space of the gap. Also, there is a substantial slip during the ejection of IL from the gap, which results in a lower normal force. Otherwise, if no slip would be present the maximal normal force at velocity $V_z = 1$ m/s should be about two orders of magnitude higher based on the bulk viscosity coefficient calculated in section 3.3.

Partial filling of the gap due to the motion of the walls is even better observable in the results for the interval II. While the equilibrium characteristic has a local maximum, check Figure 3.21, in the dynamic case there are only two characteristic points (starting and ending point $\{II_1, II_2\}$ and a monotonously increasing normal force between them. At point II_1 at $d_z = 22$ Å in the static case, we notice that at the midpoint between the plates there is a broad maximum of the cation density distribution, see Figure 3.23. In the static case we notice that, similar to the transition from one to two anionic layers within the interval I, there is a transition from two to three anionic layers within the interval II, which happens in proximity of the point $d_z = 24$ Å. At point II_2 we notice two sharp anionic layers in the proximity of the plates and the third anionic layer which is broader, less sharp and positioned in the middle of the interplate gap, check Figure 3.23. In the dynamic case the number of layers remains the same in the interval II, they just get separated during the extension and a formation of additional ionic layers by the ions flowing from the lateral reservoirs into the gap does not take place, check Figure 3.23.

We can conclude that in a confined system with strong interaction between the walls and the IL, the major driving force that pulls IL into the gap between the plates is the interaction with the wall atoms rather than the inter–IL interactions. In order to visualize what happens in the vicinity of the plates, we are presenting

snapshots of xy cross–section configurations in the intervals I and II, check Figures 3.24 and 3.25, respectively. Even on a cursory look, one sees that the phase behaviour of the confined IL is complex: in Figure 3.24 there was no movement of the IL in and out of the gap and the IL formed a two–dimensional square crystal on both surfaces during the dynamic case. In the equilibrium configurations, there are probably enough ions in the gap that allow the IL to obtain its liquid–like character. On the other hand, in Figure 3.25, we observe a salt–like ordering taking place in all representative points $\{I_1, I_2, I_3\}$ of the static configurations. In the dynamic case the IL exhibits some level of ordering for a small gap (I_1) and it is amorphous in the other two points.

At this point, we would like to quantify how could the processes described above contribute to the energy losses. If two macroscopically smooth surfaces come into contact, initially they only touch at a few of these asperity points. A motion of two bodies in contact lubricated by an ionic liquid would involve the generation of new contacts and the separation of the existing ones. Ionic liquids are characterized by strong Coulombic interactions between the particles. By calculating the area covered within the average cycle of the $F_z\left(d_z\right)$ curves in Figure 3.26, we calculate the amount of work invested per average dynamic cycle, i.e., the hysteretic energy losses. There is a big difference in the amount of invested work in the two intervals: $3.5236 \text{ pN} \cdot \text{Å}$ for the interval I compared to $0.2844 \text{ pN} \cdot \text{Å}$ for the interval II, where the vertical displacement of the Top plate in the two intervals is roughly the same $\Delta d_z \approx 5 \text{ Å}$). This is consistent with a strongly decreasing trend of the maximal normal force which can be sustained by the system as the number of ionic layers confined between the plates increases, i.e. for the two ionic layers the maximal normal force $F_{z,max}^I = 3 \text{ pN}$, while for the three ionic layers it is $F_{z,max}^{II} = 0.25 \text{ pN}$, corresponding to the two maxima of the static force–distance characteristic in Figure 3.21.

3.4.1.3   Tribological behaviour of confined salt model of ionic liquid

- Tribological behaviour under different conditions in terms of interplate gap and external pressure

Following the detailed study of the static and dynamic system, we turn our focus to

exploring tribological behaviour of confined SM ionic liquid under given conditions. Namely we impose a relative motion between the plates in the x-direction and as a result frictional forces can be observed. The dynamics of the plates impact the IL and result in an overall longitudinal force acting on each solid body. In order to evaluate the trends of specific friction we have performed simulations at different plate velocities and at two interplate distances. The simulations have been performed for a broad range of the Top plate velocities $V_x = \{0.1, 0.2, 0.5, 1, 2, 5, 10\}$ m/s, with the Bottom plate kept fixed. We have compared cases with different external pressures applied on the IL: $p_{\text{ext}} = \{0, 120, 250\}$ kPa and two different interplate distances $d_z = 17$ and 27 Å. The simulations were performed as follows: Points (C) and (G) in Figure 3.20 were chosen as the starting configurations. The simulations ran until the Top plate had covered a distance of $d_x = 50$ Å along the x-direction.

Table 3.4: Results for the coefficients a, b in the relation $\langle F_x \rangle / \langle F_z \rangle = a \log(V_x/V_{\text{ref}}) + b$, where $V_{ref} = 1$ m/s. The results were obtained using the least-squares method.

Case	a	b	R^2
(A) $d_z = 17$ Å, $p_{ext} = 0$ kPa	-0.0006(2)	0.0039(2)	0.63
(B) $d_z = 27$ Å, $p_{ext} = 0$ kPa	0.016(5)	0.036(3)	0.72
(C) $d_z = 27$ Å, $p_{ext} = 120$ kPa	0.007(2)	0.017(2)	0.26
(D) $d_z = 27$ Å, $p_{ext} = 250$ kPa	0.002(1)	0.003(1)	0.62

Therefore, the cases with lower velocities required an increased total time. The forces acting on the Top plate were monitored, as shown in Figure 3.27 for a randomly chosen case. It was observed that the normal force remained roughly the same after the onset of the simulation. Steady–state conditions were assumed following a displacement of $d_x = 10$ Å, and then average values were calculated using the statistics until the completion of the simulation. The results for the specific friction $\langle F_x \rangle / \langle F_z \rangle$ are shown as a function of the sliding velocity V_x in Figure 3.28. The specific friction $\langle F_x \rangle / \langle F_z \rangle$ is defined as the ratio of the time averaged frictional and normal force F_x and F_z respectively and is different to the Coulomb friction coefficient $\mu = \partial F_x / \partial F_z$. In our simulated cases we have observed either a weak or a logarithmic dependence of specific friction on velocity. The numerical values
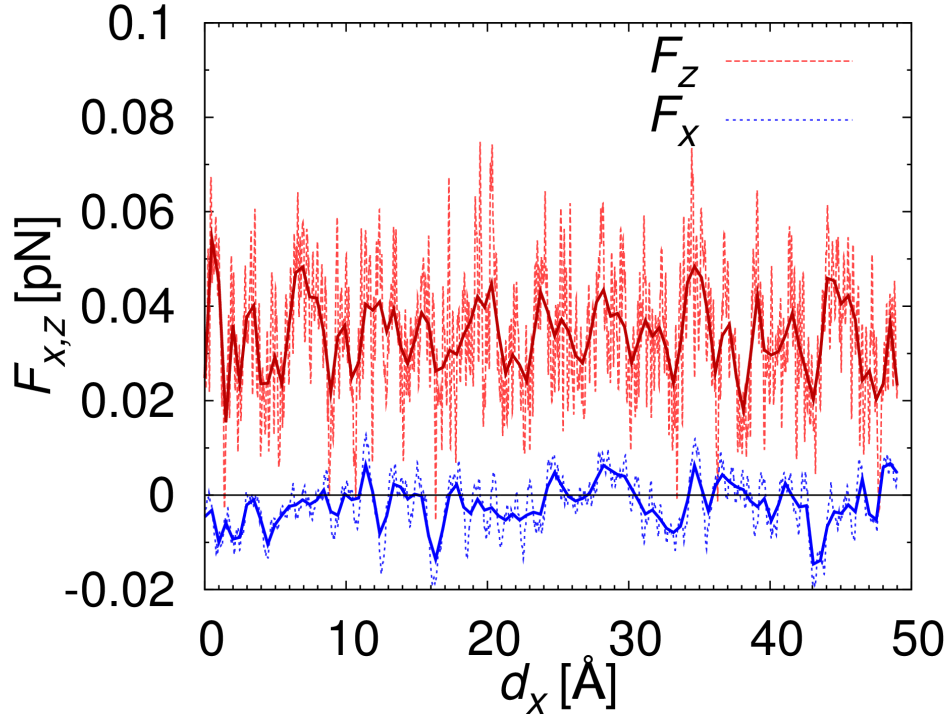
Figure 3.27: Temporal evolution of total normal and axial forces acting on sliding surface for the interplate distance $d_z = 27$ Å and Top plate axial velocity $V_x = 10$ m/s. Dashed lines show the raw numerical data which are smoothed using the solid lines for a clearer identification of trends.

were fitted to a linear function of the form $\langle F_x \rangle / \langle F_z \rangle = a \log (V_x / V_{ref}) + b$, where $V_{ref} = 1$ m/s. The coefficients a, b obtained from the simulation data are listed in Table 3.4. A reasonable fit to the linear regression curve can be observed for most cases. In the case of $p_{ext} = 120$ kPa, the system is potentially in a transition between the two significantly different cases of zero and high pressure, which can explain the poorer quality of the fit to the linear curve. The logarithmic dependence indicates typical elasto-hydrodynamic lubrication conditions [119]. On the other hand, the weak dependence of specific friction on velocity has also been observed in previous studies of IL lubrication, check Reference [39, 56].

   - Impact of ionic liquid confinement gap and pressurization

The influence of the interplate distance on specific friction was initially analyzed, while the applied external pressure on the IL p_{ext} was kept equal to zero. In contrast
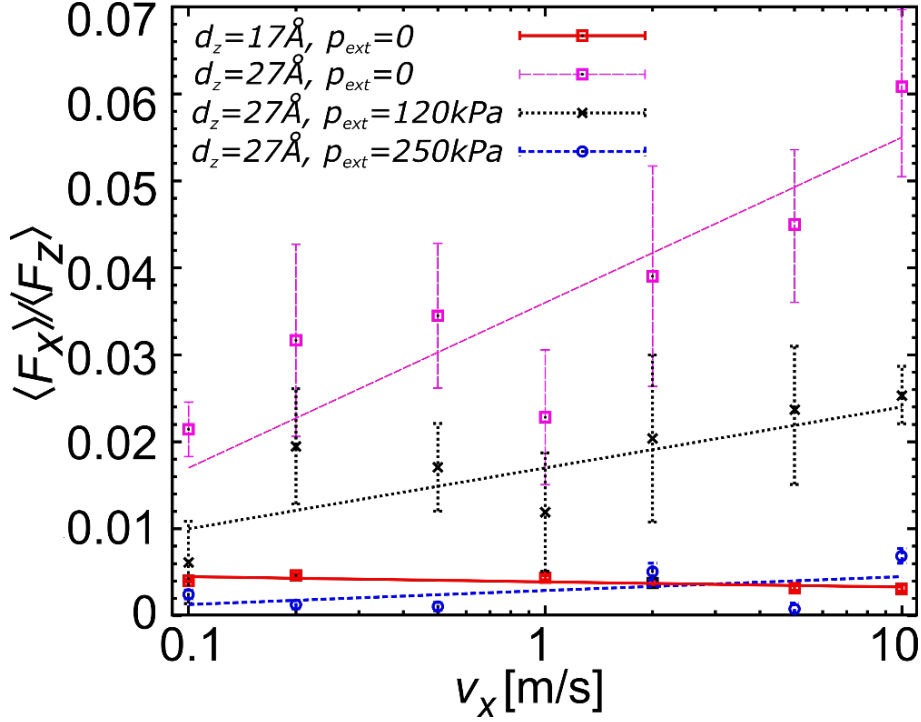
Figure 3.28: Dependence of specific friction $\langle F_x \rangle / \langle F_z \rangle$ on velocity V_x at external pressures $p_{ext} = \{0, 120, 250\}$ kPa and interplate distances $d_z = 17$ and 27 Å. The error bars represent the standard deviation of the average values obtained from the simulation data. The curves showing the specific friction trends were obtained by linear regression and the corresponding parameters are listed in Table 3.4.

to the previous studies of *IL* lubrication [39, 56], our system has shown a strong crystalline ordering induced by confinement. The normal force was roughly ten times higher in the case of the smaller interplate distance, i.e., for $d_z = 17$ Å compared to $d_z = 27$ Å. On the other hand, the lateral force F_x remained at similar levels, therefore leading to a sharp decrease of the specific friction values. At the same time, the weaker confinement and the smaller normal force for $d_z = 27$ Å resulted in a steeper slope of the curve $\langle F_x \rangle / \langle F_z \rangle$.

In order to understand the potential correlation of the *IL* structure with the arising frictional forces, the confinement zone was observed in detail using Figure 3.29, where a side view (left side) and top view (right side) of the system is shown. In the top view, the system is shown with the solid and *IL* particles above the upper plate's plane removed. In this plot the ions are depicted with their corresponding *LJ* radii in order to achieve a realistic visualization of the structure. The anions

form a locally cubic structure, check right panel Figure 3.29(A), while the crystal direction of the cubic structure is indicated with the dashed lines. If we look into the structure of the IL in the confinement zone, Figure 3.29(A) and (B), we can observe a single, well-resolved crystal structure in the case of $d_z = 17$ Å, while in the case of $d_z = 27$ Å some defects are present. It can also be observed that outside the gap, the IL remains in a disordered, liquid state.

Further clarification can be attained by plotting the ionic density distribution profiles inside and outside the gap in Figures 3.30(A) and (B). It can be observed that at the plate-to-plate distance $d_z = 17$ Å, both cation and anion peaks of density distribution function inside the gap are narrow and sharp. In addition, both the anion and cation peaks in each paired layer are located at approximately the same z location. These findings confirm that under these conditions the IL is in a crystalline, "solid-like" state with minimum disorder. In the case of a wider gap $d_z = 27$ Å the anion peaks next to the walls remain narrow, with a third broader one appearing in the center. The cation arrangement is more dispersed, with double peaks appearing above and below each anion peak. These statistics indicate a more layered, less strictly ordered state.

(A) $d_z=17\text{Å}$, $p_{ext}=0$

(B) $d_z=27\text{Å}$, $p_{ext}=0$

(C) $d_z=27\text{Å}$, $p_{ext}=120\text{kPa}$

(D) $d_z=27\text{Å}$, $p_{ext}=250\text{kPa}$
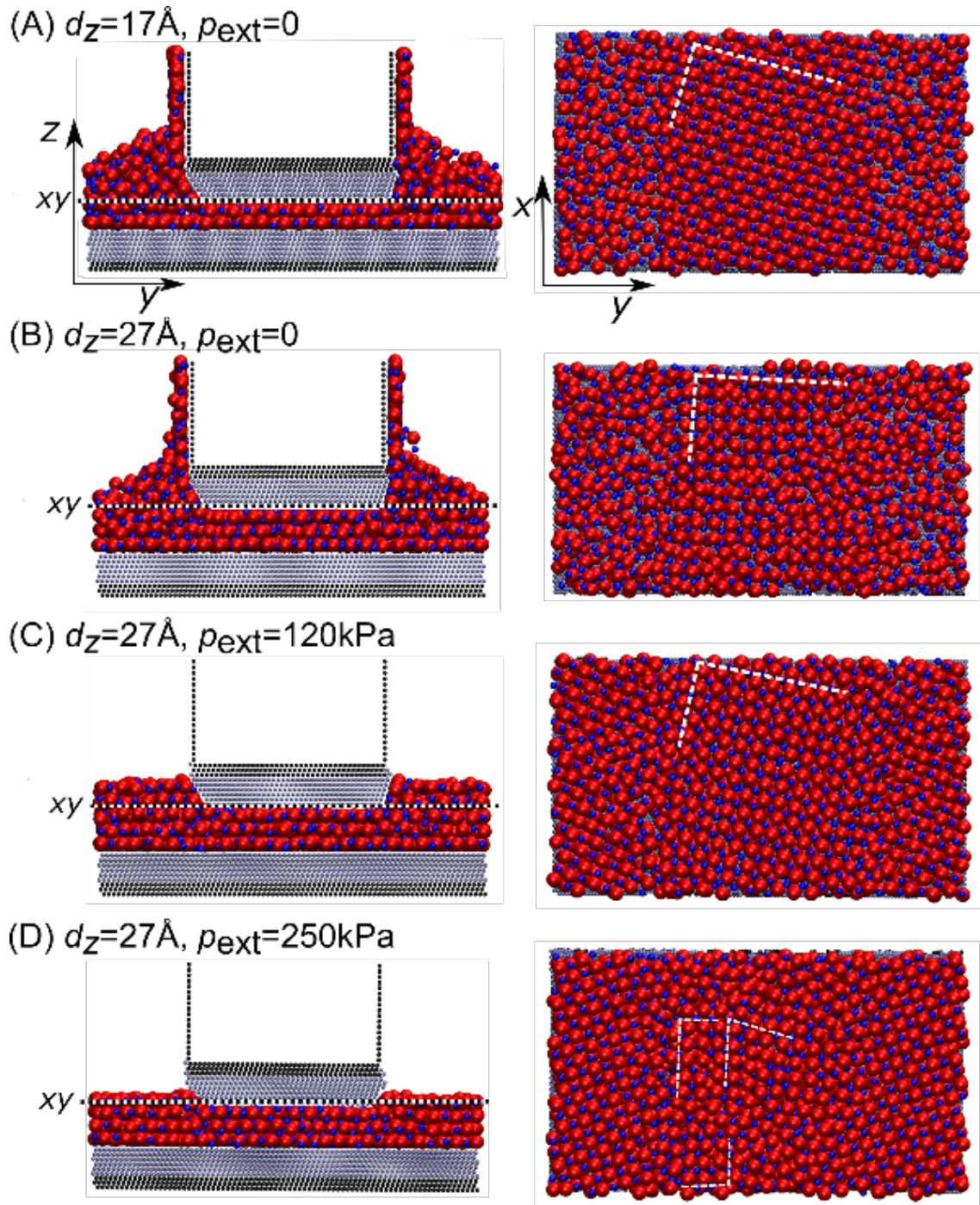
Figure 3.29: Side (yz) and top (xy) views of the snapshots from four separate friction simulations. The top views correspond to the planes marked with dashed lines in the side views and do not include the solid and IL particles above the upper plate plane. The ions are depicted according to their LJ radii in order to visualize the crystalline structures. The dashed lines in the top views denote the crystal direction of self-formed cubic structures.
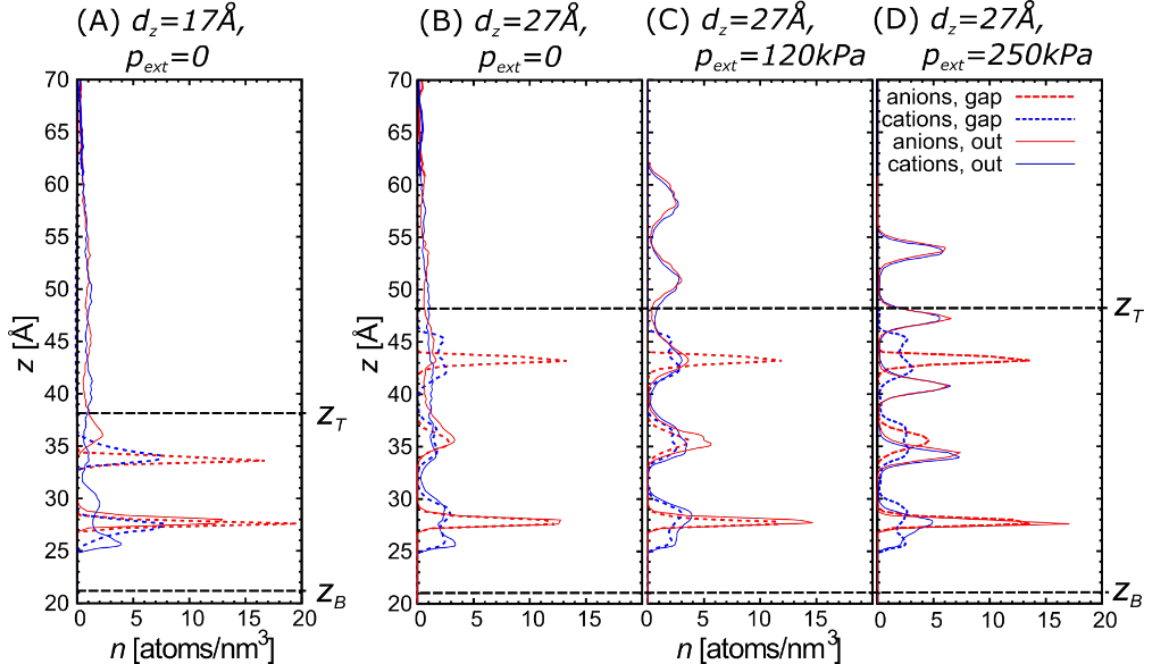
Figure 3.30: Density distributions of ions along the z axis inside (dashed lines) and outside (solid lines) the confinement zone between the solid plates for configurations shown in Figure 3.29. The position of the atomic centers of the innermost layer of the Top and Bottom plate is denoted with z_T and z_B, respectively. Bottom plate is fixed with $z_B = 21$ Å.

The difference in the extent of confinement-induced crystallization is a probable reason for the observed steep slope of specific friction since the observed defects can interact more strongly with the upper plate at higher velocities and contribute to the increase of friction force. Our observations show some similarity to the behaviour previously seen in Lennard-Jones systems where systems at pressures above a certain critical value and at sufficiently low velocities exhibited such behaviour. In these studies, check Reference [42], the shape of fluid molecule was identified as the main parameter that controls crystallization through the promotion or prevention of internal ordering.

In addition to the impact of different confinement gaps, the effect of IL pressurization was studied, while the interplate distance was kept constant. More specifically, a gap of $d_z = 27$ Å was used, while different pressures $p_{ext} = \{0, 120, 250\}$ kPa were applied.

Through observation of Figure 3.30(B)-(D), it can be seen that the application of external pressure prevents the wetting of the side walls of the Top plate and leads to a distinct crystallization of the unconfined IL. On the other hand, the ion density profiles inside the confinement zone are moderately influenced.

Friction results for increasing values of applied pressure p_{ext} are consistent with the observations from Figure 3.28 with specific friction decreasing as the ordering of the IL increases. It can be seen that for high external pressure, i.e., $p_{\text{ext}} = 250$ kPa, the slope of the specific friction curve almost vanishes.

Figure 3.29(C) shows that for $p_{\text{ext}} = 120$ kPa the local cubic structure induced by confinement between the plates served as a nucleus for further crystallization between the plates and a well-ordered single crystallite was formed in this region. Outside the confinement zone another crystallite was formed with a different orientation. Further increase of external pressure to $p_{\text{ext}} = 250$ kPa forced the IL in the void space to crystallize, while at the same time the IL in the confinement zone was converted to a number of smaller crystallites, check Figures 3.29(D) and 3.30(D).

The reported results show a dual nature of IL lubrication, with EHL characteristics at low to medium pressures and confinement gaps that allow more than two distinct anion/cation pair layers to form. At higher pressures and smaller distances, which can be translated as mixed lubrication conditions, the IL is transformed into a solid-like body, while specific friction decreases to low values which are independent of the sliding velocity. This behaviour can be beneficial in engineering applications such as the piston ring–cylinder liner system, where it can be assumed that the IL crystallization can potentially help in preventing the solid contact between the solid surfaces, along with the associated high friction and wear.

- Shear behaviour of confined salt model of ionic liquid

In order to study the behaviour of our confined SM ionic liquid under shearing we apply a relative motion between the plates along the x direction. The Bottom plate is kept fixed and a constant velocity V_{x} is imposed on the Top plate. We are interested in establishing how does the lateral (frictional) force F_{x} depend on the confinement gap $d_{\text{z}} = \{12, 14, 16, 18, 22, 25\}$ Å. In Figure 3.31 we are showing the dependence of the time averaged frictional force divided by the contact area of the
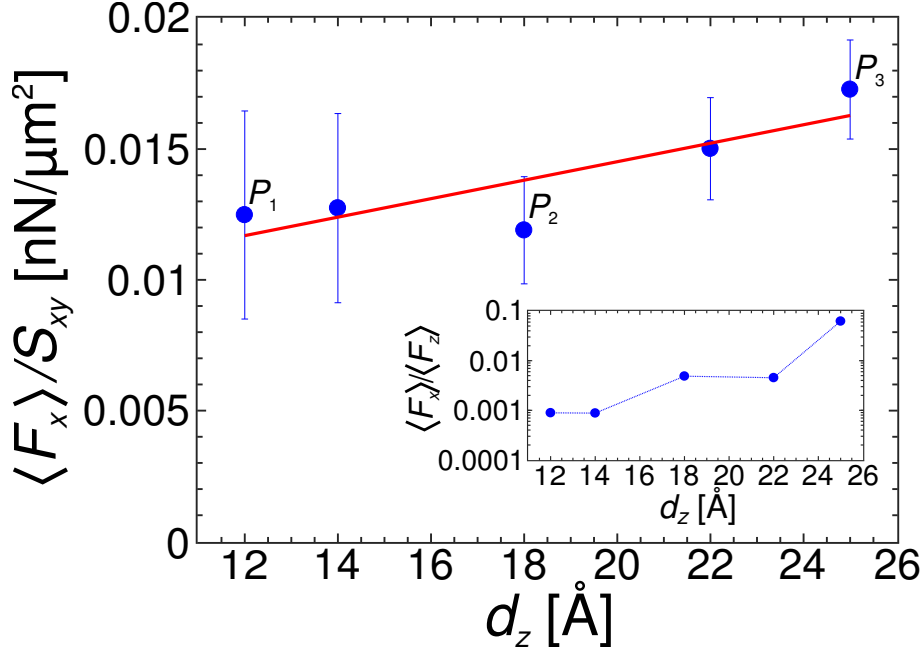
Figure 3.31: Dependence of the frictional force divided by the contact area of the Top plate with IL lubricant $\langle F_x \rangle / S_{xy}$ on the interplate distance d_z. The three representative points $\{P_1, P_2, P_3\}$ are marked. Points obtained in simulations are shown as circle markers, accompanied with errors along the y axis. Linear fit through those points is shown as a solid line. In the inset dependence of specific friction $\langle F_x \rangle / \langle F_z \rangle$ on the interplate distance d_z is shown, with y axis in log scale. Simulation points are shown as circle markers, while the dashed line serves as a visual guide.

Top plate and the IL lubricant, i.e. $\langle F_x \rangle / S_{xy}$ on the interplate distance d_z. We observe a linear increase of the frictional force per contact area with the increase of the interplate distance, with a slope of 4 nN/μm^3. In the inset of Figure 3.31, we are showing the dependence of specific friction defined as the ratio of the time averaged frictional and normal force $\langle F_x \rangle / \langle F_z \rangle$ on the interplate distance d_z. By comparing Figure 3.31 with the results for the bulk liquid in Figure 3.12 we observe that there is no correlation with the lubricant viscosity (i.e., otherwise frictional force would be three orders of magnitude higher). This leads us to the assumption that our pressurized systems, whether they form a crystalline lattice or not, do not lie in a typical hydrodynamic regime and operate under full slip conditions in which the ionic liquid moves together with one of the walls. As there is no solid–solid contact between the two surfaces, but lubrication through very thin, highly viscous films which are solid–like, mixed or dry lubrication are the two potential regimes
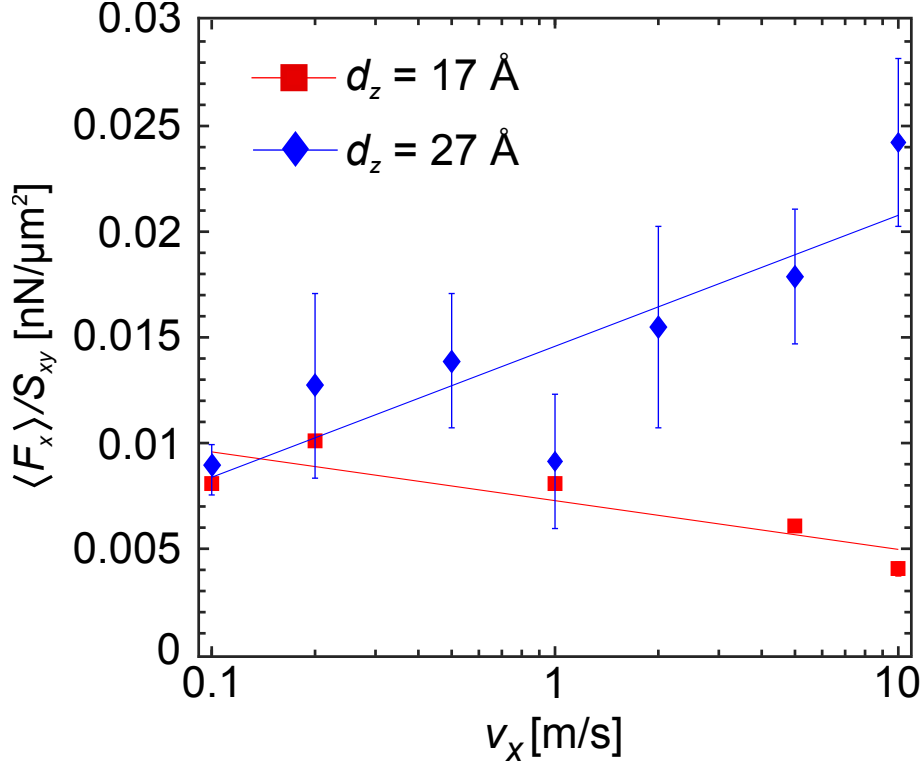
Figure 3.32: Dependence of the frictional force divided by the contact area of the Top plate with IL lubricant $\langle F_x \rangle / S_{\mathrm{xy}}$ on the Top plate's lateral velocity $V_x = 0.1-10\,\mathrm{m/s}$. The error bars represent the standard deviation of the average values obtained from the simulation data. The lines showing the friction trends are obtained by linear regression.

that can describe the observed conditions. A parametric study on different shearing velocities $V_{\mathrm{x}} = 0.1-10\,\mathrm{m/s}$ at two wall separations $d_{\mathrm{z}} = 17, 27\,\text{Å}$ provides additional information for the characterization of the tribological regime of our system. In Figure 3.32 one can observe a logarithmic (weak) dependence of the frictional force per contact area on lateral velocity of the Top plate's movement, which is consistent with the observations of previous studies of IL lubrication, check Refs. [39, 56].

From Figure 3.31 we have selected three representative points with $d_{\mathrm{z}} = \{12, 18, 25\}\,\text{Å}$ labeled as $\{P_1, P_2, P_3\}$ respectively. We provide an overview of the yz configuration cross–sections together with ionic density distributions along the z axis (check Figure 3.33) at the simulation onset $t = 0$ and after $t = 3$ ns. In the panels of Figure 3.34 we have highlighted the confined region with dashed lines (the Top plate's width along the y axis is half of the total system's width) and we have also
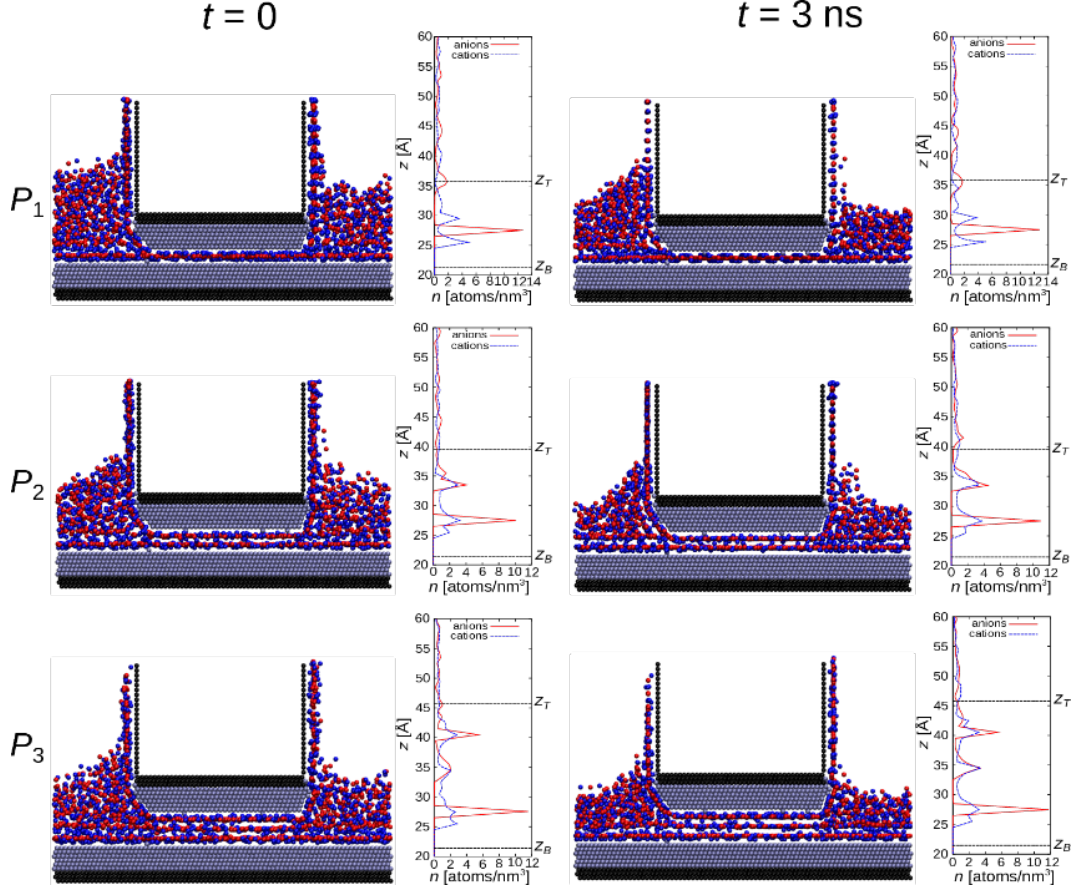
Figure 3.33: Configuration snapshots (yz cross–section) accompanied with ionic density distribution along the z direction in three representative points $\{P_1, P_2, P_3\}$. Left panels correspond to the start of friction simulations $t = 0$, while right panels correspond to the end of friction simulations $t = 3$ ns. Top plate's lateral velocity is set to $V_x = 2$ m/s, total simulation time is $t_{\text{tot}} = 3$ ns, hence all friction simulations have run until the Top plate had covered a distance of $d_x = V_x \cdot t_{\text{tot}} = 60$ Å along the x direction.

sketched crystallization patterns with solid lines. In Figures 3.33 and 3.34 we show initial configurations at the input of shearing simulations, together with the final configurations obtained after the shearing simulations. We observe that any initial crystallization is not lost due to the lateral motion of the Top plate, but only slightly modified due to the motion, which suggests that the lateral movement does not alter the ordering. This is a significant finding since the longitudinal movement, i.e., movement along the z-axis does alter the local ordering (it destroys the crystal structure in small gaps and induces it in larger ones).
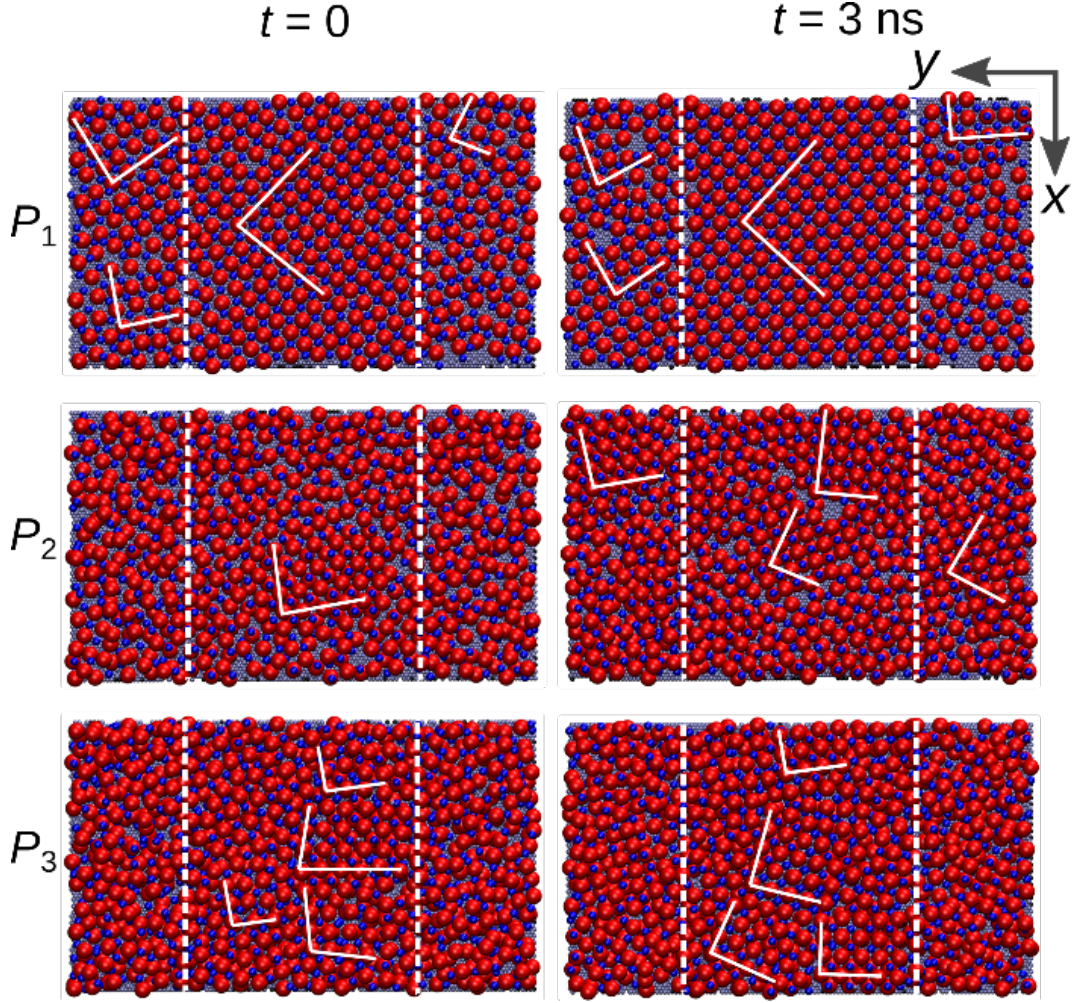
Figure 3.34: Configuration snapshots (xy cross–section) in three representative points $\{P_1, P_2, P_3\}$. Left panels correspond to the start of friction simulations $t = 0$, while right panels correspond to the end of friction simulations $t = 3$ ns. We have highlighted the confined region with dashed lines (Top plate's width along the y axis is a half of the total system's width) and also we have sketched crystallization patterns with solid lines. Top plate's lateral velocity is set to $V_x = 2$ m/s, total simulation time is $t_{\text{tot}} = 3$ ns, hence all friction simulations have run until the Top plate had covered a distance of $d_x = V_x \cdot t_{\text{tot}} = 60$ Å along the x direction.

3.4.2 Confined tailed models of ionic liquid

For the study of TM ionic liquids under confinement, we use the MD simulation setup of ILs under confinement shown in Figure 3.5 in section 3.2. We use that setup throughout this section in order to investigate both the static and dynamic behaviour of confined TM ionic liquids, as well as, their lubrication performance.

We keep the simulation setup geometry fixed, and we change the ionic liquid.

3.4.2.1 Static force-distance characteristic

Confinement induces layering in IL thin films [64, 116]. In order to understand how does an interplay between layering and molecular geometry of TM ionic liquids alter the load bearing capability of IL thin films, we calculate the quasi-static force-distance characteristic. We follow the evolution of the normal load F_z acting on the Top plate as a function of the interplate distance d_z. In order to ensure static conditions, the interplate distance is changed through a series of alternating steps, called *move* and *stay* steps, related to the movement of the Top plate and subsequent relaxation of the IL structure, respectively. We provide a detailed description of the procedure of modifying the interplate gap in the simulations of the static behaviour of confined ionic liquid: Top plate is moved along the z axis at a constant velocity $V_z = 5$ m/s for a period of time $t_{move} = 5$ ps; During the *move* period the elastic constant of cation–tail bonds takes its original value of $K = 80$ kCal/molÅ^2. After the transition regime happening during the *move* period finishes, we apply conjugate gradient (CG) minimization (for the details about CG minimization method check) on the ions, in order to minimize their internal energy and relax them after the *move* period. As the ion minimization procedure is done, ions take positions which ensure their minimal internal energy. In case of SM model of IL, ion minimization procedure performs fine, enabling well–relaxed IL [64]. However, we have noticed that in case of TM models of IL, due to a rather high value of the elastic constant of cation–tail bonds, ion minimization procedure does not perform fine. The key action of minimization procedure is the repositioning of the charged particles (i.e. cations and anions), since they interact strongly via Coulombic potential. Cations are bonded to neutral tails via bonds, hence they do not have that much freedom to rearrange during the minimization procedure, compared to anions. We have solved this problem by taking a low value of the elastic constant (i.e., 1% of its original value, $K^{min} = K/100 = 0.8$ kCal/molÅ^2) during the ion minimization procedure. As the ion minimization procedure finishes, elastic constant K gradually increases and restores to the original value. This gradual increase is realized

via subsequent steps in which elastic constant takes the values from the next list: $K \in \{0.8, 2, 4, 10, 20, 40\}$ kCal/molÅ^2, where elastic constant takes each of the listed values for a period of time $\Delta t = 2.5$ ps. As the elastic constant gets restored to the original value, Top plate stays fixed for another $2\Delta t = 5$ ps during which period the average value of the normal force F_z is calculated and that value is presented as a simulation point in $F_z(d_z)$ static characteristic, i.e., in Figure 3.35. Hence, a *stay* period is made up of: ion minimization procedure with elastic constant $K^{min} = K/100$, the stepwise increase of K for $6\Delta t = 15$ ps and the calculation of the average value of the normal force F_z with the original elastic constant K for $2\Delta t = 5$ ps. In total, the time duration of the *stay* period is $t_{stay} = 20$ ps. In order to avoid a systematic error due to the initial position or direction, the Top plate movement is performed in different directions and from different initial configurations, hence Figure 3.35 shows the averages. The Top plate movement procedure consisting of *move* and *stay* periods is repeated until the distance $d_z^{min} = 11$ Å is reached.

The results for the force-distance characteristic of the three *TM ILs* are presented in Figure 3.35, where three different markers correspond to the three *IL* models. The normal force F_z strongly and non-monotonically depends on the distance d_z. These changes of the normal force F_z are correlated with the squeezing in and out of cation/anion layer pairs into the gap, as already observed experimentally [117] and theoretically [64]. The normal force becomes negative, i.e., $F_z < 0$ only in the case of small tails (*TM3*). The negative values are a result of the *IL* trying to reduce the plate-to-plate distance due to the adhesion forces inside of *IL*. The increasing tail size seems to reduce the effect of adhesion: for large tails (*TM9*) the normal force at the minimum is close to zero, while for symmetric cation molecule (*TM5*) it becomes positive, i.e., $F_z = 2$ pN. For all three curves corresponding to the three *TM* ionic liquids we can identify three characteristic ranges of the plate-to-plate distance d_z:

Segment(1): initial segment (11 Å$\leq d_z \leq 13.8$ Å) characterized by a monotonous and steep decrease of the normal force F_z

Segment(2): interval I (13.8 Å$\leq d_z \leq 19.8$ Å) characterized by the presence of local minima and maxima peaks of the normal force F_z, and
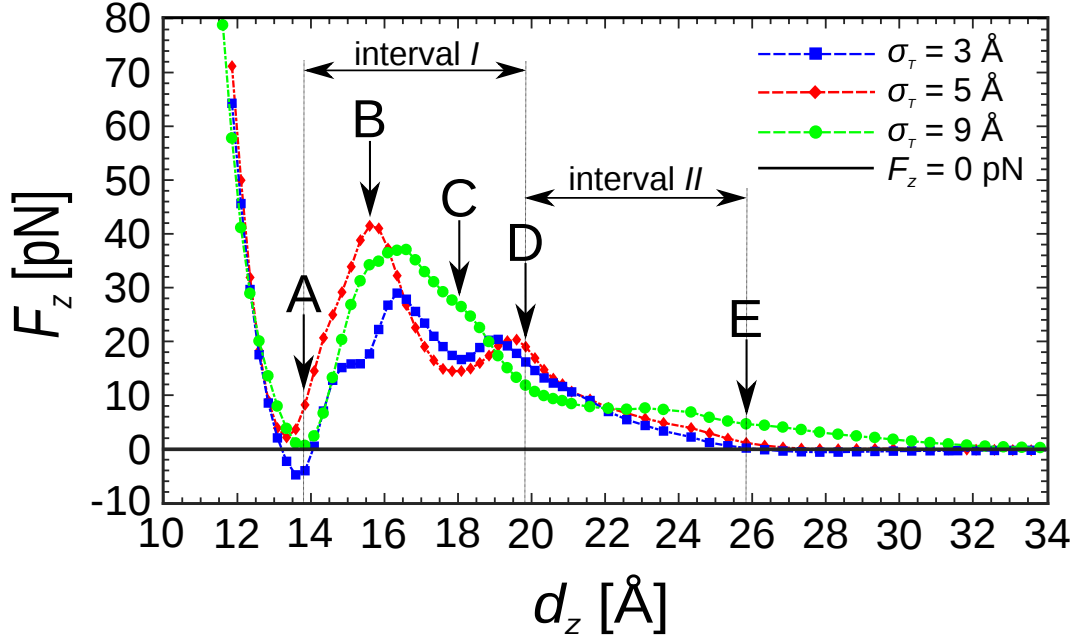
Figure 3.35: Dependence of normal force F_z on interplate distance d_z. Five characteristic points denoted with $\{A, B, C, D, E\}$ with corresponding interplate distances $d_z = 13.8, 15.5, 18.0, 19.8, 25.8$ Å, respectively, are marked in the figure. They are chosen in the way that: point A is located in the proximity of a local minimum for all three cases; point B corresponds to a local maximum for $TM5$ model; point C is located in the proximity of a local minimum for $TM3$ and $TM5$ model; point D is located in the proximity of a local maximum for $TM3$ and $TM5$ model; point E is chosen according to the condition $\overline{DE} = \overline{AD}$. For reference, the black horizontal line denotes $F_z = 0$. The lines connecting points (averages of normal force) serve as visual guide.

Segment(3): interval II and beyond ($d_z \geq 19.8$ Å) characterized by a continuous and gentle decrease of the normal force F_z, where in all three cases the normal force practically becomes zero when $d_z > 32$ Å.

We will briefly describe the segments of $F_z(d_z)$ curves, pointing out similarities and differences between the different IL models. In the initial segment, (i.e., for small gaps $d_z < 13$ Å), the normal force F_z is practically the same for all three systems, meaning that it does not depend on the tail size. The steep rise of the normal force with compression in the range $d_z < 13$ Å is a sign of a very high resistance of the single anionic layer left in the gap to squeezing out. On the other hand, at large gap values (i.e., $d_z > 32$ Å), the normal load F_z in all three TM ionic liquids is similar and small. We can conclude that at large gaps there is a low resistance of IL to the

gap changes. Significant differences in the force-distance curves, depending on the tail size, exist only in the interval I, (i.e., 13.8 Å$\leq d_z \leq$ 19.8 Å). In the case of the $TM3$ model, the $F_z(d_z)$ characteristic has two local minima and maxima and one saddle point, in the $TM5$ model there are two local minima and maxima, and in the $TM9$ model, there is one local minimum and maximum.

In the present setup, IL lubricant remains an infinite continuous body in x and y directions. However, there is a difference in $IL's$ structure depending on the fact whether it is confined inside the gap between the Top and Bottom plate or it is located in the lateral reservoirs (LRs), see Figure 3.38. Ionic liquid confined inside the gap forms alternating cationic–anionic layers, while ionic layering in LRs is less pronounced beyond first two layers, see Figure 3.38. Besides that, from Figure 3.38, we notice that in all three systems the layer closest to the solid plates is formed by cation–tail dimmers. We might label the layers formed alongside the solid plates as fixed layers, since they always form first. Inside the interplate gap ionic ordering is dictated according to the layers formed next to the solid plates:

(i) Bottom plate - cation–tail layer - anionic layer, looking from the bottom,

(ii) Top plate - cation–tail layer - anionic layer, looking from the top, where bottom and top correspond to the position along the z axis.

In Figures 3.36 and 3.37 we present 5×3 panels of configuration snapshots for 5 chosen characteristic points of 3 TM models. The atoms are depicted keeping the ratios of their sizes.
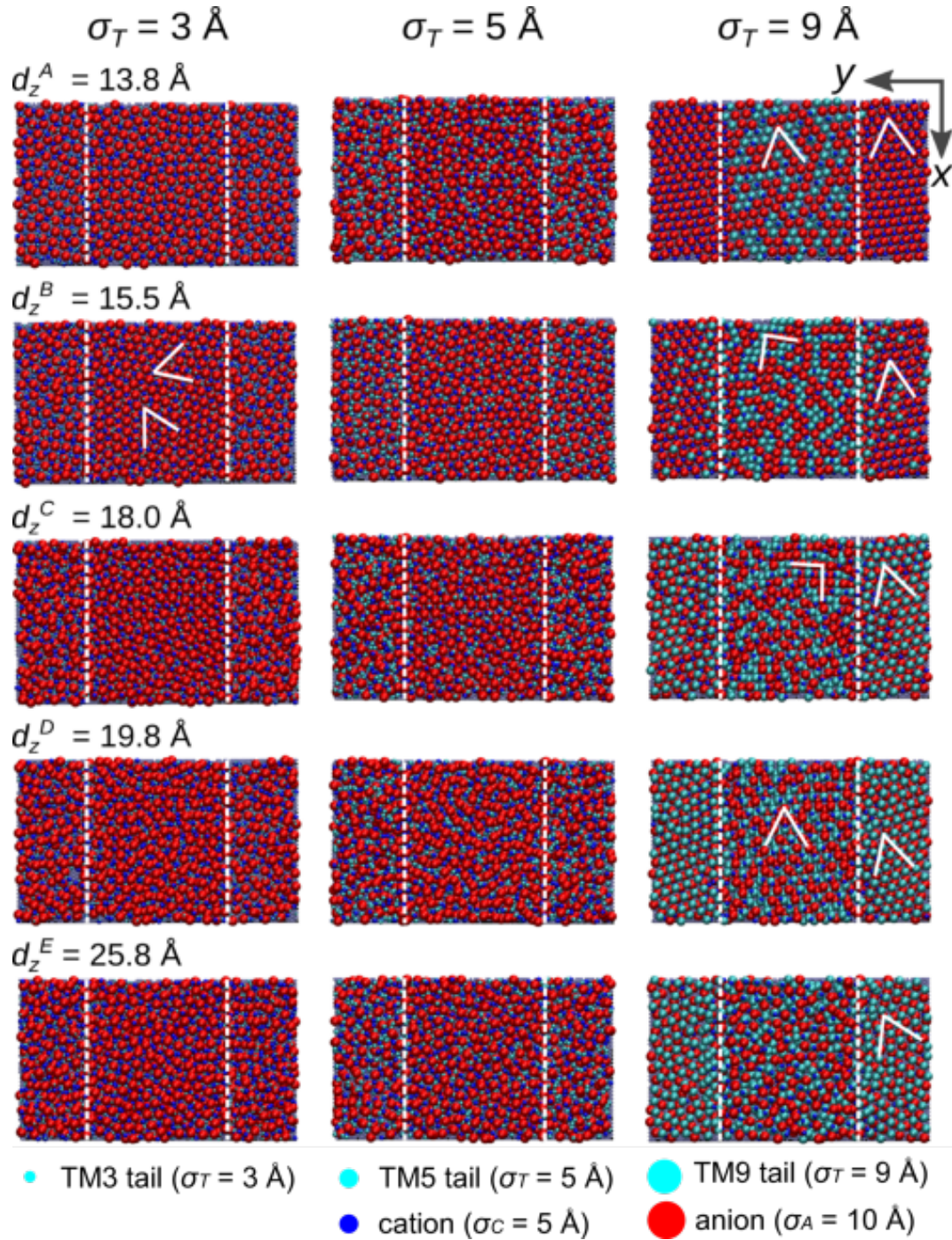
Figure 3.36: Configuration snapshots (xy cross section) of $TM3$, $TM5$ and $TM9$ models in five characteristic points $\{A, B, C, D, E\}$. Five characteristic points, denoted with $\{A, B, C, D, E\}$, have corresponding interplate distances $d_z = \{13.8, 15.5, 18.0, 19.8, 25.8\}$ Å, respectively (see also Figure 3.35).

- IL structure inside and outside the interplate gap

In Figure 3.39 we are showing the ionic density distribution along the z axis for
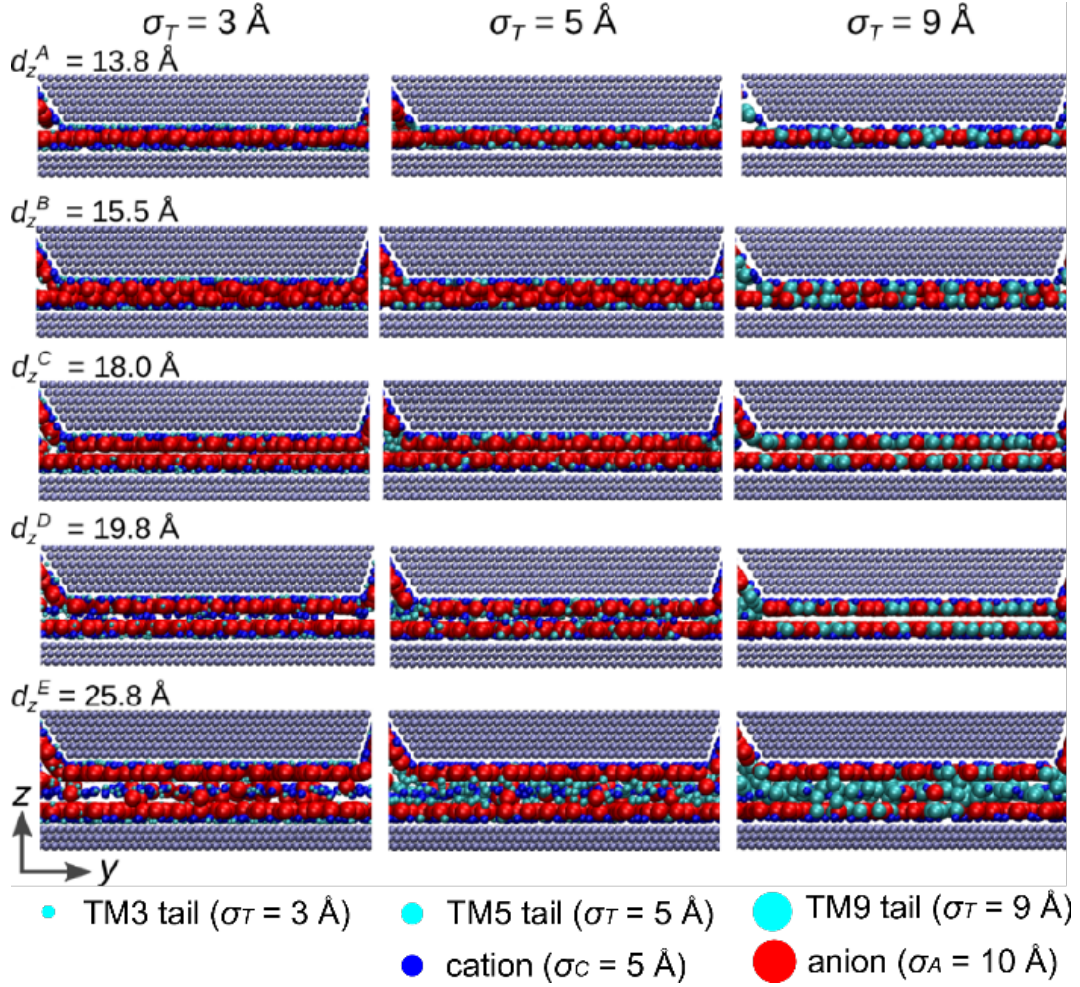
Figure 3.37: Configuration snapshots (yz cross section) of $TM3$, $TM5$ and $TM9$ models in five characteristic points $\{A, B, C, D, E\}$ (see also Figure 3.35). This figure presents the changes taking place in the confined ionic layers as the interplate distance changes in case of static force–distance simulations.

the three IL models, in points A to E, i.e, $d_z = \{13.8, 15.5, 18.0, 19.8, 25.8\}$ Å. A common feature of all investigated IL models is the formation of *fixed* cationic layers along the whole length of the solid plates (Top and Bottom plate). The fixed layers and their stability are a result of strong LJ interactions between the plates and ions. In general, the smallest particles form the first layer next to the plates.
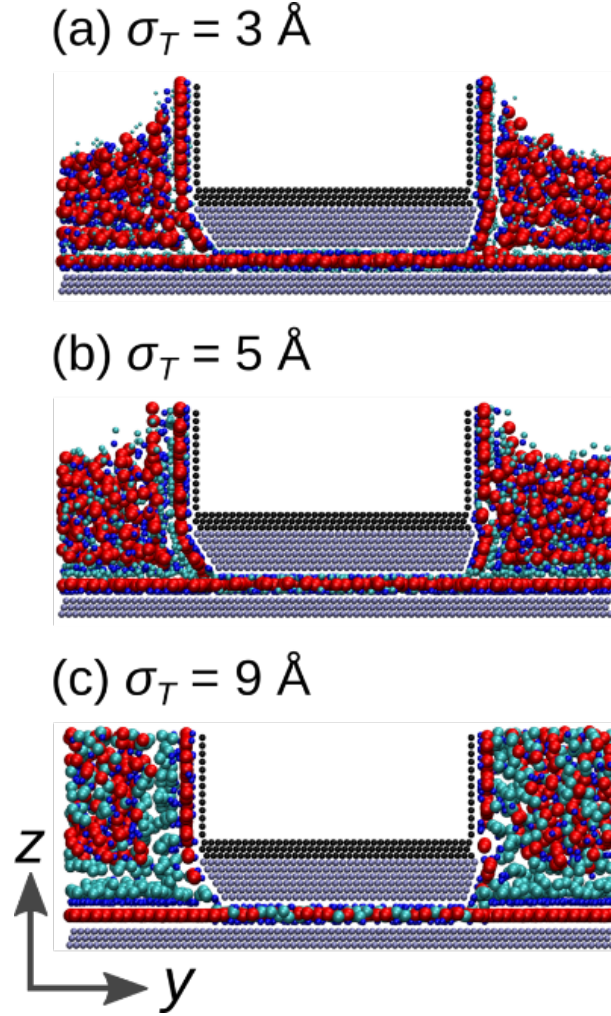
Figure 3.38: Configuration snapshots (yz cross section) of $TM3$, $TM5$ and $TM9$ models in a characteristic point A marked in Figure 3.35. This figure represents an illustration of ionic layering.

For $TM3$ the first layer to the plates is formed by the tail particles (which are part of the cation-tail pair), while for $TM5$ and $TM9$ models these particles are the cations. The consecutive layers are formed inside the interplate gap via combined volume exclusion and Coulombic interactions and their ordering is consistent with the fixed layers. As a result, tails migrate to the plates in $TM3$ model, they mix with the cationic layer when cation-tail dimer is symmetric in $TM5$ model, and finally they mix into the anionic layer when they are large in $TM9$ model. Since Coulombic interactions cause the layering with alternating charge sign, anionic layers always separate cationic layers. We focus on analyzing the changes in the segment between the points A and D, i.e., the interval I. The normal force F_z
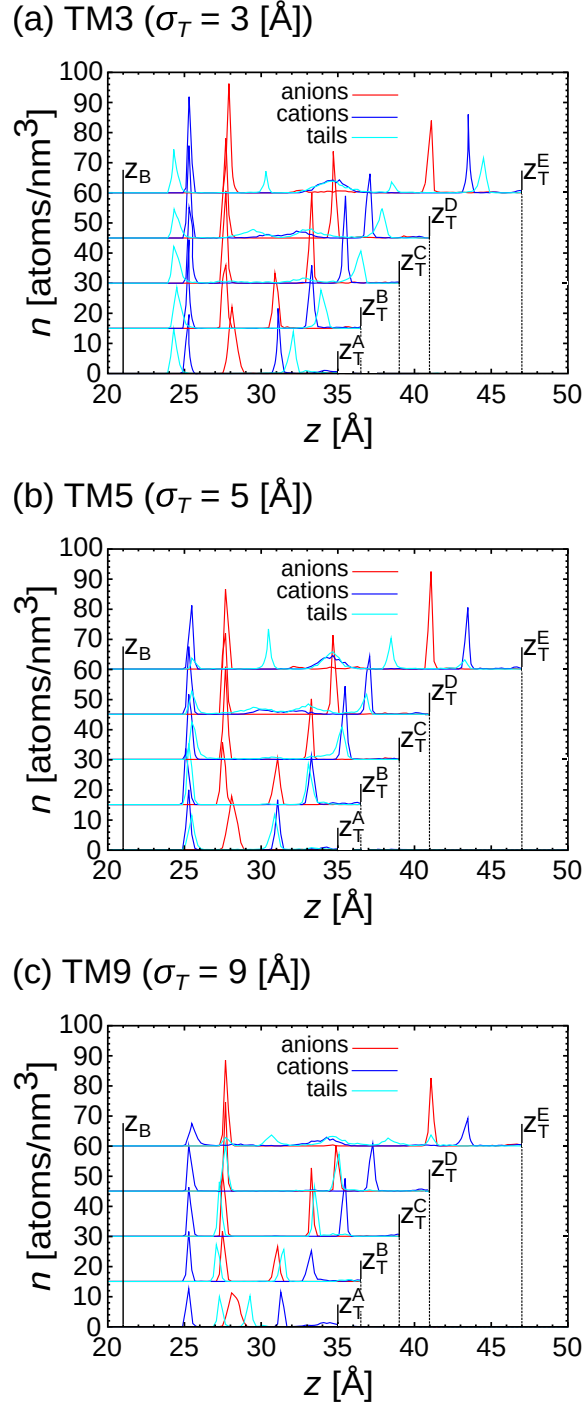
Figure 3.39: Ionic density distribution of ions inside the interplate gap of (a) $TM3$, (b) $TM5$ and (c) $TM9$ models in characteristic points $\{A, B, C, D, E\}$ taken from the static force–distance characteristic presented in Figure 3.35. The positions of the atomic centers of the innermost atomic layers of the (moving) Top and the (fixed) Bottom plate are labeled as z_T^{A-E} and z_B, respectively.
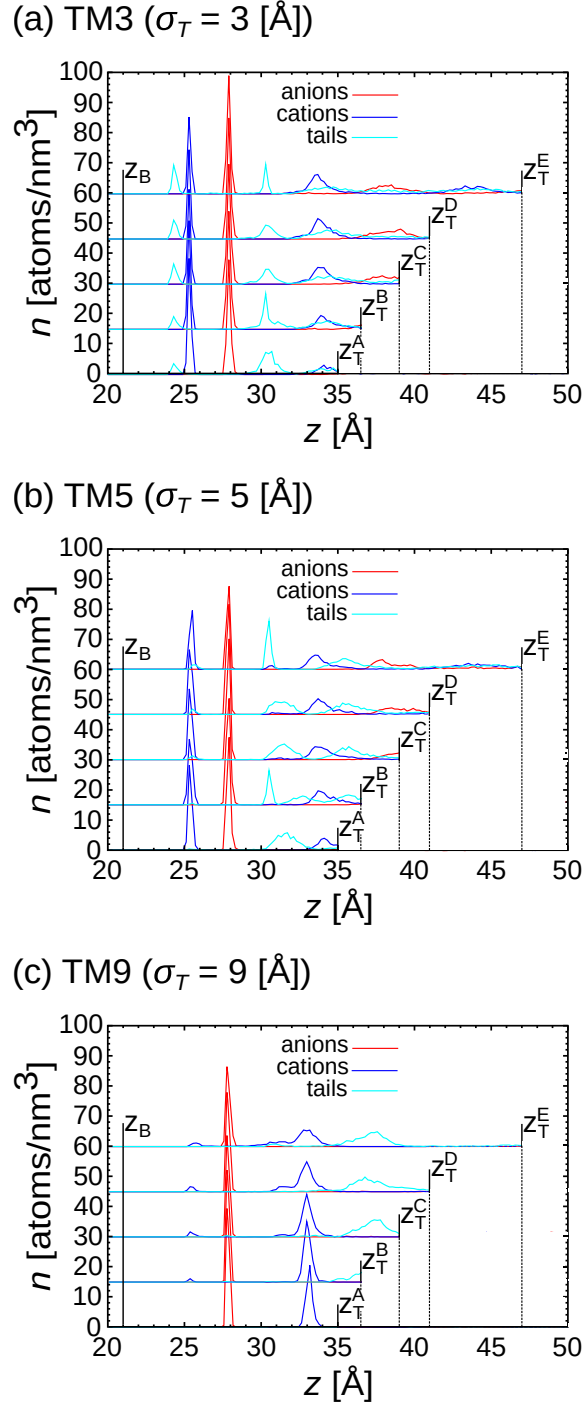
Figure 3.40: Ionic density distribution of ions outside the interplate gap of (a) $TM3$, (b) $TM5$ and (c) $TM9$ models in characteristic points $\{A, B, C, D, E\}$ taken from the static force–distance characteristic presented in Figure 3.35. The positions of the atomic centers of the innermost atomic layers of the (moving) Top and the (fixed) Bottom plate are labeled as z_T^{A-E} and z_B, respectively.

changes rapidly and non-monotonically with the interplate distance d_z in the interval I, check Figure 3.35. For the minimum of F_z in the vicinity of point A, i.e., for the interplate distance $d_z^A = 13.8$ Å, we can observe a well-defined anionic layer in Figure 3.39. The most interesting change takes place during the transition A $\rightarrow$ B when the single layer of anions is split into two layers, check Figure 3.39. As a result, the normal force F_z increases and reaches a local maximum in the proximity of point B, i.e., for plate-to-plate distance $d_z^B = 15.5$ Å. We observe that additional anion-cation pairs are pulled inside the gap in Figure 3.41. We also observe that the two anionic layers in Figure 3.39 for point B and the one for point A have the same maximum number density. As we increase d_z further, the number of anionic layers confined inside the gap remains unchanged and the normal load drops slowly. At the same time, the number of ions inside the gap steadily increases with the gap width. Nevertheless, this increase is not sufficient to keep the density of IL inside of the gap constant (check Figure 3.41). Looking into the changes in the spatial distribution of IL components, as more cation-anion pairs are pulled into the gap (going from A $\rightarrow$ E), we observe a steady increase of the concentration of anions in the layer next to the Bottom plate. In the case of $TM5$ model we have an increase from $n_{\mathrm{TM5}}^A = 18$ atoms/nm^3 to $n_{\mathrm{TM5}}^D = 27$ atoms/nm^3, check Figure 3.39. When we further look at configuration snapshots for $TM3$ and $TM5$ model, a formation of additional layers inside the gap is visible, between the points C and D. This can also be clearly observed in Figure 3.39 and results in smaller maximum around $d_z =$19 Å, in Figure 3.35. We can conclude that the form of the normal force-plate distance characteristic is not correlated with the number density of the IL molecules inside the gap, but the layer formation seen in Figure 3.39. As the interplate distance d_z increases further, from point D to E, we notice additional cations in the middle of the gap and formation of a third cationic layer in all three systems. We can make an interesting observation that for all three models the tails in the middle of the confinement are grouped in three regions: with cations at $z = 34$ Å, and in the middle between cationic and anionic layers, i.e., $z = 30, 38$ Å, check in Figure 3.39. This outcome is reminiscent of the findings from Reference [71] where the authors have experimentally obtained the formation of the tail–to–tail bilayer of cationic
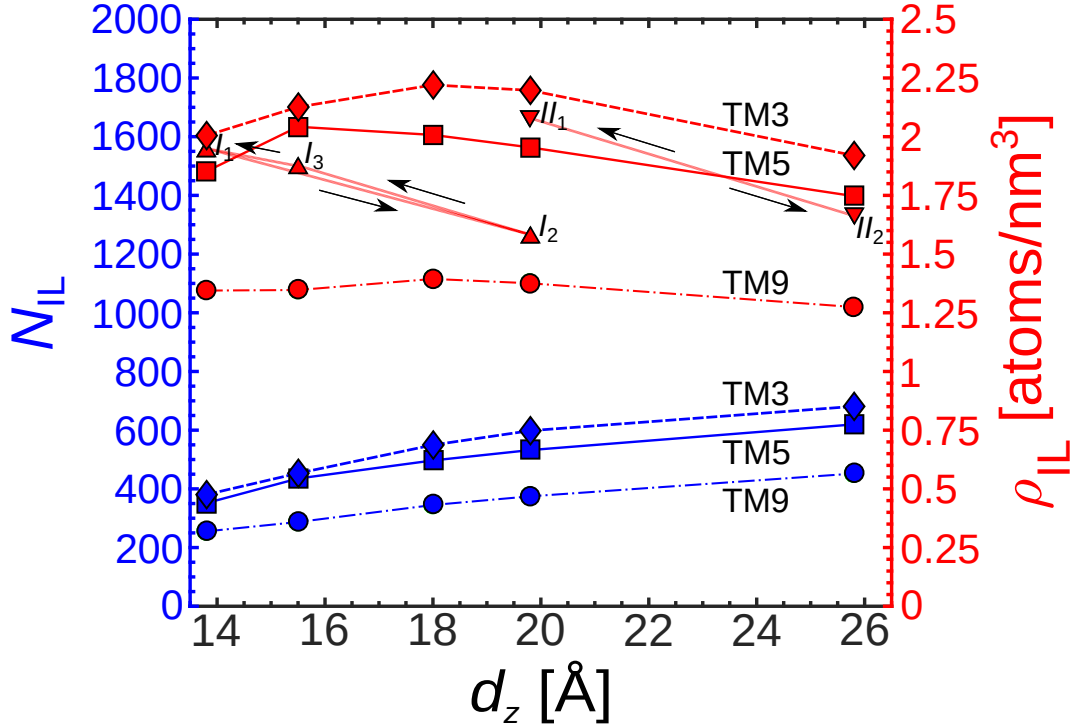
Figure 3.41: Evolution of the number of confined ionic liquid (IL) molecules (bottom curves) and density (top curves) inside the gap with gap width d_z for $TM3$, $TM5$ and $TM9$ models in characteristic points $\{A, B, C, D, E\}$ selected from the static force–distance characteristic (Figure 3.35). The corresponding axes for the number of IL molecules and the density are given on the left and right side, respectively. The densities at characteristic points for the dynamic cases (intervals I, II) of $TM5$ model are also given, i.e., $I_{1,2,3}$ and $II_{1,2}$, for the purpose of comparison with the static case of $TM5$ model.

dimers in case the alkyl chain length is oversized. In Figure 3.42 we present how do the number of confined IL molecules and density depend on the interplate distance d_z in dynamic cases for $TM3$, $TM5$ and $TM9$ models. In all three TM models, we notice the same tendencies for both N_{IL} and ρ_{IL} dependences on d_z.
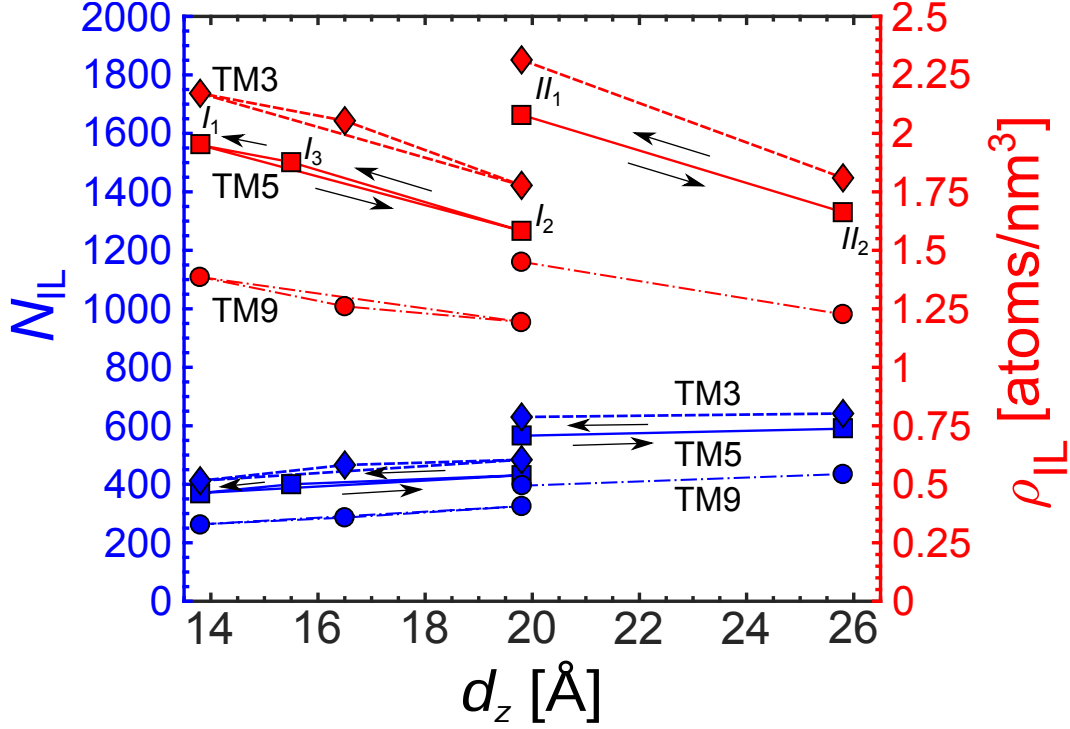
Figure 3.42: Evolution of the number of confined ionic liquid (IL) molecules (bottom curves) and density (top curves) inside the gap with gap width d_z for $TM3$, $TM5$ and $TM9$ models for the dynamic cases (intervals I, II), i.e., $I_{1,2,3}$ and $II_{1,2}$. The corresponding axes for the number of IL molecules and the density are given on the left and right side, respectively.

- IL crystallinity: influence of the gap

We show the xy cross-section snapshots in Figure 3.36 in order to observe the $IL's$ in-plane structure at the cross-section just below the Top plate. We mark the boundaries of the Top plate spatial region with the vertical dashed lines. The central area of the panels in Figure 3.36 corresponds to the interplate gap region and it represents a half of the total cross-section's width in the y direction, while the remaining area corresponds to the lateral reservoirs. The solid lines mark the orientation of crystal grains in those areas, where we can observe the presence of structural ordering. In the case of $TM3$ model, we observe the presence of partial triangular ordering only at point B when the structure is the most compressed. We do not notice any crystallization for symmetric dimers ($TM5$ model), which confirms that the symmetric tail prevents ordering both under confinement and in the bulk. Contrary to the previous two cases, we observe crystallization for all configurations

with the large tail ($TM9$ model). Additionally, we observe changes in the type of crystalline structure. While in the lateral reservoirs a triangular lattice arrangement is always present, depending on the amount of compression we observe triangular lattice arrangements in points A and D and square lattice arrangements in points B and C. Even more surprisingly, the order is lost when the tail–to–tail bilayer is formed in point E.

3.4.2.2 Dynamic force-distance characteristic

The Top plate was moved between the two limiting points of the intervals I ($d_\mathrm{z}^A \leq d_\mathrm{z} \leq d_\mathrm{z}^D$) and II ($d_\mathrm{z}^D \leq d_\mathrm{z} \leq d_\mathrm{z}^E$). We have investigated the dynamic behaviour of the confined IL thin film during the cyclic movement of the Top plate along the z axis, i.e., the interplate gap was periodically extended (*extension* half–cycle) and compressed (*compression* half–cycle). We have investigated our system at three velocities $V_z = \{0.1, 1, 10\}$ m/s, but we did not observe any velocity dependent differences in the system behaviour. The confined ionic liquid lubricant responds to the cyclic movement of the Top plate with a hysteresis in normal force $F_\mathrm{z}\,(d_\mathrm{z})$ shown in Figure 3.43. We present the detailed results of the $TM5$ model dynamic behaviour in (a) and (c) panels of Figure 3.43. Also, in (b) and (d) panels of the same figure, we present together smooth average cycles of our three IL models ($TM3$, $TM5$, and $TM9$).

- Narrow gap (interval I): normal force hysteresis

We will now discuss in detail the response of the $TM5$ model to the cyclic motion of the Top plate, in the interval I shown in Figure 3.43(a). Ten cycles of compression-extension are shown (thin lines) with an *average* cycle superimposed on them (thick line). We identify three points of interest: $\{I_1, I_2, I_3\}$, i.e., the two terminal points of the cycle and the point with the maximal normal force, respectively. These three points also correspond to the points $\{A, D, B\}$ respectively, in the static characteristics shown in Figure 3.35. Point I_3 corresponds to the maximum of normal force F_z both in the cyclic compression cycle and in the static characteristic of $TM5$ model, which makes the comparison more straightforward.

The normal force F_z decreases down to a value close to zero during the *extension*
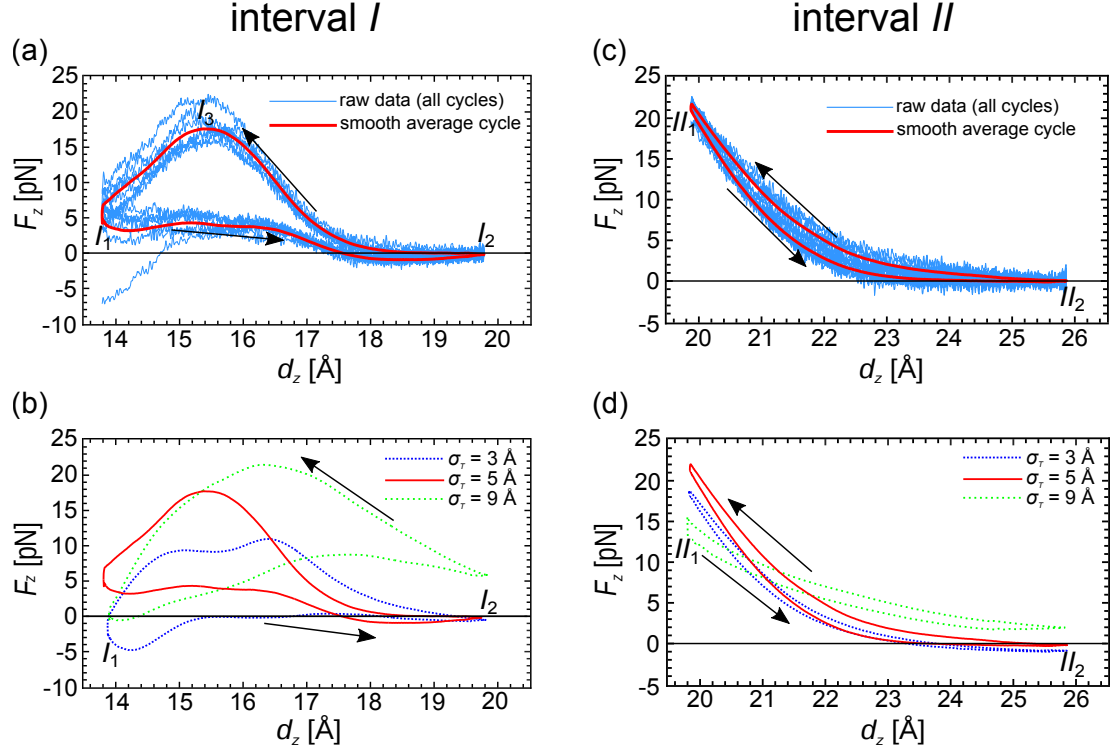
Figure 3.43: The results of dynamic extension–compression cycles are shown for the intervals I and II. In the panels (a) and (c) we present dynamic $F_z(d_z)$ characteristic in case of $TM5$ model, for the intervals I and II, respectively; thin lines represent the hystereses of ten dynamic cycles, solid line on top of them is the smooth average hysteresis. There is also a solid horizontal line which corresponds to $F_z = 0$. In (a) points I_1, I_2, I_3 denote representative points: I_1 - starting point, I_2 - ending point, I_3 - global maximum of the $F_z(d_z)$ curve. In (c) points II_1 and II_2 denote representative points: II_1 - starting point and II_2 - ending point. The arrows show the direction of hysteresis (extension $I/II_1 \rightarrow I/II_2$ followed by compression $I/II_2 \rightarrow I/II_1$). In the panels (b) and (d) we show together smooth average hystereses $F_z(d_z)$ of our three TM ionic liquids, for the intervals I and II, respectively. Starting and ending points and arrows are denoted, analogous to the panels (a) and (c).

half of the cycle $I_1 \rightarrow I_2$. The anion-cation pairs are pulled into the gap from the lateral reservoirs as the gap is extended and at point I_2 an additional anionic layer is fully formed inside the gap. Actually, instead of the two fixed layers of cations which share one anionic layer, we obtain two separate anionic layers. The total number of ions pulled in is about 60 atoms or 0.22 atoms/(nm^{2}ns) at 1 m/s plate linear speed. In the first part of the compression half-cycle, $I_2 \rightarrow I_3$, the ions are compressed and the density and the normal force F_z increase. Somewhat surprisingly, we observe that

an equal number of ions flows out while the normal force increases, i.e., $I_2 \rightarrow I_3$ and during its sharp drop $I_3 \rightarrow I_1$ (check Figure 3.41). The sharp decrease of the normal force F_z in the segment $I_3 \rightarrow I_1$ is therefore a result of two processes: out-flow of the ions from the gap and the collapse of the anionic double layer and its rearrangement into a single anionic layer. The resulting final density $\rho_{IL}^{dyn} = 1.95$ atoms/nm^3 of the system is slightly higher than in the static case $\rho_{IL}^{stat} = 1.85$ atoms/nm^3, check Figure 3.41. The value of the normal force F_z at point I_1 is similar, i.e., $F_z = 4$ pN in both static and dynamic case.

In Figure 3.43(b), we observe that each one of the three investigated ionic liquids ($TM3$, $TM5$, and $TM9$) exhibits different behaviour in the average $F_z(d_z)$ cycle during the extension and compression half-cycle. First, at the onset of the extension half-cycle, i.e. in the point I_1, the normal force F_z has a positive value for symmetric cations ($TM5$ model), it is close to zero for large tails ($TM9$ model), and it is negative for small tails ($TM3$ model). Somewhat surprisingly, the normal force increases for both TM ILs with asymmetric cations ($TM3/TM9$ models) while it decreases for symmetric cation ($TM5$ model). The reason for this behaviour is the strong interaction of the fixed layers of ions adjacent to the plates with the plate particles. This interaction drives as many ions inside the gap as possible, resulting in the non-intuitive behaviour of the normal force due to an interplay of density and intra-IL LJ interactions. During the compression half-cycle for all three ILs the maximal normal force sustained was about 50% smaller than in the quasi-static case, i.e., for $TM5$ model the maximal force is $F_z^{max} = 17$ pN in the dynamic case and $F_z^{max} = 40$ pN in the static case (see Figures 3.43(b) and 3.35). This observation indicates that the Top plate's motion prevents the IL to fill the gap. We can also conclude that the mechanical response is mainly due to a rearrangement of the fixed layer and that the mobility of the IL molecules is too low to significantly increase the normal force resisting to the compression. If we analyze the rate of mass transfer outside of the gap, we conclude that there is a substantial slip, which results in a lower normal force. Without slip at a velocity $V_z = 1$ m/s, the normal force calculated based on the bulk viscosity coefficient would be roughly two orders of magnitude higher. Figure 3.44 shows configurations snapshots accompanied with
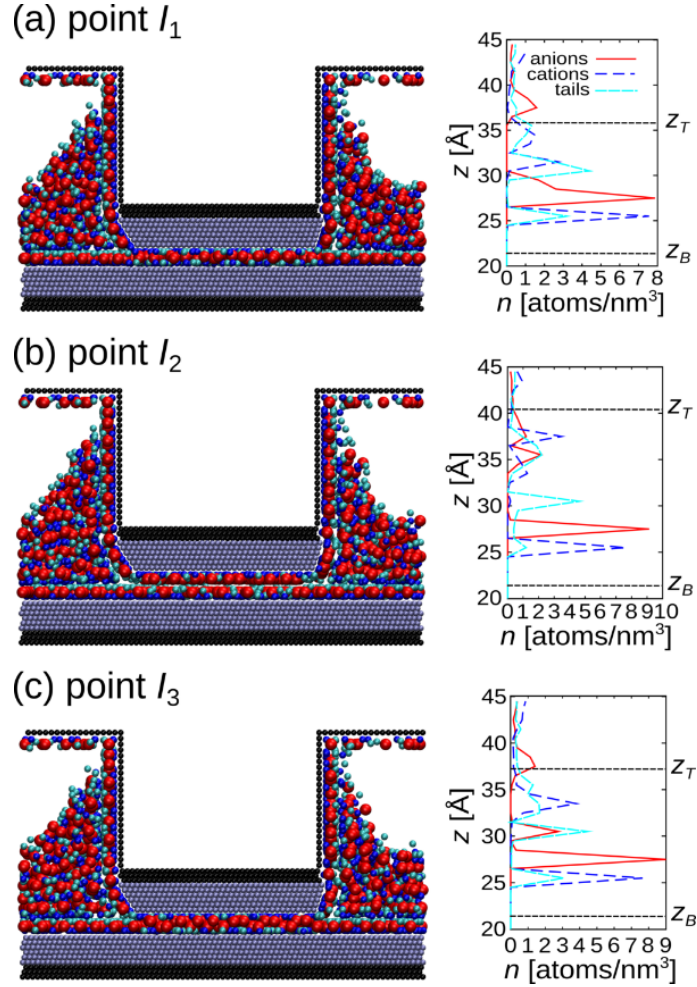
Figure 3.44: Configuration snapshots accompanied with ionic density distribution along the z direction in the three characteristic points (I_1, I_2, I_3) from the panel (a) of Figure 3.43.

the ionic density distribution along the z direction, for the interval I of dynamic cycle of $TM5$ modeled ionic liquid. In the point I_1 there is one compact anionic layer leading to a rather low positive value of the normal force F_z. In the *extension* half–cycle ions from the LRs get taken into the gap. This leads to the formation of another compact anionic layer, which means that from one compact anionic layer at the starting point I_1, we arrive at two compact anionic layers at the ending point I_2. In the return *compression* half–cycle, those extra ions get pushed back into the LRs, leading to the reduction of the number of compact anionic layers confined inside the gap to one.

- Wide gap (interval II): monotonic force-distance characteristics

The extension-compression force-distance characteristic for the interval II in case of $TM5$ model is given in Figure 3.43(c). The difference from the quasi-static extension/compression in Figure 3.35 is the monotonic behaviour during the cycle. The quasi-static characteristics in the interval II featured local minima and maxima in the case of $TM3$ and $TM5$ models. In the dynamic case, there are only two characteristic points (starting and ending point II_1 and II_2, respectively and a monotonically changing normal force between them. In the *extension* half–cycle there is a continuous decrease of the normal force F_z followed by its continuous increase in the *compression* half–cycle. The difference in the normal force between the cycles is small. In the dynamic characteristic of the interval II the layer structure is similar to the static case, i.e., two fixed layers stay-in-place and the tail double layer is formed during the extension half-cycle (check Figure 3.45). In contrast to the interval I, the formation of the additional layer of tails is not a result of the ions flowing from the lateral reservoirs into the gap. The density inside the gap is 10% higher in the dynamic case and a few atoms (less than 30) are displaced during the cycle. We should note that the gap is also 50% larger in the interval I compared to the interval II, therefore the drop in density is even less striking. Actually, the cyclic motion has a tendency to increase the density inside the gap. Since there is no large displacement of the ions in and out of the gap in the interval II, there is also no maximum of the normal force F_z, similar to the one we have seen in the case of the interval I, check Figure 3.43(a). In order to make comparisons of different TM ionic liquid models, in Figure 3.43(d) we show together $F_z(d_z)$ average cycle dynamic characteristics of all three TM models of ionic liquid (i.e., $TM3$, $TM5$, $TM9$ model) for the interval II. Compared to the interval I, the tail size does not have such a pronounced impact on $F_z(d_z)$ hysteresis curves in the interval II. Figure 3.45 shows configurations snapshots accompanied with the ionic density distribution along the z direction, for the interval II of dynamic cycles of $TM5$ model IL. In the point II_1 there are two compact anionic layers opposite to each other leading to a high positive value of the normal force F_z. In the *extension* half–cycle the fixed layers become separated, and a marginal number of cation–tail dimers diffuses from the lateral reservoirs (LRs) into the gap. However, another anionic layer does not form,
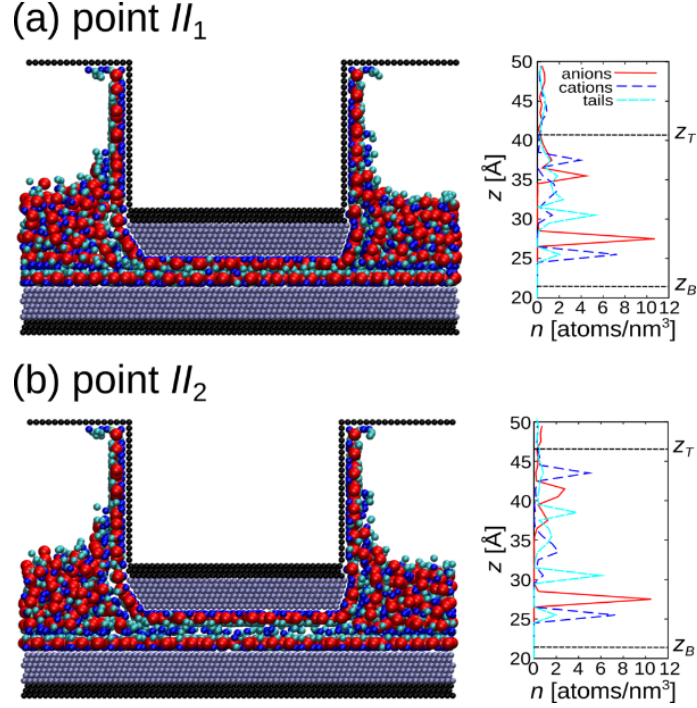
Figure 3.45: Configuration snapshots accompanied with ionic density distribution along the z direction in the two characteristic points (II_1, II_2) from the panel (c) of Figure 3.43.

which means that from the two compact anionic layers with the cationic layer in-between at the starting point II_1, we arrive at two separated layers in the ending point II_2 with the tail bi-layer in-between.

- Energy losses due to cyclic extension-compression

At this point, we would like to quantify how do the processes arising during the dynamic cyclic movement of the Top plate contribute to energy losses. We calculate the area covered during the extension-compression cycle (i.e., the area inside the $F_z(d_z)$ hysteresis). This area is equivalent to the work invested per average dynamic cycle, i.e., the hysteretic energy losses. We show the dependence of the energy losses on the tail size for both intervals I and II in Figure 3.46. We observe a clear tendency of the increase of the invested work per dynamic cycle, with the increase of the tail diameter. This is primarily due to the larger volume occupied by the tails resulting in larger normal forces resisting compression. There is a striking difference in the amount of invested work between the two intervals I and II (e.g. 27 pN · Å for the interval I of $TM9$ model compared to 5 pN · Å for the interval II of $TM9$ model).
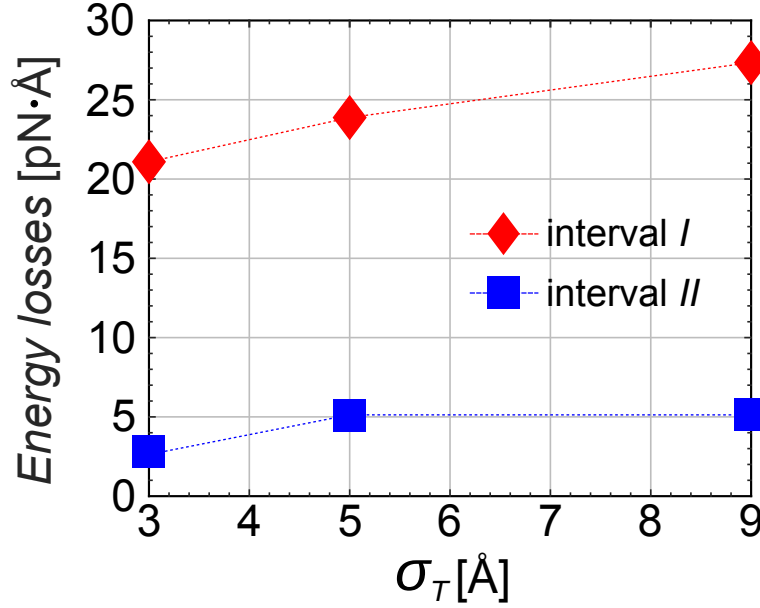
Figure 3.46: Energy losses per average cycle in function of the tail size, for intervals *I* and *II* of dynamic extension–compression cycles.

This difference is proportional to the maximal normal force which is sustained by the systems in the two intervals (check Figure 3.35).

3.4.2.3   Tribological behaviour of confined tailed models of ionic liquid

We have conducted static and dynamic characteristic analysis of the three generic *IL* models, focusing on the influence of their molecular structure on the anti-wear performance. In order to obtain a full picture, it is crucial to determine $IL's$ friction behaviour under different shear conditions. In this section we apply a relative motion between the plates by moving the Top plate along the x-axis (see Figure 3.5 from section 3.2) and we observe the resulting frictional force (also along the x-axis, i.e., F_x). We have performed two types of friction simulations:

(*i*) at a constant Top plate's velocity $V_x = 2$ m/s, the simulations are performed at different fixed values of the gap: $d_z = 12$ Å to 25.5 Å, and

(*ii*) at a fixed gap $d_z = 15$ Å Top plate's lateral velocity takes five different values: $V_x = \{0.1, 0.3, 1.0, 3.0, 10.0\}$ m/s.

In all friction simulations, the total distance covered by the Top plate was $\Delta_x = 100$ Å in the x direction. The dependence of the time-averaged frictional force $\langle F_x \rangle$

on the interplate gap d_z for the three IL models is shown in Figure 3.47. The points obtained in the simulations are shown as markers. Linear fits through these points are provided as visual guides. For the $TM3$ model ionic liquid, we observe a decrease of the frictional force $\langle F_x \rangle$ with the size of the gap. On the other hand, the frictional force weakly depends on the gap width in case of $TM5$ and $TM9$ model ionic liquids. Both the $TM3$ and $TM9$ have high zero shear-rate (Green-Kubo) bulk viscosities correlated with extent of their ordering, i.e., $\eta_{\mathrm{TM3}}^{\mathrm{GK}} > \eta_{\mathrm{TM9}}^{\mathrm{GK}} > \eta_{\mathrm{TM5}}^{\mathrm{GK}}$. When comparing with their tribological performance in a thin film we can conclude that there is no correlation since the $TM5$ ionic liquid has the highest average frictional force. In Figure 3.48, we show the dependence of specific friction $\langle F_x \rangle / \langle F_z \rangle$ on the Top plate's lateral velocity V_x in case of $TM5$ model ionic liquid. We obtain specific friction values of the order $\langle F_x \rangle / \langle F_z \rangle \approx 0.01$ which are comparable to the result from Reference [53] for symmetric $[PF_6]^-$ anion. We observe also a similar tendency of decreasing friction force with respect to tail size, as reported in the same Reference [53]. The specific friction $\langle F_x \rangle / \langle F_z \rangle$ is defined as the ratio of the time averaged frictional $\langle F_x \rangle$ and normal $\langle F_z \rangle$ force and it is different from the Coulombic friction coefficient $\mu = \partial F_x / \partial F_z$. Consistently with our previous results for model ionic liquids, we have observed a logarithmic dependence of specific friction on the lateral velocity, check Reference [64]. The numerical values are fitted to a linear function of the form $\langle F_x \rangle / \langle F_z \rangle = a \log (V_x / V_{ref}) + b$, where $V_{\mathrm{ref}} = 1 \ \mathrm{m/s}$. The coefficients of the linear fit took those values: $a = 0.001, b = 0.008$. A reasonable fit to the linear regression curve can be observed. The logarithmic dependence indicates typical elastohydrodynamic lubrication (EHL) conditions [119].
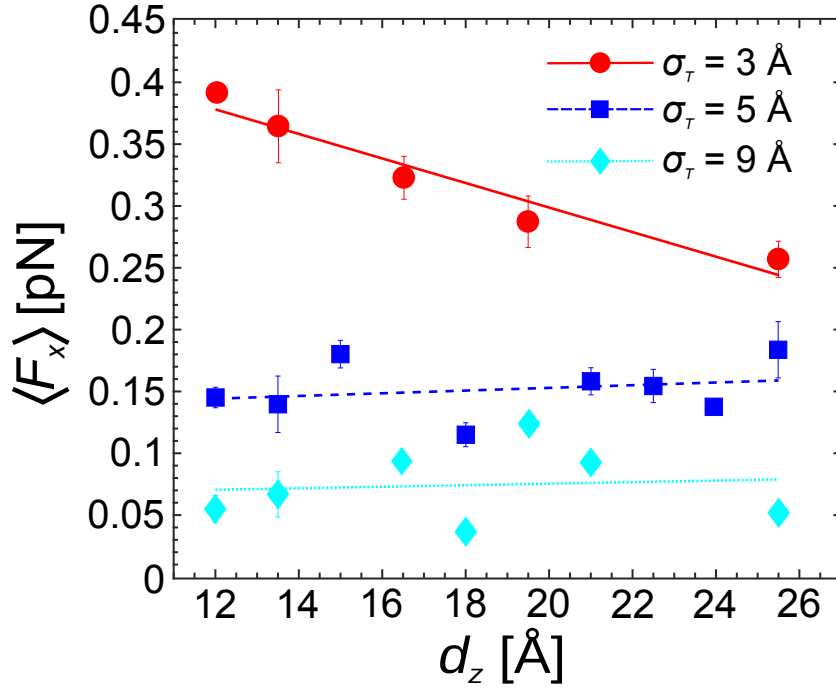
Figure 3.47: Average frictional force $\langle F_x \rangle$ acting on the Top plate as a function of the interplate distance d_z for confined $TM3$, $TM5$ and $TM9$ ionic liquid lubricant. In case of $TM3$ model there is a clear linear dependence showing the decrease of frictional force intensity with the gap increase, while on the other side in case of $TM5$ and $TM9$ model frictional force is practically constant and does not depend on the gap.
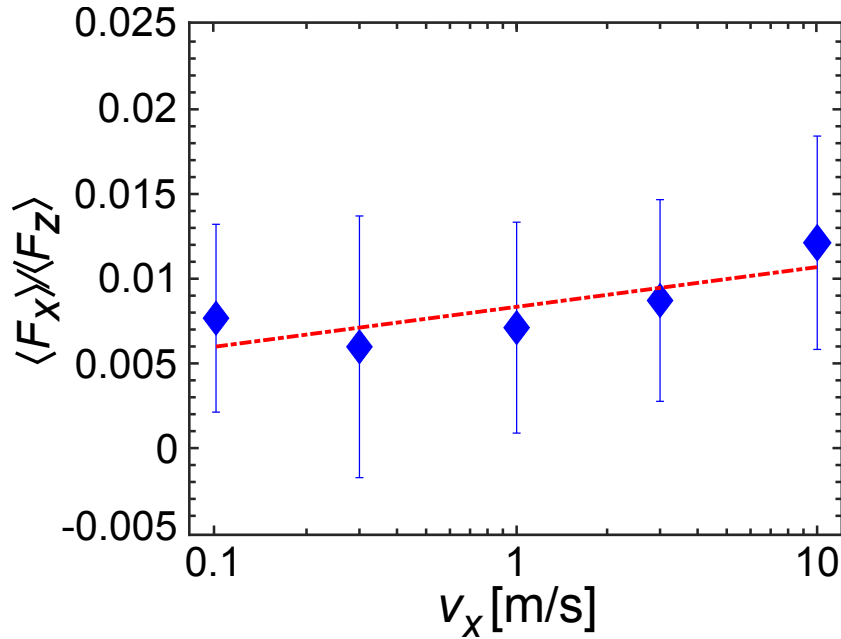
Figure 3.48: Specific friction $\frac{\langle F_x \rangle}{\langle F_z \rangle}$ dependence on Top plate's lateral velocity V_x in case of $TM5$ model.

Chapter 4   Conclusions

In this doctoral thesis two research topics, related to dipolar and ionic systems, namely tubes and helices composed of dipolar hard spheres and ionic liquids, have been modeled and investigated. Pronounced ordering under the conditions of spatial confinement has been obtained in both systems. The ordering is a consequence of the dominant long-range interactions, i.e., dipole-dipole interaction in dipolar structures and Coulombic interaction in ionic liquids. In both systems long-range interactions have led to the ordering that spans the system. A rich phase behaviour, sensitive to: variations of packing in case of dipolar systems and particle shape in case of ionic systems, has been obtained.

4.1   Confined dipolar systems

A study about cohesive energy of helical and tubular structures composed of hard spheres with permanent dipole moments has been presented. Helices were created by replication of a particle or patch of particles on a confining cylindrical surface. Even for the most simple situation, namely the single thread helix, a non-trivial behaviour is found when monitoring the cohesive energy as a function of surface packing (i.e., axial compression).

In particular, a non-monotonic dependence of the cohesive energy on the packing fraction (or equivalently the amount of compression) as a result of a delicate interplay of dipole-dipole interactions and excluded volume effects can be observed. The lowest cohesive energy is achieved at the highest packing fraction with touching turns. In parallel, the polarization order parameter, i.e., the mean dipole moment per particle $\langle m_z \rangle$, also displays a striking non-monotonic behavior as a function of the extent of compression. In the regime of very high surface packing fraction with

local triangular arrangement compatible with certain cylinder radius R over particle diameter d ratio (R/d), a pronounced cohesive energy is found.

Accordingly, the polarization order parameter indicates a sharp change in the dipole moment orientation, which tends to be parallel to the helix axis. Finally, cohesive energies of dense multiple (i.e., double or quadruple) helices, as well as, AB and ZZ tubes made up of stacking rings that can also be seen as special multiple helices have been compared. A remarkable finding is the enhanced cohesive energy for the ZZ tube structure. The latter already emerges at strong substrate curvature with cohesive energies very close to that obtained at vanishing curvatures. In these ZZ tube structures, an alignment of the helix threads with its axis is a microstructural signature for this low cohesive energy. As a final note, it should be emphasized that the implemented model of dipolar tubes and helices mimics nicely the geometry and microstructure of biological microtubules. It could also provide a possible clue about the self-assembly mechanisms and cohesion within microtubular structures.

4.2   Ionic liquids

4.2.1   Salt model of ionic liquid

In the study conducted in this doctoral research an molecular dynamics (MD) simulation setup in order to study the behaviour of model ionic liquids (ILs) confined between plates which are in close proximity while being in relative motion has been implemented. In the framework of this doctoral thesis the MD setup was developed in a way that allows the mesoscopic study of the lubrication processes in automotive applications such as the piston ring–cylinder liner interaction inside the internal combustion engine. More specifically, the geometry was selected in order to allow a variable lubricant confinement gap combined with a varying lubricant quantity in the gap, while avoiding the squeeze-out of the lubricant into vacuum. Odd-number layering and near-wall solidification was observed between the solid plates, similar to published experimental findings. The friction simulations have uncovered an interesting behaviour of ILs, with a logarithmic dependence of specific friction on velocity hinting at elasto-hydrodynamic lubrication at low loads. This behaviour

completely changed under more critical conditions of high load, with specific friction decreasing to lower values and becoming independent of sliding velocity. This behaviour was strongly correlated with the internal structure of the IL and can provide guidance for implementing lubrication concepts that can lead to friction reduction in internal combustion engines.

Also, the implemented MD simulation setup has been used in order to study the response of a model ionic liquid to imposed mechanical deformation. The properties of bulk and confined ionic liquid have been investigated under both static and dynamic conditions. First, it has been shown that the Green–Kubo viscosity coefficient fits the shearing simulation results of the bulk salt model ionic liquid, indicating its liquid state. The simulation results have shown the significant impact of the confinement and interaction with the walls on the ionic liquid response to mechanical deformation. The force–distance hysteresis surface under cyclic loading is smaller than one would expect considering only the viscosity value of the liquid. The simulations have also shown the transition from a liquid to a highly dense and ordered, potentially solidified state of the IL taking place under variable normal load and under shear. The wall slip has a profound influence on all the forces which arise as a response to the mechanical deformation. It has also been observed that the interaction of the IL with the walls represents a principal driving force for all processes observed in the dynamic regime for a range of studied velocities. If sufficient time is allowed for the system to reach the equilibrium, inter–ionic interactions pull more ionic liquid inside the confinement gap.

Ionic liquids feature strong long–ranged Coulombic forces and their models require significant computational effort. Coarse grained models, such as the salt model implemented in the current study, are useful for bridging the gap between the molecular processes that control the lubrication phenomena and the macroscopic performance in engineering applications. The implementation of simplified models that describe fundamental physicochemical phenomena at a reduced computational cost can provide deep insights which shed light onto the mechanisms and processes that can render ILs as potentially interesting lubricant candidates.

4.2.2 Tailed models of ionic liquid

Since ionic liquids interact via long–ranged Coulombic forces and their models require high–performance computational resources, there rises a question of the minimal model needed to capture the properties of the molecular processes governing lubrication mechanisms and the macroscopic performance relevant for engineering applications. A generic tailed-model (TM) of ionic liquids which includes: an asymmetric cation consisting of a positively charged head and a neutral tail of variable size and a large spherical negatively charged anion has been investigated. It has been observed that, though simple, this model results in striking differences of the equilibrium IL bulk structure governed by the tail size relative to cationic head:

(i) simple cubic lattice for the small tail,

(ii) liquid-like state for symmetric cation-tail dimer, and

(iii) molecular layer structure for the large tail.

The influence of the molecular structure of cation dimer on the response of the three representative ionic liquids to confinement and mechanical strain has been investigated using MD simulations. Properties of three IL models are compared in and out of equilibrium. The evolution of normal force with inter-plate distance has been related to the changes in the number and structure of the confined IL layers. It has been found that the density inside the gap has a secondary effect on the evolution of the normal force. It has been observed that symmetric molecule offsets intra-IL adhesion due to the ordering of IL. As a result, the thin layer of symmetric IL molecules exhibits non-negative normal force independent of the gap width. In analogy to the experimental observations, a tail–to–tail bilayer is formed for wide gaps in all three investigated model ILs. A mutual feature of all investigated model ILs is the formation of fixed (stable) layers of cations along the solid plates. The fixed layer formation is a result of strong LJ interaction between the plates and ions. A consequence of the fixed layer stability is a steep rise of the normal force at small interplate gaps. The steep rise of the normal force is an effect useful for preventing solid-solid contact and accompanying wear. The tails attached to the cations in the fixed layer migrate with increasing tail size. Small tails form the first layer next to

the plates. For symmetric molecules the tails form a mixed layer with cations, while large tails form a mixed layer with anions.

The dynamic behaviour of IL thin film under cyclic extension–compression movements of the Top plate has been explored. Two intervals of the interplate distances are investigated: narrow gap interval, where the anionic layer is split into two, and a wide gap interval where tail–to–tail layer is formed. For the narrow gap interval, a significant flow of ions during the cyclic motion of the Top plate has been observed. A sharp decrease of the normal force at the final stage of compression is not only a consequence of the density change due to the flow, but it is also a result of merging of two anionic layers that repel each-other by the electrostatic Coulombic forces into a single one. The mobility of ions in and out of the gap is driven by their interaction with plates, i.e., filling of the fixed layers. As a result, for the narrow gap, the number of ions that entered the gap is 50% smaller in the dynamic case than in the static case. This results in a smaller density inside the moving narrow gap. The difference between dynamic and static cases for the wide gap was even more striking, the number of ions that entered the gap is 80% smaller in the dynamic case than in the static case. Surprisingly, in wide gap the density is higher in dynamic case due to the lack of mobility of ions. The invested work per average cycle increases with the tail size increase for all three IL models. As one could expect, the invested work is higher for the narrow gap, where the number of confined ionic layers changes during the cycle. Nevertheless, the low hysteretic losses suggest the presence of strong slip inside the gap facilitating in– and out– flow of ions in the gap. An increase of the tail size reduces friction force in the implemented TM model of ionic liquid. Depending on the tail size, friction force decreases with increasing gap for small tails and it increases for large tails.

Understanding the interplay between the different processes taking place in thin lubricant films is important due to the conflicting demands imposed on how IL lubricant should behave in dynamic confinement. On the one hand, a high load-carrying capability requires strong adsorption of the lubricant to the surface, while on the other hand fast self-healing and low friction require high mobility/low viscosity. The obtained results confirm that the behaviour of ILs in confinement can

be unrelated to their bulk behaviour and therefore it should be possible to achieve simultaneously, typically conflicting, low friction and good anti–wear performance. A search for optimal IL lubricants, either using synthesis and test methods or state-of-the-art computer-based molecular design methods [120], should take into account the microscale properties of lubricating thin films (e.g., normal force vs. number of layers characteristics), in which the effects of molecular-level processes are more pronounced. Directing the optimization efforts to the microscale would enable us a better differentiation of the qualities of different ionic liquids.

Appendix A   Lekner-type summation method for $1D$ periodic dipolar structures

A.1   Total interaction energy in the selected Lekner–type method

Let us consider N particles with $i-$th particle ($i = \overline{1, N}$) having a dipole moment $\overrightarrow{\mu_i}$. Its position is defined as $\overrightarrow{r_i} = (x_i, y_i, z_i)$. Position vector between dipoles i and j is given as $\overrightarrow{r_{ij}} = \overrightarrow{r_i} - \overrightarrow{r_j}$. We use the notation for the projection of the vectors $\overrightarrow{r_{ij}}$ and $\overrightarrow{\mu_i}$ on the xy plane: $\overrightarrow{\rho_{ij}}$ and $\overrightarrow{\mu_i}^\rho$, respectively. Precisely speaking, $\overrightarrow{\rho_{ij}} = (x_{ij}, y_{ij}, 0)$ and $\overrightarrow{\mu_i}^\rho = (\mu_i^x, \mu_i^y, 0)$. Projection of the above mentioned vectors on the z axis is noted as: z_{ij} and μ_i^z.

This is the expression for the potential energy of the DDI between the dipole $\overrightarrow{\mu_i}$ positioned at $\overrightarrow{r_i}$ and the dipole $\overrightarrow{\mu_j}$ positioned at $\overrightarrow{r_j}$:

$$u_{\mathrm{dd}} = C \left[\frac{\overrightarrow{\mu_i} \cdot \overrightarrow{\mu_j}}{r_{ij}^3} - 3 \frac{(\overrightarrow{\mu_i} \cdot \overrightarrow{r_{ij}})(\overrightarrow{\mu_j} \cdot \overrightarrow{r_{ij}})}{r_{ij}^5} \right], \tag{A.1}$$

where C represents a constant which depends on the intervening medium and for simplicity reasons we set $C = 1$ in the following derivations.

Knowing the interaction energy u_{dd} in case of a pair of dipoles i and j ($i, j = \overline{1, N}$) let us form the expression for the total interaction energy of the system whose elementary cell contains N dipoles. We take into account the fact $u_{\mathrm{dd}} \propto r^{-2s}$ which replaces $u_{\mathrm{dd}} \propto r^{-3}$:

$$
\begin{aligned}
E_{\mathrm{dd}} &= \frac{1}{2} \sum_{i,j=1}^{N} \sum_{m'} \left\{ \frac{\overrightarrow{\mu_i} \cdot \overrightarrow{\mu_j}}{\left[\rho_{ij}^2 + (z_{ij} + mL_z)^2 \right]^s} \right. \\
&\left. -3 \frac{[\overrightarrow{\mu_i}^\rho \cdot \overrightarrow{\rho_{ij}} + \mu_i^z (z_{ij} + mL_z)] [\overrightarrow{\mu_j}^\rho \cdot \overrightarrow{\rho_{ij}} + \mu_j^z (z_{ij} + mL_z)]}{\left[\rho_{ij}^2 + (z_{ij} + mL_z)^2 \right]^{s+1}} \right\},
\end{aligned} \tag{A.2}
$$

where the quantity L_z has a physical meaning of length, i.e., it determines the periodicity of a structure along the z-direction. The elementary cell contains N particles and it is positioned in the way that for its each particle i stands $z_i \geq 0$ (i.e., the lower end of the elementary cell is placed at $z = 0$). The $1/2$ factor regulates the fact that we consider the interaction of each i, j pair twice, due to the double sum $\sum_{i,j=1}^{N}$. In each i, j pair the i-th particle belongs to the elementary cell, while the particle j can belong to the elementary cell or to the one of elementary cell's copies along the z axis. Hence, $m = 0$ corresponds to the elementary cell, while $m \neq 0$ counts the copies. This is why we define the distance between two dipoles along the z axis as: $z_{ij} + mL_z$. It is clear that m is an integer which counts how many periods along the z axis is a given copy shifted from the elementary cell. Summation index m is denoted as m' in Equation A.2 to mark the fact that for $m = 0$ the terms with $i = j$ are excluded, since the dipoles do not auto-interact. Let us define the lattice sums $\Psi_r(s)$ and $\Xi_{r,\xi}(s)$ for $\overrightarrow{r} \neq 0$ as:

$$\Psi_r(s) = \frac{1}{L_z^{2s}} \sum_m \left[\left(\frac{\rho}{L_z} \right)^2 + \left(\frac{z}{L_z} + m \right)^2 \right]^{-s}, \tag{A.3}$$

$$\Xi_{r,\xi}(s) = \frac{e^{-i\overrightarrow{\xi_\rho} \cdot \overrightarrow{\rho}}}{L_z^{2s}} \sum_m \left[\left(\frac{\rho}{L_z} \right)^2 + \left(\frac{z}{L_z} + m \right)^2 \right]^{-s} e^{-i\xi_z(z+mL_z)}. \tag{A.4}$$

By comparing Equations A.3 and A.4 we notice that $\Xi_{r,\xi}(s) = e^{-i\overrightarrow{\xi_\rho} \cdot \overrightarrow{\rho}} e^{-i\xi_z(z+mL_z)} \Psi_r(s)$. The terms $e^{-i\overrightarrow{\xi_\rho} \cdot \overrightarrow{\rho}}$ and $e^{-i\xi_z(z+mL_z)}$ are introduced in order to enable the conversion of real-space sums into reciprocal-space sums, in the further steps of derivation. Quantity $\overrightarrow{\xi}$ has the physical meaning of reciprocal length and it can be represented as: $\overrightarrow{\xi} = \left(\overrightarrow{\xi_\rho}, \xi_z \right)$, $\overrightarrow{\xi_\rho} = (\xi_x, \xi_y)$.

Using the lattice sums $\Psi_r(s)$ and $\Xi_{r,\xi}(s)$ we can rewrite Equation A.2 coming up with:

$$
\begin{aligned}
E_{\text{dd}} &= \frac{1}{2} \sum_{i=1}^{N} \sum_{j=1,j\neq i}^{N} \left[\overrightarrow{\mu_i} \cdot \overrightarrow{\mu_j} \Psi_{r_{ij}}(s) + 3 \left(\overrightarrow{\mu_i} \cdot \nabla_\xi \right) \left(\overrightarrow{\mu_j} \cdot \nabla_\xi \right) \Xi_{r_{ij},\xi}(s+1)|_{\xi=0} \right] \\
&\quad + \frac{1}{2} \sum_{i=1}^{N} \left[|\overrightarrow{\mu_i}|^2 - 3 \left(\mu_i^z \right)^2 \right] \Psi_0(s), \tag{A.5}
\end{aligned}
$$

where the condition $\xi = 0$ ensures that the terms intentionally introduced in the definition of the lattice sum $\Xi_{r,\xi}(s)$ in Equation A.4 are $e^{-i\vec{\xi_\rho}\cdot\vec{\rho}} = 1$ and $e^{-i\xi_z(z+mL_z)} = 1$.

A.2   Derivation of the expression for the self energy

From the expression for the total energy of interaction in Equation A.5 we can extract the expression for the self energy:

$$
\begin{aligned}
E_{\text{self}}(s) &= \frac{1}{2}\sum_{i=1}^{N}\left[|\vec{\mu_i}|^2 - 3(\mu_i^z)^2\right]\Psi_0(s), \\
\Rightarrow E_{\text{self}}(s) &= \frac{1}{2}\sum_{i=1}^{N}\left[|\vec{\mu_i}^\rho|^2 - 2(\mu_i^z)^2\right]\Psi_0(s), \quad\quad\quad\text{(A.6)}
\end{aligned}
$$

taking into account that: $|\vec{\mu_i}|^2 = |\vec{\mu_i}^\rho|^2 + (\mu_i^z)^2$.

From Equation A.3 we see that the lattice sum $\Psi_0(s)$ for $\vec{r} = 0$ is:

$$
\Psi_0(s) = \frac{1}{L_z^{2s}}\sum_{m\neq 0}|m|^{-2s} = \frac{1}{L_z^{2s}}\left(\sum_{m=-\infty}^{-1}|m|^{-2s} + \sum_{m=+1}^{+\infty}|m|^{-2s}\right). \quad\text{(A.7)}
$$

A fact that: $\displaystyle\sum_{m=-\infty}^{-1}|m|^{-2s} = \sum_{m=+1}^{+\infty}|m|^{-2s}$, leads to the next form of Equation A.7:

$$
\Psi_0(s) = \frac{2}{L_z^{2s}}\sum_{m=+1}^{+\infty}|m|^{-2s}. \quad\quad\quad\text{(A.8)}
$$

By replacing $\Psi_0(s)$ from Equation A.8 into Equation A.6 and according to the definition of the Riemann zeta function, $\zeta(s) = \displaystyle\sum_{m=+1}^{+\infty}m^{-s}$, we arrive to the general expression for the self energy $E_{\text{self}}(s)$:

$$
E_{\text{self}}(s) = \frac{1}{L_z^{2s}}\sum_{i=1}^{N}\left[|\vec{\mu_i}^\rho|^2 - 2(\mu_i^z)^2\right]\zeta(2s). \quad\quad\quad\text{(A.9)}
$$

By applying $s = 3/2$ we obtain the expression for the self energy in case of the DDI:

$$E_{\text{self}}\left(\frac{3}{2}\right) = \frac{1}{L_z^3} \sum_{i=1}^{N} \left[|\overrightarrow{\mu_i^{\rho}}|^2 - 2(\mu_i^z)^2\right] \zeta(3), \qquad (A.10)$$

where $\zeta(3)$ is a numerical factor with the value of $\zeta(3) = 1.2020569031...$ [76].

A.3 Derivation of the expression for the cross energy

Let us start from the expression for the cross energy from Equation A.5:

$$E_{\text{cross}}(s) = \frac{1}{2} \sum_{i=1}^{N} \sum_{j=1, j\neq i}^{N} \left[\overrightarrow{\mu_i}\overrightarrow{\mu_j}\Psi_{\text{r}_{ij}}(s) + 3(\overrightarrow{\mu_i} \cdot \nabla_\xi)(\overrightarrow{\mu_j} \cdot \nabla_\xi)\Xi_{\text{r}_{ij},\xi}(s+1)|_{\xi=0}\right]. \quad (A.11)$$

There are the two lattice sums in Equation A.11 (i.e., $\Psi_{\text{r}}(s)$, $\Xi_{\text{r},\xi}(s+1)$) which should be determined. We will calculate them following the procedure presented in [89] by using the integral representation of the Gamma function [121]:

$$a^{-s} = \frac{1}{\Gamma(s)} \int_{t=0}^{+\infty} t^{s-1} e^{-at} dt. \qquad (A.12)$$

In Equation A.3 we recognize that we might write down:

$$a = \left(\frac{\rho}{L_z}\right)^2 + \left(\frac{z}{L_z} + m\right)^2. \qquad (A.13)$$

According to this observation we can rewrite Equation A.3 as:

$$\Psi_r(s) = \frac{1}{L_z^{2s}} \sum_m a^{-s}. \qquad (A.14)$$

By replacing a in the right-hand side of Equation A.12 with the expression from Equation A.13 and keeping the left-hand side as a^{-s} we arrive at:

$$a^{-s} = \frac{1}{\Gamma(s)} \int_{t=0}^{+\infty} t^{s-1} e^{-\left[\left(\frac{\rho}{L_z}\right)^2 + \left(\frac{z}{L_z} + m\right)^2\right] t} dt. \qquad (A.15)$$

Now we replace the factor a^{-s} in Equation A.14 with the right-hand side expression from Equation A.15:

$$\Psi_r(s) = \frac{1}{L_z^{2s}\Gamma(s)} \sum_m \int_{t=0}^{+\infty} t^{s-1} e^{-\left[\left(\frac{\rho}{L_z}\right)^2 + \left(\frac{z}{L_z}+m\right)^2\right]t} \mathrm{d}t. \tag{A.16}$$

In the next step we switch the order of the sum and integral and extract the summation over m inside the integral:

$$\Psi_r(s) = \frac{1}{L_z^{2s}\Gamma(s)} \int_{t=0}^{+\infty} t^{s-1} e^{-\left(\frac{\rho}{L_z}\right)^2 t} \sum_m e^{-\left(\frac{z}{L_z}+m\right)^2 t} \mathrm{d}t. \tag{A.17}$$

We use the general form of the Poisson summation formula [122], thus converting from the real-space summation to the reciprocal-space summation:

$$\sum_{m=-\infty}^{+\infty} e^{-\left(\frac{u+c}{L_0}+m\right)^2 t} = \left(\frac{\pi}{t}\right)^{\frac{1}{2}} \sum_{k=-\infty}^{+\infty} e^{i2\pi k \frac{u+c}{L_0}} e^{-\frac{\pi^2 k^2}{t}}. \tag{A.18}$$

Looking at Equation A.17, we decide to write down those identities: $u+c = z$, $L_0 = L_z$. We apply the Poisson summation formula, taking into account the previously mentioned identities, therefore coming up with:

$$\sum_m e^{-\left(\frac{z}{L_z}+m\right)^2 t} = \left(\frac{\pi}{t}\right)^{\frac{1}{2}} \sum_{k=-\infty}^{+\infty} e^{i2\pi k \frac{z}{L_z}} e^{-\frac{\pi^2 k^2}{t}}. \tag{A.19}$$

$$\begin{aligned}
\Rightarrow \Psi_r(s) &= \frac{1}{L_z^{2s}\Gamma(s)} \int_{t=0}^{+\infty} t^{s-1} e^{-\left(\frac{\rho}{L_z}\right)^2 t} \left(\frac{\pi}{t}\right)^{\frac{1}{2}} \\
&\quad \times \left[\sum_{k=-\infty, k\neq 0}^{+\infty} e^{i2\pi k \frac{z}{L_z}} e^{-\frac{\pi^2 k^2}{t}} + 1 \right] \mathrm{d}t.
\end{aligned} \tag{A.20}$$

At this point we switch the order of the sum and integral, hence the integral comes inside the sum over k:

$$\Psi_r(s) = \frac{\pi^{1/2}}{L_z^{2s}\Gamma(s)} \sum_{k=-\infty,k\neq 0}^{+\infty} e^{i2\pi k\frac{z}{L_z}} \int_{t=0}^{+\infty} t^{s-3/2} e^{-\left(\frac{\rho}{L_z}\right)^2 t} e^{-\frac{\pi^2 k^2}{t}} \mathrm{d}t$$

$$+ \frac{\pi^{1/2}}{L_z^{2s}\Gamma(s)} \int_{t=0}^{+\infty} t^{s-3/2} e^{-\left(\frac{\rho}{L_z}\right)^2 t} \mathrm{d}t. \tag{A.21}$$

From Equation A.21 we can extract the integral:

$$I = \int_{t=0}^{+\infty} t^{s-3/2} e^{-\left(\frac{\rho}{L_z}\right)^2 t} e^{-\frac{\pi^2 k^2}{t}} \mathrm{d}t. \tag{A.22}$$

We have solved this integral in Mathematica software package [76]:

$$I = 2^{3/2-s} \left(\frac{L_z}{\rho}\right)^{s-1/2} (2\pi k)^{s-1/2} K_{s-1/2}\left(2\pi k \frac{\rho}{L_z}\right), \tag{A.23}$$

where $K_n(u)$ is the modified Bessel function of the second kind [123].

This expression can be simplified in the following manner:

$$I = 2^{3/2-s} \left(2\pi k \frac{L_z}{\rho}\right)^{s-1/2} K_{s-1/2}\left(2\pi k \frac{\rho}{L_z}\right). \tag{A.24}$$

By replacing the expression for the integral I from Equation A.24 to the sum in the first term in Equation A.21, we obtain:

$$\sum_{k=-\infty,k\neq 0}^{+\infty} e^{i2\pi k\frac{z}{L_z}} \left[2\left(\pi k \frac{L_z}{\rho}\right)^{s-1/2} K_{s-1/2}\left(2\pi k \frac{\rho}{L_z}\right)\right] = \sum_{k=-\infty,k\neq 0}^{+\infty} e^{i2\pi k\frac{z}{L_z}} f(k). \tag{A.25}$$

Applying the identity:

$$\cos\left(2\pi k \frac{z}{L_z}\right) = \frac{e^{i2\pi k\frac{z}{L_z}} + e^{-i2\pi k\frac{z}{L_z}}}{2}, \tag{A.26}$$

we come up with the next expression:

$$\sum_{k=-\infty,k\neq 0}^{+\infty} e^{i2\pi k\frac{z}{L_z}} f(k) = \left(2\sum_{k=1}^{+\infty} \cos\left(2\pi k \frac{z}{L_z}\right) f(k)\right). \tag{A.27}$$

Hence, the first term of Equation A.21 is equal to:

$$\frac{\pi^{1/2}}{L_z^{2s}\Gamma(s)} \times 4 \sum_{k=1}^{+\infty} \cos\left(2\pi k \frac{z}{L_z}\right) \left(\pi k \frac{L_z}{\rho}\right)^{s-1/2} K_{s-1/2}\left(2\pi k \frac{\rho}{L_z}\right).$$

So far we have computed the first term in Equation A.21 for $k \neq 0$ and now we should compute the second term which corresponds to $k = 0$, which means that we should compute the integral:

$$II = \int_{t=0}^{+\infty} t^{s-3/2} e^{-\left(\frac{\rho}{L_z}\right)^2 t} \mathrm{d}t. \tag{A.28}$$

We notice that Equation A.12 which represents the integral representation of the Gamma function can be a good starting point for this. Setting the exponent to $s - 1/2$ instead of s gives us:

$$a^{-(s-1/2)} = \frac{1}{\Gamma(s-1/2)} \int_{t=0}^{+\infty} t^{s-3/2} e^{-at} \mathrm{d}t, \tag{A.29}$$

$$\Rightarrow a^{-(s-1/2)} \Gamma(s-1/2) = \int_{t=0}^{+\infty} t^{s-3/2} e^{-at} \mathrm{d}t. \tag{A.30}$$

By comparing the right-hand side of Equations A.30 and A.28 we conclude that we can say $a = \left(\frac{\rho}{L_z}\right)^2$ which enables the solution of the integral II:

$$II = a^{-(s-1/2)} \Gamma(s-1/2). \tag{A.31}$$

Hence, the second term of Equation A.21 is equal to $\frac{\pi^{1/2}}{L_z^{2s}\Gamma(s)} \left(\frac{\rho}{L_z}\right)^{1-2s} \Gamma\left(s - \frac{1}{2}\right)$.

Finally, the expression for the lattice sum $\Psi_r(s)$ is:

$$\begin{aligned}
\Psi_r(s) &= \frac{4\pi^{1/2}}{L_z^{2s}\Gamma(s)} \sum_{k=1}^{+\infty} \left(\cos\left(2\pi k \frac{z}{L_z}\right) \left(\frac{\pi^2 k^2 L_z^2}{\rho^2}\right)^{s/2-1/4} K_{s-1/2}\left(2\pi k \frac{\rho}{L_z}\right) \right) \\
&\quad + \frac{\pi^{1/2}}{L_z^{2s}\Gamma(s)} \left(\frac{\rho}{L_z}\right)^{1-2s} \Gamma\left(s - \frac{1}{2}\right).
\end{aligned} \tag{A.32}$$

The other unknown lattice sum from Equation A.11 is $\Xi_{\mathrm{r},\xi}(s)$. Let us apply a procedure analogous to the previous derivation of the unknown lattice sum $\Psi_r(s)$.

In the first step, using the integral representation of the Gamma function from Equation A.12 and the definition of the parameter a as in Equation A.13 we obtain:

$$\Xi_{r,\xi}(s) = \frac{e^{-i\vec{\xi_\rho}\cdot\vec{\rho}}}{L_z^{2s}\Gamma(s)} \sum_m e^{-i\xi_z(z+mLz)} \int_{t=0}^{+\infty} t^{s-1}e^{-\left[\left(\frac{\rho}{L_z}\right)^2+\left(\frac{z}{L_z}+m\right)^2\right]t}\mathrm{d}t. \tag{A.33}$$

Now we use the complete Poisson summation formula from Equation A.18 ($\xi_z \neq 0$) which leads to:

$$\Xi_{r,\xi}(s) = \frac{e^{-i\vec{\xi_\rho}\cdot\vec{\rho}}\pi^{1/2}}{L_z^{2s}\Gamma(s)} \int_{t=0}^{+\infty} t^{s-3/2}e^{-\left(\frac{\rho}{L_z}\right)^2 t} \sum_{k=-\infty}^{+\infty} e^{i2\pi k\frac{z}{L_z}}e^{-\frac{(2\pi k+\xi_z L_z)^2}{4t}}\mathrm{d}t. \tag{A.34}$$

By placing the sum in front of the integral (which is the same step like in Equation A.21) we obtain:

$$\Xi_{r,\xi}(s) = \frac{e^{-i\vec{\xi_\rho}\cdot\vec{\rho}}\pi^{1/2}}{L_z^{2s}\Gamma(s)} \sum_{k=-\infty}^{+\infty} e^{i2\pi k\frac{z}{L_z}} \int_{t=0}^{+\infty} t^{s-3/2}e^{-\left(\frac{\rho}{L_z}\right)^2 t}e^{-\frac{(2\pi k+\xi_z L_z)^2}{4t}}\mathrm{d}t. \tag{A.35}$$

In the expression for $\Xi_{r,\xi}(s)$ in Equation A.35 we have encountered the same integral I like in Equation A.22. By replacing its solution from Equation A.23 into Equation A.35 we obtain the final expression for the lattice sum $\Xi_{r,\xi}(s)$:

$$
\begin{aligned}
\Xi_{r,\xi}(s) &= \frac{e^{-i\vec{\xi_\rho}\cdot\vec{\rho}}\pi^{1/2}}{L_z^{2s}\Gamma(s)} \sum_{k=-\infty}^{+\infty} e^{i2\pi k\frac{z}{L_z}}2^{3/2-s}\left(\frac{L_z}{\rho}\right)^{s-1/2} \\
&\quad \times (2\pi k + \xi_z L_z)^{s-1/2} K_{s-1/2}\left(|2\pi k + \xi_z L_z|\frac{\rho}{L_z}\right).
\end{aligned}
\tag{A.36}
$$

Simplification of the previous expression leads to:

$$
\begin{aligned}
\Xi_{r,\xi}(s) &= \frac{2\pi^{1/2}e^{-i\vec{\xi_\rho}\cdot\vec{\rho}}}{L_z^{2s}\Gamma(s)} \sum_{k=-\infty}^{+\infty} e^{i2\pi k\frac{z}{L_z}}\left(\frac{(\xi_z L_z + 2\pi k)^2 L_z^2}{4\rho^2}\right)^{s/2-1/4} \\
&\quad \times K_{s-1/2}\left(|\xi_z L_z + 2\pi k|\frac{\rho}{L_z}\right).
\end{aligned}
\tag{A.37}
$$

Now, as we have derived the general expression for the lattice sum $\Xi_{r,\xi}(s)$, we can proceed to the derivation of the general expression for the cross energy from Equation A.11. The next step is the application of the operator:

$$(\overrightarrow{\mu_i} \cdot \bigtriangledown_\xi)(\overrightarrow{\mu_j} \cdot \bigtriangledown_\xi),$$

where due to the simplicity reasons we introduce the variables: $\eta^z = \frac{2\pi z}{L_z}$ and $\eta^\rho = \frac{2\pi \rho}{L_z}$. We first apply the next scalar product:

$$(\overrightarrow{\mu_j} \cdot \bigtriangledown_\xi) = \left(\mu_j^x \frac{\partial}{\partial \xi_x} + \mu_j^y \frac{\partial}{\partial \xi_y} + \mu_j^z \frac{\partial}{\partial \xi_z} \right). \qquad (A.38)$$

We can introduce the substitution $A = \frac{2\pi^{1/2}}{L_z^{2s}\Gamma(s)}$ and label the part of the function $\Xi_{r,\xi}(s)$ that depends just on ξ_z as $F(\xi_z)$:

$$\Xi_{r,\xi}(s) = Ae^{-i(\xi_x x + \xi_y y)} F(\xi_z), \qquad (A.39)$$

$$
\begin{aligned}
F(\xi_z) \;=\; & \sum_{k=-\infty}^{+\infty} e^{i2\pi k \frac{z}{L_z}} \left(\frac{(\xi_z L_z + 2\pi k)^2 \, L_z^2}{4\rho^2} \right)^{s/2-1/4} \\
& \times K_{s-1/2}\left(|\xi_z L_z + 2\pi k| \, \frac{\rho}{L_z} \right).
\end{aligned}
\qquad (A.40)
$$

Application of the operator $(\overrightarrow{\mu_j} \cdot \bigtriangledown_\xi)$ on $\Xi_{r,\xi}(s)$ gives:

(i)

$$\mu_j^x \frac{\partial}{\partial \xi_x} \Xi_{r,\xi}(s) = \mu_j^x (-ix) A e^{-i(\xi_x x + \xi_y y)} F(\xi_z). \qquad (A.41)$$

(ii)

$$\mu_j^y \frac{\partial}{\partial \xi_y} \Xi_{r,\xi}(s) = \mu_j^y (-iy) A e^{-i(\xi_x x + \xi_y y)} F(\xi_z). \qquad (A.42)$$

(*iii*)

$$
\mu_j^z \frac{\partial}{\partial \xi_z} \Xi_{\mathrm{r},\xi}(s) = \mu_j^z A e^{-i\vec{\xi}_\rho \cdot \vec{\rho}} \sum_{k=-\infty}^{+\infty} e^{ik\eta^z}
$$

$$
\times \left[\left(\frac{L_z}{2\rho} \right)^{(2s-1)/2} \left(\frac{2s-1}{2} \right) (\xi_z L_z + 2\pi k)^{(2s-3)/2} L_z K_{\mathrm{s}-1/2}(\alpha) \right.
$$

$$
\left. + \left(\frac{(\xi_z L_z + 2\pi k) L_z}{2\rho} \right)^{(2s-1)/2} \rho \frac{\partial K_{\mathrm{s}-1/2}(\alpha)}{\partial \alpha} \right]. \tag{A.43}
$$

In the previous equation, due to the simplicity of the further analysis, the argument of the modified Bessel functions $K_{\mathrm{s}-1/2}$ is labeled as α:

$$
|\xi_z L_z + 2\pi k| \frac{\rho}{L_z} = \alpha.
$$

In order to obtain the full expression for $(\vec{\mu_j} \cdot \nabla_\xi) \Xi_{\mathrm{r},\xi}(s)$, let us make a summation of all three components computed in the previous equations. Prior to obtaining the final expression it is convenient to write down the terms that correspond to the x, y components separately from the terms that correspond to the z component:

$$
P_{\mathrm{xy}} = (-i) \left(\mu_j^x x + \mu_j^y y \right) \left(\frac{(\xi_z L_z + 2\pi k) L_z}{2\rho} \right)^{(2s-1)/2} K_{\mathrm{s}-1/2}(\alpha),
$$

$$
P_z = \mu_j^z \left[\left(\frac{L_z}{2\rho} \right)^{(2s-1)/2} \left(\frac{2s-1}{2} \right) (\xi_z L_z + 2\pi k)^{(2s-3)/2} L_z K_{\mathrm{s}-1/2}(\alpha) \right.
$$

$$
\left. + \left(\frac{(\xi_z L_z + 2\pi k) L_z}{2\rho} \right)^{(2s-1)/2} \rho \frac{\partial K_{\mathrm{s}-1/2}(\alpha)}{\partial \alpha} \right].
$$

The application of the scalar product $(\vec{\mu_j} \cdot \nabla_\xi)$ on the lattice sum $\Xi_{\mathrm{r},\xi}(s)$ gives:

$$
(\vec{\mu_j} \cdot \nabla_\xi) \Xi_{\mathrm{r},\xi}(s) = A e^{-i\vec{\xi}_\rho \cdot \vec{\rho}} \sum_{k=-\infty}^{+\infty} e^{ik\eta^z} \left(P_{\mathrm{xy}} + P_z \right). \tag{A.44}
$$

Bearing in mind the practical importance of simplifying the forthcoming computations, let us repeat the definition of α and introduce another two variables, β and

γ:

$$\alpha = |\xi_z L_z + 2\pi k| \frac{\rho}{L_z},$$

$$\beta = (\xi_z L_z + 2\pi k) \frac{L_z}{2\rho},$$

$$\gamma = \xi_z L_z + 2\pi k.$$

The expression in Equation A.44 can be represented as a sum of three independent terms, and each of those terms will be treated separately:

Term C_1

$$C_1 = (-i)\overrightarrow{\mu_j^\rho} \cdot \overrightarrow{\rho} A e^{-i\overrightarrow{\xi_\rho}\cdot\overrightarrow{\rho}} \sum_{k=-\infty}^{+\infty} e^{ik\eta^z} \beta^{(2s-1)/2} K_{s-1/2}(\alpha), \qquad (A.45)$$

Term C_2

$$C_2 = A e^{-i\overrightarrow{\xi_\rho}\cdot\overrightarrow{\rho}} \mu_j^z \sum_{k=-\infty}^{+\infty} e^{ik\eta^z} \left(\frac{L_z}{2\rho}\right)^{(2s-1)/2} \left(\frac{2s-1}{2}\right) \gamma^{(2s-3)/2} L_z K_{s-1/2}(\alpha), \quad (A.46)$$

Term C_3

$$C_3 = A e^{-i\overrightarrow{\xi_\rho}\cdot\overrightarrow{\rho}} \mu_j^z \sum_{k=-\infty}^{+\infty} e^{ik\eta^z} \beta^{(2s-1)/2} \rho \frac{\partial K_{s-1/2}(\alpha)}{\partial \alpha}. \qquad (A.47)$$

The next step is the application of the scalar product

$$\overrightarrow{\mu_i} \cdot \overrightarrow{\nabla_\xi} = \mu_i^x \frac{\partial}{\partial \xi_x} + \mu_i^y \frac{\partial}{\partial \xi_y} + \mu_i^z \frac{\partial}{\partial \xi_z}$$

on Equation A.44, which produces new terms.

In the mentioned scalar product there are three independent operators which act on each of the three terms $\{C_1, C_2, C_3\}$, hence producing nine new terms, numerated as C_{ij}, with $i \in \{1,2,3\}$, $j \in \{1,2,3\}$.

In the next equation we write down the term C_{11}:

Term C_{11}

$$C_{11} = \mu_i^x \frac{\partial}{\partial \xi_x} \left[(-i)\overrightarrow{\mu_j}^\rho \cdot \overrightarrow{\rho} A e^{-i\overrightarrow{\xi_\rho}\cdot\overrightarrow{\rho}} \sum_{k=-\infty}^{+\infty} e^{ik\eta^z} \beta^{(2s-1)/2} K_{s-1/2}(\alpha) \right]. \tag{A.48}$$

Since it stands

$$\frac{\partial}{\partial \xi_x} e^{-i\overrightarrow{\xi_\rho}\cdot\overrightarrow{\rho}} = (-ix)e^{-i\overrightarrow{\xi_\rho}\cdot\overrightarrow{\rho}}, \tag{A.49}$$

the final expression for the term C_{11} becomes

$$C_{11} = -x\mu_i^x \overrightarrow{\mu_j}^\rho \cdot \overrightarrow{\rho} A e^{-i\overrightarrow{\xi_\rho}\cdot\overrightarrow{\rho}} \sum_{k=-\infty}^{+\infty} e^{ik\eta^z} \beta^{(2s-1)/2} K_{s-1/2}(\alpha). \tag{A.50}$$

In the next equation we write down the term C_{21}:

Term C_{21}

$$C_{21} = \mu_i^y \frac{\partial}{\partial \xi_y} \left[(-i)\overrightarrow{\mu_j}^\rho \cdot \overrightarrow{\rho} A e^{-i\overrightarrow{\xi_\rho}\cdot\overrightarrow{\rho}} \sum_{k=-\infty}^{+\infty} e^{ik\eta^z} \beta^{(2s-1)/2} K_{s-1/2}(\alpha) \right]. \tag{A.51}$$

Since it stands

$$\frac{\partial}{\partial \xi_y} e^{-i\overrightarrow{\xi_\rho}\cdot\overrightarrow{\rho}} = (-iy)e^{-i\overrightarrow{\xi_\rho}\cdot\overrightarrow{\rho}}, \tag{A.52}$$

the final expression for the term C_{21} becomes

$$C_{21} = -y\mu_i^y \overrightarrow{\mu_j}^\rho \cdot \overrightarrow{\rho} A e^{-i\overrightarrow{\xi_\rho}\cdot\overrightarrow{\rho}} \sum_{k=-\infty}^{+\infty} e^{ik\eta^z} \beta^{(2s-1)/2} K_{s-1/2}(\alpha). \tag{A.53}$$

In the next equation we write down the term C_{12}:

Term C_{12}

$$\begin{aligned} C_{12} &= \mu_i^x \frac{\partial}{\partial \xi_x} A e^{-i\overrightarrow{\xi_\rho}\cdot\overrightarrow{\rho}} \mu_j^z \sum_{k=-\infty}^{+\infty} e^{ik\eta^z} \left(\frac{L_z}{2\rho}\right)^{(2s-1)/2} \left(\frac{2s-1}{2}\right) \\ &\quad \times \gamma^{(2s-3)/2} L_z K_{s-1/2}(\alpha). \end{aligned} \tag{A.54}$$

Taking into account Equation A.49 the final expression for the term C_{12} becomes:

$$
\begin{aligned}
C_{12} &= -ix\mu_i^x\mu_j^z A e^{-i\vec{\xi_\rho}\cdot\vec{\rho}} \sum_{k=-\infty}^{+\infty} e^{ik\eta^z} \left(\frac{L_z}{2\rho}\right)^{(2s-1)/2} \left(\frac{2s-1}{2}\right) \\
&\quad \times \gamma^{(2s-3)/2} L_z K_{s-1/2}(\alpha).
\end{aligned}
\tag{A.55}
$$

In the next equation we write down the term C_{22}:

Term C_{22}

$$C_{22} = \mu_i^y \frac{\partial}{\partial \xi_y} A e^{-i\vec{\xi_\rho} \cdot \vec{\rho}} \mu_j^z \sum_{k=-\infty}^{+\infty} e^{ik\eta^z} \left(\frac{L_z}{2\rho}\right)^{(2s-1)/2} \left(\frac{2s-1}{2}\right)$$
$$\times \gamma^{(2s-3)/2} L_z K_{s-1/2}(\alpha). \tag{A.56}$$

Taking into account Equation A.52 the final expression for the term C_{22} becomes:

$$C_{22} = -iy\mu_i^y \mu_j^z A e^{-i\vec{\xi_\rho} \cdot \vec{\rho}} \sum_{k=-\infty}^{+\infty} e^{ik\eta^z} \left(\frac{L_z}{2\rho}\right)^{(2s-1)/2} \left(\frac{2s-1}{2}\right)$$
$$\times \gamma^{(2s-3)/2} L_z K_{s-1/2}(\alpha). \tag{A.57}$$

In the next equation we write down the term C_{13}:

Term C_{13}

$$C_{13} = \mu_i^x \frac{\partial}{\partial \xi_x} \left[A e^{-i\vec{\xi_\rho} \cdot \vec{\rho}} \mu_j^z \sum_{k=-\infty}^{+\infty} e^{ik\eta^z} \beta^{(2s-1)/2} \rho \frac{\partial K_{s-1/2}(\alpha)}{\partial \alpha} \right]. \tag{A.58}$$

Taking into account Equation A.49 the final expression for the term C_{13} becomes:

$$C_{13} = -ix\mu_i^x \mu_j^z A e^{-i\vec{\xi_\rho} \cdot \vec{\rho}} \sum_{k=-\infty}^{+\infty} e^{ik\eta^z} \beta^{(2s-1)/2} \rho \frac{\partial K_{s-1/2}(\alpha)}{\partial \alpha}. \tag{A.59}$$

In the next equation we provide the term C_{23}:

Term C_{23}

$$C_{23} = \mu_i^y \frac{\partial}{\partial \xi_y} \left[A e^{-i\vec{\xi_\rho} \cdot \vec{\rho}} \mu_j^z \sum_{k=-\infty}^{+\infty} e^{ik\eta^z} \beta^{(2s-1)/2} \rho \frac{\partial K_{s-1/2}(\alpha)}{\partial \alpha} \right]. \tag{A.60}$$

Taking into account Equation A.52 the final expression for the term C_{23} becomes:

$$C_{23} = -iy\mu_i^y \mu_j^z A e^{-i\vec{\xi_\rho} \cdot \vec{\rho}} \sum_{k=-\infty}^{+\infty} e^{ik\eta^z} \beta^{(2s-1)/2} \rho \frac{\partial K_{s-1/2}(\alpha)}{\partial \alpha}. \tag{A.61}$$

In the next equation we provide the term C_{31}:

Term C_{31}

$$C_{31} = \mu_i^z \frac{\partial}{\partial \xi_z} \left[(-i)\overrightarrow{\mu_j^\rho} \cdot \overrightarrow{\rho} A e^{-i\overrightarrow{\xi_\rho} \cdot \overrightarrow{\rho}} \sum_{k=-\infty}^{+\infty} e^{ik\eta^z} \beta^{(2s-1)/2} K_{s-1/2}(\alpha) \right]. \qquad (A.62)$$

In the term C_{31} we encounter two constituents of the expression depending on ξ_z (i.e., $\beta^{(2s-1)/2}$ and $K_{s-1/2}(\alpha)$) and therefore we obtain two terms inside the square brackets, according to the product rule for derivatives:

$$\begin{aligned}
C_{31} &= (-i)\overrightarrow{\mu_j^\rho} \cdot \overrightarrow{\rho} \mu_i^z A e^{-i\overrightarrow{\xi_\rho} \cdot \overrightarrow{\rho}} \\
&\times \sum_{k=-\infty}^{+\infty} e^{ik\eta^z} \left[\frac{(2s-1)}{2} \beta^{(2s-3)/2} \frac{L_z^2}{2\rho} K_{s-1/2}(\alpha) \right. \\
&\left. + \beta^{(2s-1)/2} \rho \frac{\partial K_{s-1/2}(\alpha)}{\partial \alpha} \right].
\end{aligned} \qquad (A.63)$$

In the next equation we write down the term C_{32}:

Term C_{32}

$$\begin{aligned}
C_{32} &= \mu_i^z \frac{\partial}{\partial \xi_z} A e^{-i\overrightarrow{\xi_\rho} \cdot \overrightarrow{\rho}} \mu_j^z \sum_{k=-\infty}^{+\infty} e^{ik\eta^z} \left(\frac{L_z}{2\rho} \right)^{(2s-1)/2} \left(\frac{2s-1}{2} \right) \\
&\times \gamma^{(2s-3)/2} L_z K_{s-1/2}(\alpha).
\end{aligned} \qquad (A.64)$$

Similarly to the case of term C_{31} we obtain:

$$\begin{aligned}
C_{32} &= \mu_i^z \mu_j^z A e^{-i\overrightarrow{\xi_\rho} \cdot \overrightarrow{\rho}} \left(\frac{L_z}{2\rho} \right)^{(2s-1)/2} Lz \left(\frac{2s-1}{2} \right) \\
&\times \sum_{k=-\infty}^{+\infty} e^{ik\eta^z} \left[\left(\frac{2s-3}{2} \right) \gamma^{(2s-5)/2} L_z K_{s-1/2}(\alpha) \right. \\
&\left. + \gamma^{(2s-3)/2} \rho \frac{\partial K_{s-1/2}(\alpha)}{\partial \alpha} \right].
\end{aligned} \qquad (A.65)$$

In the next equation we write down the term C_{33}:

Term C_{33}

$$C_{33} = \mu_i^z \frac{\partial}{\partial \xi_z} \left[A e^{-i\vec{\xi_\rho} \cdot \vec{\rho}} \mu_j^z \sum_{k=-\infty}^{+\infty} e^{ik\eta^z} \beta^{(2s-1)/2} \rho \frac{\partial K_{s-1/2}(\alpha)}{\partial \alpha} \right]. \tag{A.66}$$

Similarly to the previous two terms we obtain:

$$
\begin{aligned}
C_{33} &= \mu_i^z \mu_j^z A e^{-i\vec{\xi_\rho} \cdot \vec{\rho}} \\
&\times \sum_{k=-\infty}^{+\infty} e^{ik\eta^z} \rho \left[\left(\frac{2s-1}{2} \right) \beta^{(2s-3)/2} \left(\frac{L_z^2}{2\rho} \right) \frac{\partial K_{s-1/2}(\alpha)}{\partial \alpha} \right. \\
&\left. + \beta^{(2s-1)/2} \rho \frac{\partial^2 K_{s-1/2}(\alpha)}{\partial \alpha^2} \right].
\end{aligned} \tag{A.67}
$$

As we have obtained all nine terms $C_{ij}, i, j \in \{1, 2, 3\}$, the next step is grouping them according to the mutual sum over k or mutual constituent terms.

Group 1

This group includes the sum $\sum_{k=-\infty}^{+\infty} e^{ik\eta^z} \beta^{(2s-1)/2} K_{s-1/2}(\alpha)$, hence $GR_1 = C_{11} + C_{21}$,

$$
\begin{aligned}
GR_1 &= -(\vec{\mu_i^\rho} \cdot \vec{\rho})(\vec{\mu_j^\rho} \cdot \vec{\rho}) A e^{-i\vec{\xi_\rho} \cdot \vec{\rho}} \\
&\times \sum_{k=-\infty}^{+\infty} e^{ik\eta^z} \beta^{(2s-1)/2} K_{s-1/2}(\alpha).
\end{aligned} \tag{A.68}
$$

Group 2

This group includes the sum $\sum_{k=-\infty}^{+\infty} e^{ik\eta^z} \left(\frac{L_z}{2\rho} \right)^{(2s-1)/2} \left(\frac{2s-1}{2} \right) \gamma^{(2s-3)/2} L_z K_{s-1/2}(\alpha)$, hence $GR_2 = C_{12} + C_{22}$,

$$
\begin{aligned}
GR_2 &= (-i)(\vec{\mu_i^\rho} \cdot \vec{\rho}) \mu_j^z A e^{-i\vec{\xi_\rho} \cdot \vec{\rho}} \\
&\times \sum_{k=-\infty}^{+\infty} e^{ik\eta^z} \left(\frac{L_z}{2\rho} \right)^{(2s-1)/2} \left(\frac{2s-1}{2} \right) \gamma^{(2s-3)/2} L_z K_{s-1/2}(\alpha).
\end{aligned} \tag{A.69}
$$

Group 3

This group includes the sum $\sum_{k=-\infty}^{+\infty} e^{ik\eta^z} \beta^{(2s-1)/2} \rho \frac{\partial K_{s-1/2}(\alpha)}{\partial \alpha}$, therefore $GR_3 = C_{13} +$

C_{23},

$$
\begin{aligned}
GR_3 &= (-i)\,(\overrightarrow{\mu_i^{\rho}} \cdot \overrightarrow{\rho})\,\mu_j^z A e^{-i\overrightarrow{\xi_\rho}\cdot\overrightarrow{\rho}} \\
&\times \sum_{k=-\infty}^{+\infty} e^{ik\eta^z}\beta^{(2s-1)/2}\rho\frac{\partial K_{\mathrm{s}-1/2}(\alpha)}{\partial\alpha}.
\end{aligned}
\tag{A.70}
$$

Group 4

This group includes the mutual factor $\mu_i^z\mu_j^z$, therefore $GR_4 = C_{32} + C_{33}$,

$$
\begin{aligned}
GR_4 &= \mu_i^z\mu_j^z A e^{-i\overrightarrow{\xi_\rho}\cdot\overrightarrow{\rho}} \\
&\times \sum_{k=-\infty}^{+\infty} e^{ik\eta^z}\left\{\left(\frac{L_z}{2\rho}\right)^{(2s-1)/2}\left(\frac{2s-1}{2}\right)\left(\frac{2s-2}{3}\right)\gamma^{(2s-5)/2}L_z^2 K_{\mathrm{s}-1/2}(\alpha)\right. \\
&+ \left(\frac{L_z}{2\rho}\right)^{(2s-1)/2}\left(\frac{2s-1}{2}\right)\gamma^{(2s-2)/3}L_z\rho\frac{\partial K_{\mathrm{s}-1/2}(\alpha)}{\partial\alpha} \\
&+ \rho\left(\frac{2s-1}{2}\right)\beta^{(2s-3)/2}\left(\frac{L_z^2}{2\rho}\right)\frac{\partial K_{\mathrm{s}-1/2}(\alpha)}{\partial\alpha} \\
&\left.+ \beta^{(2s-1)/2}\rho^2\frac{\partial^2 K_{\mathrm{s}-1/2}(\alpha)}{\partial\alpha^2}\right\}.
\end{aligned}
\tag{A.71}
$$

Group 5

This group includes the factor $(\overrightarrow{\mu_j^{\rho}} \cdot \overrightarrow{\rho})\,\mu_i^z$, hence $GR_5 = C_{31}$,

$$
\begin{aligned}
GR_5 &= (-i)\,(\overrightarrow{\mu_j^{\rho}} \cdot \overrightarrow{\rho})\,\mu_i^z A e^{-i\overrightarrow{\xi_\rho}\cdot\overrightarrow{\rho}} \\
&\times \sum_{k=-\infty}^{+\infty} e^{ik\eta^z}\left[\frac{(2s-1)}{2}\beta^{(2s-3)/2}\left(\frac{L_z^2}{2\rho}\right)K_{\mathrm{s}-1/2}(\alpha)\right. \\
&\left.+ \beta^{(2s-1)/2}\rho\frac{\partial K_{\mathrm{s}-1/2}(\alpha)}{\partial\alpha}\right].
\end{aligned}
\tag{A.72}
$$

At this point let us overview what have we realized up to this step, towards obtaining the expression for the cross energy from Equation A.11. We have derived the expression for $\Psi_r(s)$ and the expressions for $(\overrightarrow{\mu_i} \cdot \bigtriangledown_\xi)(\overrightarrow{\mu_j} \cdot \bigtriangledown_\xi)\Xi_{\mathrm{r},\xi}(s)$, written down as $GR_{\mathrm{i}}, i = \overline{1,5}$, bearing in mind that $(\overrightarrow{\mu_i} \cdot \bigtriangledown_\xi)(\overrightarrow{\mu_j} \cdot \bigtriangledown_\xi)\Xi_{\mathrm{r},\xi}(s) = \sum_{i=1}^{5} GR_{\mathrm{i}}$. By applying $s = 3/2$ in Equation A.11 we obtain the expression for the cross energy in case of the DDI, hence we should compute the terms: $\overrightarrow{\mu_i}\overrightarrow{\mu_j}\Psi_{\mathrm{r_{ij}}}(3/2)$ and $(\overrightarrow{\mu_i} \cdot \bigtriangledown_\xi)(\overrightarrow{\mu_j} \cdot \bigtriangledown_\xi)\Xi_{\mathrm{r_{ij}},\xi}(5/2)|_{\xi=0}$. We proceed the derivations by determining the first term

in Equation A.11, i.e., $\overrightarrow{\mu_i}\overrightarrow{\mu_j}\Psi_{r_{ij}}(3/2)$:

$$
\begin{aligned}
\Psi_r(3/2) \;=\; & \frac{4\sqrt{\pi}}{L_z^3\Gamma(3/2)}\sum_{k=1}^{+\infty}\cos\left(k\eta^z\right)\left(\frac{\pi k L_z}{\rho}\right)K_1\left(k\eta^\rho\right) \\
& +\frac{\sqrt{\pi}}{L_z^3\Gamma(3/2)}\left(\frac{\rho}{L_z}\right)^{-2}\Gamma(1).
\end{aligned}
\tag{A.73}
$$

Taking into account the facts that $\Gamma(3/2) = \frac{\sqrt{\pi}}{2}, \Gamma(1) = 1$ [76],

$$
\Rightarrow \Psi_r(3/2) = \frac{8\pi}{L_z^2\rho}\sum_{k=1}^{+\infty}k\cos\left(k\eta^z\right)K_1\left(k\eta^\rho\right)+\frac{2}{L_z\rho^2}.
\tag{A.74}
$$

We might write the scalar product $\overrightarrow{\mu_i}\cdot\overrightarrow{\mu_j}$ as:

$$
\left(\overrightarrow{\mu_i}^\rho,\mu_i^z\right)\cdot\left(\overrightarrow{\mu_j}^\rho,\mu_j^z\right) = \overrightarrow{\mu_i}^\rho\cdot\overrightarrow{\mu_j}^\rho+\mu_i^z\mu_j^z.
\tag{A.75}
$$

$$
\begin{aligned}
\Rightarrow \overrightarrow{\mu_i}\overrightarrow{\mu_j}\Psi_{r_{ij}}(3/2) \;=\; & \left(\overrightarrow{\mu_i}^\rho\cdot\overrightarrow{\mu_j}^\rho+\mu_i^z\mu_j^z\right)\frac{8\pi}{L_z^2\rho}\sum_{k=1}^{+\infty}k\cos\left(k\eta^z\right)K_1\left(k\eta^\rho\right) \\
& +\left(\overrightarrow{\mu_i}^\rho\cdot\overrightarrow{\mu_j}^\rho+\mu_i^z\mu_j^z\right)\frac{2}{L_z\rho^2}.
\end{aligned}
\tag{A.76}
$$

We have obtained the first term in Equation A.11 and now we proceed the derivations by obtaining the second term, i.e., $3(\overrightarrow{\mu_i}\cdot\bigtriangledown_\xi)(\overrightarrow{\mu_j}\cdot\bigtriangledown_\xi)\Xi_{r_{ij},\xi}(5/2)|_{\xi=0}$. By taking $s = 5/2$ and setting $\xi = 0$ we come up with:

Group 1 $(s = 5/2)|_{\xi=0}$

$$
\begin{aligned}
GR_1\left(s = 5/2\right)|_{\xi=0} \;=\; & -\left(\overrightarrow{\mu_i}^\rho\cdot\overrightarrow{\rho}\right)\left(\overrightarrow{\mu_j}^\rho\cdot\overrightarrow{\rho}\right)\frac{2}{3L_z^3\rho^2} \\
& \times\sum_{k=-\infty}^{+\infty}e^{ik\eta^z}4\pi^2k^2K_2\left(k\eta^\rho\right).
\end{aligned}
\tag{A.77}
$$

Group 2 $(s = 5/2)\,|_{\xi=0}$

$$
\begin{aligned}
GR_2\left(s = 5/2\right)|_{\xi=0} \;=\; & (-i)\,(\overrightarrow{\mu_i^\rho} \cdot \overrightarrow{\rho})\,\mu_j^z\,\frac{2}{3L_z^3\rho^2} \\
& \times \sum_{k=-\infty}^{+\infty} e^{ik\eta^z}\,4\pi k L_z K_2\left(k\eta^\rho\right).
\end{aligned}
\tag{A.78}
$$

Group 3 $(s = 5/2)\,|_{\xi=0}$

$$
\begin{aligned}
GR_3\left(s = 5/2\right)|_{\xi=0} \;=\; & (-i)\,(\overrightarrow{\mu_i^\rho} \cdot \overrightarrow{\rho})\,\mu_j^z\,\frac{2}{3L_z^3\rho^2} \\
& \times \sum_{k=-\infty}^{+\infty} e^{ik\eta^z}\,4\pi^2 k^2 \rho\,\frac{\partial K_2\left(k\eta^\rho\right)}{\partial\left(k\eta^\rho\right)}.
\end{aligned}
\tag{A.79}
$$

Group 4 $(s = 5/2)\,|_{\xi=0}$

$$
\begin{aligned}
GR_4\left(s = 5/2\right)|_{\xi=0} \;=\; & \mu_i^z \mu_j^z\,\frac{2}{3L_z^3\rho^2} \\
& \times \sum_{k=-\infty}^{+\infty} e^{ik\eta^z}\left\{ \frac{1}{2^{-1}} L_z^2 K_2\left(k\eta^\rho\right) \right. \\
& + 4L_z\pi k\rho\,\frac{\partial K_2\left(k\eta^\rho\right)}{\partial\left(k\eta^\rho\right)} \\
& + 4\rho\pi k L_z\,\frac{\partial K_2\left(k\eta^\rho\right)}{\partial\left(k\eta^\rho\right)} \\
& \left. + 4\pi^2 k^2 \rho^2\,\frac{\partial^2 K_2\left(k\eta^\rho\right)}{\partial\left(k\eta^\rho\right)^2} \right\}.
\end{aligned}
\tag{A.80}
$$

Group 5 $(s = 5/2)\,|_{\xi=0}$

$$
\begin{aligned}
GR_5\left(s = 5/2\right)|_{\xi=0} \;=\; & (-i)\,(\overrightarrow{\mu_j^\rho} \cdot \overrightarrow{\rho})\,\mu_i^z\,\frac{2}{3L_z^3\rho^2} \\
& \times \sum_{k=-\infty}^{+\infty} e^{ik\eta^z}\left[\frac{1}{4^{-1}}\pi k L_z K_2\left(k\eta^\rho\right) \right. \\
& \left. + 4\pi^2 k^2 \rho\,\frac{\partial K_2\left(k\eta^\rho\right)}{\partial\left(k\eta^\rho\right)} \right].
\end{aligned}
\tag{A.81}
$$

We notice that in all GR_i terms a modified Bessel function of the second kind with index 2, i.e., $K_2\left(u\right)$ figures, together with its first and second derivative. In order to simplify the above mentioned terms, we express $K_2\left(u\right)$, as well as its derivatives, in

function of $K_0\left(u\right)$ and $K_1\left(u\right)$. Let us remind about the recurrence relations which apply to the modified Bessel function of the second kind [123]:

$$\frac{2\nu}{u}F_\nu\left(u\right) = F_{\nu-1}\left(u\right) - F_{\nu+1}\left(u\right), \tag{A.82}$$

and to its derivative [123]:

$$\frac{\partial F_\nu\left(u\right)}{\partial u} = F_{\nu-1}\left(u\right) - \frac{\nu}{u}F_\nu\left(u\right) = F_{\nu+1}\left(u\right) + \frac{\nu}{u}F_\nu\left(u\right), \tag{A.83}$$

where $F_\nu\left(u\right) = e^{i\pi\nu}K_\nu\left(u\right)$.

Utilizing the above mentioned relations and knowing that $F_0\left(u\right) = K_0\left(u\right), F_1\left(u\right) = -K_1\left(u\right), F_2\left(u\right) = K_2\left(u\right)$ we come up with the expression for $K_2(u)$ in function of $K_0(u)$ and $K_1(u)$:

$$K_2\left(u\right) = K_0\left(u\right) + \frac{2}{u}K_1\left(u\right). \tag{A.84}$$

For its first derivative we get:

$$\frac{\partial K_2\left(u\right)}{\partial u} = -K_1\left(u\right) - \frac{2}{u}K_2\left(u\right), \tag{A.85}$$

where, replacing $K_2(u)$ from Equation A.84, we get:

$$\frac{\partial K_2\left(u\right)}{\partial u} = -\frac{2}{u}K_0(u) - K_1(u) - \frac{4}{u^2}K_1(u). \tag{A.86}$$

The second derivative $\frac{\partial^2 K_2(u)}{\partial u^2}$ is computed straightforward by taking the first derivative of Equation A.86:

$$\begin{aligned}
\frac{\partial^2 K_2\left(u\right)}{\partial u^2} &= -2\left(-\frac{K_0(u)}{u^2} + \frac{1}{u}\frac{\partial K_0\left(u\right)}{\partial u}\right) - \frac{\partial K_1\left(u\right)}{\partial u} \\
&\quad -4\left(-\frac{2}{u^3}K_1(u) + \frac{1}{u^2}\frac{\partial K_1\left(u\right)}{\partial u}\right).
\end{aligned} \tag{A.87}$$

From the recurrence relation given in Equation A.83 we obtain:

$$\frac{\partial K_0\left(u\right)}{\partial u} = -K_1(u), \frac{\partial K_1\left(u\right)}{\partial u} = -K_2(u) + \frac{1}{u}K_1(u), \tag{A.88}$$

which together with Equation A.84 leads to the final expression for the second derivative $\frac{\partial^2 K_2(u)}{\partial u^2}$:

$$\frac{\partial^2 K_2(u)}{\partial u^2} = K_0(u) + \frac{6}{u^2}K_0(u) + \frac{3}{u}K_1(u) + \frac{12}{u^3}K_1(u). \qquad (A.89)$$

Now we replace $K_2(u), \frac{\partial K_2(u)}{\partial u}, \frac{\partial^2 K_2(u)}{\partial u^2}$ (knowing that $u = k\eta^\rho$) in Equations A.77 to A.81, coming up with:

Group 1 $(s = 5/2)|_{\xi=0}$

$$GR_1\left(s = 5/2\right)|_{\xi=0} = -\left(\overrightarrow{\mu_i}^\rho \cdot \overrightarrow{\rho}\right)\left(\overrightarrow{\mu_j}^\rho \cdot \overrightarrow{\rho}\right)\frac{2}{3L_z^3\rho^2}$$
$$\times \sum_{k=-\infty}^{+\infty} e^{ik\eta^z}4\pi^2 k^2\left(K_0\left(k\eta^\rho\right) + \frac{2}{k\eta^\rho}K_1\left(k\eta^\rho\right)\right), (A.90)$$

$$\Rightarrow GR_1\left(s = 5/2\right)|_{\xi=0} = -\left(\overrightarrow{\mu_i}^\rho \cdot \overrightarrow{\rho}\right)\left(\overrightarrow{\mu_j}^\rho \cdot \overrightarrow{\rho}\right)\left[\frac{8\pi^2}{3L_z^3\rho^2} \times \sum_{k=-\infty}^{+\infty} k^2 e^{ik\eta^z}K_0\left(k\eta^\rho\right)\right.$$
$$\left. + \frac{8\pi}{3L_z^2\rho^3} \times \sum_{k=-\infty}^{+\infty} k e^{ik\eta^z}K_1\left(k\eta^\rho\right)\right]. \qquad (A.91)$$

Group 2 $(s = 5/2)|_{\xi=0}$

$$GR_2\left(s = 5/2\right)|_{\xi=0} = (-i)\left(\overrightarrow{\mu_i}^\rho \cdot \overrightarrow{\rho}\right)\mu_j^z\frac{2}{3L_z^3\rho^2}$$
$$\times \sum_{k=-\infty}^{+\infty} e^{ik\eta^z}4\pi kL_z\left(K_0\left(k\eta^\rho\right) + \frac{2}{k\eta^\rho}K_1\left(k\eta^\rho\right)\right), (A.92)$$

$$\Rightarrow GR_2\left(s = 5/2\right)|_{\xi=0} = (-i)\left(\overrightarrow{\mu_i}^\rho \cdot \overrightarrow{\rho}\right)\mu_j^z\left[\frac{8\pi}{3L_z^2\rho^2} \times \sum_{k=-\infty}^{+\infty} k e^{ik\eta^z}K_0\left(k\eta^\rho\right)\right.$$
$$\left. + \frac{8}{3L_z\rho^3} \times \sum_{k=-\infty}^{+\infty} e^{ik\eta^z}K_1\left(k\eta^\rho\right)\right]. \qquad (A.93)$$

Group 3 $(s = 5/2, \xi = 0)$

$$GR_3 \left(s = 5/2\right)|_{\xi=0} = (-i) \left(\overrightarrow{\mu_i^\rho} \cdot \overrightarrow{\rho}\right) \mu_j^z \frac{2}{3L_z^3 \rho^2} \times \sum_{k=-\infty}^{+\infty} e^{ik\eta^z} 4\pi^2 k^2$$

$$\left(-\frac{2}{k\eta^\rho} K_0 \left(k\eta^\rho\right) - K_1 \left(k\eta^\rho\right) - \frac{4}{(k\eta^\rho)^2} K_1 \left(k\eta^\rho\right)\right) \text{(A.94)}$$

$$\Rightarrow GR_3 \left(s = 5/2\right)|_{\xi=0} = (-i) \left(\overrightarrow{\mu_i^\rho} \cdot \overrightarrow{\rho}\right) \mu_j^z \left[-\frac{8\pi}{3L_z^2 \rho^2} \times \sum_{k=-\infty}^{+\infty} k e^{ik\eta^z} K_0 \left(k\eta^\rho\right)\right.$$

$$-\frac{8\pi^2}{3L_z^3 \rho} \times \sum_{k=-\infty}^{+\infty} k^2 e^{ik\eta^z} K_1 \left(k\eta^\rho\right)$$

$$\left.-\frac{8}{3L_z \rho^3} \times \sum_{k=-\infty}^{+\infty} e^{ik\eta^z} K_1 \left(k\eta^\rho\right)\right]. \tag{A.95}$$

Group 4 $(s = 5/2)|_{\xi=0}$

$$GR_4 \left(s = 5/2\right)|_{\xi=0} = \mu_i^z \mu_j^z \frac{2}{3L_z^3 \rho^2} \times \sum_{k=-\infty}^{+\infty} e^{ik\eta^z}$$

$$\times \left[2L_z^2 T_1 + 4L_z \pi k \rho T_2 + 4\rho \pi k L_z T_3 + 4\pi^2 k^2 \rho^2 T_4\right] \text{(A.96)}$$

where the terms T_1, T_2, T_3, T_4 are defined as:

$$T_1 = K_0 \left(k\eta^\rho\right) + \frac{2}{k\eta^\rho} K_1 \left(k\eta^\rho\right), \tag{A.97}$$

$$T_2 = -\frac{2}{k\eta^\rho} K_0 \left(k\eta^\rho\right) - K_1 \left(k\eta^\rho\right) - \frac{4}{(k\eta^\rho)^2} K_1 \left(k\eta^\rho\right), \tag{A.98}$$

$$T_3 = -\frac{2}{k\eta^\rho} K_0 \left(k\eta^\rho\right) - K_1 \left(k\eta^\rho\right) - \frac{4}{(k\eta^\rho)^2} K_1 \left(k\eta^\rho\right), \tag{A.99}$$

$$T_4 = K_0 \left(k\eta^\rho\right) + \frac{6}{(k\eta^\rho)^2} K_0 \left(k\eta^\rho\right) + \frac{3}{k\eta^\rho} K_1 \left(k\eta^\rho\right) + \frac{12}{(k\eta^\rho)^3} K_1 \left(k\eta^\rho\right), \tag{A.100}$$

respectively.

$$\Rightarrow GR_4 \left(s = 5/2 \right)|_{\xi=0} = \mu_i^z \mu_j^z \left[-\frac{4\pi}{3L_z^2 \rho} \times \sum_{k=-\infty}^{+\infty} k e^{ik\eta^z} K_1 \left(k\eta^\rho \right) \right.$$
$$\left. + \frac{8\pi^2}{3L_z^3} \times \sum_{k=-\infty}^{+\infty} k^2 e^{ik\eta^z} K_0 \left(k\eta^\rho \right) \right]. \qquad (A.101)$$

Group 5 $\left(s = 5/2 \right)|_{\xi=0}$

$$GR_5 \left(s = 5/2 \right)|_{\xi=0} = \left(-i \right) \left(\overrightarrow{\mu_j^\rho} \cdot \overrightarrow{\rho} \right) \mu_i^z \frac{2}{3L_z^3 \rho^2}$$
$$\times \sum_{k=-\infty}^{+\infty} e^{ik\eta^z} \left[4\pi k L_z R_1 + 4\pi^2 k^2 \rho R_2 \right], \qquad (A.102)$$

where the terms R_1, R_2 are defined as:

$$R_1 = K_0 \left(k\eta^\rho \right) + \frac{2}{k\eta^\rho} K_1 \left(k\eta^\rho \right), \qquad (A.103)$$

$$R_2 = -\frac{2}{k\eta^\rho} K_0 \left(k\eta^\rho \right) - K_1 \left(k\eta^\rho \right) - \frac{4}{\left(k\eta^\rho \right)^2} K_1 \left(k\eta^\rho \right), \qquad (A.104)$$

respectively.

$$\Rightarrow GR_5 \left(s = 5/2 \right)|_{\xi=0} = \left(-i \right) \left(\overrightarrow{\mu_j^\rho} \cdot \overrightarrow{\rho} \right) \mu_i^z \left[-\frac{8\pi^2}{3L_z^3 \rho} \sum_{k=-\infty}^{+\infty} k^2 e^{ik\eta^z} K_1 \left(k\eta^\rho \right) \right]. \quad (A.105)$$

We can furthermore simplify the Equations A.90 to A.105 applying the relations:

$$e^{ik\eta^z} + e^{-ik\eta^z} = 2\cos \left(k\eta^z \right), e^{ik\eta^z} - e^{-ik\eta^z} = 2i \sin \left(k\eta^z \right), \qquad (A.106)$$

that allow us to switch from the $\sum_{k=-\infty}^{+\infty}$ summation to the $\sum_{k=1}^{+\infty}$ summation, where the case $k = 0$ should be considered separately. Accordingly, let us resolve the $k = 0$ case first:

$$\left(\overrightarrow{\mu_i} \cdot \nabla_\xi \right) \left(\overrightarrow{\mu_j} \cdot \nabla_\xi \right) \Xi_{r_{ij},\xi}(5/2)|_{\xi=0,k=0} = \sum_{i=1}^{5} GR_i \left(s = 5/2|_{\xi=0,k=0} \right). \qquad (A.107)$$

Based on the next relations [123]:

$$u^2 K_1(u) \to 0, \, u^2 K_0(u) \to 0, \, u K_1(u) \to 1, \qquad \text{(A.108)}$$

which are valid when $k \to 0$, setting that $u = k\eta^\rho$ we obtain that:

$$
\begin{aligned}
\sum_{i=1}^{5} GR_{\mathrm{i}}\left(s=5/2\right)|_{\xi=0,k=0} \; = \; & -\frac{8\pi}{3L_z^2\rho^3}\frac{L_z}{2\pi\rho}\left(\overrightarrow{\mu_i^\rho}\cdot\overrightarrow{\rho}\right)\left(\overrightarrow{\mu_j^\rho}\cdot\overrightarrow{\rho}\right) \\
& -\frac{4\pi}{3L_z^2\rho}\frac{L_z}{2\pi\rho}\mu_i^z\mu_j^z,
\end{aligned}
\qquad \text{(A.109)}
$$

$$\Rightarrow \sum_{i=1}^{5} GR_{\mathrm{i}}\left(s=5/2\right)|_{\xi=0,k=0} = -\frac{4}{3L_z\rho^4}\left(\overrightarrow{\mu_i^\rho}\cdot\overrightarrow{\rho}\right)\left(\overrightarrow{\mu_j^\rho}\cdot\overrightarrow{\rho}\right) - \frac{2}{3L_z\rho^2}\mu_i^z\mu_j^z. \quad \text{(A.110)}$$

Now we resolve the $k \neq 0$ case:

$$(\overrightarrow{\mu_i}\cdot\nabla_\xi)(\overrightarrow{\mu_j}\cdot\nabla_\xi)\Xi_{\mathrm{r_{ij}},\xi}(5/2)|_{\xi=0,k\neq0} = \sum_{i=1}^{5} GR_{\mathrm{i}}\left(s=5/2\right)|_{\xi=0,k\neq0}. \qquad \text{(A.111)}$$

Let us modify the expressions for $GR_{\mathrm{i}}\left(s=5/2\right)|_{\xi=0}$ following the Equation A.106:

Group 1 $\left(s=5/2\right)|_{\xi=0,k\neq0}$

$$
\begin{aligned}
GR_1\left(s=5/2\right)|_{\xi=0,k\neq0} \; = \; & -\left(\overrightarrow{\mu_i^\rho}\cdot\overrightarrow{\rho}\right)\left(\overrightarrow{\mu_j^\rho}\cdot\overrightarrow{\rho}\right)\left[\frac{16\pi^2}{3L_z^3\rho^2}\times\sum_{k=1}^{+\infty}k^2\cos\left(k\eta^z\right)K_0\left(k\eta^\rho\right)\right. \\
& \left. +\frac{16\pi}{3L_z^2\rho^3}\times\sum_{k=1}^{+\infty}k\cos\left(k\eta^z\right)K_1\left(k\eta^\rho\right)\right].
\end{aligned}
\qquad \text{(A.112)}
$$

Group 2 $\left(s=5/2\right)|_{\xi=0,k\neq0}$

$$
\begin{aligned}
GR_2\left(s=5/2\right)|_{\xi=0,k\neq0} \; = \; & \left(\overrightarrow{\mu_i^\rho}\cdot\overrightarrow{\rho}\right)\mu_j^z\left[\frac{16\pi}{3L_z^2\rho^2}\times\sum_{k=1}^{+\infty}k\sin\left(k\eta^z\right)K_0\left(k\eta^\rho\right)\right. \\
& \left. +\frac{16}{3L_z\rho^3}\times\sum_{k=1}^{+\infty}\sin\left(k\eta^z\right)K_1\left(k\eta^\rho\right)\right].
\end{aligned}
\qquad \text{(A.113)}
$$

Group 3 $(s = 5/2)|_{\xi=0, k\neq 0}$

$$
\begin{aligned}
GR_3\left(s=5/2\right)|_{\xi=0,k\neq 0} \;=\; & \left(\overrightarrow{\mu_i^\rho} \cdot \overrightarrow{\rho}\right)\mu_j^z\left[-\frac{16\pi}{3L_z^2\rho^2}\times\sum_{k=1}^{+\infty}k\sin\left(k\eta^z\right)K_0\left(k\eta^\rho\right)\right. \\
& -\frac{16\pi^2}{3L_z^3\rho}\times\sum_{k=1}^{+\infty}k^2\sin\left(k\eta^z\right)K_1\left(k\eta^\rho\right) \\
& \left.-\frac{16}{3L_z\rho^3}\times\sum_{k=1}^{+\infty}\sin\left(k\eta^z\right)K_1\left(k\eta^\rho\right)\right].
\end{aligned}
\tag{A.114}
$$

Group 4 $(s = 5/2)|_{\xi=0, k\neq 0}$

$$
\begin{aligned}
GR_4\left(s=5/2\right)|_{\xi=0,k\neq 0} \;=\; & \mu_i^z\mu_j^z\left[-\frac{8\pi}{3L_z^2\rho}\times\sum_{k=1}^{+\infty}k\cos\left(k\eta^z\right)K_1\left(k\eta^\rho\right)\right. \\
& \left.+\frac{16\pi^2}{3L_z^3}\times\sum_{k=1}^{+\infty}k^2\cos\left(k\eta^z\right)K_0\left(k\eta^\rho\right)\right].
\end{aligned}
\tag{A.115}
$$

Group 5 $(s = 5/2)|_{\xi=0, k\neq 0}$

$$
GR_5\left(s=5/2\right)|_{\xi=0,k\neq 0}=\left(\overrightarrow{\mu_j^\rho}\cdot\overrightarrow{\rho}\right)\mu_i^z\left[-\frac{16\pi^2}{3L_z^3\rho}\sum_{k=1}^{+\infty}k^2\sin\left(k\eta^z\right)K_1\left(k\eta^\rho\right)\right].
\tag{A.116}
$$

We can now compute the summation from Equation A.111:

$$
\begin{aligned}
\sum_{i=1}^{5}GR_i\left(s=5/2\right)|_{\xi=0,k\neq 0} \;=\; & -\frac{8\pi}{3L_z^2}\left[\frac{2\left(\overrightarrow{\mu_i^\rho}\cdot\overrightarrow{\rho_{ij}}\right)\left(\overrightarrow{\mu_j^\rho}\cdot\overrightarrow{\rho_{ij}}\right)}{\rho_{ij}^3}+\frac{\mu_i^z\mu_j^z}{\rho_{ij}}\right] \\
& \times\sum_{k=1}^{+\infty}k\cos\left(k\eta_{ij}^z\right)K_1\left(k\eta_{ij}^\rho\right) \\
& -\frac{16\pi^2}{3L_z^3}\left[\frac{\left(\overrightarrow{\mu_i^\rho}\cdot\overrightarrow{\rho_{ij}}\right)\mu_j^z+\left(\overrightarrow{\mu_j^\rho}\cdot\overrightarrow{\rho_{ij}}\right)\mu_i^z}{\rho_{ij}}\right] \\
& \times\sum_{k=1}^{+\infty}k^2\sin\left(k\eta_{ij}^z\right)K_1\left(k\eta_{ij}^\rho\right) \\
& -\frac{16\pi^2}{3L_z^3}\left[\frac{\left(\overrightarrow{\mu_i^\rho}\cdot\overrightarrow{\rho_{ij}}\right)\left(\overrightarrow{\mu_j^\rho}\cdot\overrightarrow{\rho_{ij}}\right)}{\rho_{ij}^2}-\mu_i^z\mu_j^z\right] \\
& \times\sum_{k=1}^{+\infty}k^2\cos\left(k\eta_{ij}^z\right)K_0\left(k\eta_{ij}^\rho\right).
\end{aligned}
\tag{A.117}
$$

Adding up the result from Equation A.110 for $k = 0$ to the result from Equa-

tion A.117 for $k \neq 0$ we obtain:

$$
\begin{aligned}
(\overrightarrow{\mu_i} \cdot \bigtriangledown_\xi)(\overrightarrow{\mu_j} \cdot \bigtriangledown_\xi) \Xi_{r_{ij},\xi}(5/2)|_{\xi=0} &= -\frac{8\pi}{3L_z^2} \left[\frac{2\left(\overrightarrow{\mu_i}^\rho \cdot \overrightarrow{\rho_{ij}}\right)\left(\overrightarrow{\mu_j}^\rho \cdot \overrightarrow{\rho_{ij}}\right)}{\rho_{ij}^3} + \frac{\mu_i^z \mu_j^z}{\rho_{ij}} \right] \\
&\quad \times \sum_{k=1}^{+\infty} k \cos\left(k\eta_{ij}^z\right) K_1\left(k\eta_{ij}^\rho\right) \\
&\quad -\frac{16\pi^2}{3L_z^3} \left[\frac{\left(\overrightarrow{\mu_i}^\rho \cdot \overrightarrow{\rho_{ij}}\right)\mu_j^z + \left(\overrightarrow{\mu_j}^\rho \cdot \overrightarrow{\rho_{ij}}\right)\mu_i^z}{\rho_{ij}} \right] \\
&\quad \times \sum_{k=1}^{+\infty} k^2 \sin\left(k\eta_{ij}^z\right) K_1\left(k\eta_{ij}^\rho\right) \\
&\quad -\frac{16\pi^2}{3L_z^3} \left[\frac{\left(\overrightarrow{\mu_i}^\rho \cdot \overrightarrow{\rho_{ij}}\right)\left(\overrightarrow{\mu_j}^\rho \cdot \overrightarrow{\rho_{ij}}\right)}{\rho_{ij}^2} - \mu_i^z \mu_j^z \right] \\
&\quad \times \sum_{k=1}^{+\infty} k^2 \cos\left(k\eta_{ij}^z\right) K_0\left(k\eta_{ij}^\rho\right) - \frac{2}{3L_z} \\
&\quad \times \left[\frac{2\left(\overrightarrow{\mu_i}^\rho \cdot \overrightarrow{\rho_{ij}}\right)\left(\overrightarrow{\mu_j}^\rho \cdot \overrightarrow{\rho_{ij}}\right)}{\rho_{ij}^4} + \frac{\mu_i^z \mu_j^z}{\rho_{ij}^2} \right]. \text{(A.118)}
\end{aligned}
$$

At this point, let us rewrite the expression defining the cross energy:

$$
E_{\text{cross}} = \frac{1}{2} \sum_{i=1}^{N} \sum_{j=1,j\neq i}^{N} \left[\overrightarrow{\mu_i}\,\overrightarrow{\mu_j}\, \Psi_{r_{ij}}(3/2) + 3(\overrightarrow{\mu_i} \cdot \bigtriangledown_\xi)(\overrightarrow{\mu_j} \cdot \bigtriangledown_\xi)\Xi_{r_{ij},\xi}(5/2)|_{\xi=0} \right]. \quad \text{(A.119)}
$$

From Equation A.76 we take the term $\overrightarrow{\mu_i}\,\overrightarrow{\mu_j}\,\Psi_{r_{ij}}(3/2)$ and from Equation A.118 we take the term $(\overrightarrow{\mu_i} \cdot \bigtriangledown_\xi)(\overrightarrow{\mu_j} \cdot \bigtriangledown_\xi)\Xi_{r_{ij},\xi}(5/2)|_{\xi=0}$ and multiply it by 3, which leads to

the final form of the cross energy:

$$
\begin{aligned}
E_{\text{cross}} \;=\; & \frac{1}{2}\sum_{i=1}^{N}\sum_{j=1,j\neq i}^{N}\Bigg\{ -\frac{8\pi}{L_z^2}\left[\frac{2\,(\overrightarrow{\mu_i^\rho}\cdot\overrightarrow{\rho_{ij}})\,(\overrightarrow{\mu_j^\rho}\cdot\overrightarrow{\rho_{ij}})}{\rho_{ij}^3}-\frac{(\overrightarrow{\mu_i^\rho}\cdot\overrightarrow{\mu_j^\rho})}{\rho_{ij}}\right] \\
& \times\sum_{k=1}^{+\infty} k\cos\left(k\eta_{ij}^z\right)K_1\left(k\eta_{ij}^\rho\right) \\
& -\frac{16\pi^2}{L_z^3}\left[\frac{(\overrightarrow{\mu_i^\rho}\cdot\overrightarrow{\rho_{ij}})\,\mu_j^z+(\overrightarrow{\mu_j^\rho}\cdot\overrightarrow{\rho_{ij}})\,\mu_i^z}{\rho_{ij}}\right] \\
& \times\sum_{k=1}^{+\infty} k^2\sin\left(k\eta_{ij}^z\right)K_1\left(k\eta_{ij}^\rho\right) \\
& -\frac{16\pi^2}{L_z^3}\left[\frac{(\overrightarrow{\mu_i^\rho}\cdot\overrightarrow{\rho_{ij}})\,(\overrightarrow{\mu_j^\rho}\cdot\overrightarrow{\rho_{ij}})}{\rho_{ij}^2}-\mu_i^z\mu_j^z\right] \\
& \times\sum_{k=1}^{+\infty} k^2\cos\left(k\eta_{ij}^z\right)K_0\left(k\eta_{ij}^\rho\right) \\
& -\frac{2}{L_z}\left[\frac{2\,(\overrightarrow{\mu_i^\rho}\cdot\overrightarrow{\rho_{ij}})\,(\overrightarrow{\mu_j^\rho}\cdot\overrightarrow{\rho_{ij}})}{\rho_{ij}^4}-\frac{(\overrightarrow{\mu_i^\rho}\cdot\overrightarrow{\mu_j^\rho})}{\rho_{ij}^2}\right]\Bigg\}. \qquad (A.120)
\end{aligned}
$$

We should note that the expressions for $\Psi_r(s)$, $\Xi_{r,\xi}(s)$ and consequently for E_{cross} are undefined in case $\overrightarrow{\rho}=0$. Hence, the previously written expressions are valid under the condition $\overrightarrow{\rho}\neq 0$. For the special case $\overrightarrow{\rho}=0$, i.e., when two dipoles have the same x and y coordinate (the position vector connecting them is parallel to the z axis), the next equation for $\Psi_r(s=3/2)$ applies [89]:

$$
\Psi_r(3/2)|_{\overrightarrow{\rho}=0}=-\frac{1}{L_z^3}\left[\Psi''\left(\frac{|z|}{L_z}\right)+\pi^3\cos\left(\frac{\pi|z|}{L_z}\right)\sin^{-3}\left(\frac{\pi|z|}{L_z}\right)\right], \qquad (A.121)
$$

where Ψ'' is the tetra-gamma function [123]. Using Equations A.118 and A.121 we obtain the cross energy in case $\overrightarrow{\rho_{ij}}=0$ as:

$$
E_{\text{cross}}|_{\overrightarrow{\rho_{ij}}=0}=\frac{1}{2}\sum_{i=1}^{N}\sum_{j=1,j\neq i}^{N}\left\{T_p\left[\Psi''\left(\frac{|z_{ij}|}{L_z}\right)+\pi^3\cos\left(\frac{\pi|z_{ij}|}{L_z}\right)\sin^{-3}\left(\frac{\pi|z_{ij}|}{L_z}\right)\right]\right\}, \tag{A.122}
$$

where the term T_p is defined as:

$$
T_p=-\frac{(\overrightarrow{\mu_i^\rho}\cdot\overrightarrow{\mu_j^\rho})-2\mu_i^z\mu_j^z}{L_z^3}. \qquad (A.123)
$$

Appendix B   Conjugate gradient method

The conjugate gradient (CG) method represents a general method for minimizing function $f(\vec{x})$, where f can be any function of argument $\vec{x}$ in N-dimensional space [124]. In our case, we want to minimize the potential energy of atoms in the system, hence $f = V$, where the independent variable $\vec{x}$ are the positions of our atoms $\vec{r_i}, i = 1, ..., N$. The parameter space over which the minimization is realized is $3N$-dimensional, since it stands that:

$$\vec{r} = \left(r_{1x}, r_{1y}, r_{1z}, r_{2x}, r_{2y}, r_{2z}, r_{3x}, r_{3y}, r_{3z}, ..., r_{Nx}, r_{Ny}, r_{Nz} \right). \tag{B.1}$$

We can state that we are interested in minimization of the function $V(\vec{r})$. In the CG method, the gradient of the function, which is in our case the force, since it stands $\vec{F} = -\nabla V$, is used for finding the minimum of the function. The gradient determines in which direction the function changes the most rapidly. Bearing this in mind, we can come up with a natural, but not very efficient way to minimize the energy, which is to always move in the direction of the negative gradient, since negative gradient means lowering the function value. This method is known as *steepest descent method* and for MD systems its algorithm can be defined as [125]:

Step(0): start from the point $\vec{r}_0$ setting up $j = 0$

Step(1): calculate $V_j(\vec{r_j})$ and $\vec{F_j} = -\nabla V_j(\vec{r_j})$

Step(2): if $V_{j-1} - V_j < \epsilon$ (where ϵ is the chosen convergence tolerance, usually at the order of 10^{-6}) then end the algorithm

Step(3): minimize $V\left(\vec{r_j} + \alpha \vec{F_j} \right)$ by varying the scalar quantity α

Step(4): update $\vec{r}_{j+1} = \vec{r_j} + \alpha \vec{F_j}; j = j + 1$

Step(5): return to the step (1)

The line minimization in step (3) is a one dimensional operation in which the min-

imum of a function is looked for by moving in a defined direction $\alpha \vec{F}_j$. Let us now explain how does the line minimization work. The line minimization is a straightforward operation which is carried out in two steps [124]:

(i) confirm that there is a minimum and bracket it

(ii) search for that minimum with a given accuracy

Step (i) is easy to conduct: starting from a point $\vec{r}$ and known direction $\vec{F}$, we move forward along some direction $\beta \vec{F}$. If the following conditions are met (for the illustration check Figure B.1):

$$V\left(\vec{r}+\frac{\beta \vec{F}}{2}\right) < V\left(\vec{r}\right), V\left(\vec{r}+\frac{\beta \vec{F}}{2}\right) < V\left(\vec{r}+\beta \vec{F}\right), V\left(\vec{r}\right) < V\left(\vec{r}+\beta \vec{F}\right) \quad \text{(B.2)}$$

then the minimum is bracketed with these three points:

$$\left\{ V\left(\vec{r}\right), V\left(\vec{r}+\frac{\beta \vec{F}}{2}\right), V\left(\vec{r}+\beta \vec{F}\right) \right\}. \quad \text{(B.3)}$$

In case the above mentioned conditions are not met, we increase β and try again until we meet the conditions.

As the step (i) of bracketing the minimum is completed, we move on to the step (ii) of searching for that minimum within the given accuracy. One way of doing this is applying bisection. However, it turns out that it is better to apply golden section rule, which means that the new guess for the minimum is distant from either ends $\left(\frac{1+\sqrt{5}}{2}-1\right) \cdot 100\% = 61.803\%$ of the distance between the ends, i.e., points (1) and (2) from Figure B.1 are the ends in the first iteration of the procedure. Later on, the bracketing narrows around the minimum with the goal of converging to it. The golden section rule tells us how should we narrow down the bracketing interval, i.e., the distance between the ends. Besides the line minimization which includes bracketing and golden section rule search for the minimum, there is another method which is called *inverse parabolic interpolation*. The name comes from the fact that a parabola is fitted through the points $\{a, b, c\}$ which correspond to the points (1), (2), (3) from Figure B.1. Our guess for the minimum of the curve we are looking for,
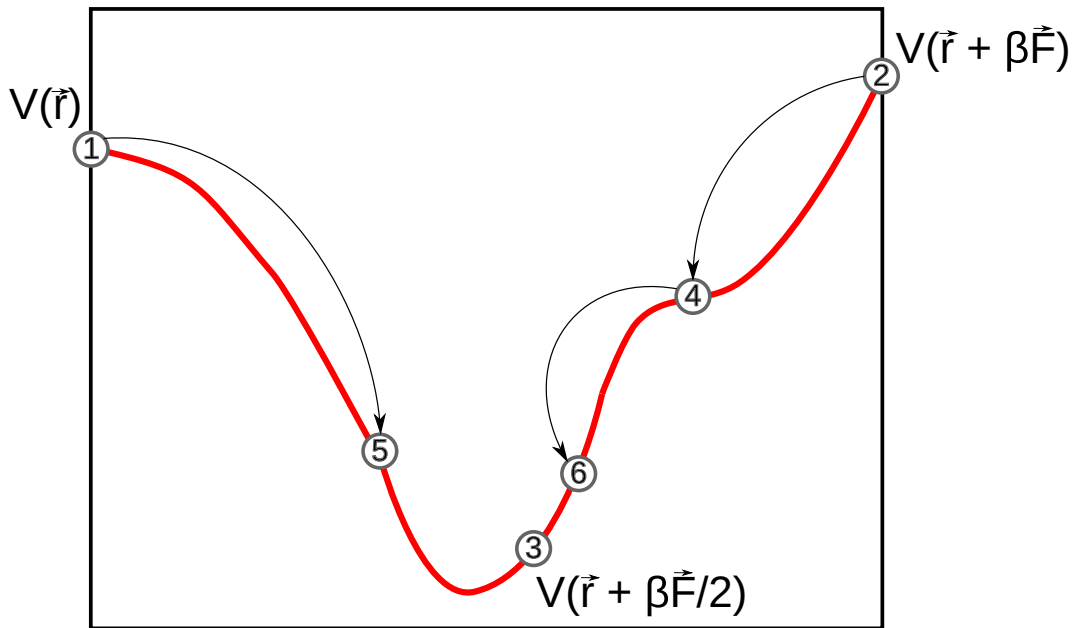
Figure B.1: Bracketing a minimum, points (1), (2) and (3) are the initial bracketing points, jumps to the points (4), (5) and (6), respectively, illustrate the process of line minimization and convergence towards the minimum of the given red curve.

is the minimum of the fitting parabola x, which is computed by the formula [124]:

$$x = b - \frac{1}{2} \frac{(b-a)^2 \left[V(b) - V(c) \right] - (b-c)^2 \left[V(b) - V(a) \right]}{(b-a) \left[V(b) - V(c) \right] - (b-c) \left[V(b) - V(a) \right]}. \tag{B.4}$$

After the current parabola is fitted, we replace one of the ending points a or c by point x (this depends on which side of point b is current x) and the inverse parabolic interpolation is repeated. This process of inverse parabolic interpolation continues until the minimum is found with the given accuracy. An advanced method of line minimization built-up upon the previously presented ones is the Brent's method [124]. It employs the inverse parabolic interpolation (IPI) and changes to the golden section in case that there are problems with IPI. We have explained the basis of the steepest descent (SD) approach and the Brent's line minimization. A further step in advancing the minimization algorithms would be their combination. However, such a combined minimization method is not too efficient in many-dimensional parameter spaces because there is a high chance of SD falling into a zig-zag trajectory, which means that the convergence towards the minimum would be very inefficient. A question rises: how can we eliminate this obstacle of the steepest descent method
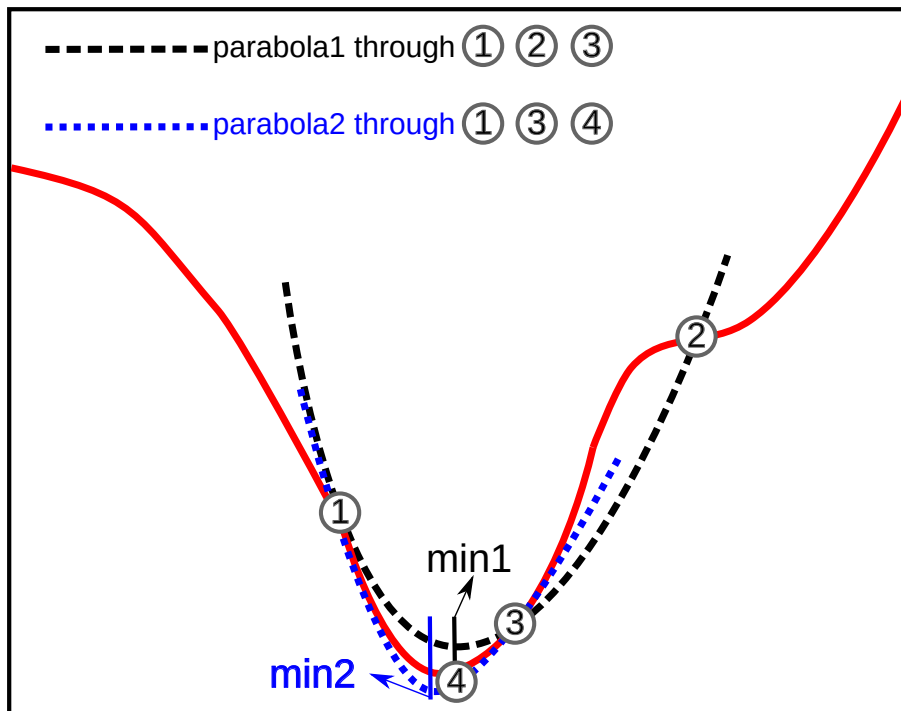
Figure B.2: Inverse parabolic interpolation through the points (1), (2) and (3) via parabola1 leads to the point (4) as that parabola's minimum, noted as *min1*. In the next iteration inverse parabolic interpolation through the points (1), (3) and (4) via parabola2 leads to that parabola's minimum, noted as *min2*, which is closer to the minimum of the red curve which we are looking for. Further inverse parabolic interpolations lead to the convergence towards the minimum of the given red curve.

and achieve efficient convergence? The solution comes with the conjugate gradient (CG) method where a new direction, known as *conjugate* direction, is chosen and it depends on the previous direction, hence the zig-zag trajectory can be avoided. Let us explain what does it mean to have two directions that are conjugate. Let us take an arbitrary function $f(\vec{x})$ where the argument $\vec{x}$ is N-dimensional and write down its Taylor series around a certain point $\vec{T}$ [125]:

$$f(\vec{x}) = f\left(\vec{T}\right) + \sum_i \frac{\partial f}{\partial x_i} x_i + \frac{1}{2} \sum_{i,j} \frac{\partial^2 f}{\partial x_i \partial x_j} x_i x_j + ... \approx c - \vec{b} \cdot \vec{x} + \frac{1}{2}\vec{x} \cdot \mathbf{A} \cdot \vec{x}, \quad \text{(B.5)}$$

where the scalar c is defined as $c = f\left(\vec{T}\right)$, the vector $\vec{b}$ is defined as $\vec{b} = -\nabla f|_T$ and the matrix $\mathbf{A}$ is defined as $\mathbf{A} = \frac{\partial^2 f}{\partial x_i \partial x_j}|_T$ and it is known as the *Hessian matrix*. Let us label the previous direction of movement as $\vec{u}$ and the gradient as $\vec{g}$. We want to

determine the next direction of movement $\vec{v}$. Bearing in mind that the gradient and the previous direction of movement in a current point are orthogonal, i.e., $\vec{g} \cdot \vec{u} = 0$ and that we want, after the next step, new gradient to be orthogonal to the previous direction of movement, i.e., $\vec{g^*} \cdot \vec{u} = 0$, we come up with the condition:

$$\vec{u} \cdot \delta\left(\nabla f\right) = 0 \tag{B.6}$$

which means that the change of the gradient labeled as $\delta\left(\nabla f\right)$ should be also perpendicular to the previous direction of movement $vecu$. We start the derivation from the quadratic form of the function f, which is given as: $f\left(\vec{x}\right) = c - \vec{b} \cdot \vec{x} + \frac{1}{2}\vec{x} \cdot \mathbf{A} \cdot \vec{x}$. The gradient of the function f derived from its quadratic form is:

$$\nabla f = \mathbf{A} \cdot \vec{x} - \vec{b}. \tag{B.7}$$

Now from the Equation B.7 we calculate the change of the gradient ∇f along a certain distance labeled as $\delta\vec{x}$ is:

$$\delta\left(\nabla f\right) = \mathbf{A} \cdot \delta\vec{x} \tag{B.8}$$

and now by setting that $\delta\vec{x}$ corresponds to the new direction of movement $\vec{v}$, i.e., $\delta\vec{x} = \vec{v}$, we return to Equation B.6:

$$\vec{u} \cdot \delta\left(\nabla f\right) = \vec{u} \cdot \mathbf{A} \cdot \vec{v} = 0. \tag{B.9}$$

Summing up the previous discussion, if the relation $\vec{u} \cdot \mathbf{A} \cdot \vec{v} = 0$ holds, we say that the directions $\vec{u}$ and $\vec{v}$ are conjugate. The main task of the CG method is the computation of the new direction along which to move, hence the two vectors $\vec{g}$ and $\vec{h}$ are used for the realization of this task. At the start, there are arbitrary initial vectors $\vec{g}_0$ and $\vec{h}_0 = \vec{g}_0$. The next equations define how are they iterated $(i = 0, 1, 2, 3, ...)$ [124]:

$$\vec{g}_{i+1} = \vec{g}_i - \lambda_i\left(\mathbf{A} \cdot \vec{h}_i\right), \vec{h}_{i+1} = \vec{g}_{i+1} + \gamma_i\vec{h}_i. \tag{B.10}$$

In Equation B.10 scalars λ_i and γ_i are figuring, they are defined as [124]:

$$\lambda_i = \frac{\vec{g}_i \cdot \vec{g}_i}{\vec{h}_i \cdot \mathbf{A} \cdot \vec{h}_i} = \frac{\vec{g}_i \cdot \vec{h}_i}{\vec{h}_i \cdot \mathbf{A} \cdot \vec{h}_i} \tag{B.11}$$

and

$$\gamma_i = \frac{\vec{g}_{i+1} \cdot \vec{g}_{i+1}}{\vec{g}_i \cdot \vec{g}_i}. \tag{B.12}$$

Those vectors $\vec{g}$ and $\vec{h}$ fulfill the orthogonality and conjugation conditions [124]:

$$\vec{g}_i \cdot \vec{g}_j = 0, \vec{h}_i \cdot \mathbf{A} \cdot \vec{h}_j = 0, \vec{g}_i \cdot \vec{h}_j = 0 \tag{B.13}$$

From Equations B.10, B.11, B.12 and B.13, by knowing the Hessian matrix $\mathbf{A}$, we are able to determine successive conjugate directions $\vec{h}_i$ along which the line minimization is conducted. With n such steps, where n is the dimensionality of the problem, we can find the minimum of the quadratic form $f\vec{x}$. However, since the dimensions of the Hessian matrix $\mathbf{A}$ are $3N \times 3N$, the dimensionality of the problem is $n = 3N$ in case of energy minimization of an MD system with N particles. It is highly inefficient to operate with the Hessian matrix in case of MD systems since the number of particles in the system N can be up to 10^6. Hopefully, there is a theorem which solves the problem by circumventing the usage of the Hessian matrix $\mathbf{A}$. It claims that if we minimize the function f in the direction $\vec{h}$ to a point $\vec{x}_{i+1}$, the new gradient can be calculated as [124]:

$$\vec{g}_{i+1} = -\nabla f\left(\vec{x}_{i+1}\right) \tag{B.14}$$

In that case, this vector $\vec{g}_{i+1}$ would be the same as if it had been determined via Equation B.10. More details and the proof of this theorem can be found in the chapter 10 "Minimization or maximization of functions" of the book [124]. Based on the previously presented equations we can come up with a sketch of the CG algorithm for the energy minimization of an MD system consisting of N particles [125]:

Step(0): start from the point $\vec{r}_0$ setting up $j = 0$, $V_0 = V(\vec{r}_0)$, $\vec{q}_0 = -\nabla V(\vec{r}_0)$, $\vec{g}_0 = \vec{h}_0 = \vec{q}_0$
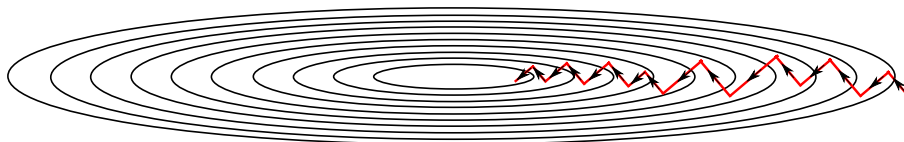
Figure B.3: Steepest descent method can easily fall into a zig-zag trajectory.

Step(1): minimize $V\left(\vec{r}_{j} + \alpha \vec{q}_{j}\right)$ with respect to the scalar α, after that update $\vec{r}_{j+1} = \vec{r}_{j} + \alpha \vec{q}_{j}$ and compute $V\left(j+1\right) = V\left(\vec{r}_{j+1}\right)$

Step(2): if $V_{j+1} - V_{j} < \epsilon$ (where ϵ is the chosen convergence tolerance, usually at the order of 10^{-6}) then end the algorithm

Step(3): compute $\vec{q}_{j} = -\nabla V\left(\vec{r}_{j+1}\right)$ and set $V_{j} = V\left(\vec{r}_{j+1}\right)$

Step(4): compute $\gamma = \vec{q}_{j} \cdot \vec{q}_{j} / \vec{g}_{j} \cdot \vec{g}_{j}$

Step(5): set $\vec{g}_{j+1} = \vec{q}_{j}$

Step(6): set $\vec{h}_{j+1} = \vec{g}_{j+1} + \gamma \vec{h}_{j}$ and $\vec{q}_{j+1} = \vec{h}_{j+1}$

Step(7): increase the counter of iterations: $j = j + 1$ and return to the step(1)

The algorithm we have presented is known as *Fletcher-Reeves* algorithm. Sometimes it is more efficient to use its modification, known as *Polak-Ribiere* algorithm. The only difference between the two algorithms is in the step (4) which is in the later case [125]:

Step(4)∗: compute $\gamma = \left(\vec{q}_{j} + \vec{g}_{j}\right) \cdot \vec{q}_{j} / \vec{g}_{j} \cdot \vec{g}_{j}$.

As a concluding remark, CG method is efficient in finding a local minimum and it is often the method of choice in MD simulations.

Bibliography

[1] Weijia Wen, Ning Wang, D. W. Zheng, C. Chen, and K. N. Tu, Two- and three-dimensional arrays of magnetic microspheres, *Journal of Materials Research* **14**(4), 1186–1189 (1999). 2

[2] David J Sellmyer, Applied physics: Strong magnets by self-assembly, *Nature* **420**(6914), 374–375 (2002). 2

[3] George M. Whitesides and Bartosz Grzybowski, Self-assembly at all scales, *Science* **295**(5564), 2418–2421 (2002). 2

[4] Ken F Jarrell and Mark J McBride, The surprisingly diverse ways that prokaryotes move, *Nature Reviews Microbiology* **6**(6), 466 (2008). 3

[5] Iain M Cheeseman and Arshad Desai, Molecular architecture of the kinetochore–microtubule interface, *Nature Reviews Molecular Cell Biology* **9**(1), 33 (2008). 3

[6] Jonathon Howard and Anthony A Hyman, Growth, fluctuation and switching at microtubule plus ends, *Nature Reviews Molecular Cell Biology* **10**(8), 569–574 (2009). 3

[7] X. B Zhang, X. F Zhang, D Bernaerts, G. van Tendeloo, S Amelinckx, J. van Landuyt, V Ivanov, J. B Nagy, Ph Lambin, and A. A Lucas, The texture of catalytically grown coil-shaped carbon nanotubes, *Europhysics Letters (EPL)* **27**(2), 141–146 (1994). 3

[8] Shawn M Douglas, James J Chou, and William M Shih, Dna-nanotube-induced alignment of membrane proteins for nmr structure determination,

Proceedings of the National Academy of Sciences **104**(16), 6644–6648 (2007). 3

[9] G Daniel Lilly, Ashish Agarwal, Sudhanshu Srivastava, and Nicholas A Kotov, Helical assemblies of gold nanoparticles, *Small* **7**(14), 2004–2009 (2011). 3

[10] Toshimi Shimizu, Mitsutoshi Masuda, and Hiroyuki Minamikawa, Supramolecular nanotube architectures based on amphiphilic molecules, *Chemical reviews* **105**(4), 1401–1444 (2005). 3

[11] Yohei Yamamoto, Takanori Fukushima, Yuki Suna, Noriyuki Ishii, Akinori Saeki, Shu Seki, Seiichi Tagawa, Masateru Taniguchi, Tomoji Kawai, and Takuzo Aida, Photoconductive coaxial nanotubes of molecularly connected electron donor and acceptor layers, *Science* **314**(5806), 1761–1764 (2006). 3

[12] Wei Zhuang, Edis Kasëmi, Yi Ding, Martin Kröger, A Dieter Schlüter, and Jürgen P Rabe, Self-folding of charged single dendronized polymers, *Advanced Materials* **20**(17), 3204–3210 (2008). 3

[13] E Alphandéry, Y Ding, AT Ngo, ZL Wang, LF Wu, and MP Pileni, Assemblies of aligned magnetotactic bacteria and extracted magnetosomes: what is the main factor responsible for the magnetic anisotropy?, *ACS Nano* **3**(6), 1539–1547 (2009). 3

[14] Peter Atkins and Julio De Paula, *Physical chemistry for the life sciences*, Oxford University Press, USA (2011). 3

[15] Molly M Bloomfield, Lawrence J Stephens, et al., *Chemistry and the living organism*, J. Wiley (1996). 3

[16] Hao Zeng, Jing Li, J Ping Liu, Zhong L Wang, and Shouheng Sun, Exchange-coupled nanocomposite magnets by nanoparticle self-assembly, *Nature* **420**(6914), 395 (2002). 3

[17] Mila Boncheva, Stefan A Andreev, L Mahadevan, Adam Winkleman, David R Reichman, Mara G Prentiss, Sue Whitesides, and George M Whitesides, Mag-

netic self-assembly of three-dimensional surfaces from planar sheets, *Proceedings of the National Academy of Sciences* **102**(11), 3924–3929 (2005). 3

[18] Taisia A Prokopieva, Victor A Danilov, Sofia S Kantorovich, and Christian Holm, Ground state structures in ferrofluid monolayers, *Phys. Rev. E: Stat. Phys., Plasmas, Fluids, Relat. Interdiscip. Top.* **80**(3), 031404 (2009). 3

[19] Gurvinder Singh, Henry Chan, Artem Baskin, Elijah Gelman, Nikita Repnin, Petr Král, and Rafal Klajn, Self-assembly of magnetite nanocubes into helical superstructures, *Science* p. 1254132 (2014). 3

[20] Djamal Zerrouki, Jean Baudry, David Pine, Paul Chaikin, and Jérôme Bibette, Chiral colloidal clusters, *Nature* **455**(7211), 380 (2008). 3

[21] Galen T Pickett, Mark Gross, and Hiroko Okuyama, Spontaneous chirality in simple systems, *Physical Review Letters* **85**(17), 3652 (2000). 3

[22] EC Oğuz, R Messina, and H Löwen, Helicity in cylindrically confined yukawa systems, *Europhysics Letters (EPL)* **94**(2), 28005 (2011). 3

[23] Matthew A Lohr, Ahmed M Alsayed, Bryan G Chen, Zexin Zhang, Randall D Kamien, and Arjun G Yodh, Helical packings and phase transformations of soft spheres in cylinders, *Phys. Rev. E: Stat. Phys., Plasmas, Fluids, Relat. Interdiscip. Top.* **81**(4), 040401 (2010). 3

[24] Andreas Mershin, Alexandre A Kolomenski, Hans A Schuessler, and Dimitri V Nanopoulos, Tubulin dipole moment, dielectric constant and quantum behavior: computer simulations, experimental results and suggestions, *Biosystems* **77**(1-3), 73–85 (2004). 3

[25] Erik D Spoerke, George D Bachand, Jun Liu, Darryl Sasaki, and Bruce C Bunker, Directing the polar organization of microtubules, *Langmuir* **24**(14), 7039–7043 (2008). 4

[26] Michal Cifra, Jirí Pokornỳ, Daniel Havelka, and O Kučera, Electric field generated by axial longitudinal vibration modes of microtubule, *BioSystems* **100**(2), 122–131 (2010). 4

[27] IS Jacobs and CP Bean, An approach to elongated fine-particle magnets, *Physical Review* **100**(4), 1060 (1955). 4

[28] P. G. de Gennes and P. A. Pincus, Pair correlations in a ferromagnetic colloid, *Physik der kondensierten Materie* **11**(3), 189–198 (1970). 4

[29] René Messina, Lara Abou Khalil, and Igor Stanković, Self-assembly of magnetic balls: From chains to tubes, *Phys. Rev. E: Stat. Phys., Plasmas, Fluids, Relat. Interdiscip. Top.* **89**(1), 011202 (2014). 4, 34, 41, 43, 46, 48

[30] Dominic Vella, Emmanuel du Pontavice, Cameron L Hall, and Alain Goriely, The magneto-elastica: from self-buckling to self-assembly, In *Proc. R. Soc. London, Ser. A* volume 470 p. 20130609 (2014). 4

[31] David Tománek, Seong Gon Kim, Philippe Jund, Peter Borrmann, Heinrich Stamerjohanns, and Eberhard R. Hilf, Self-assembly of magnetic nanostructures, *Zeitschrift für Physik D Atoms, Molecules and Clusters* **40**(1), 539–541 (1997). 4

[32] Gergő Pál, Ferenc Kun, Imre Varga, Dóra Sohler, and Gang Sun, Attraction-driven aggregation of dipolar particles in an external magnetic field, *Phys. Rev. E: Stat. Phys., Plasmas, Fluids, Relat. Interdiscip. Top.* **83**(6), 061504 (2011). 4

[33] Vikash Malik, Andrei V Petukhov, Le He, Yadong Yin, and Marius Schmidt, Colloidal crystallization and structural changes in suspensions of silica/magnetite core–shell nanoparticles, *Langmuir* **28**(41), 14777–14783 (2012). 4

[34] Nicolas Vandewalle and Stéphane Dorbolo, Magnetic ghosts and monopoles, *New Journal of Physics* **16**(1), 013050 (2014). 4

[35] D. A. Wood, C. D. Santangelo, and A. D. Dinsmore, Self-assembly on a cylinder: a model system for understanding the constraint of commensurability, *Soft Matter* **9**, 10016–10024 (2013). 4, 21

[36] Bharat Bhushan, Jacob N Israelachvili, and Uzi Landman, Nanotribology: friction, wear and lubrication at the atomic scale, *Nature* **374**(6523), 607 (1995). 7, 12, 96, 102

[37] Seong-Jun Heo, Susan B Sinnott, Donald W Brenner, and Judith A Harrison, Computational modeling of nanometer-scale tribology, In *Nanotribology and Nanomechanics* pages 623–691. Springer (2005). 7

[38] Kenneth Holmberg, Peter Andersson, and Ali Erdemir, Global energy consumption due to friction in passenger cars, *Tribology International* **47**, 221–234 (2012). 7, 10, 11

[39] Ana C. F. Mendonça, Agílio A. H. Pádua, and Patrice Malfreyt, Nonequilibrium molecular simulations of new ionic lubricants at metallic surfaces: Prediction of the friction, *Journal of Chemical Theory and Computation* **9**(3), 1600–1610 (2013). 7, 9, 13, 65, 70, 107, 108, 114

[40] D. M. Heyes, E. R. Smith, D. Dini, H. A. Spikes, and T. A. Zaki, Pressure dependence of confined liquid behavior subjected to boundary-driven shear, *The Journal of Chemical Physics* **136**(13) (2012). 7, 13

[41] Chiara Gattinoni, David M. Heyes, Christian D. Lorenz, and Daniele Dini, Traction and nonequilibrium phase behavior of confined sheared liquids at high pressure, *Phys. Rev. E: Stat. Phys., Plasmas, Fluids, Relat. Interdiscip. Top.* **88**, 052406 (2013). 7, 13

[42] Laetitia Martinie and Philippe Vergne, Lubrication at extreme conditions: A discussion about the limiting shear stress concept, *Tribology Letters* **63**(2) (2016). 7, 13, 111

[43] Nicolas Voeltzel, Andrew Giuliani, Nicolas Fillot, Philippe Vergne, and Laurent Joly, Nanolubrication by ionic liquids: molecular dynamics simulations reveal an anomalous effective rheology, *Physical Chemistry Chemical Physics* **17**, 23226–23235 (2015). 7, 9, 13, 66

[44] Feng Zhou, Yongmin Liang, and Weimin Liu, Ionic liquid lubricants: designed chemistry for engineering applications, *Chemical Society Reviews* **38**(9), 2590–2599 (2009). 8, 9, 11, 12

[45] K Mistry, M F Fox, and M Priest, Lubrication of an electroplated nickel matrix silicon carbide coated eutectic aluminium—silicon alloy automotive cylinder bore with an ionic liquid as a lubricant additive, *Proceedings of the Institution of Mechanical Engineers, Part J: Journal of Engineering Tribology* **223**(3), 563–569 (2009). 8

[46] Jun Qu, Dinesh G Bansal, Bo Yu, Jane Y Howe, Huimin Luo, Sheng Dai, Huaqing Li, Peter J Blau, Bruce G Bunting, Gregory Mordukhovich, et al., Antiwear performance and mechanism of an oil-miscible ionic liquid as a lubricant additive, *ACS applied materials & interfaces* **4**(2), 997–1002 (2012). 8

[47] Jun Qu, Peter J Blau, Sheng Dai, Huimin Luo, and Harry M Meyer, Ionic liquids as novel lubricants and additives for diesel engine applications, *Tribology Letters* **35**(3), 181–189 (2009). 8

[48] María-Dolores Bermúdez, Ana-Eva Jiménez, José Sanes, and Francisco-José Carrión, Ionic liquids as advanced lubricant fluids, *Molecules* **14**(8), 2888–2908 (2009). 8

[49] Oscar Yovany Fajardo, Fernando Bresme, Alexei A Kornyshev, and Michael Urbakh, Electrotunable friction with ionic liquid lubricants: how important is the molecular structure of the ions?, *The Journal of Physical Chemistry Letters* **6**(20), 3998–4004 (2015). 8, 9, 10, 65, 66, 68, 71, 72, 73, 74, 75, 90

[50] Robert Hayes, Gregory G Warr, and Rob Atkin, At the interface: solvation and designing ionic liquids, *Physical Chemistry Chemical Physics* **12**(8), 1709–1723 (2010). 9

[51] OY Fajardo, F Bresme, AA Kornyshev, and M Urbakh, Electrotunable lu-

bricity with ionic liquid nanoscale films, *Scientific Reports* **5** (2015). 9, 10, 65, 66, 68, 69, 72, 74, 75

[52] R Capozza, A Vanossi, A Benassi, and E Tosatti, Squeezout phenomena and boundary layer formation of a model ionic liquid under confinement and charging, *The Journal of Chemical Physics* **142**(6), 064707 (2015). 9, 10, 65, 66, 68, 69, 71, 73, 74, 76, 77

[53] Christian Dold, Tobias Amann, and Andreas Kailer, Influence of structural variations on imidazolium-based ionic liquids, *Lubrication Science* **4**(25), 251–268 (2013). 9, 12, 74, 136

[54] F. Varnik, L. Bocquet, J.-L. Barrat, and L. Berthier, Shear localization in a model glass, *Physical Review Letters* **90**, 095702 (2003). 9

[55] Anatolii V. Mokshin and Jean-Louis Barrat, Shear-induced crystallization of an amorphous system, *Phys. Rev. E: Stat. Phys., Plasmas, Fluids, Relat. Interdiscip. Top.* **77**, 021505 (2008). 9

[56] Filippo Federici Canova, Hiroki Matsubara, Masashi Mizukami, Kazue Kurihara, and Alexander L. Shluger, Shear dynamics of nanoconfined ionic liquids, *Physical Chemistry Chemical Physics* **16**, 8247–8256 (2014). 9, 13, 66, 107, 108, 114

[57] Jianping Gao, W. D. Luedtke, D. Gourdon, M. Ruths, J. N. Israelachvili, and Uzi Landman, Frictional forces and amontons' law: From the molecular to the macroscopic scale, *The Journal of Physical Chemistry B* **108**(11), 3410–3425 (2004). 10, 13

[58] Mark O Robbins and Martin H Müser, Computer simulations of friction, lubrication, and wear, In Bharat Bhushan, editor, *Modern Tribology Handbook, Two Volume Set* Mechanics & Materials Science. CRC Press (2000). 10, 13

[59] R. E. Rudd and J. Q. Broughton, Coarse-grained molecular dynamics and the atomic limit of finite elements, *Physical Review B* **58**, R5893–R5896 (1998). 10, 13

[60] Y. Wang, W. Jiang, T. Yan, and G. A. Voth, Understanding ionic liquids through atomistic and coarse-grained molecular dynamics simulations, *Accounts of Chemical Research* **40**(11), 1193–1199 (2007). 10, 13

[61] Zhantao Wang and Craig Priest, Impact of nanoscale surface heterogeneity on precursor film growth and macroscopic spreading of [rmim][ntf2] ionic liquids on mica, *Langmuir* **29**(36), 11344–11353 (2013). 10, 12

[62] David A Beattie, Rosa M Espinosa-Marzal, Tracey TM Ho, Mihail N Popescu, John Ralston, Ce´line JE Richard, Pasindu MF Sellapperumage, and Marta Krasowska, Molecularly-thin precursor films of imidazolium-based ionic liquids on mica, *The Journal of Physical Chemistry C* **117**(45), 23676–23684 (2013). 10, 12

[63] Alexander M Smith, Kevin RJ Lovelock, Nitya Nand Gosvami, Tom Welton, and Susan Perkin, Quantized friction across ionic liquid thin films, *Physical Chemistry Chemical Physics* **15**(37), 15317–15320 (2013). 10, 12, 93

[64] Konstantinos Gkagkas, Veerapandian Ponnuchamy, Miljan Dašić, and Igor Stanković, Molecular dynamics investigation of a model ionic liquid lubricant for automotive applications, *Tribology International* **113**, 83–91 (2017). 10, 11, 68, 69, 70, 71, 72, 74, 92, 117, 118, 136

[65] W Liu, C Ye, Y Chen, Z Ou, and DC Sun, Tribological behavior of sialon ceramics sliding against steel lubricated by fluorine-containing oils, *Tribology International* **35**(8), 503–509 (2002). 11

[66] AS Pensado, MJP Comunas, and J Fernández, The pressure–viscosity coefficient of several ionic liquids, *Tribology Letters* **31**(2), 107–118 (2008). 12

[67] Ichiro Minami, Ionic liquids in tribology, *Molecules* **14**(6), 2286–2305 (2009). 12, 74

[68] Ibrahim Bou-Malham and Lionel Bureau, Nanoconfined ionic liquids: effect of surface charges on flow and molecular layering, *Soft Matter* **6**(17), 4062–4065 (2010). 12

[69] Anthony E. Somers, Patrick C. Howlett, Douglas R. MacFarlane, and Maria Forsyth, A review of ionic liquid lubricants, *Lubricants* **1**(1) (2013). 12, 92, 93, 96, 102

[70] Hideto Kamimura, Takeru Chiba, Tomoo Kubo, Hidetaka Nanao, Ichiro Minami, and Shigeyuki Mori, Relationship between structure and tribological properties of ionic liquids composed of imidazolium cations, *Japanese Journal of Tribology* **51**(6), 675–687 (2006). 12

[71] Susan Perkin, Lorna Crowhurst, Heiko Niedermeyer, Tom Welton, Alexander M Smith, and Nitya Nand Gosvami, Self-assembly in the electrical double layer of ionic liquids, *Chemical Communications* **47**(23), 6572–6574 (2011). 12, 126

[72] Haizhong Wang, Qiming Lu, Chengfeng Ye, Weimin Liu, and Zhaojie Cui, Friction and wear behaviors of ionic liquid of alkylimidazolium hexafluorophosphates as lubricants for steel/steel contact, *Wear* **256**(1-2), 44–48 (2004). 13

[73] AE Jiménez, MD Bermudez, P Iglesias, FJ Carrión, and G Martínez-Nicolás, 1-n-alkyl-3-methylimidazolium ionic liquids as neat lubricants and lubricant additives in steel–aluminium contacts, *Wear* **260**(7-8), 766–782 (2006). 13

[74] Zonggang Mu, Feng Zhou, Shuxiang Zhang, Yongmin Liang, and Weimin Liu, Effect of the functional groups in ionic liquid molecules on the friction and wear behavior of aluminum alloy in lubricated aluminum-on-steel contact, *Tribology International* **38**(8), 725–731 (2005). 13

[75] Igor Stanković, Miljan Dašić, and René Messina, Structure and cohesive energy of dipolar helices, *Soft Matter* **12**, 3056–3065 (2016). 15

[76] Wolfram Research, Inc., Mathematica, Version 11.3, Champaign, IL, 2018. 21, 147, 149, 161

[77] William Thomson Baron Kelvin, *The molecular tactics of a crystal*, Clarendon Press (1894). 22

[78] Simon W de Leeuw, John William Perram, and Edgar Roderick Smith, Simulation of electrostatic systems in periodic boundary conditions. i. lattice sums and dielectric constants, *Proceedings of the Royal Society of London. Series A, Mathematical and Physical Sciences* **373**(1752), 27–56 (1980). 30, 31

[79] DM Heyes, The surface potential of point charge and point dipole lattices, *Surface Science Letters* **110**(2), L619–L624 (1981). 30, 31

[80] David M Heyes, Pressure tensor of partial-charge and point-dipole lattices with bulk and surface geometries, *Physical Review B* **49**(2), 755 (1994). 30, 31

[81] A Grzybowski, E Gwóźdź, and A Bródka, Ewald summation of electrostatic interactions in molecular dynamics of a three-dimensional system with periodicity in two directions, *Physical Review B* **61**(10), 6706 (2000). 30, 31

[82] A Grzybowski and A Bródka, Computationally efficient method for summing interactions of point dipoles in three dimensions with two-dimensional periodicity, *Chemical Physics Letters* **361**(3-4), 329–333 (2002). 30, 31

[83] A Bródka and A Grzybowski, Electrostatic interactions in computer simulations of a three-dimensional system periodic in two directions: Ewald-type summation, *The Journal of Chemical Physics* **117**(18), 8208–8211 (2002). 30, 31

[84] A Bródka, Ewald type summation method for electrostatic interactions in computer simulations of a three-dimensional system periodic in one direction, *Chemical Physics Letters* **363**(5-6), 604–609 (2002). 30, 31

[85] John Lekner, Summation of coulomb fields in computer-simulated disordered systems, *Physica A: Statistical Mechanics and its Applications* **176**(3), 485–498 (1991). 31

[86] AT Clark, TJ Madden, and PB Warren, Summation of electrostatic interactions in quasi-two-dimensional simulations, *Molecular Physics* **87**(5), 1063–1069 (1996). 31

[87] SY Liem and JH R Clarke, Calculation of coulomb interactions in two-dimensionally periodic systems, *Molecular Physics* **92**(1), 19–25 (1997). 31

[88] Niels Gronbech-Jensen, Gerhard Hummer, and Keith M Beardmore, Lekner summation of coulomb interactions in partially periodic systems, *Molecular Physics* **92**(5), 941–946 (1997). 31

[89] A Grzybowski and A Bródka, Electrostatic interactions in molecular dynamics simulation of a three-dimensional system with periodicity in one direction, *Molecular Physics* **100**(5), 635–639 (2002). 31, 147, 170

[90] A Grzybowski and A Bródka, Coulomb interactions in a computer simulation of a system periodic in two directions, *Molecular Physics* **100**(7), 1017–1023 (2002). 31

[91] A Grzybowski and A Bróadka, Lekner type method for summing the dipole—dipole interactions in computer simulations of one- and two-dimensionally periodic systems, *Molecular Physics* **101**(8), 1079–1088 (2003). 31, 32

[92] L Assoud and R Messina, Penalty method to predict crystal structures involving hard-core interactions, *Phys. Rev. E: Stat. Phys., Plasmas, Fluids, Relat. Interdiscip. Top.* **83**(3), 036113 (2011). 34

[93] fmincon description, https://www.mathworks.com/help/optim/ug/fmincon.html. 34, 35, 36

[94] K De'Bell, AB MacIsaac, IN Booth, and JP Whitehead, Dipolar-induced planar anisotropy in ultrathin magnetic films, *Physical Review B* **55**(22), 15108 (1997). 37

[95] Sona Prakash and Christopher L Henley, Ordering due to disorder in dipolar magnets on two-dimensional lattices, *Physical Review B* **42**(10), 6574 (1990). 37

[96] Igor Stanković, Miljan Dašić, Jorge A. Otálora, and Carlos García, A platform for nanomagnetism – assembled ferromagnetic and antiferromagnetic dipolar tubes, *Nanoscale* **11**, 2521–2535 (2019). 39

[97] René Messina and Igor Stanković, Assembly of magnetic spheres in strong homogeneous magnetic field, *Physica A: Statistical Mechanics and its Applications* **466**, 10–20 (2017). 42

[98] Steve Plimpton, Fast parallel algorithms for short-range molecular dynamics, *Journal of Computational Physics* **117**(1), 1–19 (1995). 51, 64

[99] Michael Rubinstein, Ralph H Colby, et al., *Polymer physics* volume 23, Oxford university press New York (2003). 51, 56, 59, 63

[100] Ju Li, Basic molecular dynamics, In *Handbook of Materials Modeling* pages 565–588. Springer (2005). 52

[101] William Humphrey, Andrew Dalke, and Klaus Schulten, VMD – Visual Molecular Dynamics, *Journal of Molecular Graphics* **14**, 33–38 (1996). 64, 65

[102] Jiri Kolafa and John W Perram, Cutoff errors in the ewald summation formulae for point charge systems, *Molecular Simulation* **9**(5), 351–368 (1992). 64

[103] David S Cerutti, Robert E Duke, Thomas A Darden, and Terry P Lybrand, Staggered mesh ewald: an extension of the smooth particle-mesh ewald method adding great versatility, *Journal of Chemical Theory and Computation* **5**(9), 2322–2338 (2009). 64

[104] David J Hardy, John E Stone, and Klaus Schulten, Multilevel summation of electrostatic potentials using graphics processing units, *Parallel Computing* **35**(3), 164–177 (2009). 64, 69

[105] Jianping Gao, W. D. Luedtke, and Uzi Landman, Layering transitions and dynamics of confined liquid films, *Physical Review Letters* **79**, 705–708 (1997). 68, 92, 93

[106] Murray S Daw and Michael I Baskes, Embedded-atom method: Derivation and application to impurities, surfaces, and other defects in metals, *Physical Review B* **29**(12), 6443 (1984). 69

[107] Igor Stankovic, Siegfried Hess, and Martin Kröger, Structural changes and viscoplastic behavior of a generic embedded-atom model metal in steady shear flow, *Phys. Rev. E: Stat. Phys., Plasmas, Fluids, Relat. Interdiscip. Top.* **69**(2), 021509 (2004). 69

[108] Astrid Gubbels-Elzas and Barend J Thijsse, Ionic motion during field-assisted oxidation of aluminium studied by molecular dynamics simulations, *Computational Materials Science* **90**, 196–202 (2014). 69

[109] F. Iori and S. Corni, Including image charge effects in the molecular dynamics simulations of molecules on metal surfaces, *Journal of Computational Chemistry* **29**(10), 1656–1666 (2008). 69

[110] Miljan Dašić, Igor Stanković, and Konstantinos Gkagkas, Molecular dynamics investigation of the influence of the shape of the cation on the structure and lubrication properties of ionic liquids, *Physical Chemistry Chemical Physics* **21**, 4375–4386 (2019). 71

[111] Dašić, Miljan, Stanković, Igor, and Gkagkas, Konstantinos, Influence of confinement on flow and lubrication properties of a salt model ionic liquid investigated with molecular dynamics, *The European Physical Journal E* **41**(11), 130 (2018). 71

[112] Sébastien Viscardy, James Servantie, and Pierre Gaspard, Transport and helfand moments in the lennard-jones fluid. i. shear viscosity, *The Journal of Chemical Physics* **126**(18), 184512 (2007). 79

[113] Denis J Evans and GP Morriss, Nonlinear-response theory for steady planar couette flow, *Physical Review A* **30**(3), 1528 (1984). 79

[114] Peter J Daivis and BD Todd, A simple, direct derivation and proof of the

validity of the sllod equations of motion for generalized homogeneous flows, *The Journal of Chemical Physics* **124**(19), 194103 (2006). 79

[115] Robert Hayes, Gregory G Warr, and Rob Atkin, Structure and nanostructure in ionic liquids, *Chemical Reviews* **115**(13), 6357–6426 (2015). 87

[116] Susan Perkin, Ionic liquids in confined geometries, *Physical Chemistry Chemical Physics* **14**, 5052–5062 (2012). 92, 93, 117

[117] Robert Hayes, Natalia Borisenko, Matthew K Tam, Patrick C Howlett, Frank Endres, and Rob Atkin, Double layer structure of ionic liquids at the au (111) electrode interface: an atomic force microscopy investigation, *The Journal of Physical Chemistry C* **115**(14), 6855–6863 (2011). 93, 118

[118] P. D. Kaplan, J. L. Rouke, A. G. Yodh, and D. J. Pine, Entropically driven surface phase separation in binary colloidal mixtures, *Physical Review Letters* **72**(4), 582–585 (1994). 96

[119] Scott Bair, Laetitia Martinie, and Philippe Vergne, Classical ehl versus quantitative ehl: A perspective part ii—super-arrhenius piezoviscosity, an essential component of elastohydrodynamic friction missing from classical ehl, *Tribology Letters* **63**(3), 37 (2016). 107, 136

[120] Kamil Paduszyn´ski and Urszula Doman´ska, Viscosity of ionic liquids: an extensive database and a new group contribution model based on a feedforward artificial neural network, *Journal of Chemical Information and Modeling* **54**(5), 1311–1324 (2014). 143

[121] IS Gradshteyn and IM Ryzhik, *Table of integrals, series and products (New York: Academic)*, Elsevier (1980). 147

[122] Erwin Madelung, *Die mathematischen hilfsmittel des physikers* volume 4, Springer-Verlag (2013). 148

[123] Milton Abramowitz and Irene A Stegun, *Handbook of mathematical functions: with formulas, graphs, and mathematical tables* volume 55, Courier Corporation (1965). 149, 163, 167, 170

[124] William H Press, Saul A Teukolsky, William T Vetterling, and Brian P Flannery, *Numerical recipes in C* volume 2, Cambridge university press Cambridge (1982). 171, 172, 173, 175, 176

[125] Introduction to atomistic simulations 2008, `http://www.acclab.helsinki.fi/~aakurone/atomistiset/lecturenotes/lecture_all.pdf`. 171, 174, 176, 177

Publications list

This doctoral thesis is based on the next published journal papers:

[1] I. Stanković, **M. Dašić** and R. Messina, Structure and cohesive energy of dipolar helices, *Soft Matter* **12**, 3056 (2016).

[2] K. Gkagkas, V. Ponnuchamy, **M. Dašić** and I. Stanković, Molecular dynamics investigation of a model ionic liquid lubricant for automotive applications, *Tribology International* **113**, 83 (2017).

[3] **M. Dašić**, I. Stanković and K. Gkagkas, Influence of confinement on flow and lubrication properties of a salt model ionic liquid investigated with molecular dynamics, *The European Physical Journal E* **41**, 130 (2018).

[4] I. Stanković, **M. Dašić**, J. A. Otálora and C. García, A platform for nanomagnetism - assembled ferromagnetic and antiferromagnetic dipolar tubes, *Nanoscale* **11**, 2521 (2019).

[5] **M. Dašić**, I. Stanković and K. Gkagkas, Molecular dynamics investigation of the influence of the shape of the cation on the structure and lubrication properties of ionic liquids, *Physical Chemistry Chemical Physics* **21**, 4375 (2019).

Biography

Miljan Dašić was born on 3.11.1990. in Paraćin, Republic of Serbia. He has finished elementary school "Momčilo Popović-Ozren" and "Gymnasium Paraćin" in Paraćin, both as the best student of generation. He has won numerous prizes at competitions in physics, mathematics, programming and chemistry. He has participated at Petnica Science Center (PSC) physics seminars. Miljan Dašić was a participant of "SciTech 2009", an international scientific summer programme, held at Technion (Israel Institute of Technology), where he worked on an applied mathematics project. The results of that project he presented together with his teammates at a conference held at Technion in August 2009.

Miljan Dašić graduated at the Faculty of Electrical Engineering, University of Belgrade, in July 2013, with a GPA of 9.93/10.00. His undergraduate thesis is based on the research conducted at the Nanophotonic Systems Laboratory of the University of Colorado Boulder (USA) under the mentorship of Prof. Dr. Miloš Popović. During the undergraduate studies he performed several international internships: in 2011 he participated at "UREKA 2011" summer internship at Tyndall National Institute (Cork, Ireland); in 2012 he worked as a research assistant at University of Colorado (Boulder, USA); in 2013 he participated in IAESTE programme at Lappeenranta University of Technology (Lappeenranta, Finland).

Miljan Dašić completed his master studies at the Faculty of Electrical Engineering, University of Belgrade, in July 2014, with a GPA of 10.00. His master thesis was done in the Scientific Computing Laboratory (SCL) of the Institute of Physics Belgrade (IPB) under the mentorship of Dr. Igor Stanković, in the framework of a bilateral Serbian-French project related to the self-assembly of magnetic particles.

In October 2014, Miljan Dašić started his PhD studies at the Faculty of Physics, University of Belgrade, with specialization in condensed matter physics. Since

November 2014, Miljan Dašić has participated in the National Project No. OI171017 "Modeling and Numerical Simulations of Complex Many-Particle Systems" funded by the Ministry of Education, Science and Technological Development of the Republic of Serbia, under the mentorship of Dr. Igor Stanković. He has realized a six-month internship in the Advanced Technology Division of the Technical Centre of Toyota Motor Europe in Zaventem (Belgium). During that internship he worked on the development of molecular dynamics simulations related to the nanoscopic lubrication performance of ionic liquid lubricants.

Miljan Dašić has participated in the PSC physics seminars as a lecturer and mentor on yearly projects. He has also participated in the National Committee for High School Physics Competitions as a Committee member at National-level competitions. Miljan Dašić has worked as a reviewer for international scientific journals "Tribology International" and "Optical and Quantum Electronics".

Miljan Dašić was elected as the member of the "Club Superste" for the year of 2014, in the field of natural sciences, on a competition organized by the ERSTE bank, with the goal of supporting young talents of Serbia. At the international IEEESTEC conference, held in November 2014 at the Faculty of Electronics (Niš, Serbia), he won the "Best paper award".

During his PhD studies Miljan Dašić published five papers in high quality international scientific journals and participated at several international workshops and conferences.

Прилог 1.

Изјава о ауторству

Име и презиме аутора: **Миљан Дашић**

Број индекса: **8004/2014**

Изјављујем

да је докторска дисертација под насловом

Modeling the behaviour of confined dipolar and ionic systems

(Моделовање понашања просторно ограничених дииолних и јонских система)

- резултат сопственог истраживачког рада;
- да дисертација у целини ни у деловима није била предложена за стицање друге дипломе према студијским програмима других високошколских установа;
- да су резултати коректно наведени и
- да нисам кршио ауторска права и користио интелектуалну својину других лица.

Потпис аутора

У Београду, 30.8.2019.

Прилог 2.

Изјава о истоветности штампане и електронске верзије докторског рада

Име и презиме аутора: **Миљан Дашић**

Број индекса: **8004/2014**

Студијски програм: **Физика кондензоване материје и статистичка физика**

Наслов рада: **Modeling the behaviour of confined dipolar and ionic systems (Моделовање понашања просторно ограничених диполних и јонских система)**

Ментор: **др Игор Станковић**

Изјављујем да је штампана верзија мог докторског рада истоветна електронској верзији коју сам предао за објављивање на порталу **Дигиталног репозиторијума Универзитета у Београду.**

Дозвољавам да се објаве моји лични подаци везани за добијање академског звања доктора наука, као што су име и презиме, година и место рођења и датум одбране рада.

Ови лични подаци могу се објавити на мрежним страницама дигиталне библиотеке, у електронском каталогу и у публикацијама Универзитета у Београду.

У Београду, 30.8.2019.

Потпис аутора

Прилог 3.

Изјава о коришћењу

Овлашћујем Универзитетску библиотеку „Светозар Марковић" да у Дигитални репозиторијум Универзитета у Београду унесе моју докторску дисертацију под насловом:

Modeling the behaviour of confined dipolar and ionic systems (Моделовање понашања просторно ограничених диполних и јонских система)

која је моје ауторско дело.

Дисертацију са свим прилозима предао сам у електронском формату погодном за трајно архивирање.

Моју докторску дисертацију похрањену у Дигитални репозиторијум Универзитета у Београду могу да користе сви који поштују одредбе садржане у одабраном типу лиценце Креативне заједнице (Creative Commons) за коју сам се одлучио.

1. Ауторство (CC BY)

2. Ауторство – некомерцијално (CC BY - NC)

3. Ауторство – некомерцијално – без прераде (CC BY-NC-ND)

4. Ауторство – некомерцијално – делити под истим условима (CC BY-NC-SA)

5. Ауторство – без прераде (CC BY-ND)

6. Ауторство – делити под истим условима (CC BY-SA)

(Молимо да заокружите само једну од шест понуђених лиценци.
Кратак опис лиценци је саставни део ове изјаве).

Потпис аутора

У Београду, 30.8.2019.

1. **Ауторство.** Дозвољавате умножавање, дистрибуцију и јавно саопштавање дела, и прераде, ако се наведе име аутора на начин одређен од стране аутора или даваоца лиценце, чак и у комерцијалне сврхе. Ово је најслободнија од свих лиценци.

2. **Ауторство – некомерцијално.** Дозвољавате умножавање, дистрибуцију и јавно саопштавање дела, и прераде, ако се наведе име аутора на начин одређен од стране аутора или даваоца лиценце. Ова лиценца не дозвољава комерцијалну употребу дела.

3. **Ауторство – некомерцијално – без прераде.** Дозвољавате умножавање, дистрибуцију и јавно саопштавање дела, без промена, преобликовања или употребе дела у свом делу, ако се наведе име аутора на начин одређен од стране аутора или даваоца лиценце. Ова лиценца не дозвољава комерцијалну употребу дела. У односу на све остале лиценце, овом лиценцом се ограничава највећи обим права коришћења дела.

4. **Ауторство – некомерцијално – делити под истим условима.** Дозвољавате умножавање, дистрибуцију и јавно саопштавање дела, и прераде, ако се наведе име аутора на начин одређен од стране аутора или даваоца лиценце и ако се прерада дистрибуира под истом или сличном лиценцом. Ова лиценца не дозвољава комерцијалну употребу дела и прерада.

5. **Ауторство – без прераде.** Дозвољавате умножавање, дистрибуцију и јавно саопштавање дела, без промена, преобликовања или употребе дела у свом делу, ако се наведе име аутора на начин одређен од стране аутора или даваоца лиценце. Ова лиценца дозвољава комерцијалну употребу дела.

6. **Ауторство – делити под истим условима.** Дозвољавате умножавање, дистрибуцију и јавно саопштавање дела, и прераде, ако се наведе име аутора на начин одређен од стране аутора или даваоца лиценце и ако се прерада дистрибуира под истом или сличном лиценцом. Ова лиценца дозвољава комерцијалну употребу дела и прерада. Слична је софтверским лиценцама, односно лиценцама отвореног кода.